

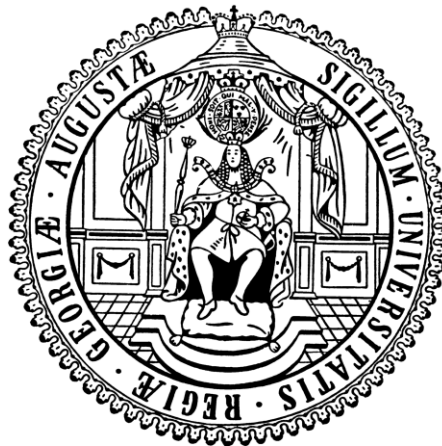
From X-ray diffraction data annealing
to comprehensive charge density analysis

Dissertation

zur Erlangung des mathematisch-naturwissenschaftlichen Doktorgrades

„*Doctor rerum naturalium*“

der Georg-August-Universität Göttingen



Im Promotionsprogramm Catalysis for Sustainable Synthesis (CaSuS)
der Georg August University School of Science (GAUSS)

Vorgelegt von
Jakob Hey
aus Oldenburg/Olb.

Göttingen, 2013

Betreuungsausschuss

Professor Dr. Dietmar Stalke, Institut für Anorganische Chemie der Georg-August-Universität Göttingen

Professor Dr. Franc Meyer, Institut für Anorganische Chemie der Georg-August-Universität Göttingen

Dr. Regine Herbst-Irmer, Arbeitskreis Stalke, Institut für Anorganische Chemie der Georg-August-Universität Göttingen

Mitglieder der Prüfungskommission

Referent: Professor Dr. Dietmar Stalke, Institut für Anorganische Chemie der Georg-August-Universität Göttingen

Korreferent: Professor Dr. Franc Meyer, Institut für Anorganische Chemie der Georg-August-Universität Göttingen

Professor Dr. George M. Sheldrick, Institut für Anorganische Chemie der Georg-August-Universität Göttingen

Juniorprofessor Dr. Guido Clever, Institut für Anorganische Chemie der Georg-August-Universität Göttingen

Privatdozent Dr. Birger Dittrich, Institut für Anorganische und Angewandte Chemie der Universität Hamburg

Juniorprofessor Dr. Ricardo A. Mata, Institut für Physikalische Chemie der Georg-August-Universität Göttingen

Tag der mündlichen Prüfung: 1. Juli 2013

“Under law the Quest for Ultimate Truth is quite clearly the inalienable prerogative of your working thinkers. Any bloody machine goes and actually finds it and we’re straight out of a job aren’t we? I mean what’s the use of our sitting up half the night arguing that there may or may not be a God if this machine only goes and gives us his bleeding phone number the next morning?” – “That’s right!” shouted Vroomfondel, “we demand rigidly defined areas of doubt and uncertainty!”

Douglas Adams, *The Hitchhiker’s Guide to the Galaxy*, Pan Books, UK, 1979.

Table of contents

Abbreviations.....	i
1. Single crystal X-ray diffraction.....	1
1.1. History of X-ray diffraction.....	1
1.2. The diffraction condition.....	1
1.3. The structure factor and the atomic scattering factor.....	3
1.4. Absorption correction, scaling and merging.....	6
1.5. The independent atom model.....	8
1.6. The multipolar refinement.....	8
1.7. Hydrogen atom refinement.....	11
1.8. Difference electron density.....	12
1.9. Observed and calculated structure factor.....	12
1.10. Figures of merit.....	14
1.11. Pitfalls in data collection with modern CCD based detectors.....	14
2. The quantum theory of atoms in molecules (QTAIM).....	19
2.1. Atomic basins.....	19
2.2. Critical points.....	20
2.3. The Laplacian.....	21
2.4. Ellipticity.....	23
2.5. The Source Function.....	23
2.6. The electrostatic potential.....	24
2.7. Non-covalent interactions.....	25
3. Tris(ammine) sodium cyclopentadienide.....	27
3.1. Theoretical work on alkali metal cyclopentadienides.....	27
3.2. Work on alkali metal ammoniacates in our workgroup.....	28
3.3. Data collection and data treatment.....	29
3.4. Structure solution and refinement (IAM).....	31
3.5. Sodium atom shift.....	34
3.6. Hydrogen out-of-plane bending.....	35
3.7. General considerations in the multipole refinement.....	36
3.8. Critical examination of the multipole refinement.....	39
3.9. The significance of the data.....	42
3.10. Refinement of resolution dependent scale factors.....	43
3.11. Preparative calculations.....	46
3.12. Molecular deformation density and Laplacian.....	49
3.13. The Source Function.....	53

3.14. Computational chemistry.....	55
3.15. Intermolecular interactions and the charge density.....	56
3.16. Conclusions.....	58
4. Bis(2-benzothiazolyl)phosphane.....	61
4.1. The importance of phosphanes in catalysis.....	61
4.2. Data collection and data processing.....	63
4.3. Setup and XD2006 refinement.....	64
4.4. Validity of the model; residuals and quality indicators.....	65
4.5. The topology of the Laplacian distribution.....	66
4.6. A few words about aromaticity and its quantification.....	69
4.7. Measures of aromaticity in the QTAIM framework.....	70
4.8. Application of the measures of aromaticity in this thesis.....	71
4.9. The bond ellipticity as an indicator for delocalisation.....	72
4.10. The Source Function as an indicator for delocalisation.....	74
4.11. Delocalisation index calculations.....	82
4.12. NICS and GIMIC calculations.....	85
4.13. About the interpretation of nonbonding VSCCs.....	86
4.14. Intermolecular bond paths.....	89
4.15. Conclusions.....	91
5. <i>N</i> -benzyl-2-(hydroxymethyl)benzamide.....	93
5.1. Data collection and IAM refinement.....	94
5.2. XD2006 multipole refinement.....	95
5.3. Analysis of the atomic graph.....	98
5.4. Bond orders from topological parameters.....	101
5.5. Atomic charges and electrostatic potential.....	101
5.6. Conclusion.....	102
6. Charge density data collection at a synchrotron source.....	103
6.1. Set-up.....	104
6.2. The data collections in April and July, 2012.....	105
6.3. Data integration.....	106
6.4. Merging of the data.....	110
6.5. Refinement and results.....	110
6.6. About possible sources of error.....	114
6.7. Conclusion and outlook.....	116
7. Low-energy contamination in focused X-rays.....	119
7.1. Design of a filter insert.....	119
7.2. A survey on existing datasets.....	120

7.3. Comparison of data collected with and without filter	122
7.4. Conclusions and outlook.....	126
8. Summary and outlook	129
9. Crystal structure determination in collaboration	133
9.1. Crystal selection and manipulation	133
9.2. Data acquisition.....	133
9.3. Data processing.....	133
9.4. Structures determined for Dr. Gašper Tavčar (Prof. Dr. H. W. Roesky).....	135
9.5. Structures determined for Dr. Ramachandran Azhakar (Prof. Dr. H. W. Roesky).....	141
9.6. Structures determined for Dr. Sakya S. Sen (Prof. Dr. H. W. Roesky).....	160
9.7. Structure determined for Sabrina Freye (Prof. Dr. G. Clever)	164
9.8. Structure determined for Muxin Han (Prof. Dr. Clever).....	167
9.9. Structures determined for Marina Frank (Prof. Dr. G. Clever)	168
9.10. Structure determined for Arne Wolpers (Prof. Dr. P. Vana).....	172
10. Appendix.....	173
10.1. Data statistics.....	173
10.2. Topological parameters from QTAIM analysis of 1	174
10.3. Topological parameters from QTAIM analysis of 2	175
10.4. Topological parameters from QTAIM analysis of 3	176
10.5. Laplacian profiles along bond paths of 2	177
10.6. Bond ellipticity profiles in 2	181
10.7. The Source Function quality criterion in calculations on 2	184
10.8. Delocalisation indices in 2	185
10.9. Delocalisation indices in benzothiazole.....	186
10.10. The filter insert for the beam path of Stalke's Bruker APEX2 Ultra	187
10.11. The impact on low energy X-ray contamination on data statistics	188
Danksagung.....	193
11. References.....	195
12. Curriculum vitae	209

Abbreviations

AIM	Atoms in Molecules
APS	Advanced Photon Source
BCP	Bond Critical Point
CCD	Charge Coupled device
CCP	Cage Critical point
CMOS	Complementary Metal Oxide Semiconductor
DI	Delocalisation Index
ED	Electron Density
GIMIC	Gauge-Including Magnetically Induced Current
GoF	Goodness of Fit
IAM	Independent Atom Model
$L(\mathbf{r}) = \nabla^2 \rho(\mathbf{r})$	Laplacian, Laplacian Field
MO	Molecular Orbital
NCI	Non-Covalent Interactions
NICS	Nucleus-Independent Chemical Shift
PDI	<i>Para</i> -Delocalisation Index
QTAIM	Quantum Theory of Atoms in Molecules
RCP	Ring Critical Point
RDG	Reduced Density Gradient
RP	Reference Point
SF	Source Function
VSEPR	Valence Shell Electron Pair Repulsion
VSCC	Valence Shell Charge Concentration

1. Single crystal X-ray diffraction

1.1. History of X-ray diffraction^[1]

Only little more than a century earlier than the publication of this thesis, *Friedrich, Knipping, and von Laue* published their postulate about the interference of X-rays with crystal-line material,^[2] and their instant confirmation of its validity heralded the rise of the large field of X-ray diffraction. *William Lawrence Bragg* with his father *William Henry Bragg* derived the fundamental laws of X-ray diffraction.^[3] With their very early and successful attempts to extract structural atomic information from the X-ray diffraction pattern of a number of crystals in the same year,^[4-5] they can be treated as the founders of crystal structure determination by means of X-ray diffraction. *Von Laue* as well as father and son *Bragg* earned Nobel prizes of the *Swedish Royal Academy of Science* in 1912 and 1915, respectively. X-ray diffraction has evolved to one of the most powerful analytic methods since the days of *Bragg* and *von Laue*, not least because of the development of the nowadays ubiquitous X-ray powder diffraction by *Peter Debye* and *Paul Scherrer*,^[6-8] and, independently, *Albert Hull* in 1917.^[9]

1.2. The diffraction condition

X-ray diffraction is a technique that uses the elastic scattering of X-ray photons at a three-dimensional lattice.^[10] The presence of maxima in the intensity distribution of the scattered radiation is caused by constructive interference of the scattered waves, and the observed positions of the maxima as well as their relative intensities make up the diffraction pattern that is used for analysis and interpretation. The physical and mathematical roots of modern single-crystal X-ray diffraction are subject of many textbooks^[11-13] and will only be outlined briefly in the following paragraphs.

Diffraction conditions can be formulated because constructive interference between two waves of identical wavelength only occurs if the phase shift between the two is equal to an integer multiple of the wavelength. Let a wave be defined by a wave vector. The difference vector $\Delta\mathbf{k}$ between the incident wave vector \mathbf{k}_0 and the diffracted wave vector \mathbf{k} is then called the scattering vector:

$$\mathbf{k} - \mathbf{k}_0 = \Delta\mathbf{k}. \quad (\text{Eq. 1})$$

The direction of \mathbf{k}_0 is parallel to the incident beam; its length is the reciprocal of the wavelength, which also is the length of the scattered wave vector \mathbf{k} in the case of elastic

scattering. Based on the interference condition, the *von Laue* diffraction conditions were formulated:

$$\Delta \mathbf{k} \cdot \mathbf{a} = |\Delta \mathbf{k}| |\mathbf{a}| \cos(\Delta \mathbf{k}, \mathbf{a}) = h, \quad (\text{Eq. 2})$$

$$\Delta \mathbf{k} \cdot \mathbf{b} = |\Delta \mathbf{k}| |\mathbf{b}| \cos(\Delta \mathbf{k}, \mathbf{b}) = k, \quad (\text{Eq. 3})$$

$$\Delta \mathbf{k} \cdot \mathbf{c} = |\Delta \mathbf{k}| |\mathbf{c}| \cos(\Delta \mathbf{k}, \mathbf{c}) = l, \quad (\text{Eq. 4})$$

where the vectors \mathbf{a} , \mathbf{b} , \mathbf{c} are the primitive lattice vectors and h , k , l are integer numbers. The latter are called *Miller* indices. All three *von Laue* conditions have to be fulfilled simultaneously for constructive interference.

The *Miller* indices form a triple of numbers that uniquely defines a point in a reciprocal lattice consisting of all points $h\mathbf{a}^* + k\mathbf{b}^* + l\mathbf{c}^*$ with the reciprocal lattice vectors \mathbf{a}^* , \mathbf{b}^* , \mathbf{c}^* . The reciprocal lattice vectors are defined by

$$\mathbf{a}^* = \frac{\mathbf{b} \times \mathbf{c}}{(\mathbf{a} \times \mathbf{b}) \cdot \mathbf{c}}; \quad \mathbf{b}^* = \frac{\mathbf{a} \times \mathbf{c}}{(\mathbf{a} \times \mathbf{b}) \cdot \mathbf{c}}; \quad \mathbf{c}^* = \frac{\mathbf{a} \times \mathbf{b}}{(\mathbf{a} \times \mathbf{b}) \cdot \mathbf{c}} \quad (\text{Eq. 5})$$

and the reciprocal lattice vector \mathbf{K} is defined as

$$\mathbf{K} = h \cdot \mathbf{a}^* + k \cdot \mathbf{b}^* + l \cdot \mathbf{c}^*. \quad (\text{Eq. 6})$$

With these definitions, the *von Laue* conditions can be reduced to one condition,

$$\Delta \mathbf{k} = \mathbf{K}. \quad (\text{Eq. 7})$$

A very illustrative construction of these dependencies was made by *Ewald* (see Figure 1). The incident wave vector \mathbf{k}_0 has its tip located in the centre of the reciprocal lattice (000)

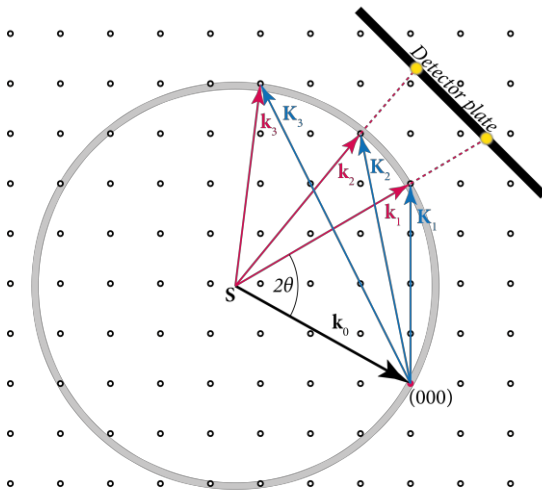


Figure 1. The *Ewald* construction of diffraction.

and its origin is the X-ray source ("S" in Figure 1). A sphere with a diameter of the reciprocal wavelength $1/\lambda$ (marked grey in Figure 1) is formed by all possible diffracted wave vectors \mathbf{k}_i around the origin of the incident wave vector. For those points of the reciprocal lattice that touch the sphere, the diffraction condition is fulfilled because the resulting difference vectors between \mathbf{k}_0 and those \mathbf{k}_i that satisfy the diffraction conditions are just the reciprocal lattice vectors \mathbf{K}_i . The reciprocal lattice rotates

around (000) as the crystal is rotated with respect to the incident beam, and a detector can be used to collect a number of reflections. Yet only a spherical detector with the sample in its centre would suffice to simultaneously detect all reflections that are possible for a given orientation of the crystal.

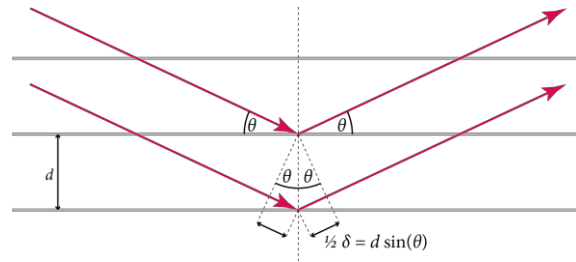


Figure 2. The *Bragg* picture of diffraction.

The *Laue* condition was reformulated by *W. L. Bragg* and *W. H. Bragg* and transformed into an equation that goes without vector representations:

$$2d \sin(\theta) = n \lambda. \quad (\text{Eq. 8})$$

In the *Bragg* equation, n is the diffraction order, λ is the X-ray wavelength, d is the lattice plane distance and θ is the incident angle with respect to the lattice plane. For the purpose of this equation, the diffraction phenomenon is treated as a reflection of waves at lattice planes (Figure 2). These planes cut through the unit cells of the crystal in a periodic manner, which is defined by the *Miller* indices. The planes are orthogonal to their corresponding reciprocal lattice vector. The lattice plane distance d can be derived from the *Miller* indices and the unit cell geometry, which in turn can be determined if a set of reflections has been obtained.

The smallest lattice plane distance d that has been measured from a crystal is often referred to as *highest resolution* of the structure. As a rule of thumb, those structural features in the electron density where distances are in the magnitude of d or larger can be resolved by means of crystal structure refinement, and structural features with distances below d cannot be resolved reliably.

1.3. *The structure factor and the atomic scattering factor*

The *von Laue* and *Bragg* conditions serve to predict the directions in which reflections can be observed if the lattice constants are known. The relative intensities of the reflections are determined by the arrangement and nature of the atoms in the lattice. Every atom in the crystal generally contributes to the intensity of the corresponding reflection if the diffraction condition is fulfilled, but the phase shifts between the scattered waves from different atoms have to be considered since the atoms in the unit cell are shifted with respect to the origin of the cell.

The structure factor F_{hkl} is a measure for the relative intensity of an observed reflection. It is characterised by its *Miller* indices (hkl) . The structure factor F_{hkl} and the electron density $\rho(\mathbf{r})$ at a point \mathbf{r} in the crystal are connected to each other. The structure factor can be written as

$$F_{hkl} = \int_V \rho(\mathbf{r}) \exp\{2\pi i (h\mathbf{a}^* + k\mathbf{b}^* + l\mathbf{c}^*)\mathbf{r}\} d\mathbf{r} \quad (\text{Eq. 9})$$

and $\rho(\mathbf{r})$ is its *Fourier* transform:

$$\rho(\mathbf{r}) = \int_V F_{hkl} \exp\{-2\pi i (h\mathbf{a}^* + k\mathbf{b}^* + l\mathbf{c}^*)\mathbf{r}\} d\mathbf{r}. \quad (\text{Eq. 10})$$

The electron density can in good approximation be obtained via summation of all F_{hkl} :

$$\rho(\mathbf{r}) = \frac{1}{V} \sum_{hkl} F_{hkl} \exp\{-2\pi i (h\mathbf{a}^* + k\mathbf{b}^* + l\mathbf{c}^*)\mathbf{r}\} \quad (\text{Eq. 11})$$

For each atom, an atomic scattering factor f defines the scattering amplitude. The atomic form factor for X-rays generally increases with higher atomic number since the X-rays interact with the electron density around the atoms. The atomic scattering factor can be obtained *via Fourier* transformation of the scattering atom's spatial ED distribution. This is most commonly derived from quantum-mechanical calculations of isolated ground-state atoms, yielding a spherically symmetric distribution of electron density around the nucleus. The structure factor can then be obtained by summation of the atomic scattering factors:

$$F_{hkl} = \sum_j f_j \exp\{2\pi i (h\mathbf{a}^* + k\mathbf{b}^* + l\mathbf{c}^*)\mathbf{r}_j\}. \quad (\text{Eq. 12})$$

It is in the nature of the *Fourier* transformation that the broader the angular ED distribution is, the narrower the atomic scattering factor will be.^[14] If the atomic scattering factor is further divided into contributions from core and valence electrons, this relation becomes even more evident: the influence of diffuse valence electron density will be strongest for those F_{hkl} with low (hkl) and thus low θ values, while the compact core electron density of the scattering atoms will scatter X-rays with high amplitude up to large angles of θ (compare Figure 3).

Thus, the core ED can be considered independent of the chemical environment of the corresponding atom in good approximation although it has been shown that this approximation is not entirely correct. Core polarisation effects become visible especially in cases where data up to very high resolution are available.^[15-19] As a rule of thumb, datasets with

$\sin(\theta)/\lambda > 1.0$ for those reflections with highest θ can be considered to be of high resolution, and very high resolution data with $\sin(\theta)/\lambda > 1.2$ are very often not available.

The structure factor is not a direct observable because it is the intensity of a reflection and not its amplitude which is measured in a diffraction experiment. The intensity, however, is proportional to F_{hkl}^2 , which means that the structure factors cannot be recovered from a measurement of the intensities because imaginary components are lost upon the raise to the second power. This dilemma has got its own name: it is *the phase problem in crystallography*. For each structure, the phase problem has to be solved in some way before the structure refinement can begin; this procedure is known as structure solution.^[20-21] Without going into too much detail, it can be stated that the exponential increase in computing power made solving a structure one of the less relevant problems for small molecule structures with less than a few hundred atoms in the unit cell but continues to be a major problem in the field of macromolecular crystallography.

If the described theoretically calculated atomic scattering factors were to be compared with those derived from measurements of X-ray diffraction intensities, the experimental atomic scattering factors would show a larger decay against θ than the calculated ones. This is mostly due to thermal motion, which can be treated mathematically with adding a normal probability distribution function. A parameter U is introduced (see also Figure 4):

$$f' = f \exp(-2\pi^2 U \mathbf{K}^2) \quad (\text{Eq. 13})$$

The parameter is most commonly called “displacement parameter” and not “thermal parameter” because it can correct for some phenomena that are temperature-independent

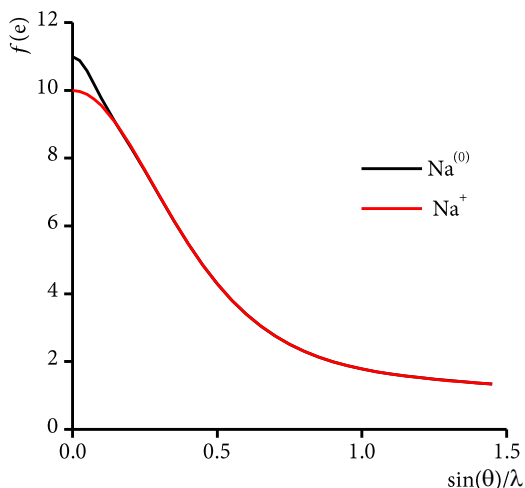


Figure 3. Atomic scattering factors of a neutral sodium atom and a sodium cation. The scattering factor is only affected by the valence density at low θ values.

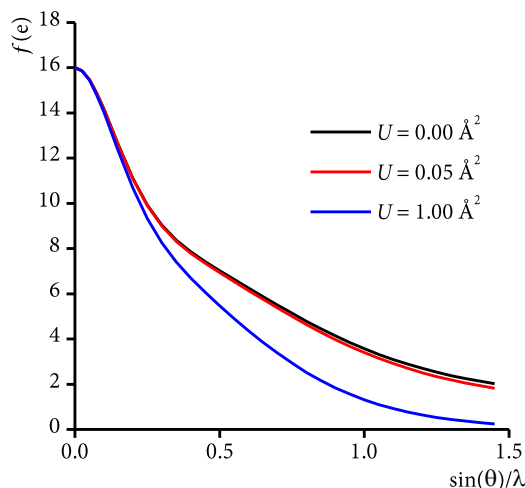


Figure 4. Atomic scattering factor of sulfur without and with displacement parameter U . The displacement parameter affects the scattering factor at high values of θ .

like small deviations from ideal periodicity in the crystal and also for systematic errors in the measured data as well.

In the iterative process of most structure refinements, the single (isotropic) displacement parameter for each atom is replaced by six anisotropic displacement parameters U_{ij} at some point. They are elements of a tensor which is used to describe an ellipsoid. The parameters are used for the modification of the atomic scattering factor:

$$f' = f \exp(-2\pi^2 \{h^2 \mathbf{a}^{*2} U_{11} + k^2 \mathbf{b}^{*2} U_{22} + l^2 \mathbf{c}^{*2} U_{33} + 2kl \mathbf{b}^* \mathbf{c}^* U_{23} + 2hl \mathbf{a}^* \mathbf{c}^* U_{13} + 2hk \mathbf{a}^* \mathbf{b}^* U_{12}\}) \quad (\text{Eq. 14})$$

As pointed out above, the electron density cannot be directly derived from the scattering amplitudes. An initial structure model, normally obtained from the program used for structure solution, is refined against the data in such a way that the squared calculated structure factors F_{calc}^2 and squared experimentally derived structure factors F_{obs}^2 are compared and the sum of differences

$$\sum_{hkl} w \Delta^2 = \sum_{hkl} w_{hkl} (s \cdot F_{obs}^2 - F_{calc}^2)^2 \quad (\text{Eq. 15})$$

is minimised in a least-squares routine. The factor w_{hkl} is an individual weighting factor for each reflection that takes errors in the determination of F_{obs} into account (see section 1.8 for details on w_{hkl}). The determination of the uncertainties $\sigma(F_{hkl})$ of individual reflections is a very important step in the experimental procedure that is necessary to get a reliable structure model.

Observed and calculated structure factors are thus not necessarily on the same absolute scale, and a scaling factor s is therefore needed to be able to compare F_{calc}^2 and F_{obs}^2 :

$$s = \frac{\sum F_{obs}^2}{\sum F_{calc}^2}. \quad (\text{Eq. 16})$$

The scaling factor is refined in each step of the refinement procedure.

1.4. Absorption correction, scaling and merging

These are three very important steps in the process of data reduction. They will only be covered briefly in this thesis and much of the contents of the following paragraphs is contained in the SADABS manual.^[22]

The program SADABS^[23] is routinely used in our workgroup. While the program may originally have been meant to correct for absorption effects in diffraction experiments, it is very efficient in correcting other effects as well.^[24] Curved mirror optics are being wide-

ly used in X-ray diffraction experiments because of the resulting higher X-ray brilliance. The side effect of mirror optics is an anisotropic and narrow beam profile, which makes proper sample (and equipment) alignment even more necessary but at the same time more difficult than in the case of sealed tube sources with graphite monochromator, which produce large and isotropic beam profiles. The interframe scaling is an indispensable feature of SADABS. Its “competitor” program SORTAV^[25] also offers this function but uses an apparently less efficiently programmed algorithm. Both programs basically generate a scale factor for the intensity of each frame, which is very useful in cases of samples that have the shape of plates or needles and it even helps mending data that has been obtained from poorly aligned samples with no constant sample illumination over the scan.

SADABS works in three stages.^[26] In the first stage, mean intensities are determined using averaged equivalent reflections. Scaling and absorption parameters are fitted to these intensities. In the second stage, SADABS identifies and rejects severe outliers that are for example due to obstructed reflections close to the beam stop. An error model is determined for the remaining reflections. This error model contains the parameters k and g , which are adjusted so that the distribution of

$$\sigma_{\text{abs}}^2 = k[\sigma_{\text{raw}}^2 + (g\langle I \rangle)^2] \quad (\text{Eq. 17})$$

results in χ^2 of approximately unity. The parameter k is a scale factor that is different for each scan, g is a global parameter. SADABS provides the parameters k in the listing file in the form of $K = \sqrt{k}$ since it is the square root which is applied to the uncertainties.

It was argued by *Jørgensen et al.*^[27] that the introduction of this error scheme artificially introduces an asymptotic behaviour for the significance $I/\sigma(I)$ with “strange errors.” This is due to the term $g\langle I \rangle^2$, which is dominant for strong reflections where $\sigma_{\text{raw}}^2 \ll (g\langle I \rangle)^2$ and hence limits the significance to a maximum value of $1/(\sqrt{k} \cdot g)$. It remains to be resolved whether this creates an incorrect bias or if in fact more realistic estimated standard deviations are obtained; the asymptotic behaviour of the significance in experimental datasets is well known to macromolecular crystallographers^[28] and even has been used to identify scientific fraud.^[29]

The third stage is the output of the corrected data and very valuable statistical plots. The data can be obtained as unmerged data or as merged data with averaged symmetry equivalents according to the crystal point group or space group. The correction can be summarised in the following equation:

$$I_c = I_0 \cdot S_n \cdot P(u, v, w) \cdot R(n, \theta) \quad (\text{Eq. 18})$$

In which: I_c – corrected intensity; I_0 – raw intensity; S_n – scale factor for frame n ; P – absorption factor; R – radiation damage term (rarely necessary for the small molecule data collected in our workgroup because it mostly affects macromolecular crystals); u, v, w – direction cosines relative to reciprocal lattice vectors $\mathbf{a}^*, \mathbf{b}^*, \mathbf{c}^*$. The terms S and P are refined to minimise $\Sigma w(\langle I_c \rangle - I_c)^2$ in which $\langle I_c \rangle$ is the averaged equivalents' intensity and w is a weighting factor. The diffracted beam absorption factor $P(u, v, w)$ is a term that consists of a series of spherical harmonics that are used to model the path of the diffracted beam through the crystal.^[30-33]

1.5. The independent atom model

The independent atom model (IAM) refers to crystal structures from refinements where the calculated structure factors are only derived from atomic scattering factors of spherical atoms and the structure model also consists only of atoms with a nucleus-centred radial-dependent, but spherically symmetric electron density distribution which are convoluted with the corresponding displacement parameters. This is the most common method for crystal structure refinement, and one of the most frequently used program for crystal structure refinement based on this model has been SHELXL-97,^[21] which has recently gotten a successor in the program SHELXL-2013.^[34] Crystal structures from spherical atom refinements yield atomic distances and angles, and the elements in the structure usually can be assigned reliably if no severe problems like disorder occur. The absolute structure can often be determined unambiguously if the anomalous dispersion of elements in the structure is sufficiently strong at the used X-ray wavelength to measure differences in the intensities of *Friedel* pairs.^[35-37]

1.6. The multipolar refinement

Much of the electron density in the unit cell is described correctly with an IAM-derived structure model, which works perfectly well if bonding valence electron density is neglected. However, the deficiency of the IAM becomes obvious especially if high resolution data collected at low temperature are used for refinement. The deconvolution of thermal motion and positional parameters works better the higher the resolution of the data is (displacement parameters tend to “absorb” some of the bonding density if only low resolution data are available), and the difference density, which can be derived from $|F_{obs}^2| - |F_{calc}^2|$, has features of high difference electron density on bonds and in regions with nonbonding electron density such as lone pairs (see Figure 5). Unfortunately, exactly the mentioned features are potentially most interesting to chemists since the science of chemistry largely depends on the properties and changes of valence electron density.^[38]

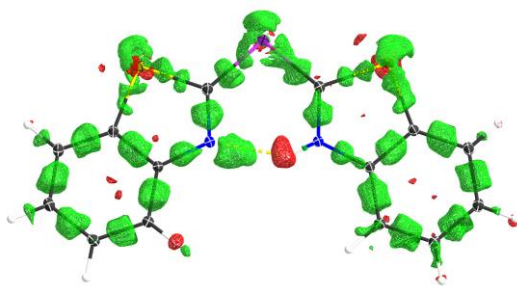


Figure 5. Difference density after IAM structure refinement of a structure with high resolution data up to $\sin(\theta)/\lambda = 1.1 \text{ \AA}^{-1}$. Contour levels: $+0.20 \text{ e \AA}^{-3}$ (green) and -0.20 e \AA^{-3} (red).

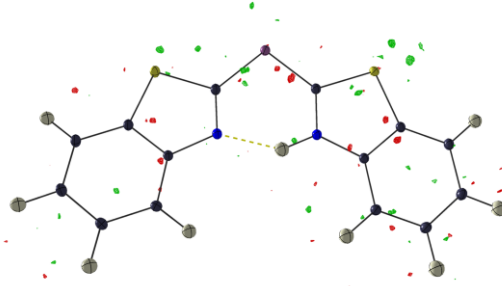


Figure 6. Difference density after multipole refinement; the data are the same as used in IAM refinement resulting in Figure 5. Contour levels were chosen at the same level as for Figure 5.

There are a number of approaches for models that describe the electron density that is not taken into account by the IAM, one of which is the multipole model introduced by *Hansen and Coppens*.^[39] This model still uses atomic contributions for the structure factor and the reconstruction of $\rho(\mathbf{r})$, but it divides the atomic densities $\rho_{at}(\mathbf{r})$ into three parts; a spherical core density $\rho_c(\mathbf{r})$, a spherical valence density $\rho_v(\mathbf{r})$, and non-spherical valence density:

$$\rho_{at}(\mathbf{r}) = P_c \rho_c(\mathbf{r}) + P_v \kappa^3 \rho_v(\kappa r) + \sum_{l=0}^{l_{\max}} \kappa'^3 R_l(\kappa' r) \sum_{m=-l}^l P_{lm} Y_{lm}\left(\frac{\mathbf{r}}{r}\right). \quad (\text{Eq. 19})$$

Those three terms contain population coefficients P_c , P_v and P_{lm} . The value of P_c is the number of core electrons and the sum $P_v + P_{00}$ delivers the number of valence electrons of the respective atom (integration over those terms with $l \neq 0$ delivers zero). The integer l_{\max} is arbitrarily limited to 4 in the popular program XD2006. The functions $\rho_c(\mathbf{r})$ and $\rho_v(\mathbf{r})$ are *Hartree-Fock* densities calculated for free atoms which are normalised to one electron; the parameter κ is used for expansion and contraction of the spherical valence density function. The radial distribution functions $R_l(r)$ are *Slater* functions

$$R_l(r) = \frac{\zeta^{n_l+3}}{(n_l+2)!} r^{n_l} \exp(-\zeta_l r) \quad (\text{Eq. 20})$$

where n_l may take any positive integer value (n_l usually ranges between 2 and 8). Those “standard” values of ζ and n_l that are used in scattering factor libraries were extracted from single- ζ wavefunctions;^[40-41] other values for the exponents n_l that deviate from standard values can also be determined empirically.^[42-43] The functions Y_{lm} are spherical harmonics (the functions are contained in ref.^[39]), which are normalised so that one electron is moved from the negative lobes to the positive ones when $P_{lm} = 1$ and *vice versa* for $P_{lm} = -1$. The last term in (Eq. 19) is responsible for the deformation of the spherical

atomic density; it can shift the valence density around the atomic core (the *pseudoatom*) in a way that a non-spherical distribution of electron density is obtained.

All parameters are usually refined at a time in small molecule IAM refinements. This is not possible for multipole refinements because of the instability caused by high correlation between certain parameters and by the large shifts of fitted parameters in the initial stages of refinement. Instead, a stepwise refinement is carried out in which groups of parameters are refined simultaneously. After convergence is reached in the refinement of those groups of parameters, refinement steps including larger groups of parameters and eventually including all parameters are added.

The more detailed description of the electron density in the unit cell has one major drawback in the high number of variables used: while one atom has three variables x , y , z for its spatial position and up to six variables U_{ij} for its displacement parameters in the IAM, the multipole model adds an additional number of 24 parameters with P_{lm} alone. A total number of up to 36 parameters per atom results together with the variables P_v , κ , and κ' which are further elements of the multipole model. The ratio of refined parameters *versus* available data should not be lower than 10 in an IAM refinement and it should be significantly higher for multipole refinements; a minimum ratio of 20 for those refinement steps with the highest number of refined parameters is desirable.

Most programs that are commonly used for multipole refinement can handle even more global and atomic variables. The most popular program packages are *XD2006*,^[44] *MoPro*,^[45] and *Jana2006*.^[46]

Each of those refinement programs has a field where it exceeds the others. *XD2006* is intended for the multipole refinement of small molecules against high-resolution and high-quality experimental or theory-derived reflection data. It does not offer restrained refinement of parameters at all, and the ability of the included charge density analysis programs to deal with structures of high crystallographic symmetry is surprisingly limited in some cases. *MoPro* has been designed primarily for multipole refinements on macromolecules where reflection data are of low resolution and possibly medium quality. In many cases only positional and displacement parameters of the pseudoatoms are refined with fixed multipole parameters that are taken from libraries although the program is capable of performing full least-squares refinement of all parameters.^[47-48] It offers the powerful possibility to include restraints between arbitrary parameters in the refinement. *Jana2006* is perhaps the most flexible of the three programs, and it may be due to its complexity that it has not become as widely used as the others; spherical harmonics to higher order than four can be refined, and on top of most of the features that are included in *MoPro* and

XD2006, it enables refinement of modulated structures and combined refinement against single crystal and powder data from X-ray and neutron diffraction experiments.

In the preparative work on this thesis, multipole pseudoatom refinements with *MoPro* and *XD2006* were carried out and evaluated, but eventually *XD2006* was favoured for the refinement of multipole models although it does not offer restrained refinement. *XD2006* turned out to have a larger convergence radius, which results in more stable refinements, and *MoPro* reproducibly showed an incorrect treatment of restraints and constraints in some cases, which could not be explained nor remedied by the authors of the program.

1.7. Hydrogen atom refinement

One of the difficulties in crystal structure modeling against data from X-ray diffraction experiment persists in the refinement of parameters associated with hydrogen atoms. This difficulty arises from the low electron density which is highly polarised along the bond and very diffuse because of relatively large libration effects that are due to the low atomic mass of hydrogen.^[49] Hydrogen atoms do not contribute to the structure factor to a very large extent because their contribution to the total electron density in the unit cell is little in most cases, and the atomic form factor decays steeply against θ (see Figure 7) so that significant information about hydrogen atoms is contained only in reflections in a limited range of low θ .

As pointed out earlier, the treatment of the atoms in a crystal structure as a sum of spherical electron density distributions is a rather coarse approximation already for heavy atoms (paragraph 1.6). It would be even more improper in the case of hydrogen atoms because they only have one valence electron and no core electrons. This problem has already been tackled very early by *Stewart, Davidson and Simpson*.^[50] They were not the first to calculate a precise molecular charge density map of the H_2 molecule,^[51] but they used an elegant way to partition the charge density to obtain an atomic form factor for a single hydrogen atom in a chemical bond.

The atomic scattering factor from *Stewart et al.* is still used in modern crystal structure refinement programs, but nonetheless there are systematic errors in the hydrogen posi-

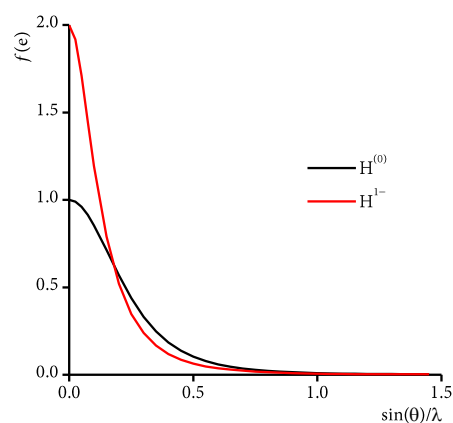


Figure 7. Atomic form factor of a hydrogen atom and a hydride ion.

tions of X-ray diffraction derived crystal structures to the effect that the bond distances are underestimated in X-ray structures.^[52] Structure refinement with the *Hansen-Coppens* multipole model has the potential to yield more realistic bond distances towards hydrogen atoms compared to results from independent atom refinements because the degree of bonding density polarisation can be modelled individually.

1.8. Difference electron density

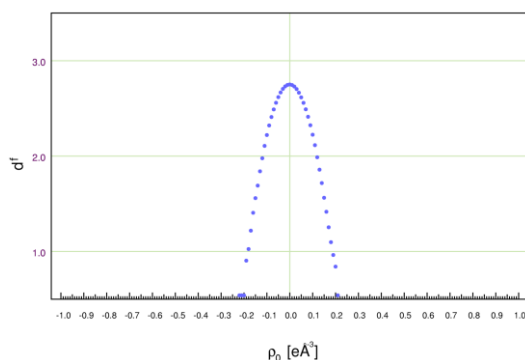


Figure 8. Fractal dimension of the residual density after multipole refinement. The residual density which is shown in Figure 6 is calculated from the same model and dataset as for this figure.

The difference electron density (also: *residual density*) is obtained from a density synthesis as in Eq. 11, but with the coefficients ($F_{\text{obs}} - F_{\text{calc}}$) and the phases from the preceding refinement. The resulting map should be flat and featureless after the multipole refinement has converged. The featurelessness is an important criterion for the adequacy of the model since the goal of the structure refinement is to obtain a precise description of the electron

density in the unit cell, and the flatness is an indication for the amount of noise in the data. *Meindl* and *Henn* have published a very elegant graphical indicator that displays both criteria at the same time by plotting the residual density against its fractal dimension.^[53] A parabolic shape of the resulting plot indicates featurelessness; a small width of the parabola indicates flatness. The fractal dimension plot in Figure 8 shows that the fractal dimension of zero difference density $d^f(0)$ is 2.75, which is another indication for featurelessness; the surfaces of zero difference density that surround the areas of positive and negative difference density should have a fractal dimension of as close to three as possible.

1.9. Observed and calculated structure factor

A very important measure for the suitability of a structural model with respect to the data is the resolution dependency of s , the scale factor in (Eq. 16) (it is termed “K” in the list file of SHELXL). A typical distribution of s after a “standard” IAM refinement is shown in Figure 9. For the purpose of the shown plot, s was calculated for several bins in the resolution range. However, only one scale factor for the whole resolution range is refined in

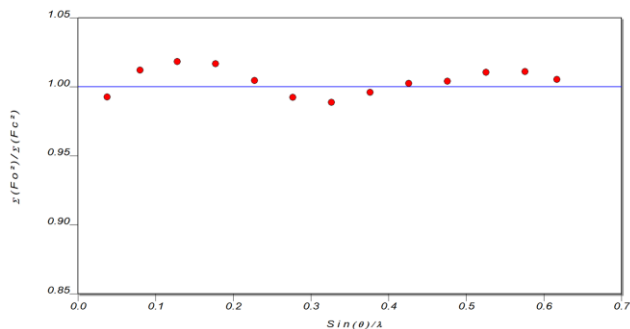


Figure 9. Resolution-dependent distribution of the scale factor.

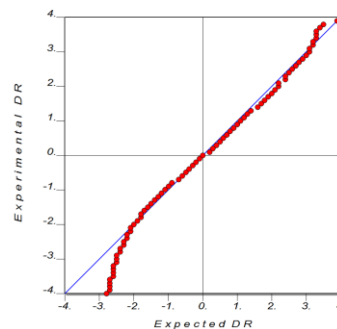


Figure 10. Normal probability plot.

most cases although more or less severe resolution dependence is present in the vast majority of the cases.

The reasons for deviations from the ideal distribution (blue line in Figure 9) can be diverse; there are many different steps from the detection of X-ray photons with an area detector to the file containing F_{hkl}^2 . A very useful article about the necessary considerations for area detector X-ray diffraction experiments was published by *Zhurov et al.* some years ago.^[54] In contrast to the point detectors of former days, which produced reflection data with relatively reliable standard uncertainties $\sigma(I)$ as well as trustworthy $I/\sigma(I)$, modern CCD-based area detectors tend to produce data with questionable $I/\sigma(I)$ if the data are not treated carefully.

In addition to the resolution dependency of s , the values of $w\Delta^2$ (the squared difference between observed and calculated F^2 , see (Eq. 15)) should follow a normal distribution. This can be checked by a plot as in Figure 10, where the experimental deviations are plotted against the expected distribution of deviations. An ideal normal probability distribution would give a line with a slope of 1 through the origin.^[55] Usually, no such ideal distribution will result if experimental weights $w_{hkl} = 1/[\sigma(F^2)]^2$ are used. A more complicated weighting scheme with two parameters a and b is commonly used and implemented in *SHELXL* and *XD2006* (negative F_{obs}^2 are substituted by 0):

$$w_{hkl} = \frac{1}{[\sigma(F_{hkl}^2)]^2 + \left[a \left(\frac{1}{3} F_{obs}^2 + \frac{2}{3} F_{calc}^2 \right) \right]^2 + b \left(\frac{1}{3} F_{obs}^2 + \frac{2}{3} F_{calc}^2 \right)} \quad (\text{Eq. 21})$$

For datasets of high quality and accurate $\sigma(F^2)$ over the whole resolution range, the parameter a is according to our experience typically very small in multipole refinements (well below 0.05).

1.10. Figures of merit

From the results of the minimisation of $\sum_{hkl} w \Delta^2$ in least-squares refinement, agreement values (“*R*-values”) can be calculated that serve as universal indicators for the agreement between model and measured data:

$$R1 = \frac{\sum_{hkl} (|F_{obs}| - |F_{calc}|)}{\sum_{hkl} |F_{obs}|} \quad (\text{Eq. 22})$$

There is no universal agreement in the crystallographic charge density community in the question whether to refine a model against datasets consisting of F or F^2 . Apart from the objection concerning the leverage of weak reflections, which can be higher in refinements against F , there are mainly historical reasons to refine against F and many practical reasons to use F^2 , which is directly related to the measured intensity.^[56] For this thesis, refinement was always performed against F^2 , in which case consequentially the value of $wR2$ is being used:

$$wR2 = \frac{\sum_{hkl} w_{hkl} (F_{obs}^2 - F_{calc}^2)^2}{\sum_{hkl} w_{hkl} F_{obs}^4} \quad (\text{Eq. 23})$$

It has to be noted nonetheless that the $R1$ continues to be used because its value cannot be cosmetically improved by changing the weighting factors. The choice of the weights can have a significant impact on the value of $wR2$. As an additional caveat, the R -values may in some cases be misleading if exclusively taken as indicators for the quality of a model. This would be the case if artefacts from systematic errors in the data were fitted with a model that actually does not reflect reality. This knowledge is crucial for charge density crystal structure refinements. Therefore, a more detailed view on the results of a refinement has to be taken.

1.11. Pitfalls in data collection with modern CCD based detectors

Some of the potential sources of error emerge in the process of data integration. Each pixel on a CCD based detector can be treated as a microscopic integration bin that collects incoming photons over a certain period of time. The positions of reflections in reciprocal space can be predicted quite precisely, so that it is in principle possible to define a boundary for each reflection and take the result from a summary over the accumulated intensity of each pixel inside that boundary. The dimensions of this integration box are mainly dependent on the mosaicity of the sample and additional factors such as the $K_{\alpha 1}/K_{\alpha 2}$ splitting of the reflections. However, there are a number of factors that make the process of data integration nontrivial. The following comments mostly apply to the integration soft-

ware SAINT 7.68A,^[57] which exclusively has been used for the data used in this thesis, and much of the following information has been extracted from the file “REFMAN._TP” that is deposited in the SAINT binary directory of the software installation and contains a reference manual:^[58]

1. *Background intensity.* Random noise is caused by the detector’s dark current; diffuse scattering intensity, not to be confused with *thermal diffuse scattering*, caused by the beam stop or adherent material on the sample such as oil or micro crystallites, and random events like radioactive decay in the X-ray sensitive layer cause additional, non-isotropic noise in the recorded frames. For CCD-based as well as for CMOS-based detectors of the latest generation, dark current still is a factor that has to be corrected for. Many corrections are already taken care of in the *black box* of the detector hardware, and the user never gets to see actual raw frames. It is still necessary to apply dark current correction in software, which requires a *dark frame* for the desired exposure time, which has been averaged over a number of frames collected with closed shutter. The values of the pixels in the dark frame are only caused by dark current and can be subtracted from those in the frames in the integration process. However, the actual background intensity distribution in recorded frames is initially taken from an average of a number of frames (10 to 20), excluding pixels exceeding three times the minimum average intensity. The bias towards a value which is a little too low is reduced by some methods in the subsequent refinement of the background during the further process of integration. The value of each pixel in the resulting mask serves as a correction value for the corresponding pixel in the data frame. Radioactive decay can occasionally cause high intensity streaks on the detector, which is corrected for by correlated exposure; the pixels of two frames taken with identical scanning parameters and 0.5 times the nominal exposure time are summed up; those pixels that significantly differ in intensity count between the two frames are eliminated and replaced by pixels from the background mask.
2. *Integration of reflections with low $I/\sigma(I)$.* The reflections recorded with area detectors have distorted three-dimensional profiles and differ in their shapes over the course of data collection because of the differing trajectories of the reflections through the *Ewald* sphere. An integration of the reflection intensity has to be performed in the boundaries of these three-dimensional profiles. There are two different ways to determine reflection profiles: the very popular method proposed by *Kabsch*^[59] and the so-called seed-skewness method.^[60] The latter uses the fact that the skewness in the intensity distribution of an integration volume is in-

creased relative to the very low noise distribution skewness if reflection intensity is present. It tries to identify those pixels that are responsible for the increase in skewness and generates an integration mask from these pixels. The first (*Kabsch*) method was used for data processing in thesis. It is very well-known and less expensive in terms of computing time and generates average profiles for all reflections. It uses strong reflections for the generation of reference profiles. This so-called *spot shape* is optimised in a least-squares refinement during the integration process, and it determines the volume of pixels in which the pixel intensities will be summed for the integrated intensity. This integration procedure, called *simple sum* procedure in SAINT, generally works well for strong reflections that have $I/\sigma(I) \gg 10$, but is error-prone for reflections with very low ratios of $I/\sigma(I)$. It is substituted by a least squares fit of the intensity, the details of which cannot be further discussed in this thesis. This least-squares fitting routine tends to overestimate the integrated intensities of weak reflections, which becomes noticeable if intensities are fitted in regions of high θ , where the intensities of the majority of reflections are in the magnitude of σ . The threshold for $I/\sigma(I)$ below which least-squares fitting is used to determine the intensity of a reflection is usually pre-set to 8.0, and the $I/\sigma(I)$ threshold above which reflections are used to update the reference profile model is 10.0.

3. *Overexposure.* CCD detectors have a physical saturation threshold above which no further intensity can be detected; the *APEX2* detector used throughout the measurements in this thesis has a hardware limited dynamic range of 16 bits per pixel, which corresponds to $6.55 \cdot 10^4$. The accepted range is further limited in the integration software because of nonlinear response for values approaching the hardware limit. The data collection strategies are usually optimised in a way that the reflections with highest θ will have sufficient intensity for data integration.

It is very often the case that samples for high-resolution data collection have few extremely bright reflections at low θ values that exceed the dynamic hardware range. The overflow is detected by the data collection software and the frame is recollected if allowed by the user; the exposure time for this retake is 1/8 of the nominal exposure time, and the previously overexposed pixel values are substituted by the corresponding pixels of the retake and subsequently scaled up accordingly. If the retake is not collected (this may happen because the shutter does not offer exposure times less than 0.5 s) or if overexposure persists in the retake, an attenuator can be automatically used for another retake which decreases the in-

tensity of the primary beam by a factor close to 10. This value has to be determined experimentally.

The integration software per-pixel intensity limit for reflection rejection is $6.0 \cdot 10^4$ unless retakes were allowed; the limit is scaled up to $4.8 \cdot 10^5$ in that case and further increased by the attenuation factor for attenuated frames. The nominal exposure times that are used in a charge density data collection on one sample vary between values of 1.0 s for low order (i. e. low θ) and several minutes for high order frames. The APEX2 detector has a hardware frame resolution of 4096 x 4096 pixels. The detector is usually run in a mode where arrays of 8 x 8 physical pixels are combined to one logical pixel (*hardware binning*); the resolution is then decreased to 512 x 512 pixels per frame. The sensitivity is increased in this mode because more photons can be harvested per pixel, but the hardware restriction to 16 bits per pixel remains in the binned modes, which frequently leads to overexposed pixels in regions of strong reflections. The detector can also be run in 1024 x 1024 pixels (4 x 4 binning) or 2048 x 2048 pixels (2 x 2 binning) to avoid overexposure, but to the cost of a higher amount of raw data per frame and an increased readout time per frame.

4. *Incident angle correction.* As pointed out by Zaleski *et al.*^[61] and Wu *et al.*,^[62] the incomplete absorption of X-rays in the phosphorescent layers used in CCD detectors causes an incident angle dependence of the integrated intensities because of the difference in path lengths through the phosphorus layer. This dependency has to be taken into account, and the respective transmission values are dependent on the used detector and the wavelength of the radiation. Wu *et al.* state that “this means that even with Mo-K α radiation (E = 17.45 keV) the correction is desirable if an accuracy of better than 5% in the intensities is required.” The correction gains importance with shorter wavelength (i. e. higher transmittance). The software that is used in our workgroup has a standard setting that is valid for Mo-K α radiation and a standard APEX2 detector; it may, however, be completely inappropriate for other wavelengths.
5. *3- λ -contamination.* It was first published 2004 in a marginal note^[63] and subsequently by a number of authors around Macchi^[64] in 2011 that a low-energy contamination in the X-ray spectrum is apparently caused by curved silicon multilayer optics. Such optics are being widely used because of the resulting high photon flux density, and all four diffractometers in our workgroup have multilayer optics. The effect is reportedly especially significant if molybdenum K α radiation

is used.^[64] The origin of the radiation is not entirely clear; the total reflection of low energy photons from the *Bremsstrahlung* at the silicon optics was discussed by *Macchi et al.* The contamination consists of a spectral distribution with a maximum at approximately three times the nominal wavelength of the used radiation. The intensities of the reflections ($3h\ 3k\ 3l$) are thus increased by a certain amount which is proportional to the intensity of the reflection ($h\ k\ l$). This implies that large samples with very strong low- θ reflections and weak higher order reflections (e. g. organic samples only with light atoms) are more seriously affected than others, as noted by *Macchi et al.* The effect can even be visually detected on the frames by radial streaks that appear along lines through the origin ($0\ 0\ 0$) and along $(n_1h\ n_2k\ n_3l)$ with n_i being integer numbers. *Macchi et al.* suggested using aluminium foil of 100 μm thickness as an effective filter that removes the contamination.

A presumably close-to-ideal experimental setup for collecting X-ray diffraction data has been described by *Zhurov et al.*^[54] The main differences between their proposed setup and the machinery available in our workgroup are: a curved image plate instead of a CCD detector and a graphite monochromator instead of curved mirror optics.

The most important consequence of their used setup is that the collected intensities are on the same absolute scale; no batch scale factors are needed then. All data can be acquired with equal exposure time since image plates have a very high dynamic range compared to CCD-based detectors. This brings the advantage that long exposure times can be used even for low order reflections with very high intensity without risking overexposure. The very low background noise of image plates allows relatively accurate determination of weak high order reflections.

The use of non-focusing graphite monochromators has the advantage that a homogenous beam profile with a wide plateau of equal flux is achieved; the crystal is completely illuminated in all angular settings of the goniometer, which is rarely the case when focusing mirror optics are used. As a consequence, the frame-to-frame scaling becomes less important (*Zhurov et al.* report typical interframe scale factors in the magnitude of 1 %).

The used equipment also has its downsides: the image plate requires very long readout and exposure times and the use of a graphite monochromator usually induces a contamination caused by the second harmonic of the nominal wavelength. The X-ray photon flux density from a graphite monochromator is not as high as the flux density from focusing optics, which is unfavourable if only very small samples are available.

2. The quantum theory of atoms in molecules (QTAIM)

The pseudoatom multiple refinement of a crystal structure yields a charge density distribution that takes valence density into account and thus can be used for a detailed picture of the chemical environment for each atom in the unit cell. However, an electron density map alone is of little use, and not much information in addition to the improved positional and displacement parameters compared to IAM is obtained.

Richard F. W. Bader, beginning with a fundamental paper from 1975,^[65] has provided us with the framework of QTAIM^[66-69] that enables us to analyse a charge density map in a straightforward way. Atoms and bonds are expressions of the observable electron density identifiable solely by means of its topology. The early development of QTAIM began with the realisation that the electron density distribution in a given system is the result from the total of all forces acting on each element of the charge density. The electron density distribution and the virial field are thus directly linked to each other.^[70] Some of the QTAIM principles, which are consequences thereof, will be presented in this chapter.

2.1. Atomic basins

One of the major achievements of *Bader's* QTAIM framework is the mathematically straightforward way of partitioning space into atomic basins. The first derivative of the charge density, $\nabla\rho(\mathbf{r})$, defines a field of gradient vectors; the vectors are directed towards the steepest increase in $\rho(\mathbf{r})$ in each respective point. Each trajectory on which these vectors are located terminates in an attractor, which is a special point in the charge density; see paragraph 2.2. Those trajectories that terminate in a common attractor belong to one atomic basin; each basin contains exactly one attractor. The boundaries of an atomic basin are determined by the vectors that do not cross the boundary surface. The name of the surface is *zero-flux surface* because of the

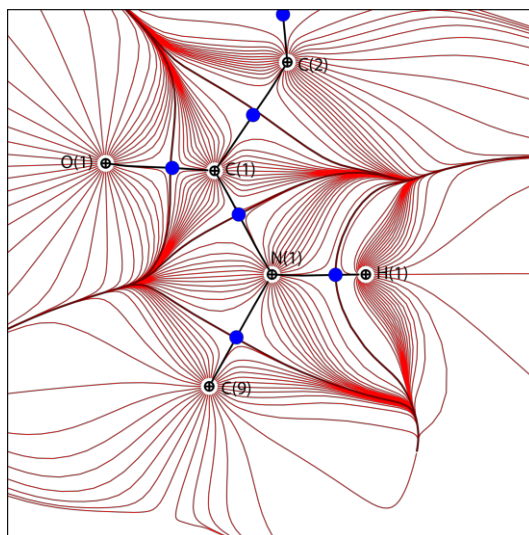


Figure 11. Trajectory plot of the gradient field in the O–C–N plane of a carboxamide (O1/C1/N1 in the diagram). The bold brown lines indicate basin boundaries and bond paths; the red lines are gradient field trajectories. Blue points are BCPs, the nuclear attractors are indicated with black crosses.

fact that it is not penetrated by trajectories of gradient vectors. The bond paths originate in the zero-flux surface and the points where the paths originate are the bond critical points. See Figure 11 for a graphical elucidation of the concept of atomic basins. An integration of the charge density in the boundaries of the zero-flux surface is defined by

$$\nabla\rho(\mathbf{r}) \cdot \mathbf{n}(\mathbf{r}) = 0. \quad (\text{Eq. 24})$$

This equation yields the scalar amount of charge density inside the basin. The *integrated atomic charge* can be obtained from this number by addition of the nuclear charge of the respective atom. This charge often differs significantly from the *monopole* or *nominal charge*, which can be calculated from the difference between valence/core population and the nuclear charge of an atom in the *Hansen/Coppens* multipole model.

2.2. Critical points

The value of $\rho(\mathbf{r})$ at special points in the topological map are used for the classification of bonds.^[19] These points are qualified by extremes in $\rho(\mathbf{r})$ and are thus located at points \mathbf{r} at which

$$\nabla\rho(\mathbf{r}) = 0 = \begin{pmatrix} \frac{\partial\rho(\mathbf{r})}{\partial x} \\ \frac{\partial\rho(\mathbf{r})}{\partial y} \\ \frac{\partial\rho(\mathbf{r})}{\partial z} \end{pmatrix}. \quad (\text{Eq. 25})$$

They are called *critical points* (CP). There are different kinds of critical points; maxima, minima, and saddle points, and each of these points has a distinct chemical significance depending on its curvature, which is represented by the Hessian matrix:

$$H(\mathbf{r}) = \begin{pmatrix} \frac{\partial^2\rho}{\partial x^2} & \frac{\partial^2\rho}{\partial x\partial y} & \frac{\partial^2\rho}{\partial x\partial z} \\ \frac{\partial^2\rho}{\partial y\partial x} & \frac{\partial^2\rho}{\partial y^2} & \frac{\partial^2\rho}{\partial y\partial z} \\ \frac{\partial^2\rho}{\partial z\partial x} & \frac{\partial^2\rho}{\partial z\partial y} & \frac{\partial^2\rho}{\partial z^2} \end{pmatrix} \quad (\text{Eq. 26})$$

The Hessian matrix is usually used in its diagonalised form, from which the eigenvalues λ_1 , λ_2 , and λ_3 (indicating the curvature) and the corresponding eigenvectors (indicating the principal axes at the critical point) can be extracted. The classification of a critical point can be made by rank (m , the number of non-zero eigenvalues) and signature (n , the algebraic sum of the signs of the eigenvalues) of the corresponding Hessian matrix. *Bader* stated that “with relatively few exceptions, the critical points of charge distributions for mol-

ecules at or in the neighbourhood of energetically stable geometrical configurations of the nuclei are all of rank three.”^[68] Crystal structures can be considered to be energetically stable geometrical configurations as there are no net forces in a crystal structure, and thus, a classification of four critical points based on their signature can be made (see Table 1).

Table 1. Classification of critical points based on their signature.

(m,n)	name of CP	chemical significance
(3,-3)	atomic position (AP)	atomic position
(3,-1)	bond critical point (BCP)	chemical bond
(3,+1)	ring critical point (RCP)	a closed ring of bond paths between at least three atoms is present
(3,+3)	cage critical point (CCP)	a closed cage of at least four atoms is present

Atomic positions and cage critical points are local maxima and minima, respectively; bond critical points and ring critical points are saddle points, and the CP represents a maximum in $\rho(\mathbf{r})$ along one (RCP) or two (BCP) of the principal axes.

The Poincaré-Hopf relationship^[71] can be applied to the *characteristic set* of critical points in a charge density map. If the set is complete, the following equation (with n being the number of the respective type of critical point) must be satisfied:

$$n_{\text{AP}} - n_{\text{BCP}} + n_{\text{RCP}} - n_{\text{CCP}} = 1 \quad (\text{Eq. 27})$$

The relationship must be satisfied in an isolated molecule.

2.3. The Laplacian

It was recognised early that it is important that the analysis of the *Laplacian* was more informative than that of the electron density or difference electron densities.^[72] The *Lapla-*

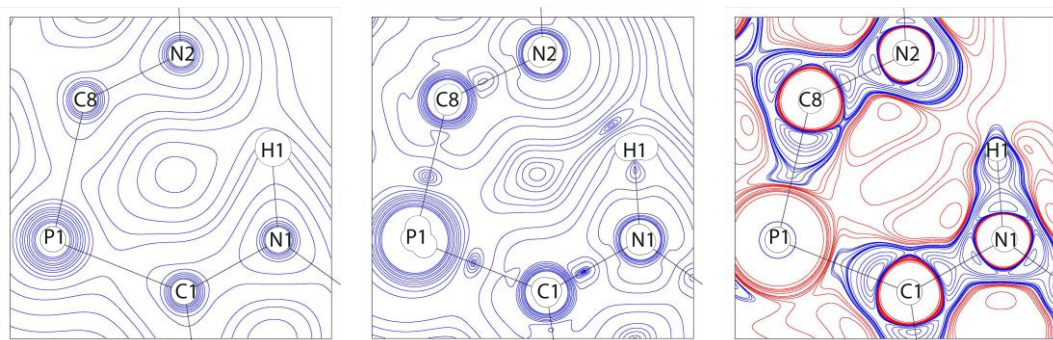


Figure 12. Isocontour plots of a charge density map. From left to right: $\rho(\mathbf{r})$, $\nabla\rho(\mathbf{r})$, $\nabla^2\rho(\mathbf{r})$. The red lines in the Laplacian plot indicate positive values, the blue lines indicate negative values and thus denote VSCCs. Bonding VSCCs are located around the carbon and nitrogen atoms; a nonbonding VSCC directed towards H1 is present at N2.

cian is the second derivative of the electron density $L(\mathbf{r}) = \nabla^2 \rho(\mathbf{r})$. It enables the visualisation of local charge accumulation ($L(\mathbf{r}) < 0$) and depletion ($L(\mathbf{r}) > 0$).^[19] The type of interaction between a pair of atoms can be classified by the sign of the Laplacian in the bond critical point; it is negative for *shared interactions* as it is anticipated for covalent bonds and it is positive in the case of ionic (*closed-shell*) interactions.^[68-69,73] This is because of the virial relationship:^[70]

$$\frac{1}{2} \nabla^2 \rho(\mathbf{r}) = 2G(\mathbf{r}) + V(\mathbf{r}) \quad (\text{Eq. 28})$$

Where $V(\mathbf{r})$ is the potential energy density, which is always negative in stationary conditions, and $G(\mathbf{r})$ is the kinetic energy density. In regions where the Laplacian is negative, the term $V(\mathbf{r})$ dominates $2G(\mathbf{r})$, which indicates that the local concentration of electron density in those regions has a stabilising effect.^[74]

A region where $L(\mathbf{r}) < 0$ is called *valence shell charge concentration* (VSCC). The charge density is locally concentrated in these areas. They are typically found directed towards a bond in the vicinity of atomic positions, but they are also present in nonbonding regions, which is typically the case for atoms with lone pairs: *Bader* and others stated that the VSCCs in a charge density map can be interpreted as a representation of the *Lewis* concept of bonding and nonbonding electron pairs.^[19,68-69,73,75-76] The geometry and distribution of valence shell charge concentrations have also been used to explain molecular recognition, for example in the solid state structure of tetrasulfur tetranitride.^[77]

Volumes of negative Laplacian values can obviously only be considered as VSCCs if they occur *in the valence shell*. This is a *caveat* which is only mentioned here because there are also regions of charge concentration in the core electron region (at very high electron densities in the magnitude of $10^3 \text{ e } \text{\AA}^{-3}$) which should not be confused with VSCCs because they are the results of core polarisation.^[15-19]

VSCCs are not always separated by regions of positive $\nabla^2 \rho(\mathbf{r})$; isosurfaces of the VSCCs tend to form banana shaped regions in which two or more local maxima in the *negative* Laplacian are combined. Proper isosurface values have to be chosen in order to separate chemically different regions in the VSCCs for visualisation purposes.^[78-80] Those local maxima in the negative Laplacian (accordingly: local minima in the Laplacian) will simply be called *maxima in the VSCCs* in the subsequent passages, referring to the increased amount of charge accumulation. The assignment of chemically different regions in VSCCs that are not separated by a region of positive $\nabla^2 \rho(\mathbf{r})$ refers to the observation of local maxima in the VSCCs.

2.4. Ellipticity

The ellipticity at a bond critical point is a measure for the deviation of the charge density from cylindrical symmetry.^[68,81-83] A value of zero indicates perfect cylindrical symmetry (see Figure 13). It is derived from the principal curvatures of the Hessian matrix:

$$\epsilon(\mathbf{r}_{\text{BCP}}) = \frac{|\lambda_1|}{|\lambda_2|} - 1 \quad (\text{Eq. 29})$$

The curvature λ_2 is defined as the negative curvature of smallest magnitude; ϵ is always positive. A deviation from cylindrical symmetry can be interpreted as indication of π bonding and delocalisation.^[84-86] The angle between the eigenvector of λ_2 and the molecular plane should be approximately 90° , e. g. in cases of “classical” C–C double bonds.^[87-88]

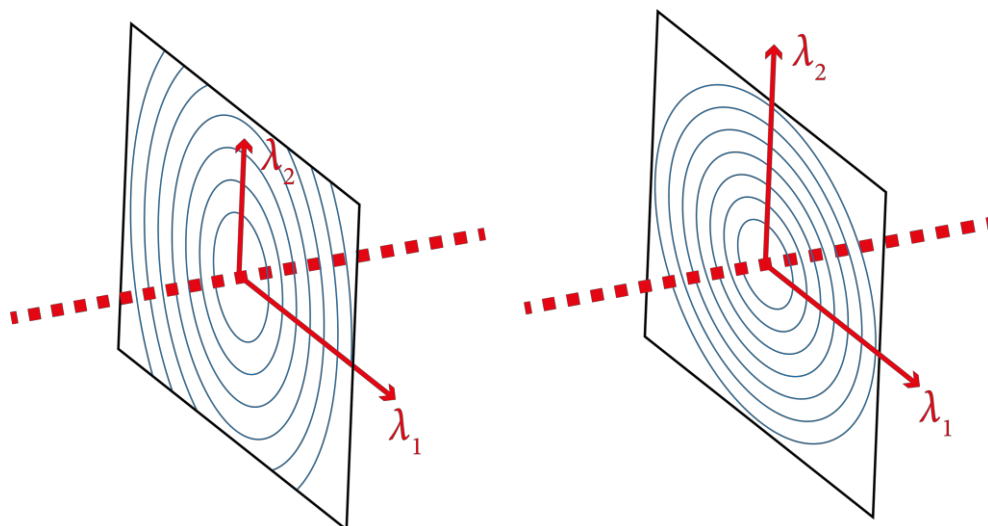


Figure 13. Graphical exemplification of the ellipticity. The dashed red line is a bond path (the eigenvector of λ_3 is directed this way); the black rectangle is perpendicular to the bond path and contains a map with charge density contour lines. The solid red arrows correspond to the eigenvectors. These vectors have a smaller length if the corresponding slope is low. Left: non-zero ellipticity (λ_2 is smaller than λ_1); right: zero ellipticity (λ_2 and λ_1 have equal lengths).

2.5. The Source Function

In analogy to the *Green's* function in the analysis of the electrostatic potential, *Bader* and *Gatti* introduced the Source Function.^[89] A *Green's* function indicates to which extent a cause at a given point in space induces an effect at another point. It facilitates the division of the charge density at a point \mathbf{r} into contributions from other points \mathbf{r}' that are determined by a Local Source Function $LS(\mathbf{r}, \mathbf{r}')$. The charge density at \mathbf{r} can be written as

$$\rho(\mathbf{r}) = \int LS(\mathbf{r}, \mathbf{r}') d\mathbf{r}, \quad (\text{Eq. 30})$$

where $LS(\mathbf{r}, \mathbf{r}')$ is given by

$$LS(\mathbf{r}, \mathbf{r}') = -\frac{\nabla^2 \rho(\mathbf{r}')}{(4\pi|\mathbf{r} - \mathbf{r}'|)}. \quad (\text{Eq. 31})$$

In this equation, the divisor is a *Green's* function indicating to which extent the cause, the Laplacian, induces the effect of the charge density.

The integrated form of the Source Function over an atomic basin yields the influence of the respective atom to the charge density at the reference point \mathbf{r} . This number divided by the total electron density at the reference point gives a percentage describing the relative influence of an atomic basin to the charge density at a reference point.

When the Source Function is calculated, the SF sums over all integrated basins for a reference point can be used as a quality criterion. This sum should always give 100 % since the SF should principally allow the complete reconstruction of the charge density. In reality, the insufficient accuracy of the numerical integration causes deviations from 100 %, but the deviations should not exceed ± 0.5 % at bond critical points with high $\rho(\mathbf{r})$ and ± 2 % for those reference points with low $\rho(\mathbf{r})$.^[90] The deviation from 100 % can thus be taken as figure of merit.

The Source Function has been used as a descriptor in addition to the “standard” QTAIM descriptors^[90-93] in order to track electron delocalisation,^[94-97] in the characterisation of metal-metal bonds^[98-100] and hydrogen bonds,^[101-102] for the rationalisation of chemical reactivity^[97,103] and for the explanation of the magnetic properties of organometallic compounds.^[96,104]

2.6. The electrostatic potential

The topology of the Laplacian map as well as the atomic charges can give valuable information to the chemist that is directly obtained from the observable of the charge density in the framework of QTAIM because it offers rationales for the chemical behaviour of a substance.^[38,105] The electrostatic potential is a complementary measure which for example has been used for the rationalisation of the pharmaceutical similarity between chemically related antibiotics^[106] or in the structure/reactivity relationship in a benzyllithium derivative.^[107]

The electrostatic potential $V(\mathbf{r})$ at a point \mathbf{r} displays the potential energy that a unit of electric charge would have at this point. It is defined as

$$V(\mathbf{r}) = \sum_j \frac{Z_j}{|\mathbf{r} - \mathbf{R}_j|} - \int \frac{\rho(\mathbf{r}')}{|\mathbf{r} - \mathbf{r}'|} d\mathbf{r}' \quad (\text{Eq. 32})$$

where \mathbf{R}_j is the position and Z_j is the charge of the nucleus j . The second term, the integral, can directly be calculated from the multipole populations.^[108] The electrostatic potential is given in units of $e \text{ \AA}^{-1}$.

As the electrostatic potential is a measure for repulsive and attractive electrostatic interactions, it can be used to visualise those regions in a molecule that are subject to electrophilic attack, where the potential would be negative, or nucleophilic attack, where the potential would be positive. Electrostatic forces are active in a relatively long range, which allows conclusions regarding the reactivity of a given compound based on the analysis of the electrostatic potential because the pathway of a reactant to the reactive site can be predicted.

2.7. Non-covalent interactions

One of the shortcomings of QTAIM is the difficulty to describe situations in which more than two atoms are involved in bonding,^[93] for example three-centre/two-electron bonds, weak C–H/ π interactions and possibly ionic interactions between contact ion pairs or weakly coordinating anions.^[109]

Johnson et al.^[110] and *Contreras-García et al.*^[111] have recently introduced the charge density-based non-covalent interactions (NCI) descriptor, which first had only been applied to theoretical charge densities and recently has been used for the analysis of experimentally derived multipole charge densities by *Saleh et al.*^[112]

The NCI descriptor is based on the reduced density gradient $s(\mathbf{r})$, which has been used for a long time for the generalised gradient approximation of the electron exchange correlation term in density functional theory:^[113-114]

$$s(\mathbf{r}) = \frac{|\nabla\rho(\mathbf{r})|}{2 \sqrt[3]{(3\pi^2)^3 [\rho(\mathbf{r})]^4}} \quad (\text{Eq. 33})$$

The reduced density gradient (RDG) is dimensionless, and $s(\mathbf{r})$ is by definition zero at all points \mathbf{r} in a homogenous electron gas. The deviation from zero indicates the deviation of the charge density from homogeneity; its value is large at points that are distant from the nuclei, i. e. where the numerator of (Eq. 33) dominates and approaches zero at regions with very high electron density, e. g. at the nuclei. It was shown that regions of certain low RDG values could be assigned to chemical interactions,^[110] and by using the sign of the second largest eigenvalue λ_2 of the Hessian matrix at each point \mathbf{r} , attractive and repulsive

interactions could be distinguished. A projection of $\rho(\mathbf{r}) \cdot \text{sign}(\lambda_2)$ onto isosurfaces of the RDG (0.5 seems to be a frequently used isovalue for the RDG, but other values could be chosen as well) were used to highlight attractive or repulsive intermolecular interactions.^[115]

3. Tris(amine) sodium cyclopentadienide

Sodium cyclopentadienide is one of the cornerstones in the synthesis of metallocenes, sandwich and half-sandwich complexes of transition metals. The earliest reports of its isolation were published almost 60 years ago by *Fischer et al.*^[116-117] and independently by *Ziegler et al.*^[118] Fifty years earlier than that, in 1901, *Thiele* was not successful in his attempt to synthesise sodium cyclopentadienide from reacting sodium metal with a solution of cyclopentadiene in benzene, but reported on his synthesis of potassium cyclopentadienide.^[119] Both *Fischer's* and *Ziegler's* reports conclude that *Thiele's* efforts to synthesise sodium cyclopentadienide was apparently hampered by *Thiele's* choice of the solvent benzene; the higher boiling temperature of xylene eventually facilitated the synthesis. They also included marginal notes on the accelerating effect of liquid ammonia, even in traces, on the synthesis of alkali cyclopentadienides from the metal and cyclopentadiene.

3.1. Theoretical work on alkali metal cyclopentadienides

The group of alkali metal cyclopentadienides has been of general theoretical interest since they are the simplest metallocenes. The term *metallocenes* includes sandwich as well as half-sandwich complexes. The type of interaction between the organic and the metallic moieties in transition metal cyclopentadienides is mostly explained by orbital-guided contributions, e. g. for ferrocene: e_{1g} (HOMO) orbitals of cyclopentadiene fragments and e_{1g} (d_{xz} , d_{yz} orbitals) of the metal. The attractive interaction in alkali metal cyclopentadienides is dominated by the *Coulomb* potential,^[121] contrary to what had been reported in very early publications on theoretical calculations on lithium cyclopentadienide.^[122]

The large importance of electrostatics in alkali metal-Cp bonding was, more recently, emphasised in an extensive theoretical study of several main group metallocenes by *Rayón* and *Frenking*.^[123] The amount of covalent contributions decreases from lithium to caesium and was calculated to be 13.4 % for [Na(Cp)]. The metal/Cp dissociation energy remains constant at around 60 kcal/mol for elements of Group 1 with the exception of lithium, in which case

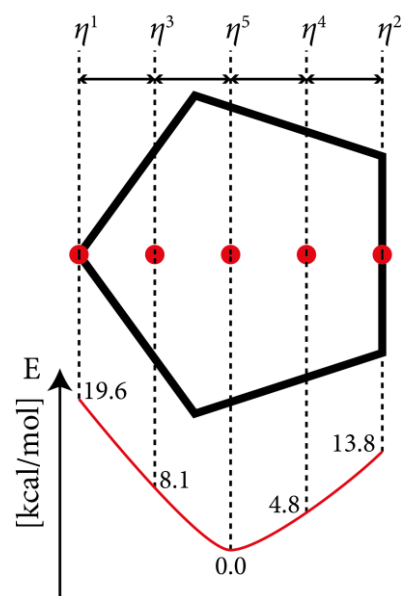


Figure 14. Schematic representation of the energy of [Li(Cp)] in dependence of the hapticity. Reproduced from data available in ref.^[120]

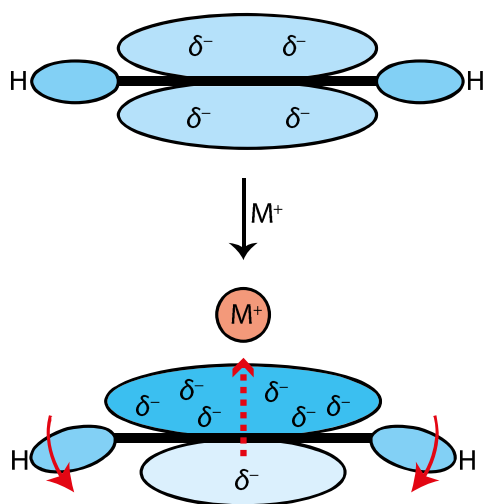


Figure 15. A simple graphical model of the electron density shift caused by hydrogen bending.

this energy is significantly higher.^[123] Thus, it is not surprising that the geometry of isolated [Li(Cp)] has been calculated to be C_{5v} and the type of interaction between Li and Cp is considered to be a η^5 -Cp-Li bond.^[121-123]

Most of theoretical calculations on alkali metallocenes are restricted to [Li(Cp)], but it was pointed out that the potential curve for the transition away from η^5 coordination is already rather shallow for lithium (see Figure 14).^[120] Having in mind that the Na/Cp interaction is even more dominated by electrostatics than it is for lithium, the curve is likely to be even more shallow for [Na(Cp)].

An out-of-plane bending of the Cp hydrogen atoms away from the metal atom was recognised in early computational studies, and the phenomenon used to be a matter of theoretical research several years ago.^[120-121,123-125] The stabilising effect caused by the hydrogen atom bending can be explained by a shift of electron density towards the hemisphere of the Cp ring which is facing towards the metal ion (see Figure 15). This is a redistribution of charge that would be favourable in terms of *Coulomb* interaction. The bending phenomenon is comparable to the “hen-or-egg” question; it can also be explained by the polarisation of the Cp ring caused by the strongly *Lewis* acidic metal ion, which leads to increasing *Pauli* repulsion between those electrons in the density of the “ π cloud” and those electrons in the C-H bonds.

It should be noted that the effect of hydrogen bending has not been uniquely reported for alkali metal cyclopentadienides. It also occurs in transition^[126-127] and main group metallocenes,^[128] but the hydrogen atoms bend towards the metal atom rather than away from it in those cases, which may serve as an additional illumination of the fundamental difference in the metal/Cp interaction compared to sodium cyclopentadienide.

3.2. Work on alkali metal ammoniacates in our workgroup

Reent Michel, a fellow PhD student in the *Stalke* workgroup, has been conducting extensive research in the field of alkali metal ammoniacates,^[129-130] and it is useful to shortly reiterate some pieces of information that emerged from his studies in order to be able to

assess the results that are going to be presented in the following paragraphs. He worked with the organic anions cyclopentadienide, indenide and fluorenone.

From his studies it can be summarised that going from lithium to caesium it is only the rather light metals lithium and sodium that form solvent-separated ion pairs at all. While it is dependent on the concentration of ammonia in the mother liquor whether a contact ion pair or a solvent separated ion pair is formed in the case of lithium and sodium, the heavier metals always form contact ion pairs, and the assembly and presumably the stability of all aggregates are determined by strong N–H/ π interactions.^[131] This is not the case if donor bases other than ammonia, say bis(2-methoxyethyl)ether (“diglyme”), are used for aggregation.^[132]

3.3. Data collection and data treatment

The synthesis of tris(ammine) sodium cyclopentadienide (**1**) was carried out by *Reent Michel*. He obtained large colourless crystals of **1** after storage of an NH₃-saturated solution of **1** in THF at –45 °C over 24 hours. The crystals were grown in a *Schlenk* flask and have to be handled in an inert atmosphere with careful exclusion of air. Their melting point is well below the ice/salt bath temperature of –15 °C (the exact melting point has not been determined), and, once crystals have been placed on a sample glass slide, even the X-Temp2 device^[133-134] for crystal handling is not sufficient to keep the crystals at a temperature low enough for them not to melt or react with residual humidity present in the mounting oil. Therefore *Reent Michel* designed a solution for this problem, which has since been applied to many of the ammine complexes from his lab. It is a block of copper which is initially cooled down in liquid N₂ and kept cool with solid CO₂; a glass slide can be mounted in it and the polarised light from the microscope glass slide is transmitted through a glass window in the copper block. The X-Temp2 device is still necessary to keep the glass slide free from precipitating humidity. The manipulation time for selecting, cutting and mounting a crystal is increased from less than a minute to approximately 15 minutes with this technique.

A crystal of the dimensions 0.38 x 0.28 x 0.20 mm³ was selected and mounted on top of a *MiTeGen micromount*[™] with a minimum of inert oil. The mounted crystal was transferred to the goniometer in liquid nitrogen and placed in the cold stream (100 K) of a Bruker Kryoflex2.

A strategy for data collection was optimised with the COSMO plugin^[135] in the APEX2 suite^[136] after unit cell determination. An overall redundancy of 8, a resolution of $d = 0.44 \text{ \AA}$ and a completeness of 100 % in all resolution shells were given as goals. A

frame width of 0.50° was selected (crystal mosaicity: 0.74°). The strategy contained 24 runs at detector positions between $0^\circ \leq 2\theta \leq 83.68^\circ$. A frame resolution of 1024×1024 pixels was chosen to avoid early detector saturation compared to the 512×512 pixels mode (see section 1.11).

Having in mind the pitfalls mentioned in section 1.11, the exposure times were adjusted carefully according to the following set of rules:

- Those reflections with highest θ on the frames have to be of sufficient intensity to be integrated. This was checked by optical inspection of the profiles of several randomly chosen reflections.
- Overexposures in terms of retakes or attenuation must be avoided (see section 1.11) by decreasing exposure time even if this means underexposure of the reflections in the rule above. This can be checked by running the command line program *SUMMARY* with the option *NOVER64*, which marks those frames that contain pixels with intensities higher than 16 bits in its output.

In addition, a filter that consisted of two layers of $25 \mu\text{m}$ aluminium and one layer of $50 \mu\text{m}$ zirconium was placed in the beam path in order to reduce the amount of low-

Table 2. Statistics from XPREP 2013/1 output after scaling and absorption correction with SADABS 2012/1.

d [Å]	Data	Theory	Compl.	Red.	<I>	<I/s>	R _{int}	R _{sigma}	R _{rim}	R _{pim}
Inf - 1.97	88	88	100 %	19.25	131.30	97.63	0.0254	0.0078	0.0261	0.0058
1.97 - 1.27	206	206	100 %	23.69	40.80	102.13	0.0240	0.0076	0.0246	0.0052
1.27 - 0.98	301	301	100 %	18.92	20.60	83.81	0.0244	0.0083	0.0251	0.0057
0.98 - 0.85	302	302	100 %	16.31	8.60	73.29	0.0286	0.0096	0.0295	0.0072
0.85 - 0.77	287	287	100 %	17.47	5.30	81.45	0.0290	0.0088	0.0299	0.0071
0.77 - 0.71	300	300	100 %	18.96	3.70	83.96	0.0319	0.0084	0.0327	0.0074
0.71 - 0.67	283	283	100 %	17.64	2.90	79.36	0.0327	0.0090	0.0337	0.0079
0.67 - 0.63	322	322	100 %	16.33	2.10	64.98	0.0395	0.0105	0.0408	0.0098
0.63 - 0.60	307	307	100 %	14.91	1.60	56.91	0.0440	0.0121	0.0455	0.0114
0.60 - 0.58	260	260	100 %	9.91	1.20	44.54	0.0286	0.0146	0.0301	0.0095
0.58 - 0.56	277	277	100 %	9.67	1.00	42.94	0.0325	0.0163	0.0344	0.0109
0.56 - 0.54	316	316	100 %	9.23	0.80	35.79	0.0389	0.0191	0.0412	0.0133
0.54 - 0.52	370	370	100 %	9.07	0.60	32.25	0.0479	0.0230	0.0508	0.0166
0.52 - 0.51	209	209	100 %	8.63	0.50	26.97	0.0591	0.0278	0.0629	0.0212
0.51 - 0.49	464	464	100 %	8.30	0.40	21.30	0.0739	0.0347	0.0789	0.0270
0.49 - 0.48	278	278	100 %	7.75	0.30	17.47	0.0891	0.0445	0.0956	0.0340
0.48 - 0.47	278	278	100 %	7.46	0.20	15.09	0.1081	0.0511	0.1165	0.0425
0.47 - 0.46	319	319	100 %	6.70	0.20	13.09	0.1139	0.0602	0.1237	0.0472
0.46 - 0.45	317	318	99.7 %	5.63	0.20	11.77	0.1202	0.0707	0.1324	0.0542
0.45 - 0.44	374	386	96.9 %	4.30	0.10	8.39	0.1480	0.0982	0.1687	0.0787
0.54 - 0.44	2609	2622	99.5 %	7.18	0.30	18.22	0.0744	0.0417	0.0802	0.0289
Inf - 0.44	5858	5871	99.8 %	11.88	6.00	45.88	0.0265	0.0091	0.0273	0.0062

energy contamination in the X-ray radiation illuminating the sample (see chapter 7 for details). This led to exposure times of 3.0 s per low-order frame with $0^\circ \leq 2\theta \leq -35^\circ$; 10.0 s for mid-order frames with $-35^\circ < 2\theta < -67.5^\circ$ and 180.0 s for frame with $-67.5^\circ \leq 2\theta \leq -83.68^\circ$. The measurement could not be completed as intended because of a software failure of the Bruker Kryoflex 2 low-temperature sample cooling device which eventually caused the crystal to melt. Nevertheless, redundancy and quality of the data on the collected frames was deemed sufficient, see Table 2.

The raw data were reduced with SAINT v7.68A.^[57] Each run was integrated with an iteratively refined individual orientation matrix in order to increase the reflection prediction accuracy. The maximum resolution for integration was adjusted if necessary. This is in cases where the exposure time had to be decreased to avoid overexposure; the reflections with highest θ on these frames often do not have sufficient intensity to be properly integrated and thus deteriorate the quality of the remaining data by biasing the least-squares profile fit. A numerical absorption correction^[137] using the indexed crystal faces that were determined in the APEX2 software suite was carried out using SADABS 2012/1.^[138] A file containing averaged reflection intensities according to the space group symmetry and corresponding standard deviations was written with SADABS. The same file was written, but according to the specifications of XD2006 with omitted reflections that are systematically absent or collected with less than zero intensity. Data statistics were determined with XPREP 2013/1 (see Table 2).^[139] A reflection file with semi-empirical absorption correction^[30-33] was also created with SADABS, but no further investigations on the impact of using these data were carried out since no fundamental difference to the data obtained by numerical absorption correction was detected in the refinement.

We also attempted to collect data at lower temperature than 100 K, but destructive phase transitions prevented data collection at temperatures between 15 K and 80 K.

3.4. Structure solution and refinement (IAM)

According to the reflection statistics that were analysed with XPREP 2013/1, the space group is *Pnma*. The structure was solved with SHELXT^[140] in its standard settings, which confirmed *Pnma*, and an IAM refinement was carried out with SHELXL-2013. Half a molecule is contained in the asymmetric unit; the crystallographic mirror plane is perpendicular to the Cp best plane and bisects the molecule (compare Figure 16). The N1 ammine group does not obey the crystallographic symmetry. It shows symmetry-induced disorder involving the hydrogen atoms, which thus have site occupation factors of 0.5. The hydrogen atom positions do not resemble threefold rotational symmetry with respect to the N–Na vector in the cases of both N1 as well as N2; the NH₃ groups are tilted. For this reason,

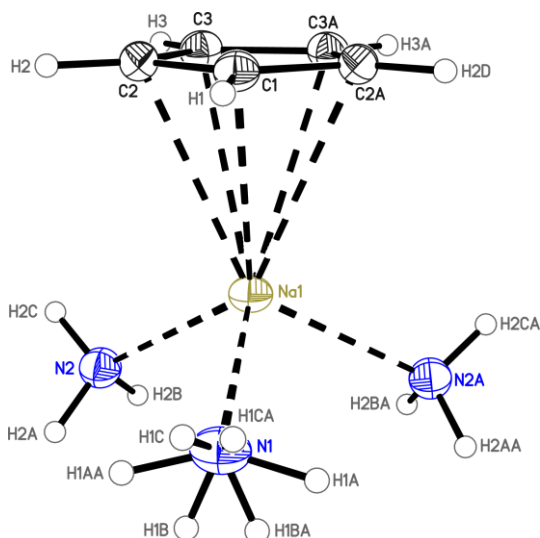


Figure 16. Crystal structure of **1** after IAM refinement with SHELXL-2012. The centroids of atoms C1, H1, Na1, and N1 are in the crystallographic mirror plane.

freely with the restraint of similar C–H distances and the constraint of equal U_{iso} . The residuals at this advanced stage of the IAM refinement seem to be quite substantial (compare Figure 17–19). These residuals correspond to the internuclear electron density that has to be modelled in the XD2006 refinement.

The disorder in the ammine group N1 was modelled by assuming that only the hydrogen atoms are involved in the disorder. The disorder is presumably not caused by rotation of the ammine group around the N–Na vector but by a tilt of the group as pointed out earli-

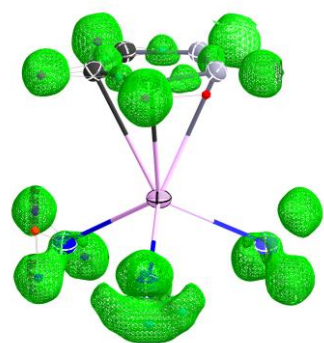


Figure 17. Residual density without hydrogen atoms included in the refinement. $wR2 = 19.0\%$. Residual density isosurface at $0.30 \text{ e } \text{\AA}^{-3}$.

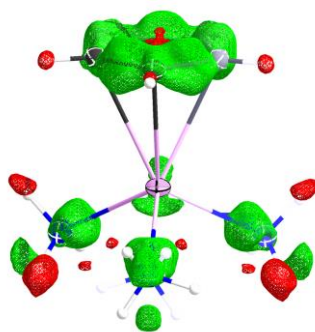


Figure 18. Residual density with hydrogen atoms fixed with riding models (AFIX 43/137) at Cp carbon and nitrogen atoms. $wR2 = 14.0\%$, Residual density isosurface at $0.12 \text{ e } \text{\AA}^{-3}$.

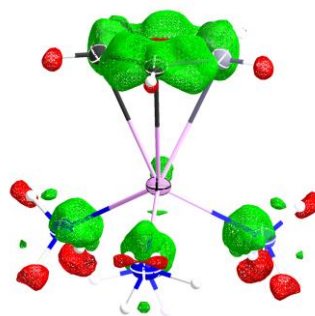


Figure 19. Hydrogen atom positions refined with distance restraints instead of constraints. $wR2 = 12.5\%$, Residual density isosurface at $0.12 \text{ e } \text{\AA}^{-3}$. Only residual density at bonding or lone pair regions is left.

the ammine hydrogen atoms were not refined with a riding model (HFIX 137)^[141] but merely with distance restraints (SADI)^[141] that restrained all N–H distances as well as all 1,3 H–H distances to be similar, respectively.

As another measure to additionally relax the structural model, the U_{iso} of the hydrogen atoms were refined, which are usually constrained to 1.5 times the U_{eq} of their pivot atoms, but with the condition that the U_{iso} of ammonia hydrogen atoms were constrained to each other. An according strategy was applied to the Cp hydrogen atoms, which were refined

er. In space group $Pnma$, the disorder is present at every atom in the unit cell which is symmetry equivalent to N1. It was checked whether the actual symmetry was lower than the apparent space group symmetry by refining the structure in space group $P\bar{1}$. The disorder remained at the respective nitrogen atoms in the lowered symmetry space group.

The coordinates of N1, which are automatically constrained to place the atom on the crystallographic mirror plane, may however not be the true coordinates of the centre of gravity around which the ammine group tilts. If removed from the special position manually, the N1 coordinates will always be refined so that the atom moves back to the special position. In order to avoid this behaviour, the structure was refined in non-centrosymmetric space group $Pn2_1a$, which is a non-standard setting of $Pna2_1$ that was used because no axes had to be transformed when changing the space group. The missing mirror plane then is the only difference to $Pnma$. The actual crystallographic symmetry was mimicked by constraints that restricted the refinement of coordinates and displacement parameters. Two symmetry equivalent atoms A and B that are connected by a mirror plane through the fractional coordinates $(x, 0.75, z)$ have the following dependencies:

$$x(A) = x(B) \quad y(A) + y(B) = 1.5 \quad z(A) = z(B) \quad (\text{Eq. 34})$$

$$\begin{aligned} U_{11}(A) &= U_{11}(B) & U_{22}(A) &= U_{22}(B) & U_{33}(A) &= U_{33}(B) \\ U_{23}(A) &= -U_{23}(B) & U_{13}(A) &= U_{13}(B) & U_{12}(A) &= -U_{12}(B) \end{aligned} \quad (\text{Eq. 35})$$

The constraints were applied either using a free variable for equivalent parameters or, in case of the y coordinates, a linear restraint (SUMP^[141]) was used that restrained the sum of the two parameters to 1.5 with its standard deviation set to zero.

This way, it was possible to create a model with a disordered N1 nitrogen atom in space

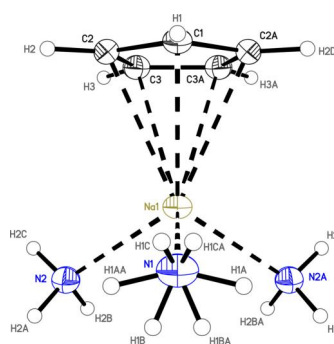


Figure 20. Model in space group $Pnma$. The ellipsoid is slightly elongated in the direction perpendicular to the mirror plane (parallel to the paper plane in this figure).

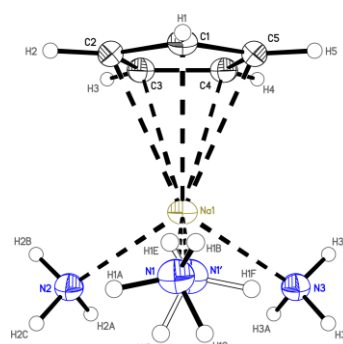


Figure 21. Model with disordered N1 atom in space group $Pn2_1a$. The N1 displacement parameters create ellipsoids that are closer to spherical shape.

group $Pr2_1a$ (compare Figure 20 and Figure 21). The distance between the two nitrogen sites after refinement of all parameters is 0.19 Å. This value is far away from the maximum resolution of 0.44 Å. It was therefore decided to omit this model in favour of the model in space group $Pnma$ without disordered N1 atoms even though the displacement parameter of N1 is slightly elongated in the direction perpendicular to the mirror plane.

3.5. Sodium atom shift

As discussed in section 3.1, the alkali metal ion would theoretically be expected to be located over the centroid of the Cp carbon atoms, which is a logical consequence of the symmetry of the Cp ring. However, the sodium atom Na1 is shifted by 0.173 Å with respect to the Cp centroid in the crystal structure.

The *Cambridge Structural Database* (CSD) was used to determine whether the observed shift was significant. This was done by an analysis of the distribution of shifts in related compounds; the condition for consideration of a crystal structure was that it contained a substituent-free $[C_5H_5]^-$ moiety with a metal atom bonded to it in a η^5 coordination mode. No restrictions were made concerning the type of metal (CSD element group “4M”, “any metal”).

The search included four parameters that were calculated for each hit (see Figure 23): the Cp centroid C, calculated from the positions of the five carbon atoms; the Cp best plane, calculated from the positions of the five carbon atoms; the distance d of the metal atom to the centroid; the angle θ between the plane normal vector and the centroid–metal atom vector. The distance \overline{CI} (“shift” in Figure 23) of the metal atom with respect to the Cp cen-

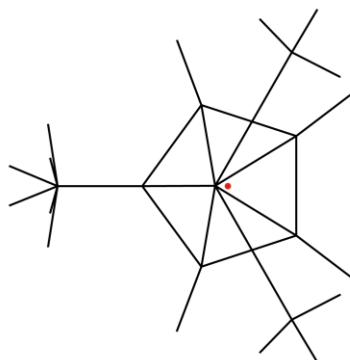


Figure 22. A wireframe representation of the result from SHELXL structure refinement of $[Na(NH_3)_3(Cp)]$, **1**. The red dot indicates the centroid of the Cp carbon atoms.

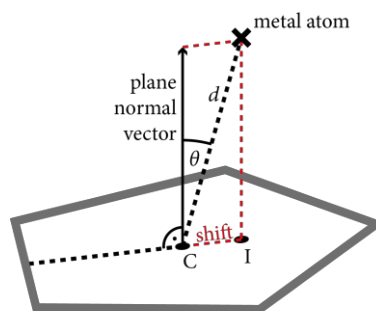


Figure 23. Parameters used in the CSD search are highlighted; please refer to the text for further explanation.

troid parallel to the Cp best plane was calculated by $\sin(\theta) \cdot d$. The mean of the distribution with 27679 data points is 0.046(40) Å and its median is 0.035 Å.

A similar search was carried out in which exclusively structural motifs with alkali and alkaline earth metals were considered. The mean and the median values for those structures are 0.122(104) Å and 0.082 Å, respectively. Both are considerably larger than the values obtained from the unrestricted search; it has to be taken into account that the statistics are based on a much smaller number of data points (237), hence the larger error. The mean and the median values further increase if also those crystal structures are taken into account in which the Cp ring is allowed to have non-hydrogen substituents (0.131(120) Å mean and 0.092 Å median from 929 data points). The distorting effect of the various substituents on the Cp ring geometry and possibly other electronic and steric influences are likely reasons for larger shifts of the metal atoms in the latter distribution. The ionic nature of Cp–alkali metal interactions^[121,124] that lead to a shallow minimum of the potential energy hypersurface for the shifting metal atoms^[120] may explain the broader distribution and the larger mean and median values of the shifts compared to those of transition metals.

What are the implications with respect to the observed shift of the sodium atom in the case of $[\text{Na}(\text{NH}_3)_3(\text{Cp})]$? The statistics demonstrate that the observed shift is not significantly outside the boundaries defined by the standard deviation from the mean value, but somewhat on the large end of that scale. The charge density distribution analysis in the crystal structure of $[\text{Na}(\text{NH}_3)_3(\text{Cp})]$ may give an explanation for the shift.

3.6. Hydrogen out-of-plane bending

The crystal structure of **1** does not indicate the out-of-plane bending of hydrogen atoms as it has been described in theoretical calculations as mentioned in section 3.1.^[120,124] According to theory, the hydrogen atoms would be expected to bend slightly away from the sodium atom. However, the SHELXL refinement rather gives an out-of-plane bending *towards*

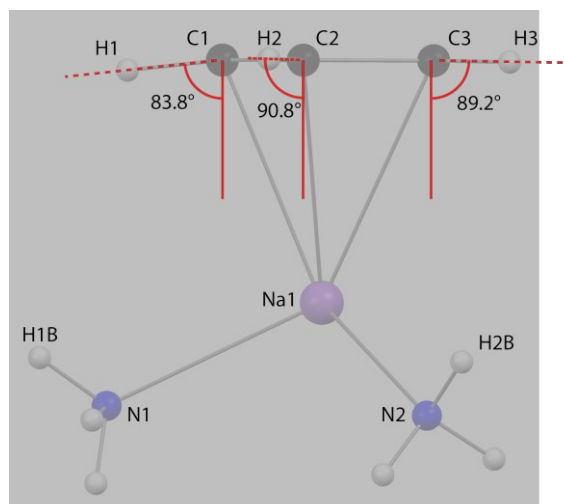


Figure 24. Projection of the crystal structure on the crystallographic mirror plane in the crystal structure of **1**. The solid red lines are parallel to the Cp best plane normal vector.

the sodium atom, at least in the case of H1 (see Figure 24). This is even more astonishing given the fact that the C1–H1 and the Na1–N1 bonds are exactly eclipsed. The estimated standard deviations for the angles given in Figure 24 are not given by the refinement program, but the corresponding e.s.d.s of H–C_α–C_β–C_γ torsion angles are between 0.7° and 1.0°, which gives significance only to the out-of-plane bending of H1. The refinement of hydrogen atom positions, let alone hydrogen isotropic displacement parameters,^[142] against X-ray diffraction data without restraints or constraints is sometimes impossible. Data of high quality and high resolution facilitate the refinement.^[143-144] Some interesting remarks encouraging the refinement of hydrogen atom positions in order to avoid systematic bias in the calculated structure factor can be found in a publication by *Cooper et al.*^[145] It is perhaps worth to mention that the initially neglected out-of-plane bending of hydrogen atoms in the crystal structure of a compound that also contains a coordinated aromatic system, bis(μ-chloro)bis(η⁶-benzene)dichlorodiruthenium(II), was used as an example in which the refinement of hydrogen atom positions without geometrical constraints led to a significant change of the geometry.

The reverse out-of-plane bending observed in the present case after SHELXL refinement had nevertheless to be verified after the subsequent multipole refinement, which is able to account for the bonding density and the polarisation more elaborate than the SHELXL independent atom model (see section 1.7).

3.7. General considerations in the multipole refinement

A few modifications had to be made to the structure obtained by SHELXL before it can be taken as a starting model for XD2006: the hydrogen atoms were shifted along their bonding vectors to distances derived from neutron diffraction experiments: those are 1.076 Å for “aromatic” C–H and 1.017 Å for “amino” N–H distances.^[52] XD2006 expects a reflection file with averaged data including merged symmetry equivalent reflections and removed systematically absent reflections; this was prepared with the program SADABS. The parameter refinement in SADABS was repeated until the recommended g-value converged (final value: g = 0.0429; see section 1.4 for details on SADABS).

The parameter file and an initial command file for XD2006 were set up with XDINI. It is of vital importance that not too many parameters are refined simultaneously in the initial stages of the refinement; some parameters correlate heavily, and large parameter shifts away from their initial values can be expected in the first steps of the refinement. The monopole and multipole parameters of chemically equivalent atoms were constrained on each other in the first steps of the refinement (see Figure 25). The danger is high that the refinement does not converge or that it converges towards a local minimum that is not

the global minimum. Therefore, a multiple refinement is usually divided into several steps where only certain parameters are refined at the same time. The convergence criterion for the maximum parameter shift is 10^{-9} times its standard uncertainty. This is a very rigid criterion, and it was not reached in all of the refinement steps. In these cases, XDLSM was configured to end the particular refinement step after 20 iterations and proceed to the next step. The refinement strategy that was eventually used for the dataset is shown in Table 3. As there is no unique criterion to judge about the validity of a certain refinement strategy, the sequence was chosen so that the magnitude of the parameter shifts was kept as low as possible for each step.

The refinement was carried out using the relativistic *Dirac-Fock* wave functions for the core and spherical valence density that are stored in the *Su-Coppens-Macchi* (SCM) bank file in XD2006.^[146-147] The non-spherical terms were refined up to the hexadecapolar level for non-hydrogen atoms; hydrogen atoms were treated with bond-directed dipoles and

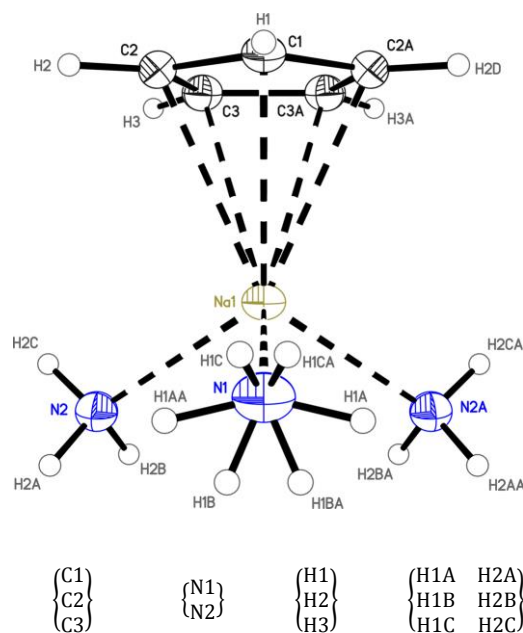


Figure 25. Atoms for which population parameters were constrained on each other during the initial steps of refinement.

Table 3. Applied XD2006 refinement strategy. Hydrogen multipole parameters were refined up to an order of $l_{\max} = 2$. The expansion and displacement parameters of hydrogen atoms were not refined. The scale factor (SCA) is refined in every step and is only mentioned in the first one. Abbreviations: D, dipoles; Q, quadrupoles; O, octapoles; H, hexadecapoles; M, monopoles; XYZ, positional coordinates; U_{ij} , displacement parameters; κ , spherical expansion parameters; κ' , aspherical expansion parameters. See also chapter 1.6. CHEMCON: the monopole and multipole populations of chemically equivalent atoms are constrained to each other in these refinement stages.

1.	SCA		12.	XYZ(Hydrogen)
2.	D, Q, O, H	(CHEMCON)	13.	XYZ(Non-Hydrogen), U_{ij}
3.	M	(CHEMCON)	14.	M, D, Q, O, H
4.	XYZ, U_{ij}	(CHEMCON)	15.	κ
5.	D, Q, O, H	(CHEMCON)	16.	κ'
6.	M	(CHEMCON)	17.	XYZ, U_{ij}
7.	M		18.	M, D, Q, O, H
8.	D, Q, O, H		19.	κ, κ'
9.	M		20.	M
10.	M, D, Q, O, H		21.	M, D, Q, O, H
11.	κ		22.	XYZ, U_{ij} , M, D, Q, O, H

quadrupoles. No symmetry restrictions were applied to the refined parameters in the final stages of the refinement other than crystallographic symmetry restrictions for atoms on special positions (Cl, H1, Na1, N1).

Due to the disorder in the N1 ammine group, the occupancy of the respective hydrogen atoms is 50 %. The parameter file for XD2006 contains information about the site multiplicity of the respective atoms; an atom on a mirror plane has a multiplicity factor of 0.5 and all population parameters are multiplied by this value. The nitrogen atom N1, which is located in the crystallographic mirror plane, has a starting value of 2.5 for its monopole population, which corresponds to 5.0 valence electrons. The disordered hydrogen atoms have to be modelled using multiplicity factors of 0.5 as well. The disorder has to be eliminated from the parameter file for subsequent calculation of properties because properties can only be calculated for the total electron density which would make proper integration and bond path tracing impossible. The elimination of disorder was done manually after refinement by division of all population parameters of the respective atoms by the occupation number and exclusion of those atoms from the generation of symmetry equivalent atoms. This procedure results in a violation of the crystallographic symmetry for the N1 ammine group, but nevertheless was necessary for sensible calculation of properties.

The displacement parameters of the hydrogen atoms were not refined. Instead, an anisotropic model for the hydrogen atoms was obtained using the www-based SHADE server^[148] which estimates hydrogen atom ADPs combining a rigid body analysis of the non-hydrogen ADPs with data from neutron studies.^[149] The atomic positions of ammonia hydrogen atoms were never refined while those of the Cp hydrogen atoms were allowed to refine freely. This was due to the inability of the XD2006 least-squares routine to apply restraints to pairs of parameters. There is no comfortable way in XD2006 to create a riding model comparable to the one used in SHELXL, and the free refinement of ammonia hydrogen atom positions without any restraints turned out to be unstable. The program MoPro^[45] contains functions for geometry restraints. A multipole refinement with MoPro was set up, but in the progress of the work on this thesis, several reproducible bugs in the software prevented the refinement from being successfully conducted. It became clear from the correspondence with one of the authors of the program that the software development struggled with implementation issues, and further efforts to use the program were eventually abandoned.

From my experience with several publications of charge density refinements, it seems to be common in the experimental charge density community to refine against a set of reflections that only includes those reflections with $I > n \sigma(I)$, in which n frequently is as high as 3 or 4. This is normally done in order to avoid refinement against reflections with

very unreliable intensities. However, it has the side effect that a potentially high number of weak reflections with high θ is arbitrarily excluded from the refinement, which can of course be a source of bias. However, it has been demonstrated that it should rather be common practice to include all reflections in least-squares refinements because even the weakest reflections carry significant information.^[150-151] It was therefore decided to eliminate any significance restriction from the refinement.

3.8. Critical examination of the multipole refinement

The low order data contain information about diffuse electron density such as bonding density, the positions of hydrogen atoms and the diffuse density associated with the $3s^1$ electron of sodium. Special attention was therefore paid to the refinement of the population parameters of the sodium atom. There is a range of atomic scattering factors available both for neutral and ionic species of the elements.^[152] Alkali metals can be modelled using scattering factors for neutral atoms or cations, compare Figure 3 (section 1.3), and the choice of scattering factors can reportedly cause significant differences, which in the case of alkali metal ions effects the reflection data with lowest θ ,^[153-154] where unfortunately only a small number of reflections are available. An initial model was refined with the standard settings of a scattering factor for a neutral sodium atom with one valence electron.

Multipole populations could not be refined to convergence in this case. The monopole (valence) population of NaI shifted to a value very close to zero if the NaI multipole populations were not refined. It was therefore decided to use the scattering factor for cationic Na^+ with a static monopole population of zero, which means that no parameters apart

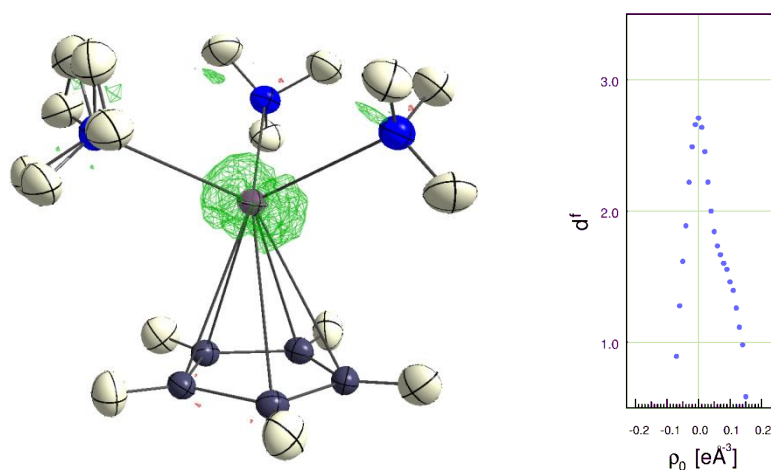


Figure 26. Left: residual density with a contour value of $0.05 \text{ e } \text{\AA}^{-3}$, Graphics rendered with MoleCoolQt,^[155] Right: the fractal dimension of the residual density after refinement.^[53]

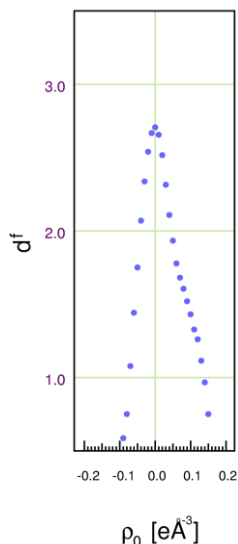


Figure 27. Fractal dimension of the residual density after refinement of the sodium atom with the Na(0) scattering factor.

from the atomic position and the U_{ij} were refined for NaI. The “missing” valence electron was distributed over the monopole populations of remaining non-hydrogen atoms (0.14 e per carbon and 0.10 e per nitrogen atom) for electroneutrality.

The population parameters of carbon, nitrogen and hydrogen atoms were refined without chemical constraints after the first initial refinement steps. This strategy led the refinement to convergence and gave reasonably low values for $R1 = 1.39\%$ and $wR2 = 3.20\%$. The resulting difference density, however, is neither flat nor featureless (see Figure 26; graphics were created with MolecoolQT^[155]). A comparatively large amount of residual density is concentrated around NaI. As the phenomenon might well originate in the treatment of NaI as cation, a refinement with the Na(0) scattering factor was carried out where the initial valence population of one electron was not allowed to be reduced, but to no avail: the residual density remained.

Since no qualitative difference between the two approaches with Na^+ and Na^0 models could be spotted (compare Figure 26 and Figure 27), the preliminary conclusion was drawn that the $3s^1$ electron could not possibly be the source of error in this case.

The plot of the resolution dependence of the ratio between mean observed and calculated structure factors^[156] (compare section 1.8) shows that there is a systematic variance, even if its magnitude is rather low ($\pm 2\%$). It has been discussed in literature that the data points should be distributed at a constant level close to unity over the whole resolution range.^[54] It is eye-catching that the first data point, representing the reflections of lowest $\sin(\theta)/\lambda$,

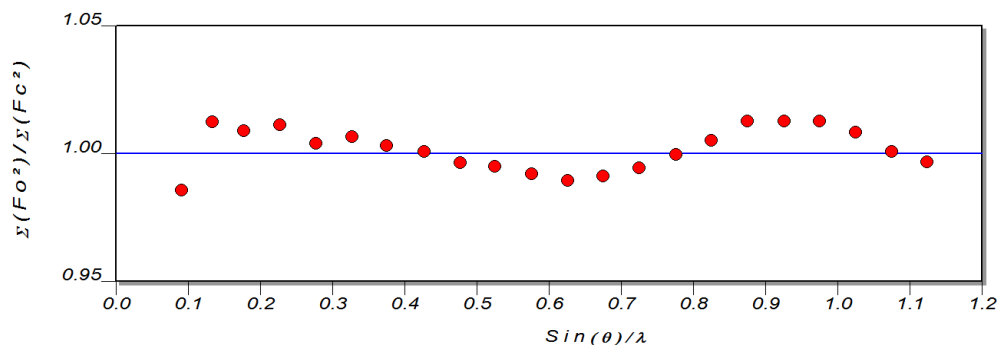


Figure 28. Resolution dependence of the ratio between mean observed and calculated structure factor.

Table 4. A list of the reflections with lowest θ . The resolution d is the corresponding quantity from the Bragg equation. *Multiplicity* is the number of observations, including symmetry equivalent reflections. The numbers in the last column correspond to the first two data points in Figure 28.

h	k	l	$\sin(\theta)/\lambda$ [Å]	d [Å]	F_{obs}^2	$F_{\text{obs}}^2/F_{\text{calc}}^2$	$F_{\text{obs}}^2/\sigma(F_{\text{obs}}^2)$	Multiplicity	$\Sigma(F_o^2)/\Sigma(F_c^2)$
1	0	1	0.0820	6.10	671.8	0.970	133.6	16	0.986
0	1	1	0.0851	5.87	274.1	0.954	122.4	15	
2	0	0	0.0856	5.84	515.4	0.943	89.64	7	
1	1	1	0.0953	5.25	984.9	1.076	167.2	28	
0	2	0	0.0972	5.14	5887.5	0.968	75.71	5	
2	1	0	0.0984	5.08	3560.7	1.007	126.82	14	
2	0	1	0.111	4.52	0.7	0.867	10.83	16	1.013
2	1	1	0.121	4.14	2384.9	1.016	191.3	34	
1	2	1	0.127	3.93	643.0	1.051	172.9	30	
2	2	0	0.130	3.86	417.5	1.018	110.2	12	
0	0	2	0.140	3.58	1054.8	1.062	77.91	6	
1	0	2	0.146	3.42	10.7	0.959	71.53	16	
3	0	1	0.146	3.42	1979.0	0.982	137.9	17	

is profoundly lower than the subsequent point while there is a smooth progression over the remaining data points (see Figure 28). It is important to note that the bins in the plot do not contain equal numbers of reflections; the reflections are divided into bins with equal steps of $\sin(\theta)/\lambda$. The exact routine that divides the reflections into bins is not documented for the program DRKPlot. A guess was made based on the values, and it turned out that only six reflections make up the lowest resolution bin and eight reflections form the next bin while many dozens of reflections are contained in the highest resolution bins. Some of the statistics concerning the reflections in the inner resolution shells are summarised in Table 4.

Some time was spent to inspect those low-order reflections in Table 4 that make up the first data point in Figure 28 because the deviation compared to the directly neighbouring data point is obvious. The inspection was conducted along the guidelines given in section 1.11 (*background intensity; measurement of weak reflections; overexposure*). The unmerged reflection file obtained from SADABS contains every measured reflection that was not rejected in the processes of data reduction. Severe outliers that are rejected can be caused by an obstruction of the reflection by the beam stop, thus decreasing the integrated intensity, or by ice or oil rings in the diffraction pattern which can interfere with reflections and lead to abnormally high integrated intensity. It is possible that the intensity of a reflection and, where applicable, of its symmetry equivalents are determined systematically wrong. The absence of such obstructions was confirmed by visual inspection of the frames with the “find a reflection” plugin in the APEX2 suite.^[136] The inspection also showed that

retakes were made in the case of reflection (0 2 0), but not in the case of the other reflections, which might have been another source of systematic errors. Extinction as the source of underestimated low-order reflection intensities could be ruled out as the isotropic extinction coefficient refined to zero. It remains unclear what the cause for the underestimation of the very low-order reflections was.

Another observation is worth a closer look: the multiplicities of the reflections in Table 4 are distributed very unevenly, which is likely due to the differing number of symmetry equivalents for each case. The refinement is performed against merged data; the reflection (2 0 0) is merged from the observations of only two symmetry equivalent reflections, while the reflections (2 1 0) and (1 1 1) result from the observations of four and eight symmetry equivalents, respectively. This apparently has an immediate effect on the significance $F^2/\sigma(F^2)$ of the reflections, giving reflections with low multiplicity a lowered significance.

3.9. The significance of the data

The influence of raw data processing software on the significance $F^2/\sigma(F^2)$ has been a topic of lively discussion recently,^[27,157-158] namely the difference in data treatment with the programs SADABS or SORTAV.^[23,25] Although SADABS created an inappropriate error model according to their reasoning, *Jørgensen et al.* concluded that the effect of different approaches on the results of a charge density refinement was low.^[27] In order to confirm this, a second refinement was carried out against data that was treated according to the procedure proposed in ref.^[27]

For this purpose, the data were scaled in SADABS, but the application of an error model was prevented by setting the parameter $g = 0$ (compare section 1.4). The script *kvalue* by

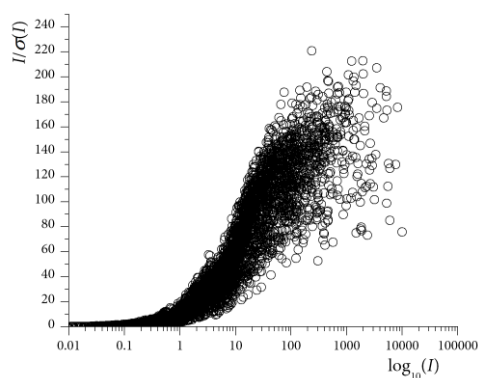


Figure 29. Diederichs plot (significance against logarithmic intensity) of the reflection data obtained from SADABS.

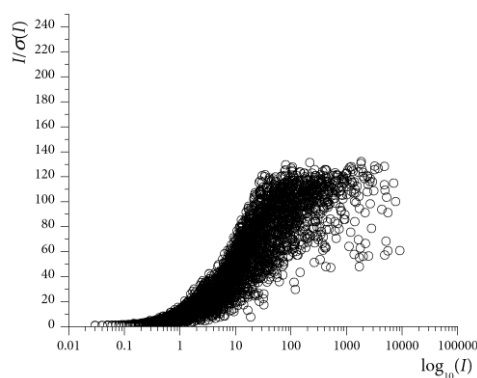


Figure 30. Diederichs plot of the reflection data obtained from combined SADABS/SORTAV processing as explained in the text.

D. Kratzert^[159] was subsequently used to remove the influence of the batch scale factor k .

The obtained data, at this point scaled and corrected for absorption, were eventually merged with the program SORTAV without the introduction of an additional error model. The option “use unit weights” was used, which overrides the use of experimental uncertainties that are calculated from the integrations program. This has the effect that the resulting uncertainties are estimated from the variance of the population of the measurement. See Figure 29 and Figure 30 for a comparison between the obtained significances. Both of the displayed distributions show the typical sigmoidal behaviour, which is more pronounced for the data that were merged in SORTAV.

The obtained GoF (*goodness of fit*) values are $\text{GoF} = 2.1264$ ($\text{GoF}_w = 1.1809$) and $\text{GoF} = 1.5629$ ($\text{GoF}_w = 1.0893$) for refinement against SADABS and SORTAV data, respectively. Slightly different weighting schemes were used that were adjusted to achieve a congruence of the experimental and the expected normal probability distribution of $\sigma(F^2)$: $a = 0.01$, $b = 0.008$ for SADABS-merged data and $a = 0.01$, $b = 0.006$ for SORTAV-merged data (see section 1.8 for a documentation of these parameters).

This indicates a slightly better GoF for the data obtained with SORTAV, which is due to the higher mean $\sigma(F^2)$. The differences between the results of the two refinements seem to be only very subtle; the populations of most monopoles and multipoles as well as the expansion parameters are equal within three times their estimated standard deviations. This is not surprising: not the intensities but only their standard uncertainties are altered by the different routines.

3.10. Refinement of resolution dependent scale factors

The systematic resolution dependence of the scale factor plot in Figure 28 cannot be explained in a straightforward way. However, it can be speculated that some systematic errors are introduced in the steps from raw data to the merged reflection file.

It is striking that the deviation shows a systematic resolution dependency as can be seen from the waviness of the diagrams in Figure 31. The shape of the diagram with a shallow minimum at medium resolution around 0.5 \AA^{-1} to 0.6 \AA^{-1} and some irregularities at the very low and very high resolution ends is commonly observed, at least in the charge density refinements in our group. The sources of the small, but apparently systematic errors in the data are very hard to tackle. Changes in the integration routine such as the variation of the limits for least-squares profile fitting seem to have no influence.

We therefore carried out an additional refinement in which we included ten resolution dependent scale factors instead of only one global scale factor in order to account for the

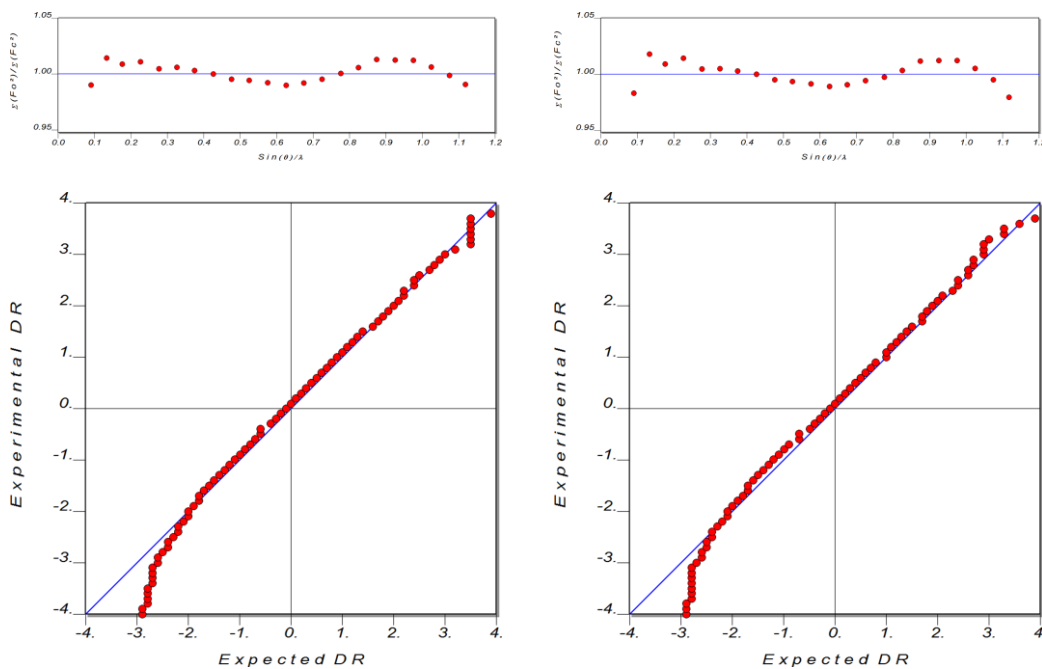


Figure 31. Resolution dependence of the scale factor (top) and the normal probability distribution of $\sigma(F^2)$ (bottom) obtained from refinement against data merged with SADABS (left column) and SORTAV (right column). The difference is largest for reflections at low and very high θ , which is partly due to the higher significance of low order/high redundancy reflections in the SADABS data and the different weighting schemes.

systematic deviation. The resolution shells were chosen in steps of 0.1 \AA^{-1} with the first bin from 0 to 0.2 \AA^{-1} . The resulting $\Sigma F_{obs}^2/\Sigma F_{calc}^2$ statistics along with the boundaries in $\sin(\theta)/\lambda$ that separate those bins with different scale factors are displayed in Figure 32.

As a result, the resulting diagram has lost its waviness. However, the deviations at very low and very high angle persist. The goodness-of-fit (GoF) has slightly improved (GoF = 2.0137; GoF_w = 1.1733; one scale factor: GoF = 2.1264; GoF_w = 1.1809) as well as the $R1 = 1.59 \%$ and $wR2 = 3.21 \%$ (one scale factor: $R1 = 1.65 \%$ and $wR2 = 3.31 \%$).

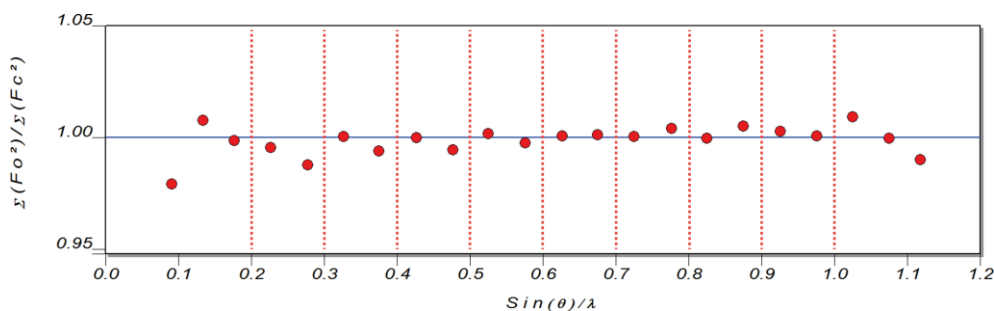


Figure 32. Resolution dependence of $\Sigma F_{obs}^2/\Sigma F_{calc}^2$ after refinement with ten resolution dependent scale factors. The boundaries between the respective bins for which different scale factors have been defined are marked with red dashed lines.

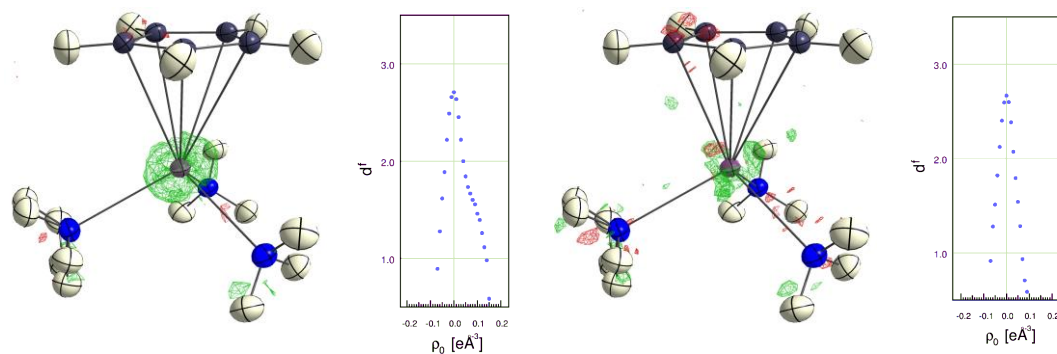


Figure 33. Residual density in the vicinity of the modelled molecule and fractal dimension of the residual density in the unit cell. Left: refinement with one scale factor; right: refinement with ten scale factors. The isosurfaces are drawn on levels of $+0.05 \text{ e \AA}^{-3}$ (green) and -0.05 e \AA^{-3} (red).

These figures merely display an improvement in the fit against data that essentially have been modified to match the calculated model. However, the goal of a charge density refinement is to describe the electron density in the unit cell so accurately that the difference density obtained by Fourier transformation of $\Sigma F_{obs}^2 - F_{calc}^2$ is flat and featureless, which means that the residual peaks of density are as low as possible and no systematic pattern should remain when the refinement of all parameters is converged.

The residual density after refinement of ten scale factors is distributed more evenly in the unit cell than it was with one scale factor. This becomes visible by the plot of the fractal dimension of the residual density (compare Figure 33). All residual density calculations were made with the programs XDFFT and XDFOUR without any resolution or significance cut-offs for the data.

3.11. Preparative calculations

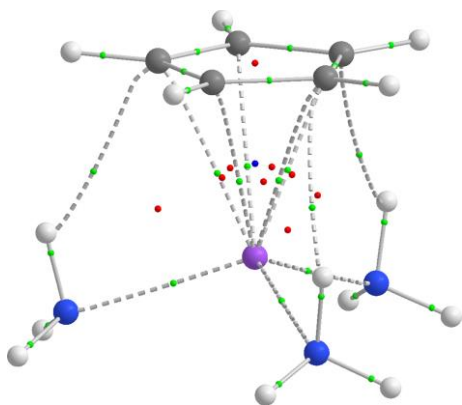


Figure 34. Molecular graph of the result from geometry optimisation of **1** at DF-LMP2/cc-pCVTZ&cc-pVTZ level of theory. All possible Na–C bond paths and the corresponding ring critical and cage critical points were found; there are even bond paths between ammonia hydrogen atoms and Cp carbon atoms.

In our collaboration with the workgroup of R. A. Mata, Göttingen, we obtained a wave function-derived charge density map of a geometry optimized structure of $[(\text{H}_3\text{N})_3\text{Na}(\text{C}_5\text{H}_5)]$, which was analysed according to QTAIM with the AIMall suite of programs.^[160] The optimisation had been conducted in MOLPRO^[161] at the LMP2/cc-pCVTZ (sodium atom) and cc-pVTZ (remaining atoms) level of theory.^[162-173]

The obtained structure turned out to be largely incongruent with the experimentally derived one although the major structural feature, the shape of a piano stool, was retained. The major incongruences are sketched in Figure 35. There is no sodium atom shift in the geometry optimised structure; it is located directly above the geometrical centre of the cyclopentadienyl ring at a distance which is 7.3 pm shorter than in the experimental structure. The Cp–Na distance is significantly decreased in the theoretical structure, and the C–Na–N angles are more acute, leading to an overall compression of the structure in the direction of the Cp best plane normal vector. The presumably relatively strong interaction between ammonia hydrogen atoms and the Cp ring, as visible from the molecular graph in Figure 34, finds its expression in the significant decrease of the distance between those hydrogen atoms

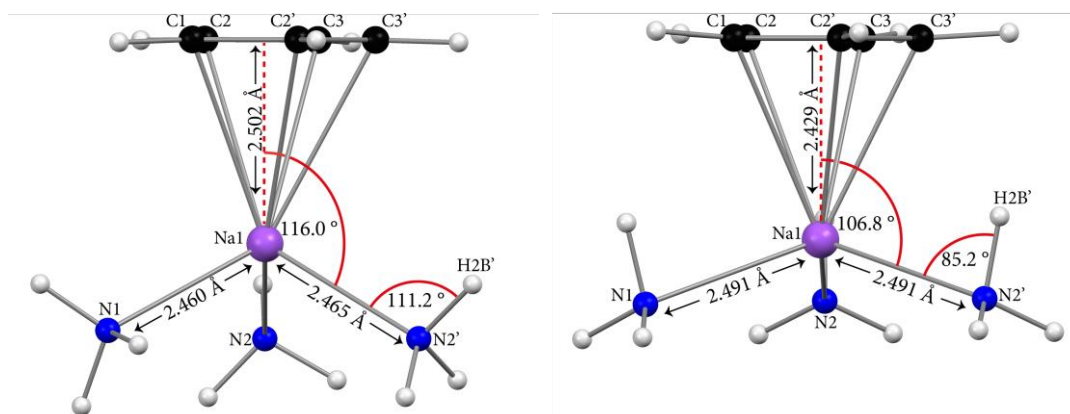


Figure 35. A comparison between the experimentally derived structure (left) and the geometry optimised structure (right). Note the more acute Na–N–H and C–Na–N angles and the smaller Na–Cp distance in the latter.

and the Cp ring plane compared to the experimental structure. The observed difference between experimentally and the theoretically derived structure is striking.

The presence of incongruities is not surprising, and the origins must be in the crystal packing, which lacks in the gas phase calculation. However, the magnitude of the observed difference between experiment and theory is interestingly high. In order to get a comprehensive picture of the intermolecular interactions, intermolecular contacts had to be visualised. A *Hirshfeld* surface according to the procedure described by *Spackman, McKinnon et al.* was calculated to obtain a defined volume for one fragment of $[(\text{H}_3\text{N})_3\text{Na}(\text{C}_5\text{H}_5)]$.^[174-176] The *Hirshfeld* surface consists of points \mathbf{r} that satisfy the following equation:

$$w(\mathbf{r}) = 0.5 = \frac{\sum_{A \in \text{molecule}} \rho_A(\mathbf{r})}{\sum_{A \in \text{crystal}} \rho_A(\mathbf{r})} \quad (\text{Eq. 36})$$

The sum of (spherical) atomic densities $\rho_A(\mathbf{r})$ of all atoms that belong to the molecule in question is divided by the sum of atomic densities in the crystal. Thus, the volume inside the surface is dominated by the density of the molecule, while the volume outside the surface is dominated by density from other molecules in the lattice.

Properties such as the electrostatic potential^[177] or the charge density^[178] can be mapped onto the surface and have given valuable insight into intermolecular interactions. The distance to the next atom inside (internal distance d_i) or outside the surface (external distance d_e) can be mapped on each pixel of the surface;^[179] this gives an idea of how strong intermolecular contacts are because those distances are not equal over the whole surface. This method has the drawback that different relative sizes of atoms are neglected. A very

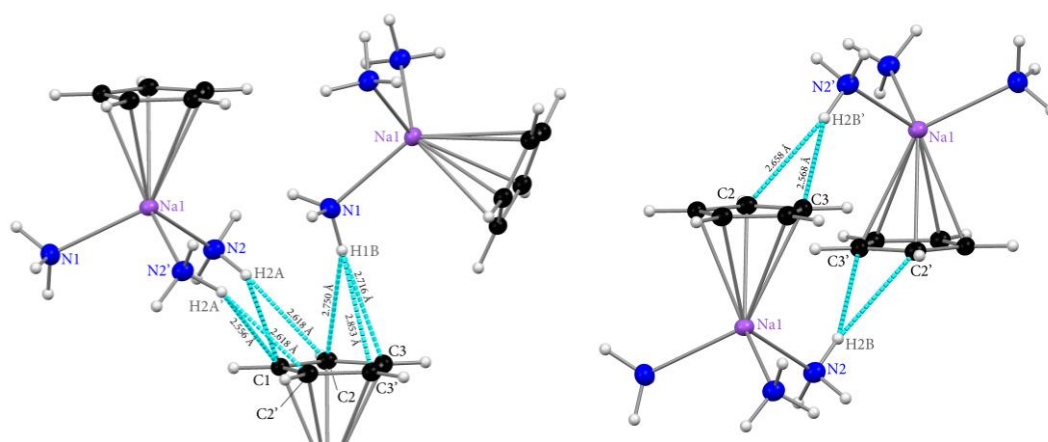


Figure 36. Dominant (i. e. shortest) intermolecular N–H/ π contacts are depicted in dashed turquoise lines. The remaining ammonia hydrogen atoms do not seem to participate in intermolecular contacts.

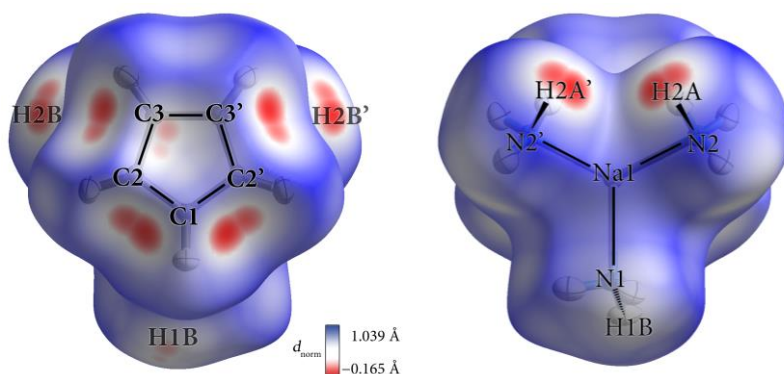


Figure 37: The normalized contact distance d_{norm} is mapped on the *Hirshfeld* surface of $[(\text{H}_3\text{N})_3\text{Na}(\text{C}_5\text{H}_5)]$. Red and blue color indicate contact distances shorter or longer, respectively, than the sum of van der Waals radii of those two atoms inside and outside the surface that are closest to the corresponding pixel on the surface. Left: view on top of the piano chair “seat cushion” approximately along the Cp–Na vector. Right: view of the “bottom” of the piano chair approximately along the Na–Cp vector; Graphics were created using the Software CrystalExplorer 3.0.^[181]

elegant and simple approach using only geometric parameters has been proposed by *McKinnon et al.* with the measure of the *normalised contact distance* d_{norm} .^[180]

$$d_{\text{norm}} = \frac{d_i - r_i^{\text{vdW}}}{r_i^{\text{vdW}}} + \frac{d_e - r_e^{\text{vdW}}}{r_e^{\text{vdW}}} \quad (\text{Eq. 37})$$

This measure has the advantage that it takes into account the different relative sizes of atoms by normalising the internal and external distances to the respective van der Waals radii r^{vdW} of the corresponding atoms. The normalised contact distance was mapped on a *Hirshfeld* surface of one $[(\text{H}_3\text{N})_3\text{Na}(\text{C}_5\text{H}_5)]$ fragment (see Figure 37). The coordinates from the XD2006 refinement were used for this purpose. A CIF-file with the structure in space group $Pn2_1a$ and without disordered ammine group had to be generated since the used program CrystalExplorer 3.0^[181] cannot treat structures containing disorder.

The intermolecular contacts that are shown in Figure 36 can be recovered in the *Hirshfeld* surface plots in Figure 37. Although the normalised contact distance only takes into account distances between *atoms*, it is clearly visible from Figure 37 that the ammonia hydrogen atoms H2A/H2A' address the C1–C2/C1–C2' *bonds* and that H2B/H2B' are closest to the C2–C3/C2'–C3' *bonds*. Among the mentioned, ammonia hydrogen atom H1B has the longest distance to the Cp ring, and its interaction does not seem to be very strong judging from the *Hirshfeld* surface plot. It is obvious from the shown plots that the C3–C3' bond is not addressed by any ammonia hydrogen atoms; the C3–C3' bond is not addressed by as many intermolecular contacts as the other C–C bonds are.

3.12. Molecular deformation density and Laplacian

After the geometric analysis revealed the mentioned distortions in the structure, it was interesting to see whether the distortions could be explained by means of a charge density analysis and if the bonding mode between sodium and Cp could be elucidated.

Apart from the agreement factors, the validity of the model had to be estimated before a charge density analysis according to QTAIM^[68] was carried out. Since no universal standard and no absolute suitability factors for charge density models besides agreement factors are available, the validity has to be estimated differently. Maps of the static deformation density through planar rings are very well suited to spot deficiencies in the model; a bone-shaped form of the deformation density can be indicative of a problem, e.g. concerning the expansion parameters κ or wrongly assigned chemical constraints. Such flaws in the model sometimes only have subtle influence on the residuals and the agreement factors. This is not the case for the obtained model, where the deformation density between the carbon atoms is distributed in an elliptical shape (see Figure 38). A map of the Laplacian can serve as another indicator for problems with the model. Bonds between atoms of the same element should have a symmetrical distribution of the Laplacian if no strong polarisation, for example because of neighbouring groups has to be anticipated.

It is visible from the maps in Figure 38 and Figure 39 that the Cp ring in $[(\text{H}_3\text{N})_3\text{Na}(\text{C}_5\text{H}_5)]$ does not have a symmetry higher than the crystallographic mirror

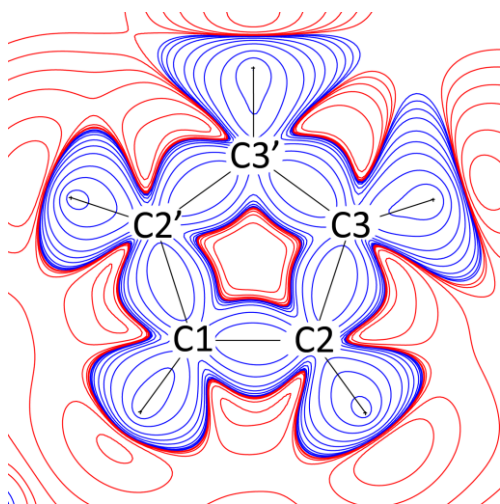


Figure 38. Map of the static deformation density in the best plane of the Cp ring in $[(\text{H}_3\text{N})_3\text{Na}(\text{C}_5\text{H}_5)]$. The contour values are chosen at levels of $(\pm 1.0 \cdot 10^{2n}, \pm 2.0 \cdot 10^{2n}, \pm 4.0 \cdot 10^{2n}, \pm 8.0 \cdot 10^{2n}, \pm 10, \pm 15, \pm 20) \text{ e } \text{Å}^{-3}$ with $n = 0, 1, 2, 3$; positive contour values are indicated by blue lines, negative values by red lines.

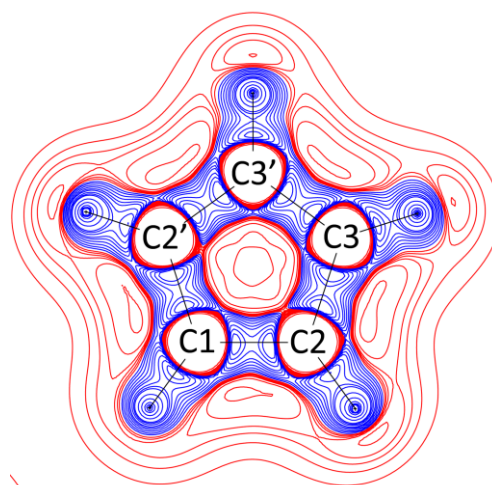


Figure 39. Map of the Laplacian in the best plane of the Cp ring in $[(\text{H}_3\text{N})_3\text{Na}(\text{C}_5\text{H}_5)]$. The contour values are depicted at levels of $(\pm 1.0 \cdot 10^{-n}, \pm 2.0 \cdot 10^{-n}, \pm 4.0 \cdot 10^{-n}, \pm 8.0 \cdot 10^{-n}, \pm 10, \pm 15, \pm 20) \text{ e } \text{Å}^{-3}$ with $n = 0, 1, 2, 3$; positive contour values are indicated by blue lines, negative values by red lines.

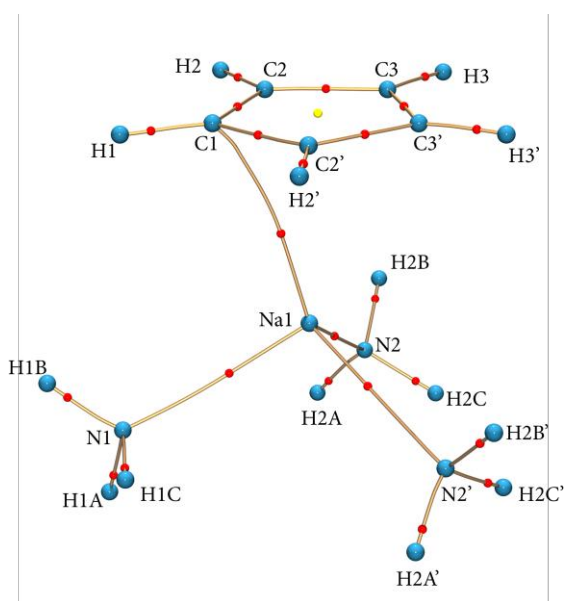


Figure 40. Atomic graph of $[(\text{H}_3\text{N})_3\text{Na}(\text{C}_5\text{H}_5)]$ from the experimentally obtained charge density map.

plane; the deformation density shows an inequivalence between the hydrogen atoms. The shift of the sodium atom as described in section 3.5 is a likely reason for this phenomenon because its polarising influence does not affect all atoms of the ring equally. The hydrogen out-of-plane bending as mentioned in section 3.6 seems to be less severe after the multipole refinement: the $\text{H}-\text{C}_\alpha-\text{C}_\beta-\text{C}_\gamma$ torsion angles are $2.3(9)^\circ$, $0.6(7)^\circ$ and $2.0(7)^\circ$ for H1, H2, and H3, respectively.

The atomic graph was calculated from the charge density of the obtained model. It is the representation of the

chemical structure solely based on the QTAIM descriptors, and it can provide information about the coordination mode between sodium atom and Cp ring. However, the atomic graph only contains one bond path between the sodium atom and the Cp ring. The virial graph, which is the equivalent of the molecular graph, but based on the electrostatic potential, is isomorphic. The paths in the virial graph represent trajectories of maximally stabilising potential energy. The presence of only one bond path might be taken as evidence for a η^1 coordination mode. The geometry of the complex is in disagreement with this hypothesis though. *Pendás et al.* reasoned that topological bond paths should rather be seen as indicators for electron correlation exchange channels.^[109] According to them, a bond path does not necessarily have to indicate the presence of a chemical bond in the sense that its existence provides evidence for an overall energetic stabilisation. As *Henn et al.* have shown, the absence of a bond path is not necessarily evidence for the absence of chemical bonding.^[182] Perhaps the term *bond path* itself causes confusion in some cases, as it implies the presence of a bond.

There are other examples where not all expected bond paths were found in π bonded systems.^[92,183] This is a classical problem in topological analysis; mathematically, there must always be a bond path between a pair of atoms, no matter how far they are apart; the situation becomes more complicated when a third atom comes into play.^[71] A bond path can, under some circumstances, easily vanish by minimal, even infinitesimal variation of the

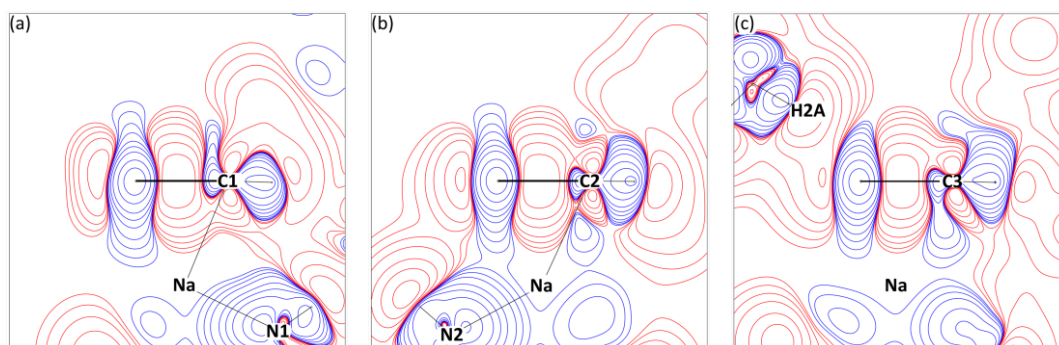


Figure 41. Maps of the static deformation density. It can be seen that (a) electron density is shifted away from the sodium ion in the case of C1; (b) electron density is distributed to both faces of the Cp plane in the case of C2; (c) a significant amount of electron density is shifted towards the sodium ion from carbon atom C3. The plane of the map is defined by the condition that it must contain the respective carbon atom–Na vector and a vector parallel to the Cp plane normal vector that passes through Na1. Contour lines are drawn at levels of $\pm 0.001, \pm 2.0 \cdot 10^n, \pm 4.0 \cdot 10^n, \pm 8.0 \cdot 10^n \text{ e } \text{\AA}^{-3}$, where $n = 0, \pm 3, \pm 2, \pm 1$; red/blue lines indicate negative/positive contour values, respectively. The Cp best plane is indicated by a bold black line.

positions of the bonding partners in the very shallow electron density between π coordinated fragments.^[68]

Maps of the static deformation density around the carbon atoms reveal parts of the additional information that can be extracted from the charge density refinement, see Figure 41. The density around atom C1 is significantly shifted away from the sodium atom, while the deformation density at C3 is rather shifted towards Na1. The carbon atom C2 has a rather symmetric deformation density distribution around itself. Nevertheless, the plots still suggest that the sodium ion is “wrapped” in a blanket of electron density that seems to originate for the greatest part from the CP carbon–carbon bonds and the nitrogen lone pairs. This is well illustrated by the closed contour lines between N2 and the bonding density opposite to C2 in the Cp ring as seen in Figure 41 (b).

The isosurface plot in Figure 42 is even more illustrative; in addition, it makes clear that the sodium ion is not shielded equally well from all sides. The dotted arrow in Figure 42 indicates the shielded side, the solid

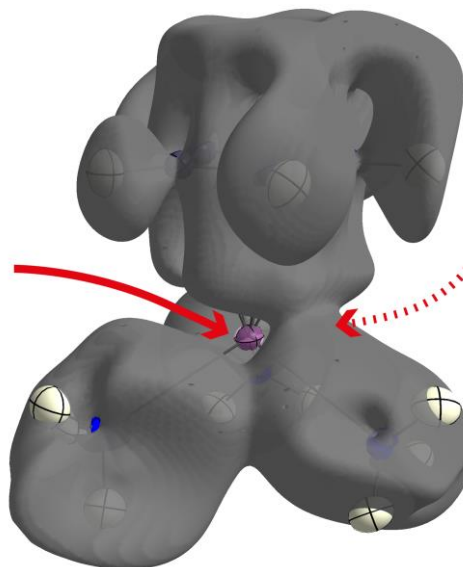


Figure 42. Isosurface of the static deformation density (isovalue: $0.001 \text{ e } \text{\AA}^{-3}$) around one fragment of $[(\text{H}_3\text{N})_3\text{Na}(\text{C}_5\text{H}_5)]$. It can be seen that the sodium ion is shielded by density from one side.

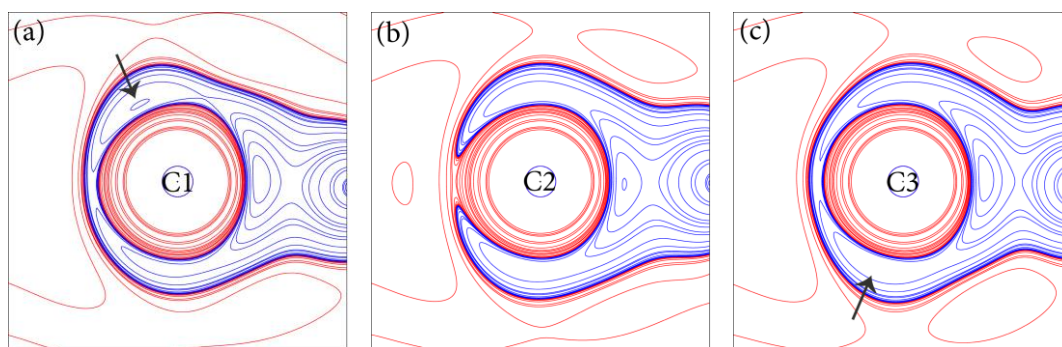


Figure 43. Maps of the Laplacian. All maps are oriented so that the Cp ring plane is aligned horizontally, the C-H bond points to the right and the sodium atom is below the bottom of the figures. These maps point out that the charge concentrations are not equally distributed if the three inequivalent carbon atoms are compared: (a) the charge concentration at C1 is at the face opposite to NaI; (b) the charge concentration around C2 is distributed symmetrically; (c) the charge concentration at C3 is rather directed towards NaI. Contour values are drawn at $\pm 0.001, \pm 2.0 \cdot 10^n, \pm 4.0 \cdot 10^n, \pm 8.0 \cdot 10^n \text{ e \AA}^{-3}$, where $n = 0, \pm 3, \pm 2, \pm 1$. Blue/red lines indicate negative/positive sign of the Laplacian, respectively.

Table 5. Atomic integrated charges as obtained from the experimental charge density map and from the DF-LMP2/cc-pCVTZ&cc-pVTZ geometry-optimised density. All atoms including symmetry equivalents are listed because the disorder of the N1 ammonia group had to be omitted for these calculations.

	Experiment	Theory
NaI	+0.92 e	+0.89 e
N1	-1.01 e	-1.14 e
N2	-1.30 e	-1.14 e
N2'	-1.30 e	-1.14 e
C1	-0.22 e	-0.16 e
C2	-0.19 e	-0.17 e
C3	-0.20 e	-0.17 e
C2'	-0.20 e	-0.17 e
C3'	-0.21 e	-0.17 e
H1	+0.07 e	-0.02 e
H2	-0.06 e	-0.01 e
H3	-0.11 e	-0.01 e
H2'	-0.07 e	-0.01 e
H3'	-0.11 e	-0.01 e
H1A	+0.43 e	+0.37 e
H1B	+0.36 e	+0.40 e
H1C	+0.32 e	+0.37 e
H2A	+0.46 e	+0.37 e
H2B	+0.43 e	+0.40 e
H2C	+0.52 e	+0.37 e
H2A'	+0.46 e	+0.37 e
H2B'	+0.44 e	+0.40 e
H2C'	+0.52 e	+0.37 e
sum	-0.06 e	0.00 e

arrow points towards the sodium ion and goes through the accessible face.

The Laplacian maps are somewhat less intuitively understandable because they have more subtle features in the cases of the Cp carbon atoms, see Figure 43. The trend that was visible in the static deformation density continues in the Laplacian: charge concentrations are directed towards NaI in the case of C3, and the concentrations at C1 point away from NaI.

The atomic integrated charges (Table 5) do not indicate very strong overall differences between the Cp carbon atoms. Those atoms that make up the ammonia groups carry high charges, a fact which is in accordance with the high dipole moment of ammonia and its good *N*-donor capability. The atomic charges can be added up to group charges, an approach that recently has been shown to deliver more helpful numbers in cases of compounds with unusual bonding situa-

tions.^[184] The group charges yield almost neutral charges of +0.11(1) e for the ammonia groups and a strong negative charge of -0.92 e for the cyclopentadienide moiety in the case of $[(\text{H}_3\text{N})_3\text{Na}(\text{C}_5\text{H}_5)]$, underlining the strongly ionic nature of the compound.

3.13. The Source Function

The Source Function was used as a measure to quantify the Na–C interactions, similar to the approach that *Farrugia et al.* used in their attempt^[92] to investigate the bonding between transition metals and carbocyclic rings, *inter alia* in the piano stool complex $[(\text{CO})_3\text{Mn}(\eta^5\text{-C}_5\text{H}_5)]$. *Farrugia et al.* argued that the Source Function (as well as the delocalisation indices, which are only accessible from wave functions) are descriptors that are much better suited for the metal–C interactions than the conventional QTAIM approach.

The results from the SF calculations are qualitatively different from those obtained by *Farrugia et al.* in that the overall contributions from the Cp ring atoms are much more negative if calculated for reference points outside the Cp atomic basins. There were actually nearly no negative atomic contributions in their results of *Farrugia et al.* The seemingly senseless role of negative SF contributions has been discussed by *Gatti et al.* to some extent.^[90] They reported about SF contributions in hydrogen bonded systems. Contributions from the hydrogen basins were positive in the case of very strong hydrogen bonds with high covalent character in the hydrogen/acceptor bond; SF contributions were more negative the longer the hydrogen/acceptor distance was, going along with a higher electrostatic character of the hydrogen bond. They concluded that the sign of SF contributions from the hydrogen basin can be used to classify different types of hydrogen bonds, ranging from isolated hydrogen bonds (highly negative SF contribution) to charge-assisted hydrogen bonds (largely positive SF contribution). In addition, the contributions from atoms other than those directly involved in the hydrogen bond (D–H...A) vastly increased with decreasing hydrogen bond strength.

The information gained from the SF contribution can be summarised by combining atomic contributions to group contributions, as it has been done with the atomic charges. If the SF contributions of the two unlike ionic moieties are summed separately, the result is that there is almost 50/50 contribution from the anionic and the cationic moiety to the reference point in Figure 44 (f) and only a minor imbalance for the Na1–C1 BCP reference point in Figure 44 (f) indicating a slightly higher contribution from the Cp moiety.

The interpretation of SF contributions still is somewhat puzzling because the majority of reports rather deal with covalently bonded systems. The ionic character of the Na–Cp and Na–N bonds in $[(\text{H}_3\text{N})_3\text{Na}(\text{C}_5\text{H}_5)]$ may be manifested in the SF contributions we calculat-

ed, but it would be dangerous to draw conclusions based only on the SF results. The highly negative contributions of the nitrogen atoms in Figure 44 (a) and of the Cp carbon atoms in Figure 44 (c) and (f) are striking, but they may not be sufficient as unambiguous descriptors for bond characteristics.

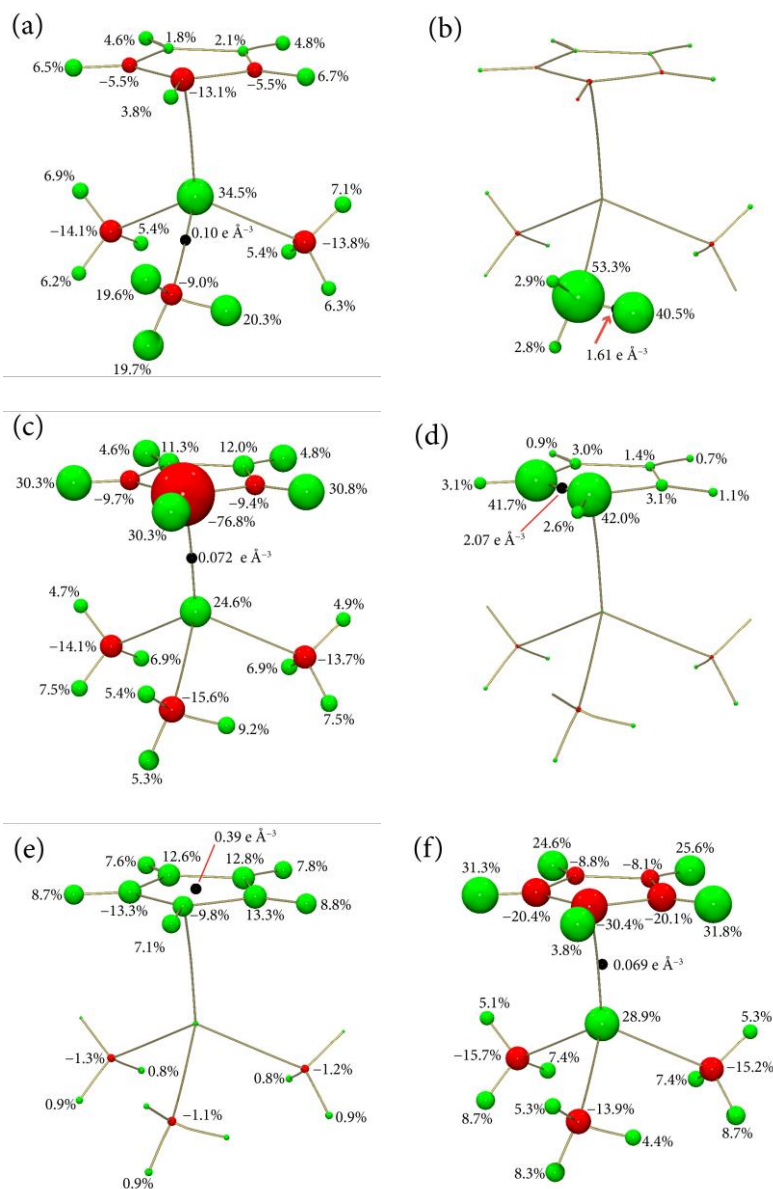


Figure 44. Graphical representation of the Source Function (SF) results. Each figure refers to one reference point (indicated as a black sphere) and consists of an atomic graph that only contains bond paths; the nuclear attractors are replaced with spheres of a volume proportional to the SF contributions to the respective reference point. Positive contributions are marked in green and negative contributions are marked in red. The value of $\rho(\mathbf{r})$ for each reference point is given next to it. Contributions with an absolute value of less than 0.5 % are not listed. The reference points in figures (a)–(d) are located on BCPs; the reference point in figure (e) is the cyclopentadienide RCP and (f) is a point on the NaI–RCP vector that has the same distance to the ring plane as the Cl–NaI BCP (emulating a CCP).

3.14. Computational chemistry

The observed discrepancy between experimental and theoretical structure was tackled by our collaborator *Diego Andrada* from the workgroup of *Ricardo A. Mata*. In order to find out whether the observed hydrogen out-of-plane bending in a direction opposite to the predicted one was an effect of the crystal packing, the solid state structure had to be simulated. The simulation of a crystal lattice would require a large amount of molecules that had to be geometry optimised; such a calculation would be too expensive in terms of processing time to be tractable by any means.

The lattice was thus simulated by building a number of point charges on the coordinates of atoms in the lattice. Each $[(\text{H}_3\text{N})_3\text{Na}(\text{C}_5\text{H}_5)]$ fragment is surrounded by twelve complexes in the crystal, and calculations were carried out with numbers of 12, 56, 152, 344 and 586 molecules surrounding one central molecule. Only the central molecule was geometry optimised at the LMP2/cc-pCVTZ&cc-pVTZ level of theory; the other atoms were included as point charges. It turned out that the out-of-plane bending of the Cp hydrogen atoms could be reproduced with a sufficiently high number of molecules in the lattice; the observed tendency of the hydrogen out-of-plane bending away from the sodium ion is already inverted when the first surrounding sphere of molecules is included in the model (see Figure 45). The experimental distance between the Cp best plane and the sodium atom could be reproduced with the calculations as well (Figure 46).

The density wave function was kindly provided by Dr. *Andrada*. The atomic graph resulting from QTAIM analysis of the theoretical density is shown in Figure 47. The structure of the experimental atomic graph is now replicated; there is only one bond path between

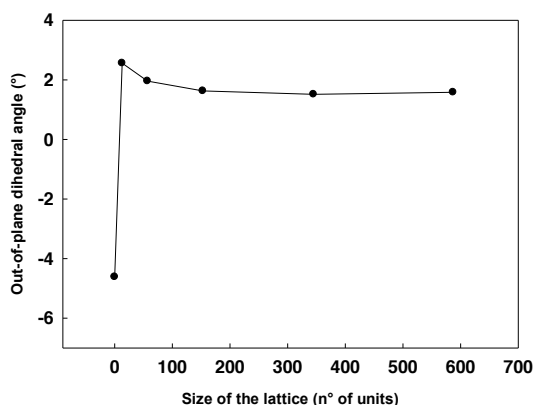


Figure 45. Plot of the out-of-plane bending dihedral angle (in °) versus the size of the lattice (in numbers of units). The experimentally observed angles are between 0.6 ° and 2.3 °.

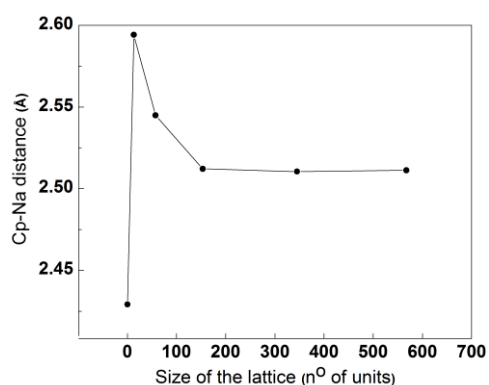


Figure 46. Plot of the Cp–Na distance versus the size of the lattice (in numbers of units). The experimentally observed distance is 2.502 Å.

the sodium ion and the cyclopentadienide ring. Only the additional existence of a cage critical point and a ring critical point is a difference to the experimental molecular graph; the theoretical graph as well as the experimental graph satisfies the Poincaré-Hopf relationship, though:

$$n_{\text{AP}} - n_{\text{BCP}} + n_{\text{RCP}} - n_{\text{CCP}} = 23 - 23 + 2 - 1 = 1 \text{ (theory);}$$

$$n_{\text{AP}} - n_{\text{BCP}} + n_{\text{RCP}} - n_{\text{CCP}} = 23 - 23 + 1 - 0 = 1 \text{ (experiment).}$$

The calculated properties at the critical points are in good agreement between experiment and theory (see Table A 2 in the appendix); it is in good quantitative agreement for properties concerning non-hydrogen atoms and in a good qualitative agreement for those properties involving hydrogen atoms. The atomic integrated Source Function contributions to critical points were calculated for the theoretical density as well; the results agree very well with the results from the experimental charge density. However, they do not add to the information that has already been obtained and are omitted for the purpose of this thesis.

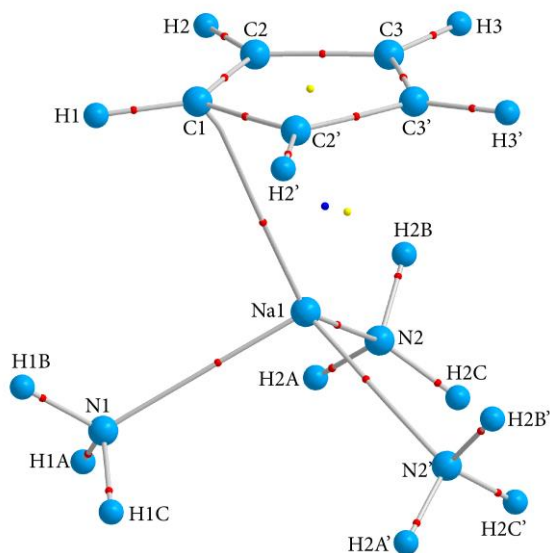


Figure 47. Molecular graph from QTAIM analysis of the LMP2/cc-p(C)VTZ density of the geometry optimised structure. Light blue spheres: NACPs; red spheres: BCPs; yellow spheres: RCPs; dark blue sphere: CCP.

3.15. Intermolecular interactions and the charge density

The important role of intermolecular interactions for the shape of the $[(\text{H}_3\text{N})_3\text{Na}(\text{C}_5\text{H}_5)]$ fragment made it worth the while to try and quantify the strength of those interactions based on QTAIM criteria, the Source Function, and the NCI descriptor (see section 2.6).

The Source Function, which was integrated over each of the atomic basins of one fragment of $[(\text{H}_3\text{N})_3\text{Na}(\text{C}_5\text{H}_5)]$, was calculated for reference points on BCPs and RCPs in neighbouring symmetry generated fragments. Those three ammonia hydrogen atoms (H1B, H2A, H2B) that were identified to be especially involved in intramolecular contacts from the Hirshfeld surface analysis (see section 3.11) also stand out in terms of their Source Function contributions: their percentage contributions to the ring critical points of those rings that are addressed are remarkably high (see Figure 48). The absolute value is

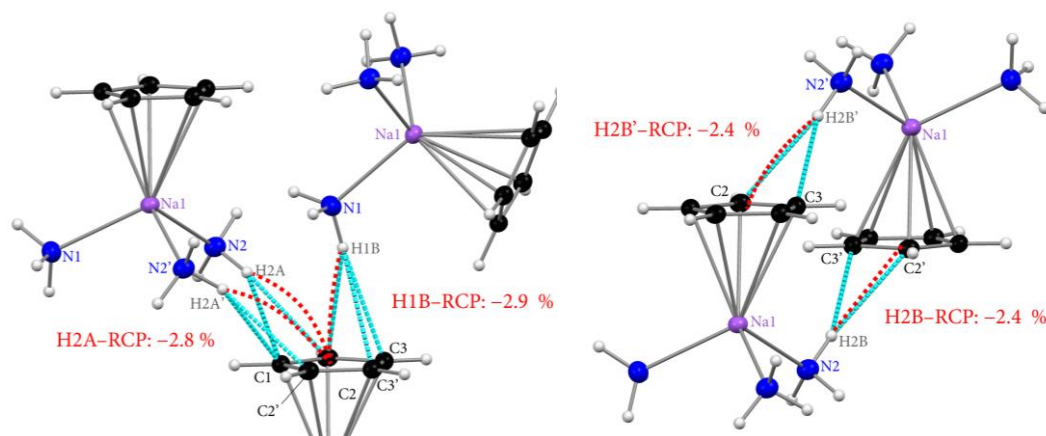


Figure 48. Left: SF percentage contributions from H1B and H2A to the ring critical point (RCP) of the addressed cyclopentadienyl ring of a neighbouring $[(\text{H}_3\text{N})_3\text{Na}(\text{C}_5\text{H}_5)]$ fragment, Right: SF percentage contribution from H2B to the RCP of a neighbouring fragment.

relatively high, but it is negative, indicating that the hydrogen atoms act as charge density “sinks.” This behaviour is reported to be typical for very weak hydrogen bonds.^[90]

The NCI descriptor (see section 2.6)^[110,112,115,185] facilitates the identification of weak attractive intermolecular interactions that are not manifested in the molecular graph by means of bond critical points and bond paths.

The program NCI milano^[186] was kindly provided by *G. Saleh* (workgroup Dr. *C. Gatti*, Milan). It calculates 3D grids of the reduced density gradient $s(\mathbf{r})$ and of the measure $\rho(\mathbf{r}) \cdot \text{sign}(\lambda_2)$ from XDLSM 3D grid files of $\rho(\mathbf{r})$ and $\nabla\rho(\mathbf{r})$. The program MoleCoolQt^[155] was used for rendering the graphics. All graphics in this section are calcu-

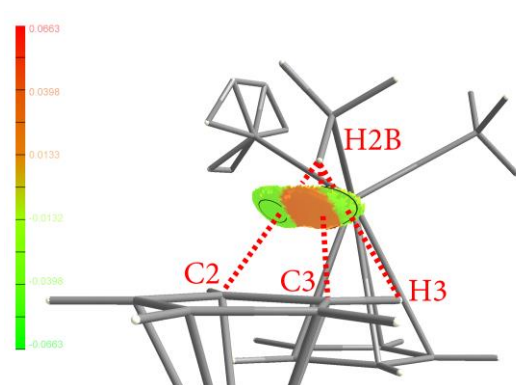


Figure 49. Non-covalent intermolecular interactions between ammonia hydrogen atom H2B and a neighbouring cyclopentadienyl ring. There not only is an attractive interaction to the Cp carbon atoms C2 and C3 but also an attractive H/H interaction between H2B and H3.

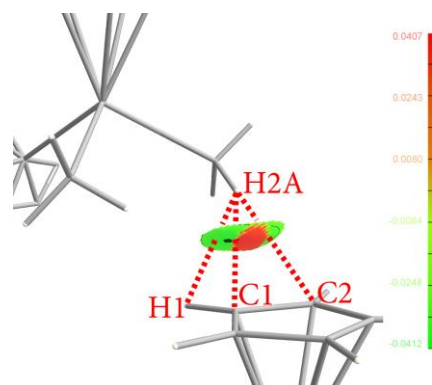


Figure 50. NCI visualisation of the intermolecular interactions between ammonia hydrogen atom H2A and a neighbouring cyclopentadienyl ring. There are attractive interactions to the Cp carbon atoms and to H1.

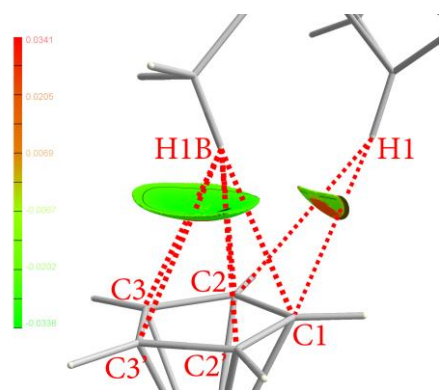


Figure 51. Non-covalent intermolecular interactions between ammonia hydrogen atom H1B and a neighbouring cyclopentadienyl ring. There also is an attractive interaction between the cyclopentadienyl hydrogen atom H1 and C1/C2.

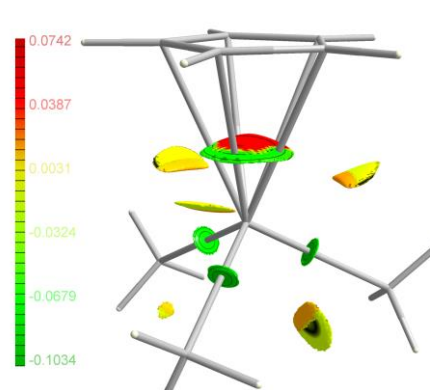


Figure 52. NCI plot for the *intramolecular* interactions in **1**. The attractive interactions between the ammonia molecules and NaI are clearly visible. It is striking that the interactions between NaI and the cyclopentadienyl ring are partly repulsive.

lated with an interaction surface at a level of $s(\mathbf{r}) = 0.5$. The property $\rho(\mathbf{r}) \cdot \text{sign}(\lambda_2)$ is mapped onto the isosurfaces, and the colour code for the values of the property is given in each figure, whereby red colours generally indicate repulsive interaction and green colours indicate attractive interaction.

The intermolecular interactions which were visible in the Hirshfeld surface plots (section 3.11) are completely recovered in the NCI plots (see Figure 50 to Figure 51): H1B, H2A, and H2B clearly are N–H $\cdots\pi$ hydrogen bond donors as indicated by the negative sign of the Hessian eigenvalue λ_2 on the respective interaction surfaces. It should be noted that almost all interaction surfaces do not only indicate attractive interactions but also contain areas indicating repulsive interactions. This should not be overestimated. The reason for this behaviour is the very shallow charge density in the intermolecular space; λ_2 changes its sign very rapidly in these regions. The N–H $\cdots\pi$ interactions and also the Cl–H1 $\cdots\pi$ interaction can generally be considered as attractive interactions based on the NCI plots.

3.16. Conclusions

This chapter of my thesis about a combined experimental and theoretical charge density investigation is the result of a challenging project. X-ray diffraction data collection on samples from the most volatile organometallic compounds has been one of the traditional specialities^[187-188] of the *Stalke* workgroup ever since the structure determination on *n*-butyllithium and *tert*-butyllithium.^[189] The class of ammoniacates is among the most volatile compounds, which is due to the very high vapour pressure of ammonia and the relatively weak thermodynamic stability of the ammoniacates. The acquisition of highly

accurate high-resolution data for this study was a challenging process because of the difficulties during crystal selection and mounting.

The multipole refinement of a disordered structure about which this chapter reported was not the first of its kind; see for example the charge density studies on N-phenylpyrrole with a statically disordered asymmetric unit,^[190] on paracetamol with a disordered methyl group^[191] or on two isomers of hexasilabenzene with a large and completely disordered ligand sphere around the inorganic core.^[192] The present study however does show that efficient methods of restraining and constraining parameters have to be implemented in future versions of least-squares multipole refinement programs. The multipole refinement program MoPro,^[45] which offers geometry restraints, could not be successfully used for the multipole refinement in this thesis because of software problems that could not be resolved with the help of the author of the program.

While the atomic positions of the *ammonia* hydrogen atoms were not refined, those of the *cyclopentadienyl* hydrogen atoms were indeed refined. The resulting experimental angles could quantum-chemically be precisely reproduced with simulated lattice calculations by Dr. D. Andrada (workgroup Prof. Dr. R. A. Mata), a fact which simultaneously demonstrates the high quality of the acquired experimental data and the general ability of multipole models to describe hydrogen atoms accurately.

The crystal structure of tris(amine) sodium cyclopentadienide posed some important challenges even before it was subject to multipolar refinement; the thorough investigation of the reflection data preceded the use of ten resolution-dependent scale factors. Resolution-dependent scaling has been used in the way described here for modern CCD-derived data only recently in a publication from our group.^[192]

The IAM crystal structure already revealed the sodium atom shift away from the geometric centre of the Cp ring as well as the hydrogen out-of-plane bending, the direction of which is qualitatively different from the theoretically predicted one. Strong intermolecular interactions based on N-H/ π contacts were identified by the use of a Hirshfeld surface analysis.

The thorough investigation of the experimentally derived charge density map by means of the QTAIM and the Source Function gave evidence for the tentatively very strong ionic character of the structure. The bonding situation between the sodium ion and the cyclopentadienide moiety from the QTAIM view is the product of a conflict catastrophe where two bond critical points vanish. Such a situation can principally result in a ring critical point, which actually exists in the theoretical charge density, but it always has the result of “missing” bond paths. Such situations as they have been theoretically described by Bader

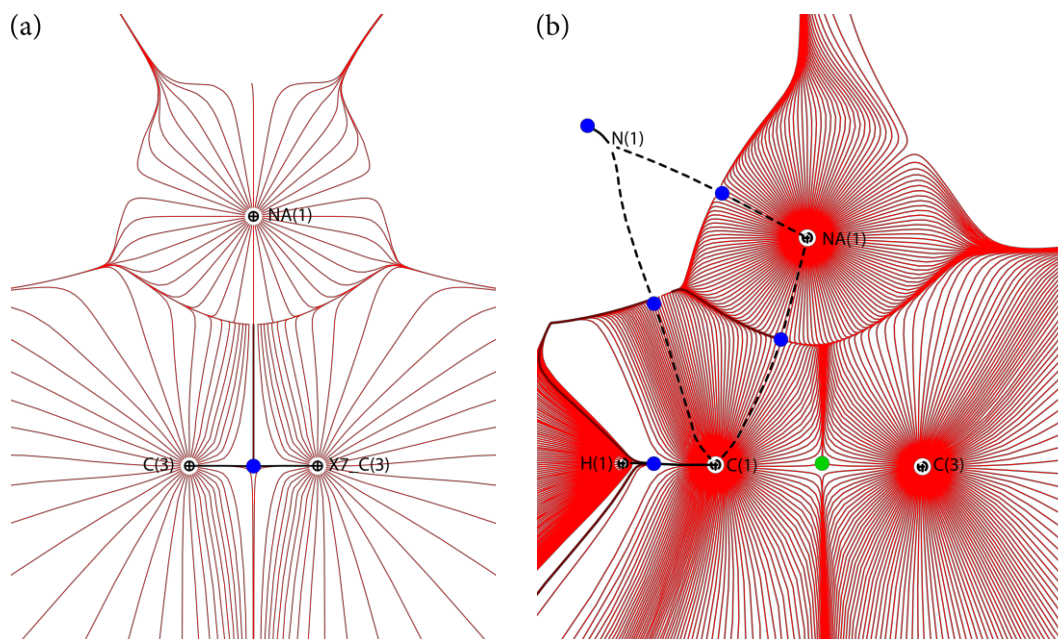


Figure 53. Gradient trajectory plots in $\rho(\mathbf{r})$. (a) in the C3/C3'/NaI plane; (b) in the crystallographic mirror plane. The bond path from C1 to N1 in this figure cannot be found in the bond path/critical point search of XDPROP.

et al.^[68] and others^[71] have already been observed experimentally, e. g. lacking bond paths in a complex containing a Mn(C₅H₄Me) fragment,^[193] a Mn(C₅H₅) fragment^[92] or in ethylenebis(1-indenyl)zirconium dichloride, where only one bond path from Zr to the C₅ perimeter was found due to the ring slippage of the indenide moieties. T-shaped bonds have been reported in acetylene complexes^[194] or even in solid materials like complex carbides.^[195] The gradient trajectory plots show how close the situation is to the formation of a T-shaped bond from NaI to the C3/C3' BCP (Figure 53).

The crystal structure of tris(ammine) sodium cyclopentadienide as well as the experimental charge density can be regarded as a spectacular illustration of the structure-determining strength of intermolecular interactions; the N–H/ π interactions are strong enough to compete with the polarising effect of the sodium cation towards the density of the cyclopentadienide ring. The structure can perhaps be considered as a crystallised metastable phase bound for the transition state between being a contact ion pair and becoming a solvent separated ion pair. The geometry with a Cp[−] ring that is slipping away from the [(H₃N)₃Na]⁺ moiety and the lack of four out of five bond paths between sodium cation and cyclopentadienyl ring may serve as an assertion of the metastability of the structure.

4. Bis(2-benzothiazolyl)phosphane

4.1. The importance of phosphanes in catalysis

The introduction of phosphane ligands, first and foremost triphenylphosphane, has been among the most important developments in transition metal-catalysed chemistry; *Wilkinson's* catalyst^[197] may serve as a classical example. In modern cross-coupling reactions such as the *Kumada* coupling,^[198-199] the *Heck* reaction,^[200-201] the *Sonogashira-Hagihara*,^[202]

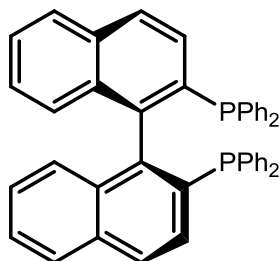


Figure 55. The BINAP ligand, which is axially chiral, facilitates several transition-metal catalysed reactions yielding high enantiomeric purity.

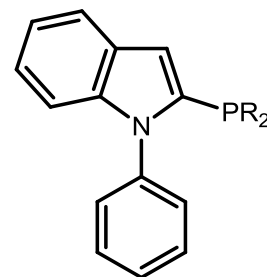


Figure 56. *Beller's* 2-phosphano-substituted 1-arylpyrroles with R = *tert*-butyl, adamantyl, cyclohexyl have the advantage of being electronically tunable.

Negishi,^[203] *Suzuki*^[204] or *Hiyama*^[205] coupling require transition metal complexes with phosphane-based ligands; which emphasises the importance of this general substance class in the field of catalysis. The development of new phosphane-based ligands has never ceased, and the next step of evolution was the introduction of chiral phosphane ligands like BINAP (see Figure 55).^[206-208] The class of 2-phosphano-substituted heterocycles like *Beller's* 2-phosphano-substituted 1-arylpyrroles (see Figure 56)^[209] have found widespread application lately because of their stability towards moisture and air and tunability regarding both steric and electronic properties.^[210]

These examples serve to emphasise the importance of multidentate and heterodentate phosphane ligands. On the quest to develop flexible phosphorus-based ligands, our workgroup reported about the synthesis and reactivity of various heterodentate ligand systems,^[211-216] amongst them the lithium bis-(2-pyridyl)methanide,^[217] lithium phosphorane amides (Figure 54),^[218] aminoiminophosphoranates,^[212] bis-(2-pyridyl)phosphane (Figure 57),^[219] and the related

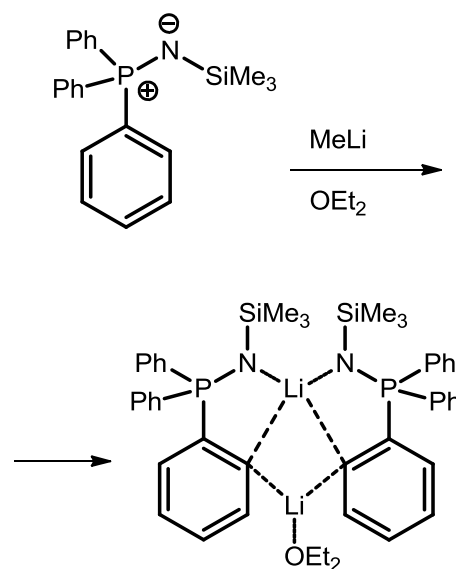


Figure 54. Iminophosphoranes react to lithium phosphorane amides with methyllithium. The P-N bond should not be considered as a double bond in order to avoid hypervalency.^[196]

bis(2-benzothiazolyl)phosphane **2** (Figure 58).^[220-223] This compound had initially been designed having in mind a secondary phosphane ligand that could be deprotonated to yield an anionic *phosphanide*. This is a class of substances which are known to act as bridging ligands, which differentiates them from the *phosphane* ligands that rarely show such behaviour.^[224-226]

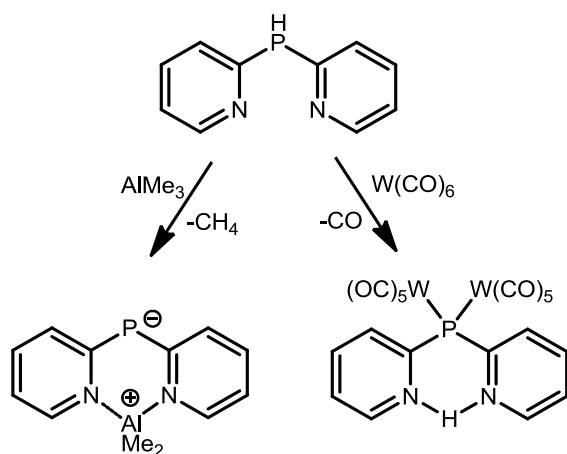


Figure 57. Bis-(2-pyridyl)phosphane acts as a bidentate ligand upon deprotonation and can be a formal 4-electron donor even in its neutral *N*-protonated form.

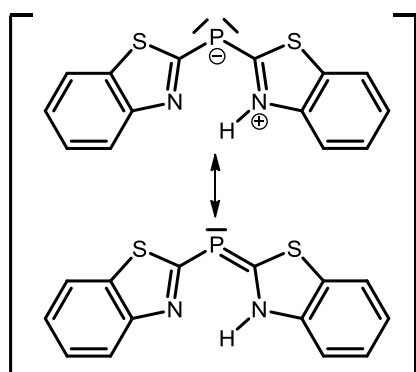


Figure 58. In the solid state, the bis-(2-benzothiazolyl)phosphane exists only as the *N*-*H* tautomer that is depicted here.

It turned out that **2** existed only as its *N*-protonated tautomer in the solid state.^[222] It was thus investigated if **2** should be regarded as a divalent phosphane ligand or a phosphanide ligand. It was established chemically^[220-221,223] by means of its coordination behaviour that it has phosphanidic (bridging) character; a theoretical charge density study by *Stey et al.*^[221] came to the same conclusion based on a topological analysis of the charge density. This falsified the canonical form in Figure 58, bottom, and gave evidence for the canonical form with formal charges. Similar conclusions were drawn in a recent study from our workgroup on the related metallaphosphane $[\text{Me}_2\text{Al}(\mu\text{-Py})\text{P}]$.^[227] These theoretical studies were mainly concerned with the nature of the P–C bonds at the time; the presence of two nonbonding valence shell charge concentrations (VSCCs) at the phosphorus atom was taken as evidence for the phosphanidic character and eventually also for the single bond nature of the P–C bonds because each VSCC was interpreted as Lewis lone pair; thus adding up to eight electrons in the valence shell including the two single bonds.

Part of the aim of this thesis was to perform a complete experimental charge density analysis of bis-(2-benzothiazolyl)phosphane and compare the results to those obtained by *Stey et al.*

4.2. Data collection and data processing

The dataset used for the charge density refinement was kindly collected by *D. Kratzert* on a Bruker *D8 Ultra* diffractometer equipped with a *Turbo X-Ray Source* (TXS) molybdenum rotating anode generator. Data were acquired in five ω scans at $2\theta = -33^\circ$ and 3 s exposure time for the low-order data and in six ω scans at $2\theta = -79^\circ$ and 30 s exposure time for the high-order data. The sample temperature was 15 K according to the temperature gauge of the open stream Oxford Diffraction *Helijet* that was used. SAINT 7.68A^[57] was employed for data reduction, and the subsequent face-indexed absorption correction^[137] as well as merging of equivalent reflections^[25] and frame-to-frame scaling was carried out with SADABS 2008/2,^[23] which was also used to write a reflection file conforming to the standards of XD2006 (merged data, omitted systematic absences and reflections with negative intensities).

Table 6. Crystallographic data on compound 2 taken from *XDLSM* multipole refinement.

Empirical formula	C ₁₄ H ₉ N ₂ PS ₂		
Formula weight	300.24 g mol ⁻¹		
Crystal system	orthorhombic		
Space group	<i>Pbca</i>		
Unit cell dimensions	$a = 14.5748(14) \text{ \AA}$, $b = 7.2463(7) \text{ \AA}$, $c = 24.444(2) \text{ \AA}$		
Volume, <i>Z</i>	$V = 2581.6(4) \text{ \AA}^3$, 8		
Density (calcd)	$\rho_{\text{calcd}} = 1.545 \text{ Mg m}^{-3}$		
Absorption coefficient	0.52 mm ⁻¹		
<i>F</i> (000)	1232		
Crystal size	0.15 x 0.10 x 0.06 mm		
θ -range for data collection	1.19 to 53.33° (max. resolution: 0.44 Å)		
Limiting indices	$-31 \leq h \leq 32$, $-16 \leq k \leq 16$, $-54 \leq l \leq 54$		
Reflections collected	195504		
Independent reflections	16791 ($R_{\text{int}} = 0.0287$)		
Completeness to θ	99.8% ($\theta = 53.312$)		
Refinement method	Full-matrix least-squares on F^2		
Data/parameter ratio	31.6		
GoF (GoF _w)	1.54 (1.30)		
<i>R</i> indices (all data)	$R1 = 0.0150$,	$R2 = 0.0148$,	$wR2 = 0.0288$
Largest diff. peak and hole	0.15 and -0.11 e\AA^{-3} (from XDFFT)		

The data collection and processing resulted in 195504 measured reflections and 15005 unique reflections (16791 taking into account the systematically absent reflections). See Table A 1 in the appendix for details on data statistics.

4.3. Setup and XD2006 refinement

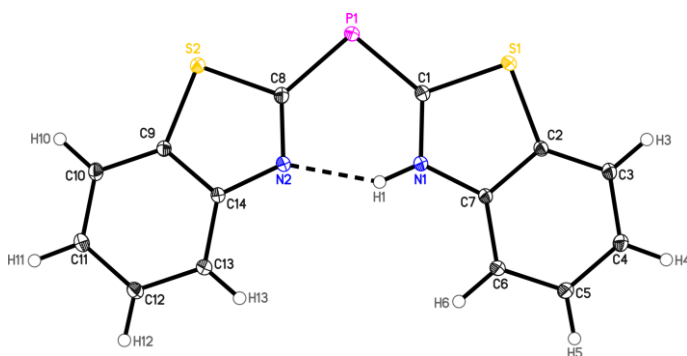


Figure 59. Graphical representation of the asymmetric unit.

The IAM refinement was carried out in a straightforward manner. After structure solution with direct methods in SHELXS-97,^[21] all atom positions could be assigned. All non-hydrogen atoms were refined with anisotropic displacement parameters; the

hydrogen atoms were refined with isotropic displacement parameters that were restrained to 1.2 times the U_{eq} of the associated pivot atom. All atomic positions were refined without restraints.

The hydrogen atom H1 is involved in a hydrogen bond to N2, and the difference density after SHELXL-97 refinement revealed a high peak close to N2 in the direction of the hydrogen bond. It was tried whether H1 was disordered over two positions. This would make sense, given the symmetry of the molecule close to C_{2v} . However, such a model only converges resulting in a physically meaningless (too short) N2–H distance, which is why a

Table 7. Applied XD2006 refinement strategy. Hydrogen multipole parameters were refined up to an order of $l_{max} = 2$. The expansion parameters of hydrogen atoms were not refined. The isotropic displacement parameters of hydrogen atoms were refined at a late stage of the refinement. The scale factor (SCA) is refined in every step and is only mentioned in the first one. Abbreviations: D, dipoles; Q, quadrupoles; O, octapoles; H, hexadecapoles; M, monopoles; XYZ, positional coordinates; U_{ij} , displacement parameters; κ , spherical expansion parameters; κ' , aspherical expansion parameters. See also section 1.6. CHEMCON: the multipole populations of chemically equivalent atoms are constrained to each other.

1.	SCA		16.	U_{ij} , XYZ(Non-H)	(CHEMCON)
2.	κ	(CHEMCON)	17.	U_{ij} , XYZ(Non-H), M, D, Q, O, H	(CHEMCON)
3.	M, D	(CHEMCON)	18.	U_{ij} , XYZ(Non-H), M, D, Q, O, H, κ	(CHEMCON)
4.	M, D, Q	(CHEMCON)	19.	U_{ij} , XYZ(Non-H), M, D, Q, O, H, κ	(CHEMCON)
5.	M, D, Q, O	(CHEMCON)	20.	XYZ(H-atoms)	(CHEMCON)
6.	M, D, Q, O, H	(CHEMCON)	21.	U_{ij} , XYZ(Non-H), M, D, Q, O, H, κ	
7.	U_{ij} , XYZ(Non-H)	(CHEMCON)	22.	U_{ij} , XYZ(H-atoms)	
8.	M	(CHEMCON)	23.	U_{ij} , XYZ(Non-H), M, D, Q, O, H, κ	
9.	κ	(CHEMCON)	24.	κ'	
10.	M, D	(CHEMCON)	25.	U_{ij} , XYZ(Non-H), M, D, Q, O, H, κ	
11.	M, D, Q	(CHEMCON)	26.	κ'	
12.	M, D, Q, O	(CHEMCON)	27.	U_{ij} , XYZ(Non-H), M, D, Q, O, H, κ , κ'	
13.	M, D, Q, O, H	(CHEMCON)	28.	U_{ij} , XYZ(H-atoms)	
14.	M, κ	(CHEMCON)	29.	U_{ij} , XYZ(Non-H), M, D, Q, O, H, κ , κ'	
15.	D, Q, O, H	(CHEMCON)			

model containing disorder was eventually discarded.

All hydrogen atoms were moved along their corresponding bond vectors to distances from neutron diffraction experiments (1.076 Å for C–H and 1.032 Å for N–H),^[52] the XD2006 starting model was created with the program XDINI, which is part of the XD2006 suite.^[44]

The chosen refinement procedure is sketched in Table 7. Different sets of radial-function parameters n_l for the phosphorus and the sulfur atoms were tried; see section 1.6 for details on these parameters. The appropriate choice of these parameters is crucial for elements of the third period because of the distinct shell structure in their core electrons in conjunction with a diffuse valence shell.^[42-43,228] The first criterion to judge about the choice of the n_l parameters was to obtain κ' values as close to unity as possible; the second criterion was the residual density, which should be as flat and featureless as possible in the neighbourhood of the respective atoms. The results suggested optimum values of $[n_1, n_2, n_3, n_4] = [2, 4, 5, 5]$ for the sulfur atoms, which is slightly different from the optimum values $[2, 4, 6, 8]$ reported by *Dominiak et al.*^[43] The standard $[4, 4, 4, 4]$ configuration turned out to be optimal for the phosphorus atom.

4.4. Validity of the model; residuals and quality indicators

The resolution dependence of the scale factor was sufficiently small so that the fit of the model to the data was assumed to be good enough for the subsequent charge density analysis (see Figure 60). After initial refinement steps only with experimental weights, a weighting scheme of $a = 0.0125$ and $b = 0$ (see section 1.9) was chosen for best congruence between expected and determined standard uncertainties as judged by the normal probability plot obtained from the program DRKPlot (see Figure 61).^[156] The distribution of $\sigma(F_{hkl}^2)$ with the used weighting scheme is largely congruent with a normal probability function. The residual density appeared flat and featureless by visual inspection in the program MolecoolQT,^[155] which was confirmed by a plot of the fractal dimension of the residual density (see Figure 62). The value for $d^f(0)$ is 2.78, indicating a close to random distribution of negative and positive residual density.

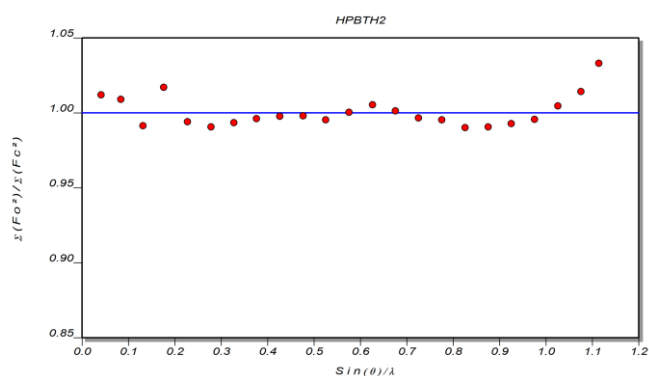


Figure 60. Resolution dependence of the ratio between mean observed and calculated squared structure factors.

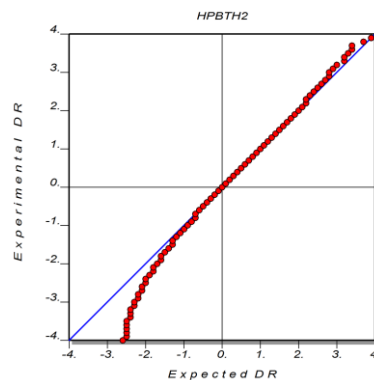


Figure 61. The normal probability distribution of $\sigma(F_{hkl}^2)$ (merged data).

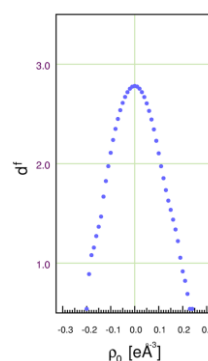
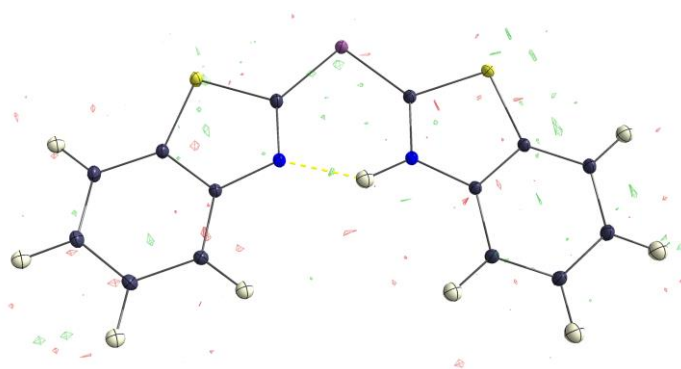


Figure 62. Residual density around the asymmetric unit (left) and the fractal dimension of the residual density in the unit cell (right). The residual density isosurfaces are drawn on levels of $-0.16 \text{ e}\text{\AA}^{-3}$ (red) and $+0.16 \text{ e}\text{\AA}^{-3}$ (green).

4.5. The topology of the Laplacian distribution

The first step, as in most charge density analyses, was the construction of the molecular graph. All expected bond critical points (BCPs) and bond paths (BPs) between the nuclear attractors and five ring critical points (RCPs) were found in the charge density map. One pair of RCPs belongs to the C_6 perimeters and another two RCPs are associated with the five-membered heterocycles; the fifth RCP was found in the central ring that is formed by the intramolecular $N1-H1\cdots N2$ hydrogen bond; see Figure 63. The properties at the bond critical points are summarised in Table A 3 (appendix). There are no cage critical points, and the Poincaré-Hopf relationship^[71] (see section 2.3) is fulfilled:

$$n_{AP} - n_{BCP} + n_{RCP} - n_{CCP} = 28 - 32 + 5 - 0 = 1.$$

The Laplacian at a BCP gives information about the nature of the particular bond. Negative values are commonly interpreted as indication for the covalent character of a bond,

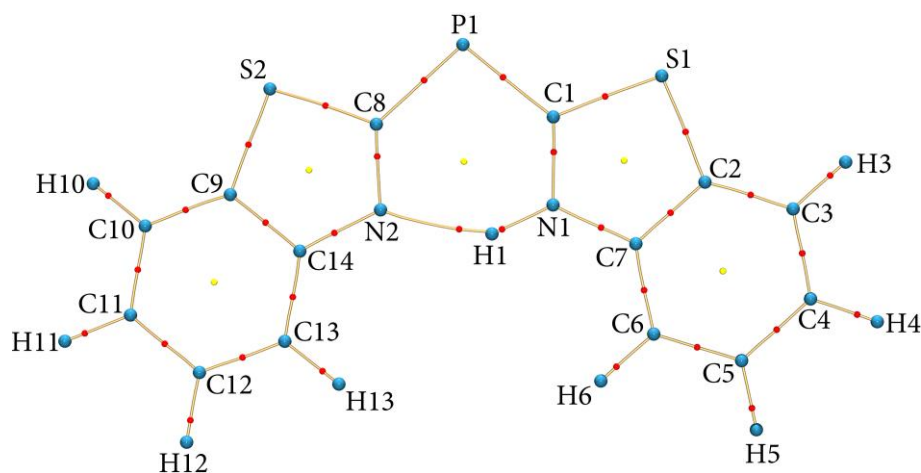


Figure 63. Molecular graph of **2**. Blue spheres are atomic positions; red dots are bond critical points (BCPs); yellow dots are ring critical points (RCPs).

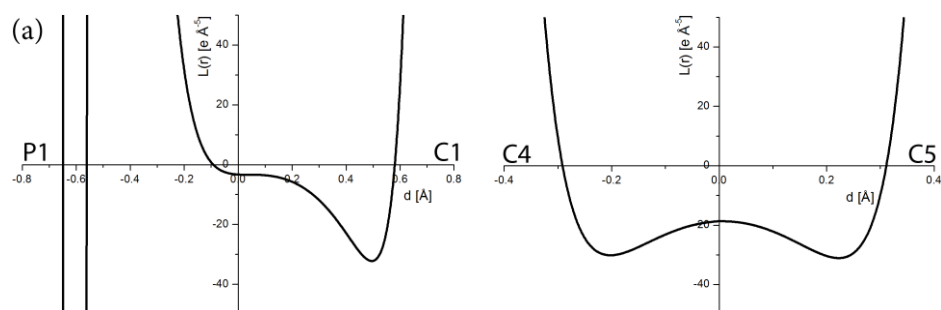


Figure 64. Plots of the Laplacian values along the bond paths (a) P1–C1; (b) C4–C5. The BCP is at ordinate $d = 0$. The distances of the nuclei to the BCPs in (a) are almost equal, but the strong polarisation of the bond is visible from the very non-symmetrical shape of the profiles.

and positive values are considered appropriate for closed-shell interactions as in mainly ionic or highly polarised bonds such as hydrogen bonds (see section 2.3). However, the properties at the bond critical point are sometimes misleading because the Laplacian undergoes large changes in the area of the BCP. This is why the distances of the nuclei to the BCP are sometimes taken as additional evidence for polarisation.^[68] These distances are only equal in non-polarised bonds while the more electronegative atom tends to have a larger atomic basin at the expense of its bonding partner's basin in the case of polarised bonds. However, the profiles of the Laplacian along the coordinates of the bond path are much more informative, especially for polar bonds in which the Laplacian undergoes large changes in its magnitude and often changes its sign in the close proximity to bond critical point. The Laplacian profiles along the polarised P–C bond and a non-polarised C–C bond in **2** are shown in Figure 64 as an example. A full set of Laplacian profiles is provided in the appendix.

The presence of two nonbonding VSCCs at the phosphorus atom was of vital importance for the argumentation of *Stey et al.*^[221] and *Henn et al.*^[227] and our experimental charge density analysis confirms the observation of two nonbonding VSCCs in the vicinity of the phosphorus atom. The bonding situation was unclear because of the P–C bond distances of 1.7689(2) Å and 1.7909(2) Å, which are between the mean values reported for P–C single and double bonds (1.826(31) Å and 1.674(28) Å, respectively).^[229] The local maxima of $-\nabla^2\rho(\mathbf{r})$ in the VSCCs at the phosphorus atom in **2** are distributed in a nearly tetrahedral geometry, which is in qualitative accordance to the results reported by *Stey et al.*^[222]

Four local maxima in the VSCCs of each of the sulfur atoms and three maxima in the VSCCs at the nitrogen atoms were found in the course of our analysis (see Figure 65). This is surprising, having in mind that the number of local maxima in the VSCCs is considered to provide a mapping of the *Lewis* electron pairs.^[19,68,73,75-76,81,230] That is to say, the consequence of this strict projection would be the structure shown in Figure 66 with two lone pairs at each sulfur atom. If, as *Stey et al.* reasoned, the presence of two lone pairs at the phosphorus atom indicated that the two P–C bonds are single bonds, the same must hold true for the sulfur atoms. This somehow conflicts with the presumption of aromati-

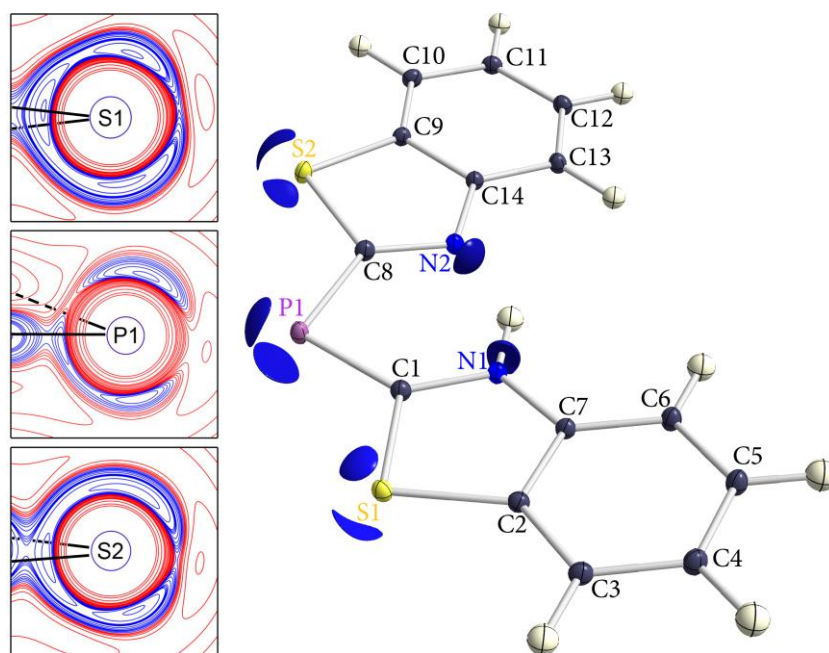


Figure 65. Left: 2D maps in the planes defined by the two points at local maxima in the nonbonding VSCCs and the respective atomic position; bonds to next atoms are sketched for clarity. Right: 3D maps of the nonbonding VSCCs. Different values for the isosurfaces were used: $-3.3 \text{ e } \text{Å}^{-3}$ for phosphorus, $-8.5 \text{ e } \text{Å}^{-3}$ for sulfur, $-45 \text{ e } \text{Å}^{-3}$ for nitrogen atoms.

ty of the heterocycles in **2** in terms of the molecular orbital theory, since two consecutive σ -type single bonds would interrupt the conjugated system. Every first-year chemistry student knows that a conjugated system of double bonds is a prerequisite for aromaticity in planar systems; this is a consequence of *all*- sp^2 hybridisation and the overlap of the p-orbitals, which enables the complete delocalisation of π -electrons. The quest was now to investigate the degree of aromaticity in order to (a) deal with the nature of the S–C and P–C bonds from a different perspective than merely from the Laplacian distributions and (b) to be able to judge about the contradicting existence of nonbonding lone pairs in a tentatively aromatic system.

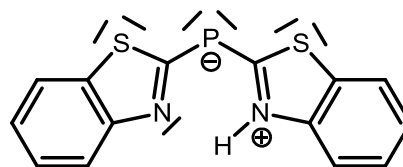


Figure 66. Lewis representation of **2** according to the rule of strict projection of lone pairs into VSCCs.

4.6. A few words about aromaticity and its quantification

Aromaticity is one of the very fundamental concepts in chemistry. It was first needed to explain the unusual stability and unique reactivity that was observed in benzenoid chemistry and its validity has been expanded to innumerable further examples. The quantification of aromaticity is a very large field of research.^[231-234]

The special characteristics of aromatic substances and all their resulting properties originate in the spatial delocalisation of electrons that is commonly associated with cyclic conjugated π -electron systems. Despite its evident existence, aromaticity remains a virtual concept and it is not an “on/off” property that is either present or absent. One of its main characteristics is ambiguity because it occurs in many gradations; heteroaromatic and annulated systems show a different degree of aromaticity compared to the aromatic archetype benzene.

It can be stated that the exact quantity of aromaticity in a given substance is hard to determine unambiguously. Many different approaches to this problem utilizing experimental observables have been proposed.^[232-233,235] They are mainly based on thermochemical (unusual energetic stabilisation compared to analogous saturated or non-conjugated systems), structural (single/double bond length equalisation with measures such as HOMA^[236] or the Bird index^[237-239]), spectroscopic (distinctive $^1\text{H-NMR}$ chemical shifts at low field)^[240-241] and magnetic properties^[242-244] as well as on quantum-chemical calculations. The latter include, amongst others, the *nucleus-independent shift* NICS^[245-246] and the *gauge including magnetically induced current* method (GIMIC).^[247]

The NICS yields a scalar property that is the negative average of the trace of the central shielding tensor of a given cyclic system. It has been criticised because of various reasons, among them its inability to discern in-plane induced currents from out-of-plane induced currents and the philosophical difficulty to assign the virtual property of NICS to the equally virtual quantity of aromaticity.^[244] The GIMIC approach seems to be more universal than the calculation of NICS values because of its independence of the molecular geometry;^[247-248] and yet it can yield a comprehensible single number (in units of nA T⁻¹) that indicates aromaticity, antiaromaticity, or non-aromaticity for whole molecules or fragments of molecules, dividing magnetically induced currents into diatropic and paratropic currents.^[249]

It is obvious that approximations are needed for basic models that are necessary for understanding and predicting observations. No chemical education would have been possible and no scientific progress would have been achieved without the introduction of simplifying concepts, gathering supporting evidence as well as disproving counter-evidence, but concepts are all too often mistaken as laws that are set in stone. *Frenking and Krapp* went so far to compare heuristically achieved bonding models in chemistry with unicorns in mythical saga;^[250] the existence of sp² hybridisation is such a persistent unicorn.^[251] The resulting atomic p orbitals that are combined to give an equal number of molecular π orbitals orthogonal to the other molecular orbitals are eventually used to determine the amount of aromatic stabilisation in a substance. Most chemistry freshmen learn MO theory^[252] in the first semesters. They also know *Hückel's* 4n+2 rule, but they are not always aware of the numerous approximations he made in his 1931 fundamental paper^[253] in which *Hückel* according to *Kutzelnigg*^[254] may well have laid the fundamentals both for the molecular orbital (MO) theory (“*zweite Methode*”) as well as for the valence bond (VB) theory (“*erste Methode*”) and presented solutions for systems like benzene in the framework of his “*second method*” which eventually led to the 4n+2 rule.

Thus, the simple MO-based concept of counting π electrons is not valid to elucidate the aromatic character of compound **2**. In addition, it is hard to categorise it by comparison with groups of similar or related compounds for which different measures already have been applied (as in some very extensive reports from *Schleyer et al.*^[245] or *Katritzky et al.*^[235]) because its bonding situation is somewhat peculiar due to the presence of tautomerism and the substitution of 2-benzothiazole with phosphorus.

4.7. Measures of aromaticity in the QTAIM framework

There is a number of approaches to extract the degree of electron delocalisation from indicators that are accessible from the QTAIM analysis.^[255-256]

Bader et al.^[66,81] and *Cremer et al.*^[82] proposed one of the earliest approaches to quantify electron delocalisation which relies on the assumption that electron delocalisation in conjugated systems mainly occurs in the π electron “cloud”: bonds of pure σ character with zero bond ellipticity therefore do not contribute to the conjugated system, and the existence of nonzero bond ellipticity (see section 2.4) is the central criterion for delocalisation in their studies. This approach has been proved to be useful in a number of QTAIM-based studies.^[87,257-258]

The Source Function (SF),^[89] as a function that can be used to reconstruct the charge density at any given point from contributions of sources, should be inherently valid to quantify the amount of electron delocalisation, e. g. by comparison of the contributions of remote atoms to a reference point. This has been exemplified by *Gatti and Monza et al.* by comparison of SF contributions in conjugated systems with the contributions in their non-conjugated analogues.^[90,94-95]

Other methods rely on the probability to find two electrons simultaneously at two positions close in space; the delocalisation index $\delta(A,B)$, as proposed by *Bader et al.*,^[259] indicates the amount of electron pair delocalisation between a pair of atoms A and B. It was found that the $\delta(A,B)$ values in six-membered rings were larger for *para*- than for *meta*-related atoms, and the *para*-delocalisation index (PDI) was proposed by *Poater et al.* based on this approach.^[260] The PDI is the mean of the $\delta(A,B)$ values between all *para* related atoms in six-membered rings. The major drawback of this approach is that a density wave function is needed to calculate the $\delta(A,B)$ values so that no experimental charge density data can be used.

4.8. Application of the measures of aromaticity in this thesis

There has been a dispute in literature regarding the question if aromaticity can be considered a one-dimensional quantity where all available descriptors show some sort of mutual dependency.^[232,246,261-263] The discussion has tended to conclude that the quantification of aromaticity not only depends heavily on the used descriptor, but also on the used samples; aromaticity should therefore be considered a multidimensional quantity and as many different complementary measurements should be made in order to get a complete picture.^[263] We therefore used all of the three mentioned approaches in our study of bis(2-benzothiazolyl)phosphane **2**; collaborations with Prof. Dr. R. A. Mata (Göttingen) and Dr. H. Fliegl (Oslo, Norway) made it possible to employ the GIMIC method as well as the calculation of NICS values. A density wave function for the calculation of $\delta(A,B)$ was kindly provided by Prof. Dr. R. A. Mata, who calculated a gas phase geometry optimisa-

tion at the DF-LMP2/cc-pVTZ^[264-265] level of theory, which additionally confirmed the stability of **2** over its P-H tautomer.

4.9. The bond ellipticity as an indicator for delocalisation

The ellipticity ε has to be evaluated carefully if conclusions are to be drawn concerning the degree of electron delocalisation. Only the eigenvalue λ_3 (corresponding to the vector pointing towards the direction of largest positive curvature) can be considered to be statically directed parallel to the bond path; the two remaining eigenvectors that are used for the construction of ε may in principle point towards any direction perpendicular to the first. For this reason, it is of great importance to know the directions of these vectors when evaluating ellipticity profiles, e. g. relative to the normal vector of the molecular plane, as it has recently been shown by *Farrugia et al.*^[87] If λ_2 , the eigenvalue corresponding to the smallest negative curvature, is taken into account, the angle φ to the normal vector of the molecular plane has to be close to zero for bonds with significant π contribution because only then the ellipticity is caused by expansion of the charge density perpendicular to the ring plane.

It is useful to have a standard to compare the obtained results with; those bonds with π

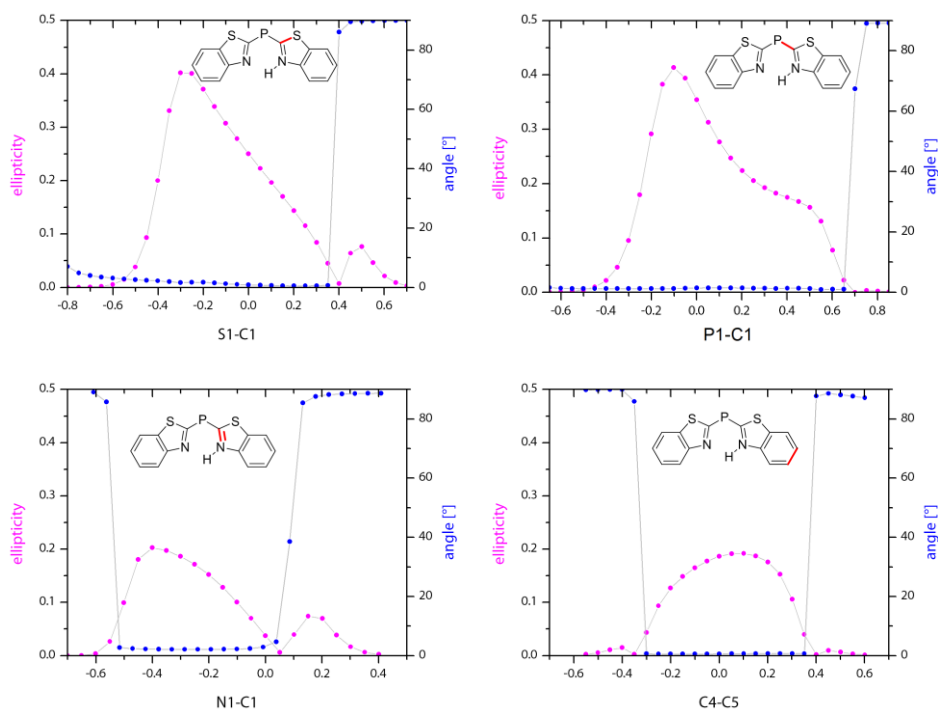


Figure 67. Ellipticity and principal vector angle profiles along some bond paths in **2**. The ordinate axis shows the distance to the BCP in Å. The angle distributions are relatively constant at right angles to the molecular plane in the zones of pronounced ellipticity in all bonds. A complete set of profiles is provided in the appendix.

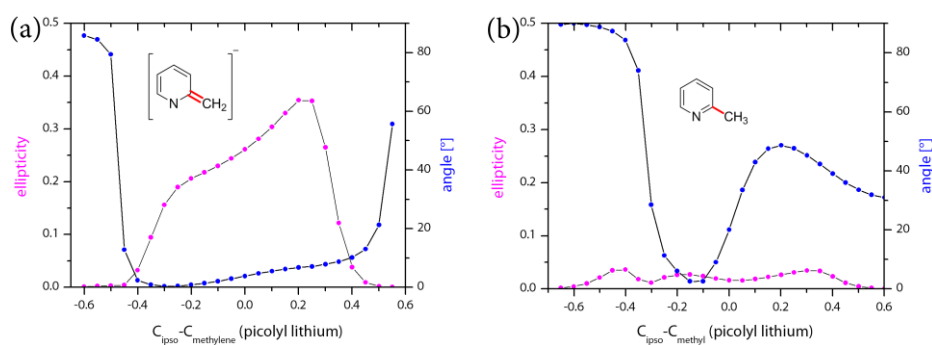


Figure 68. Ellipticity and principal vector angle profiles along the exocyclic C–C bonds in (a) picoline and (b) picolyl lithium. The ordinate axis shows the distance to the BCP in Å. The data were processed from the multipole model used by *Ott et al.*^[154] in their experimental charge density study. The angle corresponds to the angle between λ_2 vector and molecular plane (zero degrees means right angles to the plane). High ellipticity and an orientation of the eigenvector corresponding to λ_2 approximately perpendicular to the molecular plane is observed in the double bond. The orientation of the eigenvector corresponding to λ_2 is unspecific for the single bond; the ellipticity is very low in this case.

component as well as pure σ bonds will have to be distinguished. *Bader* gives values for ϵ in the C–C bond critical points of ethane, benzene, and ethylene of 0.0, 0.23, and 0.45, respectively,^[68] and ϵ as well as φ profiles including a C–C single bond and several bonds with π component are given by *Farrugia et al.*^[87] In this thesis, a previously published multipole model from *Ott et al.*^[154] was used; the structure contains 2-picoline, an aromatic system with an exocyclic C_{ar} – CH_3 single bond, which was used as a benchmark system for single bonds; it also contains 2-picolyl lithium, which is deprotonated at the methyl group and has an exocyclic double bond. The resulting profiles for the single and the double bond are shown in Figure 68. The profiles are typical for double and single bonds, respectively. There is polarisation in the case of the double bond due to the close proximity of the methylene group to one lithium cation. This is visible in Figure 68 (a). The ellipticity increases towards the methylene carbon atom and the angle φ between the eigenvector corresponding to λ_2 and the molecular plane normal that increasingly deviates from zero towards the methylene carbon atom.

The C–C bonds have maximum ϵ values around 0.2, and bonds involving heteroatoms show even larger maximum ϵ values. The angle φ always adopts values close to zero in the regions of high ellipticity, see the excerpt in Figure 67. A complete set of all profiles can be found in the appendix (pp. 183). The result from our calculations is that all bonds between non-hydrogen atoms in **2** exhibit profiles with significant ellipticity and an orientation of the eigenvector corresponding to λ_2 that is nearly perpendicular to the molecular plane. It is noteworthy because of the aforementioned ambiguous character of the phosphorus-carbon bonds that this behaviour is equally observed for both of these bonds.

The relatively high maximum values of ϵ in the cases of C–S and C–P bonds should not be erroneously interpreted to indicate strong charge accumulation: the absolute values of λ_1 , λ_2 , λ_3 , and $\nabla^2\rho(\mathbf{r})$ in the regions of high ellipticity cover a wide range; it is only the ratio of λ_1 and λ_2 which defines ϵ . The regions of high ellipticity in the phosphorus–carbon bonds have the lowest absolute values of $\nabla^2\rho(\mathbf{r})$ among all bonds in **2**.

4.10. The Source Function as an indicator for delocalisation

Monza et al. have recently demonstrated the potential of the Source Function (SF) for the evaluation of electron delocalisation and introduced a new SF-based local aromaticity descriptor that is derived from the combination of mean values of SF contributions and the comparison with benchmark systems.^[95] They investigated benzene, cyclohexadiene and cyclohexene as well as naphthalene and 1,2-dihydronaphthalene, 1,4-dihydronaphthalene and 1,2,3,4-tetrahydronaphthalene in their proof-of-principle study. The new measure is unfortunately not directly transferrable to our system because it is intended for use with homoaromatic systems.

Another approach was suggested in the same publication, which we will follow instead (results are summarised in section 4.10.2): BCPs were chosen as reference points and in addition, reference points were calculated along a line perpendicular to the bond path and directed above and below the molecular plane of the conjugated system. This approach has successfully been used on theoretical and experimental charge densities of benzene and other compounds.^[94–95] The approach was suggested because there had been some criticism by *Farrugia et al.*^[266] regarding the use of BCPs as reference points. The criticism was based on the fact that electron delocalisation is believed to take place predominantly in the conjugated π system, and BCPs are located close to the nodal planes of π orbitals in the region of σ electron density dominating the ring plane. Thus, for conjugated systems, SF contributions from remote atomic basins should increase with rising π character of the electron density at the reference point.

The result from the studies of *Gatti* and *Monza et al.* is that the contributions from remote atoms (i. e. those atoms that are not directly involved in the respective bond) *to the BCP* decrease with decreasing delocalisation: the contributions from next-nearest neighbours in benzene are more than double those in cyclohexene (5.3 % vs. 2.5 %). On the contrary, the contributions of remote atoms *to the out-of-plane reference points* dramatically increase in the case of benzene,^[94] and the same holds true for naphthalene^[95] (0.7 % contribution to the density at the BCP; 4.9 % contribution to the reference points 2.0 a_0 above/below the ring plane). The effect of increasing percentage contributions from remote atoms with rising distance from the molecular plane was also observed in cyclohex-

adiene and the hydrogenated naphthalene derivatives, but to a much lesser extent, and the contributions from next-nearest neighbours to the reference points above/below the double bond in cyclohexene decrease with rising distance. These findings are in accordance with a general picture of conjugated systems in which the delocalisation of electrons facilitates contributions of remote atoms rather than in non-conjugated systems.

4.10.1. The Source Function in a second row-heteroaromatic system

In an early attempt to evaluate the SF as an indicator for electron delocalisation in a heteroaromatic system without third-row elements, the multipole model from *Ott et al.*^[154] was used once more, this time to compare the SF contributions to the conjugated exocyclic double bond with the contributions to the exocyclic single bond.

Ott et al. concluded from their charge density study that the cyclic aromatic system in the 2-picoyl moiety gets corrupted upon deprotonation of the methyl group. The C-C bond lengths in the heterocycle of the deprotonated fragment are alternating, which indicates localised double and single bonds. In addition, the maximum ellipticities of the resulting double bonds are significantly higher than those of the single bonds, thus confirming the conclusion. *Ott et al.* discussed different possible resonance structures based on their charge density analysis and were able to conclude that the enamidic resonance structure (as in Figure 69) has the highest relevance for the deprotonated 2-picoyl structure. The system enabled us to compare the SF contributions in an aromatic system (2-picoline) with contributions in a planar non-aromatic system (deprotonated 2-picoline) without any bias from different experimental datasets.

At first sight, the contributions seem to indicate that some delocalisation is preserved among the conjugated double bonds; the qualitative differences between the two systems are not significant enough to attest a completely different character in terms of SF contributions if only those contributions from atoms in the heterocycle to reference points in the heterocycle are taken into account.

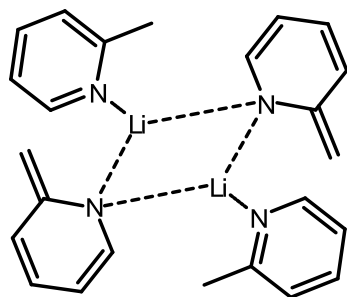


Figure 69. The Lewis diagram of the structure of $[2\text{-PicLi}:(2\text{-PicH})]_2$.^[154]

The situation is slightly different if the contributions to the charge density at the exocyclic bond are additionally considered: the contributions to the reference points at $2.0 a_0$ distance from the BCP are distinctly different for the single and the double bond, respectively; see Figure 70 (a) and (b). These reference points can be assumed to be well dominated by the π density in the case of the double bond. The

contributions to the single bond from its direct neighbours are much lower than in the double bond case; in fact, they are even highly negative.

The respective next nearest neighbours contribute a higher percentage to the single bond than to the double bond, which is readily explained by the delocalised nature of the aromatic bonds, enhancing the contribution from an atom in the aromatic system to a remote bond, even if the bond is only attached to the aromatic system and not a part of it.

This explanation can be transferred to the seemingly contradicting contributions of the ring atoms to the reference points in the ring. See Figure 70 (c) and (d) for exemplary discussion of the contributions from the carbon atom in *para* position to the nitrogen atom: the contributions are more evenly distributed in the aromatic 2-picoline than they are in the deprotonated fragment. The contributions to the out-of-plane reference points that are marked with red arrows in Figure 70 (c) are almost equal; this is not the case for

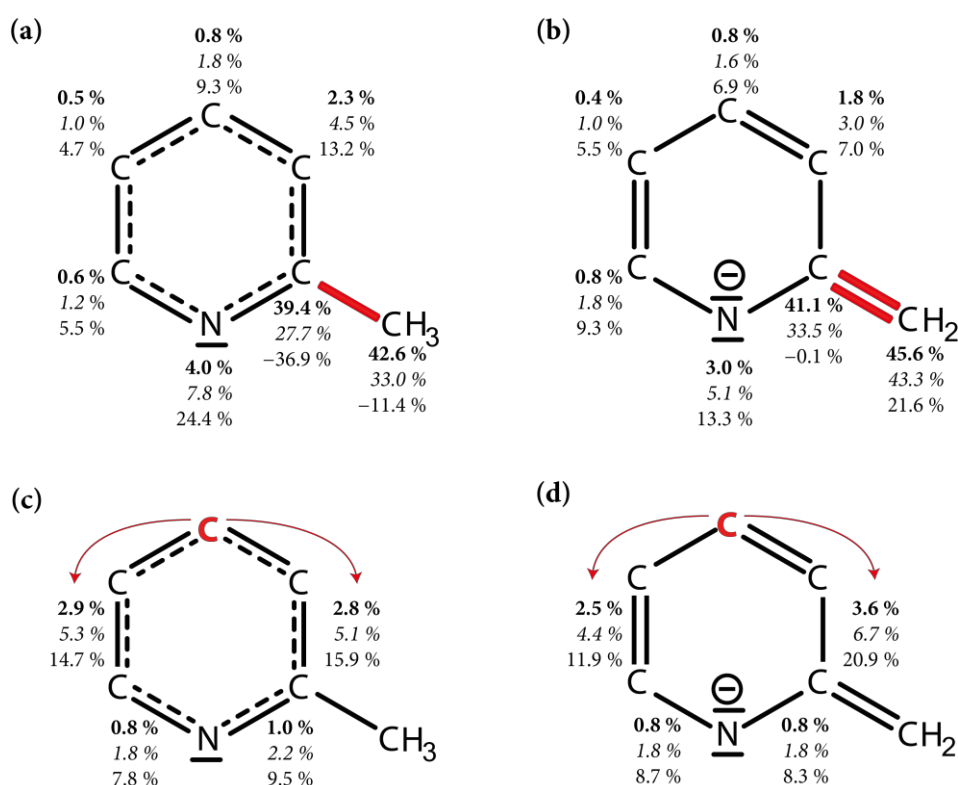


Figure 70. Results from the Source Function (SF) calculations on the 2-picoline adduct of 2-picollythium ("PicLi·2PicH"). **Bold** numbers correspond to the reference point at the BCP; *italic* numbers correspond to the reference points at $1.0 a_0$ distance from the BCP; regular numbers correspond to the reference points at $2.0 a_0$ distance from the BCP. Multipole model was adopted from Ott *et al.*^[154] with permission of the authors. (a) and (b): The values next to each atom are the SF percentage contributions to reference points at the exocyclic C-C bond (marked in red). (c) and (d): the values next to the bonds refer to the SF percentage contributions from the carbon atom marked in red.

the contributions marked with red arrows in Figure 70 (d) where there are localised double bonds. The contributions to the C–N bonds are in a similar range for both molecules.

These results and those that are not shown here allow some tentative conclusions:

- Those atoms involved in a σ -style single bond have large negative SF contributions to out-of-plane reference points of that bond. This is not as pronounced in double bonds with π character.
- Aromatic bonds promote larger SF contributions from atoms in the aromatic system to reference points of bonds located at the external periphery of the aromatic system, even if those bonds clearly are single bonds.
- C–C single bonds can be seen as “SF insulators” because the atomic contributions are always much lower if at least one C–C single bond separates the atom from the reference point.
- The electronegative nitrogen atom seems to enhance SF contributions towards its N–C bonds. It also seems to promote SF contributions along its bonds to reference points further away; the “single bond–N–single bond” system acts in the fashion of a double bond in this respect.

These conclusions still have to be considered preliminary because they merely are based on the results of the mentioned two compounds and have to be confirmed or revised by further studies on heteroaromatic and conjugated systems.

4.10.2. The Source Function in bis(2-benzothiazolyl)phosphane

The SF calculations on the experimental charge density of bis(2-benzothiazolyl)phosphane **2** were calculated in analogy to those carried out on [2-PicLi·(2-PicH)]: reference points were calculated so that they are aligned along vectors perpendicular to the respective ring plane. They were chosen at distances of 0 a_0 , 0.5 a_0 , 1.0 a_0 , 1.5 a_0 and 2.0 a_0 from the ring plane. Only the reference points at BCPs (i. e. at 0 a_0) and 2.0 a_0 distance are used in this thesis because the additional distances do not add much information and rather complicate the presentation of the results. The *Bohr* radius a_0 equals 0.529 Å.^[267] This corresponds to a maximum distance of 1.06 Å between the reference points and the ring planes. The average of the corresponding vectors was taken in the case of those bonds that belong to two rings (C2–C7 and C9–C14).

Gatti and *Saleh* suggested using the Hessian eigenvector at the BCP that corresponds to λ_2 as the reference line instead of normal vectors,^[268] but the eigenvectors are properties of a single point, and in addition, their direction can be biased by external polarisation from

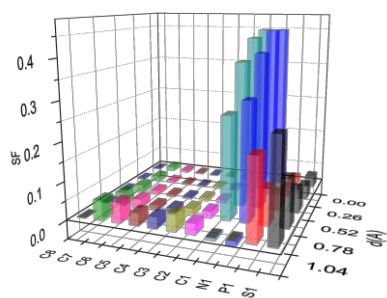


Figure 71. The “first generation” of Source Function result visualisation. This diagram displays the contributions from the given atomic basins to reference points at and above the Cl–Ni BCP.

lone pair density or inter-/intramolecular contacts. We chose to stick with the normal vectors for these reasons. Absolute contributions from every atomic basin to the total ED at all given reference points were calculated and the relative contributions were obtained from division by $\rho(\mathbf{r})$ at the reference point. The deviation from 100 % for the sum of contributions to each reference point (as figure of merit, see section 2.5) is given in the appendix. The deviation is highest in the regions of very low density at the reference points at $2.0 a_0$ distance from the ring plane; the mean standard deviation is 2.30 %.

The visualisation of the obtained SF results is a difficult task, especially with the multidimensional approach we chose that includes nine reference points per bond and contributions from all atoms in the molecule. It turned out that it was not sensible to create categories (contributions from nearest, next nearest, second nearest neighbours) to summarise our results as *Gatti et al.* did in their studies^[94-95] of benzene and naphthalene. This is not a general problem because it makes perfect sense in those homoaromatic systems; it is only the contributions in heteroaromatic systems that are too complicated.

Breaking down the results from Source Function calculations turned out to be a very hard task; the first discussions with visitors at poster presentations had to be preceded by a lengthy introduction into a rather complicated system of three-dimensional diagrams that displayed contributions from a number of atoms to a series of reference points that were located on different distances to the molecular plane. One of these diagrams is displayed more for historical than for practical reasons (Figure 71).

The next level of evolution is represented by the diagrams in Figure 70 in section 4.10.1; they are easier to digest, but still not very informative at first sight. It was therefore chosen to modify the WinXD-generated^[269] POV-Ray^[270] code that is used for the rendering of the atomic graphs so that the size of the nuclear attractor spheres corresponds to the percentage contribution of the respective atomic basin to a reference point. Analogous approaches were used by *Gatti et al.*^[90,94,98] and *Farrugia et al.*^[92,266] and a routine has recently been added to a newer version of WinXD that automatically produces POV-Ray code for Source Function visualisation. Unfortunately, the release of the updated program came too late for this study and Microsoft Excel and text editors were used instead.

Contributions to all reference points were calculated. The number of angular points for the determination of the integration rays (“NANG”) in XDPROP was 434; the number of radial points was 400. The integration step size was 0.0005 Å and the accuracy was set to 0.00005 Å. These settings are orders of magnitude more expensive in terms of CPU time than those normally used; they do not have to be set to such high settings if only atomic charges have to be calculated, but some test runs on the sulfur and phosphorus atoms indicated that the results of the SF calculations, which are highly dependent on the number of integration rays, converge at these settings. The usual computation times were two to four days per atom on an Intel Xeon at 2.40 GHz using the Windows version of XDPROP. The Linux version of XDPROP seems to be more efficient and reduces the integration time by a factor of around three.

A number of reference points were chosen that seems sensible for the presentation of the results. Reference points were placed considering all bonds involving heteroatoms since the delocalisation of charge density in the heterocycles was to be investigated.

Some SF contributions to BCPs and reference points at $2 a_0$ distance are displayed in Figure 72 and Figure 73, and the general trends in the SF contributions in **2** are summarised in the next few paragraphs:

- Percentage contributions from remote atoms increase with rising distance of the reference point from the ring plane while contributions of the atoms directly involved in the respective bond decrease. This is less pronounced in P–C and S–C bonds.
- Heteroatoms contribute stronger to out-of-plane reference points than carbon atoms; this is visible for example from contributions from sulfur, nitrogen and carbon atoms in Figure 73 (e) and (f).
- The SF contributions display the approximate C_{2v} symmetry of the molecule in the way that equivalent atoms contribute approximately equally to equivalent reference points.
- Atomic contributions to reference points in the same 2-benzothiazolyl moiety are always higher than to those in the other moiety, even if the respective reference point is separated by the same number of atoms; compare the contributions from atoms in the six-membered rings in Figure 73 (a) and (b).
- The atomic contributions to the P–C bonds are generally smaller than those to the S–C bonds, even if the contributing atoms and the bond are separated by the same number of atoms.

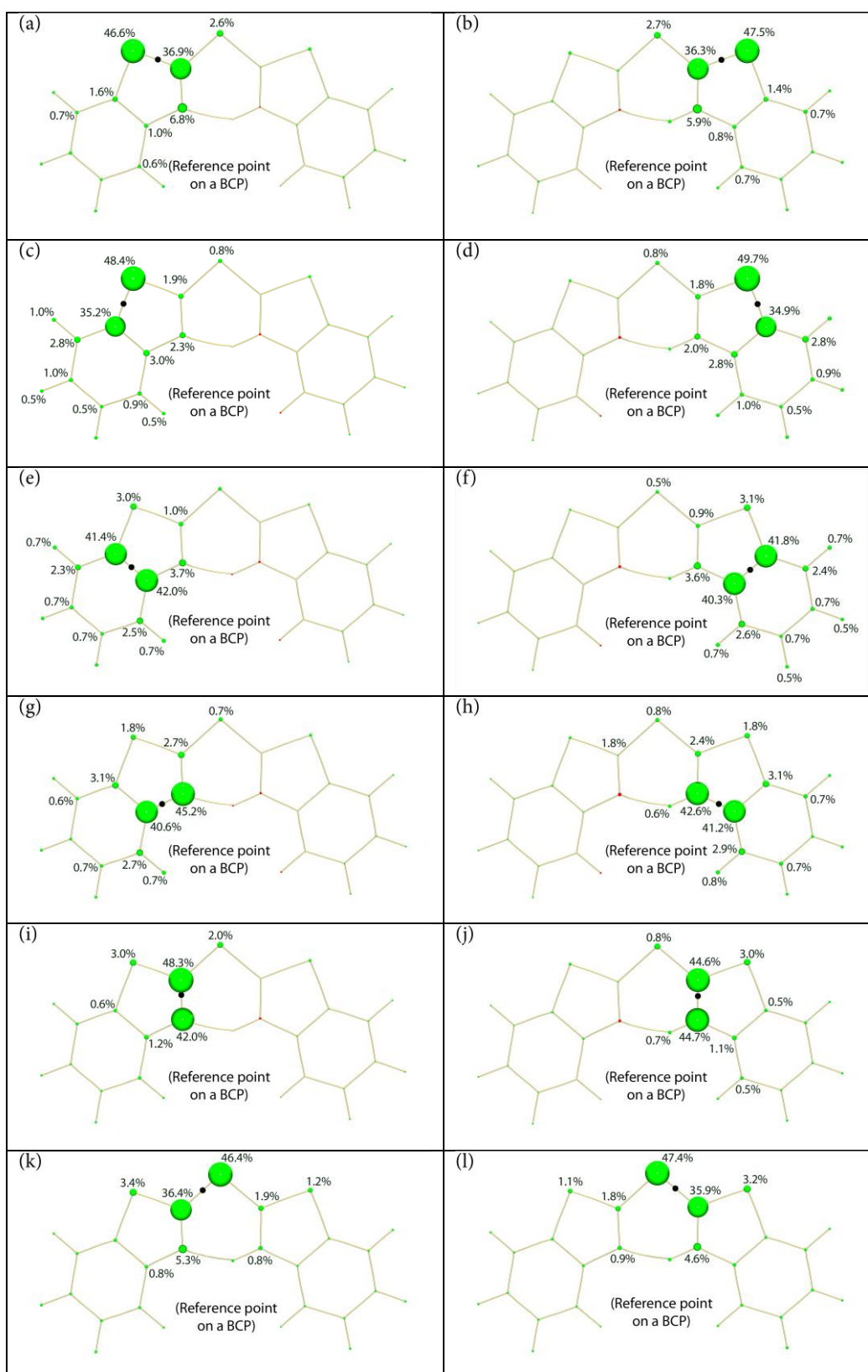


Figure 72. The percentage numbers refer only to the mean SF contributions to BCPs (i. e. ref. points in ring plane). Black dots: RP. Green spheres: positive contribution, red spheres: negative contribution.

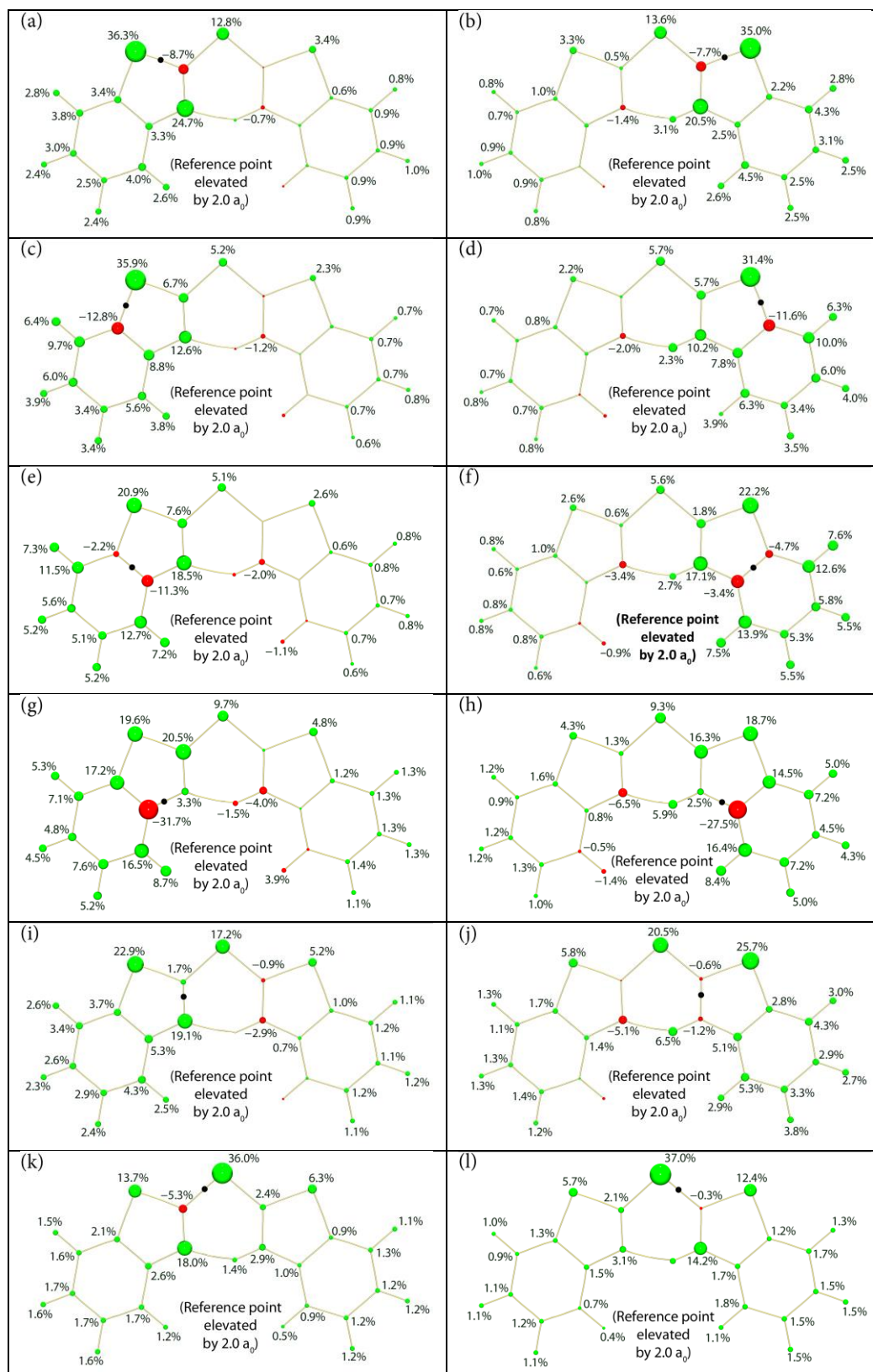


Figure 73. The percentage numbers refer only to the mean SF contributions to ref. points 2.0 a_0 distant from ring plane. Black dots: RP. Green spheres: positive contribution, red spheres: negative contribution.

While the general tendency of the significant contributions from remote atoms seems to indicate delocalisation, we can only speculate on the amount of electron delocalisation because there are no reference data from comparable heterocyclic aromatics that we could possibly refer to yet. The amount of delocalisation seems to be similar in the two halves of the molecule that are separated by the phosphorus atom.

Some other conclusions, however, can be drawn from the Source Function results. The phosphorus atom seems to act as an “SF isolator” that hinders SF contributions from one 2-benzothiazolyl moiety to the other. In this property, it is similar to the single bonds in the deprotonated 2-picolyl moiety that was discussed in section 4.10.1; this finding confirms the single bond character of the P–C bonds that had been attested by *Stey et al.*^[222] and *Henn et al.*^[227] to **2** and the related metallaphosphane [Me₂Al-(μ -Py)P] based on their QTAIM results.

Table 8. Comparison of the SF contributions and parameters at the hydrogen bond critical point in **2** and in *Gatti's* reference for the “resonance assisted hydrogen bond,” the enol-tautomer of malonaldehyde.^[90]

Sample	$d(\text{N2}\cdots\text{H})$	$d(\text{N1}-\text{H})$	$d(\text{N1}-\text{N2})$	$\rho(\text{BCP})$	$\nabla^2\rho(\text{BCP})$	SF(N1)	SF(H1)	SF(N2)
2	1.7295 Å	1.0233 Å	2.6161 Å	$0.373 \text{ e } \text{Å}^{-3}$	$+2.01 \text{ e } \text{Å}^{-5}$	22.0 %	4.3 %	26.2 %
OH...O ^[90]	1.639 Å	1.008 Å	2.538 Å	$0.378 \text{ e } \text{Å}^{-3}$	$+3.57 \text{ e } \text{Å}^{-5}$	34.7 %	2.1 %	34.0 %

The categorisation of the strength of hydrogen bonds based on SF contributions that was first proposed by *Overgaard et al.*^[102] and extended by *Gatti et al.*^[90] was applied to the intramolecular hydrogen bond in **2**. In principle, the SF contribution of the hydrogen atom to the bond critical point in the hydrogen bond can be used to classify the strength of the hydrogen bond: large negative contributions characterise weak hydrogen bonds while low positive contributions indicate rather strong, “resonance assisted” hydrogen bonds that have some delocalised character. The result, displayed in Table 8, is in accordance with the assumption of a strong, resonance-assisted hydrogen bond, which clearly is a consequence of the tautomerism in **2**.

4.11. Delocalisation index calculations

The delocalisation index $\delta(\text{A},\text{B})$ essentially is a measure for how many electrons are shared or exchanged between a pair of atoms A and B. It does however not display the bond order between the pair of atoms; the bond order can only be derived from the delocalisation index in the special case of non-polar bonds with equally shared bonding electrons. In such a situation, a value of $\delta(\text{C},\text{C}) = 1$ would be expected in a carbon/carbon single bond, $\delta(\text{C},\text{C}) = 1.89$ is reported for the double bond in ethylene.^[271-272] The value

would significantly decrease in case of polar bonds because more charge density is concentrated in one atomic basin than in the other and thus not shared between the atoms. The usefulness of the delocalisation index has been very impressively demonstrated by *Macchi*^[273] in a follow-up paper to the experimental charge density study on [2-PicLi·(2-PicH)] of *Ott et al.*^[154]

The delocalisation index is based on quantum-mechanical calculations. The results strongly vary with the used level of theory while the dependence on the size of the used basis set is little pronounced.^[260] If comparisons between different molecules are to be made, it is important to have in mind that numerical values should only be compared between results obtained from the same level of theory.

For homoaromatic systems like benzene, the delocalisation index of adjacent carbon atoms is generally larger than unity, reflecting a bond order higher than 1. The para-delocalisation index (PDI) defined as the mean of all $\delta(A,B)$ between *para*-related atoms in a ring as proposed by *Poater et al.* was calculated for the six-membered rings.^[260]

As there are no *para*-related atoms in five-membered rings, the PDI cannot be used for the thiazole moiety. For heteroaromatic rings containing only one heteroatom, the difference between the $\delta(A,B)$ values for the atoms of the formal double and the formal C–C single bonds was proposed as a comprehensive index (the smaller the difference, the more distinct the aromatic character),^[260] but this approach is only strictly valid for five-membered heterocycles with only one heteroatom: the $\delta(A,B)$ values for the atoms pairs in the formal C=C double and the formal C–C single bond are compared; the lower the difference, the higher the aromatic character. We chose to take the mean $\delta(A,B)$ values between 1,3-related atoms in the heterocycles of **2** instead.

The $\delta(A,B)$ values from an optimized structure of benzothiazole using the same level of theory and the same basis set as for **2** were calculated and used for comparison. In order to tackle the question whether the phosphorus atom is part of the delocalised system, a geometry-optimised structure of phosphorine was calculated at the same level of theory. The program AIMAll^[160] and its very efficient integration routines were used for the calculation of delocalisation indices.

It is striking that the delocalisation indices of 1,3-related atoms are always significantly higher if heteroatoms are involved, which confirms the tendency observed in the Source Function contributions. Tables of delocalisation indices are given in the appendix.

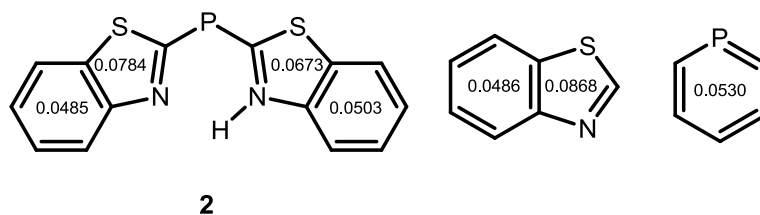


Figure 74. Delocalisation index results for **2**, benzothiazole and phosphorine. PDI values are given for the six-membered rings; the numbers in the five-membered rings correspond to the mean $\delta(A,B)$ values between 1,3 related atoms in the ring.

PDI values for the six-membered rings are 0.0503 and 0.0485 for the protonated and the non-protonated moiety, respectively (see Figure 74). The corresponding value in benzothiazole is 0.0486. The mean values for $\delta(A,B)$ between 1,3-related atoms in the five-membered rings of **2** are 0.0673 and 0.0784 for the protonated and the non-protonated rings, respectively. The mean $\delta(A,B)$ value between 1,3-related atoms in the five-membered ring in benzothiazole was found to be 0.0868, which can be interpreted as evidence for a decrease in delocalisation for the six-membered rings in **2** and a slight increase of delocalisation in the five-membered rings, each compared to the non-substituted and non-protonated parent compound benzothiazole.

The PDI value in the phosphorus-containing six-membered central ring in **2** is relatively high at 0.018. It does not seem sensible to compare the value to the PDI of phosphorine since the former ring only exists because of a hydrogen bond. Hence, the $\delta(P,C)$ for the phosphorus atom and the *para*-carbon atom for phosphorine and the respective 1,4-related $\delta(P,C)$ in **2** are given. The corresponding $\delta(P,C)$ are almost a magnitude smaller in **2** compared to phosphorine (Figure 75), indicating only little delocalisation from the phosphorus atom in **2**.

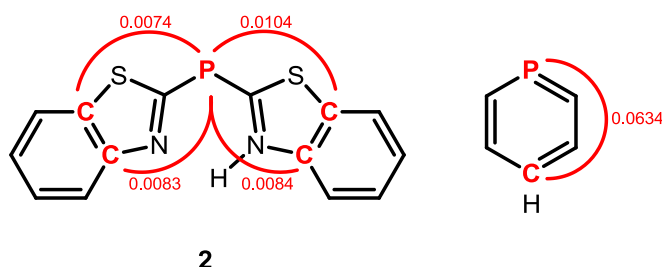


Figure 75. $\delta(P,C)$ values for 1,4 related atoms in **2** and in phosphorine.

4.12. NICS and GIMIC calculations

For the NICS calculations on **2**,^[246] the recently developed GIAO-DF-HF^[274] code was used by Prof. Dr. *Mata*, together with the cc-pVTZ basis set. Calculations on benzothiazole were conducted using the same procedures. All calculations were performed with the Molpro 2010.1 program package.^[161]

The NICS(0) values for the five-membered rings in **1** were calculated to be -6.53 ppm and -7.85 ppm for the protonated and the non-protonated ring, respectively. The benzothiazole molecule has a value of -9.86 ppm. This indicates aromaticity, but at a slightly smaller scale than the parent compound.

Magnetically induced current densities were calculated using the *gauge-including magnetically induced current* method (GIMIC).^[275-276] All calculations and analyses were done by Dr. *Heike Fliegl*. The GIMIC method has been briefly mentioned in section 4.6; the used methods and the obtained results are shortly reproduced here.

The GIMIC method yields information about the ring current strength (in nA T^{-1}). It provides information about the degree of molecular aromaticity according to the criterion that ring currents must be present in delocalised systems that are induced by a magnetic field. Information about the pathways of the induced current in complex molecular ring systems can be extracted from GIMIC as well.^[248,277-282] The current strengths and pathways are obtained by numerical integration of the current density passing through planes perpendicular to selected bonds of the studied molecules.

The sign and magnitude of the ring current strengths indicate whether molecular rings

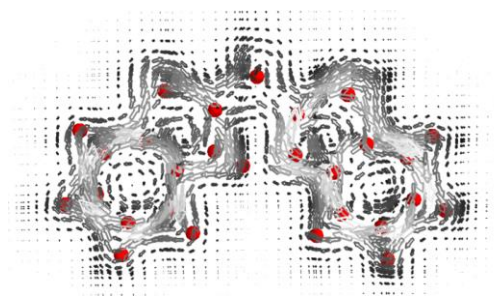


Figure 76. The magnetically induced current density for **2**. The displayed current vectors are in a plane parallel to the molecular plane 1 \AA elevated from it. Clockwise circles indicate diatropic currents; paratropic currents circle counter-clockwise. The atomic positions are displayed as red dots. The graphics are provided by *H. Fliegl*.

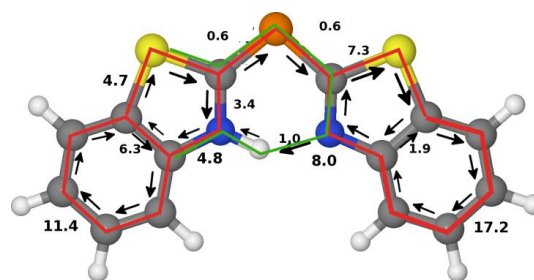


Figure 77. Schematic picture of the current pathways displayed in Figure 76. The numbers in black are integrated current strengths for selected bonds. The red lines overlaying the bonds are the dominating diatropic current pathways. The C-P-C bridge and the hydrogen bridge exhibit very small currents of 0.6 to 1.0 nA T^{-1} (marked green). The graphics are provided by *H. Fliegl*.

are aromatic, anti-aromatic, or nonaromatic by having diatropic, paratropic, or zero net ring currents.^[249] The net ring currents consist of diatropic and paratropic proportions, which can be quantified separately. Ring currents that generate a magnetic field *opposing* the external field are defined as diatropic and have positive sign, whereas currents circulating in the opposite (non-classical) direction, thus *strengthening* the external magnetic field, are defined to be paratropic and have a negative sign.^[243,275,283-284] The calculated net ring current strength for benzene is 11.8 nA/T and is used as a reference value for aromatic molecules. An overview of the GIMIC method and related applications can be found elsewhere.^[247]

The calculated magnetically induced current density as well as a schematic overview of the current pathways and integrated current strengths is displayed in Figure 76 and Figure 77. The dominating currents are found to be diatropic for all rings including the ring that is formed by the hydrogen bond although the aromatic character is not very pronounced in the latter. Thus, according to the magnetic criterion, all rings can be considered being aromatic. The strongest currents of 11.4 nA/T and 17.2 nA/T are found in the six membered rings, while the currents of 4.7 nA T⁻¹ and 7.3 nA T⁻¹ in the five-membered rings are about 60% weaker. For comparison, the current strength for benzene on the same level of theory is 11.8 nA T⁻¹. Thus, both five membered rings can be regarded as approximately half as aromatic as benzene. The smaller current strengths of 6.3 nA T⁻¹ and 1.9 nA T⁻¹ obtained for the C–C bonds fusing the five and six membered rings can be understood, since at these bonds the two current contributions flow with opposite direction and therefore partly cancel each other.

4.13. About the interpretation of nonbonding VSCCs

Ever since *Bader et al.* first interpreted^[74] the Laplacian topology and the distribution of VSCCs as a one-to-one mapping of the *Lewis* structures of bonding and nonbonding electron pairs, this approach has been fruitfully used in many cases, such as for the interpretation of the peculiar bonding situation in sulfur-nitrogen compounds.^[75,80] The general success of this interpretation is based on the fact that it provides a universal, quantum mechanics-derived model for the explanation of molecular structure^[73,230,272,285] that is easily transferrable to the basic concept of the chemical *Lewis* structure model^[286] of and *Gillespie's* VSEPR theory of molecular geometry.^[287]

Bader frequently expressed his objections against molecular orbital (MO) theory in his publications^[288] and talks.^[289] His concern was that MO theory is based on wave functions, not on the observable of the electron density. MO theory, according to *Bader*, ignores the existence of functional groups by delocalising orbitals, which is the underlying principle

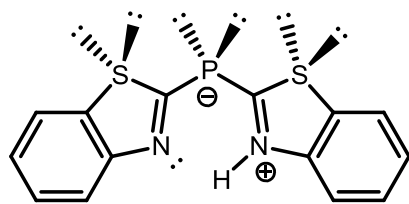


Figure 78. Lewis formula of **2** with formal charges and tetrahedral geometry at sulfur and phosphorus atoms as required by VSEPR theory.

of MO theory. The choice of individual molecular orbital contributions to a given chemical property is criticised as being arbitrary by *Bader*.^[290]

The late Professor *Bader* apparently disapproved of chemists that would value only those results from theoreticians that were useful for their immediate experimental work because they “*ignored the universal validity of physics.*”^[291] However, it appears that his idea of the interpretation of

VSCCs as projections of Lewis formulae may over the years have been used in a way that is leading away from his fundamental idea to become independent of physically questionable concepts: hybridisation states of heavy main group elements are deduced from the symmetry of the VSCC distributions^[227,292-293] although the concept of heavy element hybridisation states has been criticised by theoreticians.^[251]

Let us quickly summarise the relevant results regarding **2** before we continue. What are the implications of the findings presented in this chapter regarding the nature of the non-bonding VSCCs at the sulfur and phosphorus in **2**? The theoretically^[221] and chemically^[220-223] predicted phosphanidic nature of bis-(2-benzothiazolyl)phosphane **2** (and the conclusion that the P–C bonds have to be considered as single bonds) were confirmed by QTAIM methods. However, the reasoning behind the confirmation is only valid if the existence of two local minima in the nonbonding VSCCs at the phosphorus atom is strictly interpreted assuming the equivalence of the *Laplacian* structure to the *Lewis* structure including localised lone pairs *in the sense of VSEPR theory*. The molecular structure in terms of P–C bond distances and other QTAIM indicators such as the P–C bond ellipticities do not give reason for such a clear judgement.

If the conclusions that were drawn for the phosphorus atoms in **2** were transferred to the sulfur atoms in the same molecule, the presence of two localised lone pairs at each of these atoms and the classification of the S–C bonds as single bonds would have to be accepted as well (see Figure 78). It was proven in this thesis that aromaticity is present in both of the five-membered rings, which automatically falsified the presence of VSEPR sp^3 “rabbit ear” *localised lone pair orbital lobes*, but the possibility of two lone pairs remains.

In the VSEPR framework, maximal hybridisation is assumed according to the number of valence electron pairs and deviations from the expected geometry are explained by electron pair repulsion; lone pairs are more repulsive than bonding pairs. Thus, it is the common association of VSEPR lone pairs with sp^3 hybridisation which causes confusion

in the case of **2**. *Bader* certainly cannot have had in mind this association when he published his review article about QTAIM and VSEPR theory with *Gillespie*.^[73] It has to be noted though that the presence of aromaticity is not the reason for the absence of sp^3 hybridisation. It is the stability of the energetically low atomic s-orbitals that cause this behaviour. The oxygen atom in furan has two lone pairs and yet furan is commonly considered aromatic^[235,260] although there is no formal difference between the oxygen atom in furan and the one in a water molecule.^[294] The aromaticity of furan, thiophene and benzothiazole as well as the bond angle in water can be explained by hybridisation concepts that are equally simple as the theory of the ubiquitous valence shell electron pair repulsion (VSEPR),^[287] but more physically meaningful and less ambiguous.^[295-296] As *Henry A. Bent* postulated more than half a century ago referring to compounds of main group elements,^[297] the p-character of bonding orbitals is maximized in bonds towards more electronegative substituents. Lone pairs can be imagined as “ghost atoms” that naturally cannot have any electronegativity. *Therefore, the argumentation should perhaps rather be that it is not the lone pairs but the nature of the substituents which determines the structure of the mentioned molecules.* Both the sulfur as well as the phosphorus lone pairs can be imagined to consist of nearly equal contributions from atomic s and p orbitals, explaining the diffuse character that is evident from the very low absolute values of the Laplacian and $\rho(\mathbf{r})$ at the minima in the VSCCs (see Table 9).

Let us quickly complete the little excursus about the oxygen atom in water and furan. According to *Bent's* rule, the O–H bond in water (or the O–C bond in the case of furan) can be imagined to be constructed from higher p-orbital contributions of the oxygen atom than the 75 % that would result from sp^3 hybridisation. This facilitates the explanation of the small H–O–H angle in the water molecule in a more elegant way compared to the VSEPR predictions, which effectively lead to the reasoning that the purportedly quite space demanding lone pairs “contract” the O–H bonds to an angle smaller than the tetrahedral angle of 109.47°.

The molecular orbital (MO) theory^[298] and natural bond orbital methods^[299-301] reportedly^[295] do not get into the trouble regarding the interpretation of the lone pairs that the VSEPR theory causes. If the s- or p-character of the bonding orbitals determines the bond angle, then the percentage s-character of the S–C bonds in **2** can be estimated to be nearly zero, given the angles around S1 and S2 of 91.20° and 90.40°, respectively. This estimation indicates that the bonds towards the neighbouring carbon atoms are dominated by two of the sulfur p orbitals. Hence, the two lone pairs consist of equal p and s contributions. The phosphorus atom in **2** with its bond angle of 98.60° will presumably have a slightly larger s character in its bonds towards the carbon atoms. Following the results of

Table 9. Values for the Laplacian and $\rho(\mathbf{r})$ at the local minima in the non-bonding VSCCs in **2**.

	$\nabla^2\rho(\mathbf{r}) [e \text{ \AA}^{-5}]$	$\rho(\mathbf{r}) [e \text{ \AA}^{-3}]$
P1	-4.41 / -3.74	0.87 / 0.83
S1	-8.64 / -9.65	1.34 / 1.35
S2	-10.64 / -10.76	1.38 / 1.40
N2	-72.10	3.76

Bent's rule, one of the lone pairs can be an s-rich lone pair and the other is a lone pair with predominant p character. This, in turn, enables the delocalisation of the electrons of the p-rich lone pair into the ring, which is in accordance with the results from a theoretical study on planar conjugated systems $^+\text{CH}_2\text{-XH}$ (with X = O, S, Se, Te) by *Kapp et al.*, which indicated no decrease in the electron delocalisation descending from oxygen.^[302]

In the case of main group elements such as oxygen, the tendency to increase p character in the bonds to electronegative substituents is not only visible in the water molecule (where VSEPR admittedly gets us to the right conclusion) but also in hydrocarbons with very electronegative substituents such as in CH_3F , CH_2F_2 and CHF_3 , where despite the three fluorine lone pairs the H-C-F angles are *smaller* than the H-C-H angles.^[303-304] For heavier main group elements, the tendency is more pronounced and the s orbital is of such low energy that a hybridisation is energetically less favourable and the bonding angles approach 90° .^[251,305-307]

The shape of the VSCCs in **2** with their symmetry that is close to tetrahedral can thus not be interpreted by means of sp^3 type localised lone pairs, but the observed symmetry does not contradict the postulate of one s-rich and one p-rich lone pair according to MO/NBO theory, and there is no reason why the observed pattern in the *Laplacian* should not be caused by this constellation.

4.14. Intermolecular bond paths

Similar to the approach used in the charge density study on **1**, we searched for bond paths that might indicate possible intermolecular interactions. While no such paths were found in the intermolecular charge density of **1**, several of those intermolecular bond paths according to C-H...S and C-H...P hydrogen bonds were found in **2** (see Figure 79).

There are not many charge density studies involving C-H...S hydrogen bonds^[308-310] and to the best of our knowledge there are none where C-H...P hydrogen bonds are mentioned. Judging from the hydrogen/sulfur distances and the properties at the bond critical points, the C-H...S hydrogen bonds in **2** ($0.015 \leq \rho(\mathbf{r}) \leq 0.044 e \text{ \AA}^{-3}$ and $0.254 \leq \nabla^2\rho(\mathbf{r}) \leq 0.494 e \text{ \AA}^{-5}$) are comparable in strength to those reported in literature for thioacetamide ($\rho(\mathbf{r}) \leq 0.03 e \text{ \AA}^{-3}$ and $\nabla^2\rho(\mathbf{r}) \leq 0.36 e \text{ \AA}^{-5}$). However, it has to be noted that C-H...S hydrogen bonds in general were classified as by far the weakest in a detailed QTAIM analysis of hydrogen bonds; the values of the C-H...P hydrogen bonds in **2** even indicate a

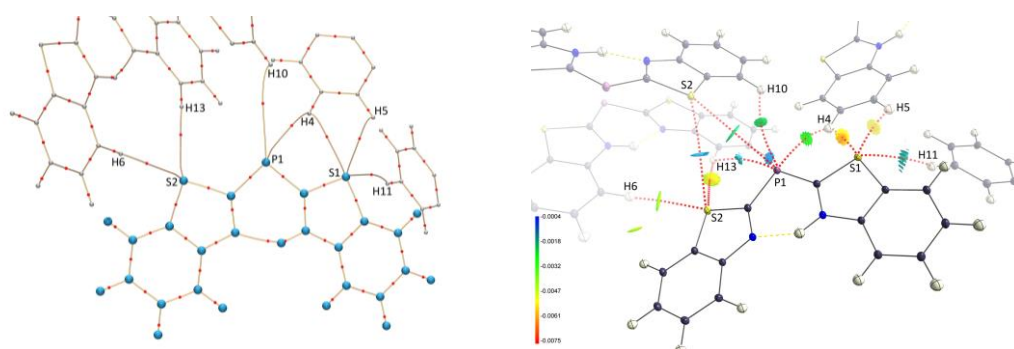


Figure 79. Left: molecular graph including intermolecular bond paths. Right: Plot of non-covalent interactions using a projection of $\rho(\mathbf{r}) \cdot \text{sign}(\lambda_2)$ on the reduced density gradient (RDG value: 0.5) using the program MoleCoolQt^[155] and data obtained from the program NCI Milano.^[112,185-186] Only negative (attractive) values for $\rho(\mathbf{r}) \cdot \text{sign}(\lambda_2)$ were taken into account for the sake of clarity. As visible from the larger absolute values of $\rho(\mathbf{r}) \cdot \text{sign}(\lambda_2)$, the S...H interactions are stronger than the P...H interactions.

somewhat weaker nature. It should nevertheless be considered out that these interactions might determine the shape of the VSCCs, at least to some extent. A plot of the non-covalent interactions (NCI)^[110,112,185-186] confirms the presence of attractive interactions in the C–H...S and C–H...P hydrogen bonds in **2** (see Figure 79, right). See section 2.6 for details on the determination of non-covalent interactions.

The VSCCs are clearly not directed towards the intermolecular contacts in the cases of the sulfur atom. A correlation of the positions of the VSCCs and the direction of the intermolecular contacts can rather be found in the case of the phosphorus atom (see Figure 80), but it is not certain that there is indeed a correlation.

In addition, a weakly attractive S...S interaction and a P...S interaction was revealed from the NCI plot which is not visible from the molecular graph. The S...S distance is 4.324 Å and the P...S distance is 4.152 Å for the mentioned interactions in **2**. Similar intermolecular interactions in 2-thiouracil (S...S distance: 3.636 Å) and L-cystine (S...S distance:

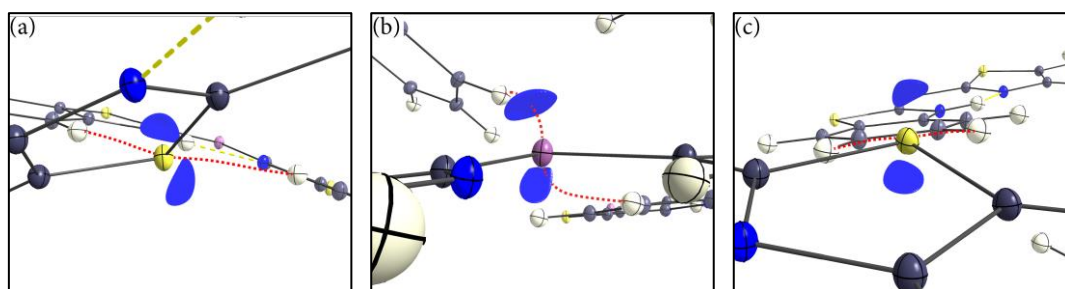


Figure 80. Nonbonding VSCCs of (a) S2; (b) P1; (c) S1. The red dashed lines are the approximate trajectories of the corresponding bond paths. The blue shapes correspond to isosurfaces at -8.5 e^{-5} for sulfur atoms and -3.3 e^{-5} for the phosphorus atom and are drawn to depict the positions of the nonbonding VSCCs.

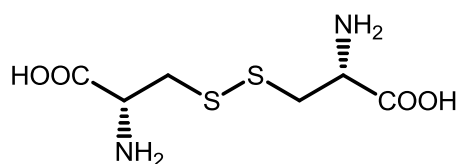


Figure 81. Structure formula of L-cystine.

3.426 Å) were classified as *van der Waals* interactions in charge density studies on these substances by *Munshi et al.*^[309] and *Dahaoui et al.*^[292] It is noteworthy that the distribution of VSCCs at the L-cystine sulfur atoms in the study of *Dahaoui et al.*^[292] qualitatively resemble

the distributions in **2**, and sp^3 hybridisation was attributed to the sulfur atoms based on the tetrahedral VSCC geometry. The deduction that the sulfur atoms must be sp^3 hybridised is not as far-fetched in the case of the non-aromatic disulfide L-cystine as it is in the case of **2**, but is still a false conclusion.

4.15. Conclusions

This chapter of my thesis shows the success of an ultra-low temperature experimental charge density study at 15 K. The data quality is very good although as much time as possible had to be saved in order to waste as little of the very costly liquid Helium that was needed to cool the sample. The achieved high data quality is due to the powerful rotating anode X-ray generator (Bruker TXS) and a precise area detector (Bruker APEX2) combined with ultra-low sample temperature technique (Oxford diffraction HeliJet). The used equipment is still cutting edge, despite the upcoming replacement of CCD technology (as used in the APEX2) by larger CMOS detectors such as the Bruker Photon detector. The upcoming generation of CMOS detectors has the advantage of larger detection area (100 cm² compared to the 38.4 cm² of the APEX2) and an air-cooled instead of a liquid-cooled Peltier system.

The charge density study on **2** was challenging because new measures of electron delocalisation had to be employed and evaluated. There is little work about the quantification of aromaticity by means of the Source Function available in literature yet. First work on the quantification of aromaticity in homoaromatic systems has been published in a proof-of-principle study, but heteroaromatic systems are more challenging and remain to be investigated extensively, possibly in a theoretical study. This thesis with Source Function calculations on three different heteroaromatic systems (2-picoline, 2-picolylolithium and 2-bis(2-benzothiazolyl)phosphane **2**) has hopefully laid the fundament for further studies in this direction.

Additional indicators of delocalisation have been applied, among them the QTAIM-based measure of bond ellipticity and the delocalisation index; the wave function derived density for the latter and NICS values were calculated in fruitful collaboration by Prof. Dr. R.

A. Mata and induced current densities were calculated by Dr. Heike Fliegl. The various applied indicators of delocalisation in the present study on bis-(2-benzothiazolyl)-phosphane **2** generally agree on the fact that aromaticity is present in all ring systems, even though its magnitude is smaller than in benzene and its parent compound benzothiazole.

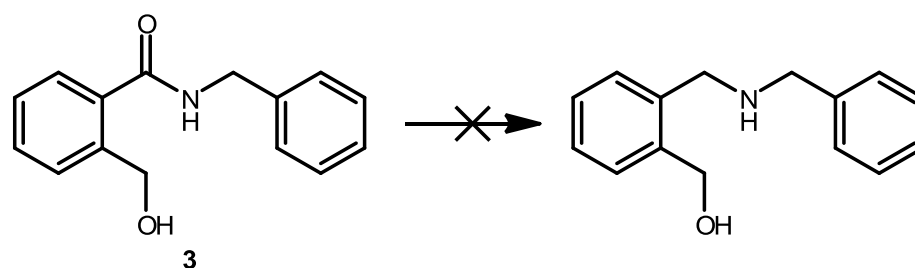
The lack of a clear indicator for the reason of the tetrahedral arrangement of the VSCCs at the phosphorus and sulfur atoms in **2** has to be accepted. As pointed out in the preceding lines, there is no reason to attribute sp^3 hybridisation to heavier main group elements than fluorine.

The concurrent presence of aromaticity and of two localised VSEPR sp^3 lone pairs each sulfur atom is contradictive. VSEPR predicts two *equivalent* lone pairs of the sp^3 type if there are two localised lone pairs at each of the sulfur atoms and at the phosphorus atom. This is for the sake of maximum separation between the lone pairs which is required in the VSEPR framework. No aromaticity could then be assumed for the five-membered rings because the rule of $4n+2$ delocalised aromatic electrons would be violated.

This chapter of my thesis essentially confirmed that the strict mapping of the features in the Laplacian field onto a Lewis diagram is bound to fail for third-row elements. This should be considered in future charge density work on compounds of heavy main group elements; at least in order to avoid false conclusions regarding bond orders, if not for the sake of physical propriety.

5. N-benzyl-2-(hydroxymethyl)benzamide

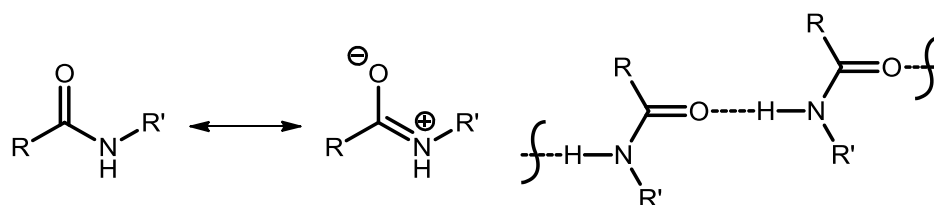
The aromatic carboxamide **3** was a part of the synthetic work for my *Diplomarbeit*.^[311] Contrary to what had been published,^[312] it has the salient behaviour to withstand its reduction to the corresponding amine by standard procedures using LiAlH_4 (Scheme 1). It is known that the class of carboxamides are relatively inert to nucleophilic additions at their carboxyl carbon atoms. They cannot be reduced by Raney-Nickel, NaBH_4 or BH_3 ,^[313] but a combination of these hydridic reducing agents with *Lewis* acids has been reported to facilitate the reduction.^[314] However, this conversion could not be reproduced in my *Diplomarbeit*.



Scheme 1. *N*-benzyl-2-(hydroxymethyl)benzamide **3** could not be reduced to *N*-benzyl-*N*-(2-hydroxymethyl)benzylamine.

The driving force to conduct an experimental charge density analysis on **3** initially was to examine if an explanation could be found for the chemically inert behaviour. It is common textbook knowledge that the $\text{C}(\text{O})\text{-N}$ bond in carboxamides has partially delocalised character, which is used to explain the high energetic barrier for a rotation around this bond.^[313] The resonance formulae in Scheme 2 visualise the delocalisation. The quantification of the amount of the delocalisation may also be used to explain the low reactivity.

The structural analysis of **3** in the solid state may admittedly not serve to entirely explain its reactivity in solution, but it brought up interesting additional features which are worth



Scheme 2. Resonance formulae describing the delocalised character of the C-N and C=O bonds in carboxamides.

Scheme 3. This type of hydrogen bond is frequently found in solid state structures of carboxamides and peptides, but not in **3**.

to be further investigated: the amide does not form intermolecular hydrogen bonds between the amido proton and the carboxyl oxygen atom of a neighbouring molecule, a type of hydrogen bond that is frequently found in polypeptides.^[315] The characterisation of intermolecular interactions is another goal of this study.

5.1. Data collection and IAM refinement

The compound crystallises as colourless needles of the orthorhombic space group $P2_12_12_1$. A crystal of suitable size had to be cut from a larger crystal. Data were collected at 100 K sample temperature on a Bruker *APEX2 Ultra* diffractometer equipped with a *Kryoflex2* sample cooling unit. The frames were collected in 180° ω scan mode at the following detector 2θ settings and exposure times: 0° (1 s); -10° (2 s); -24° (5 s); -53° (20 s); -55° (20 s); -68° (90 s); -77° (120 s). Different goniometer φ settings were used for each scan. The raw frame data were reduced with the program SAINT 7.68a.^[57] The frames for each detector 2θ setting were integrated separately using a different maximum resolution restriction for each setting. This procedure was repeated until the refined unit cell size converged. The maximum resolution was $d = 0.44 \text{ \AA}$.

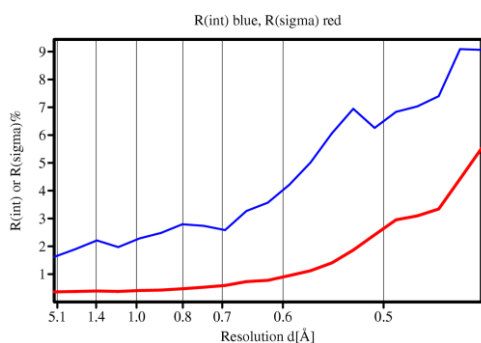


Figure 82. SADABS diagnostic plot of R_{int} and R_{sigma} as functions of the resolution. Both are on a low level and show a smooth progression.

The raw hkl data were scaled and corrected for absorption^[137] and equivalent reflections according to the space group symmetry were averaged in with SADABS 2008/2.^[23,25] The data reduction gave 161288 measured reflections with an internal agreement value of $R_{\text{r.i.m.}} = 0.0230$ ^[316] over the whole dataset ($R_{\text{r.i.m.}} = 0.0929$ in the outermost resolution shell from $d = 0.45$ to 0.44 \AA) and 14677 unique reflections. The completeness over

the whole resolution is 99.6 % and the average multiplicity is 10.8. The progression of R_{int} and R_{sigma} over the resolution does not show irregularities (See Figure 82).

The structure solution was carried out with a beta version of SHELXS-97 and an IAM refinement of the structure was carried out with SHELXL-97.^[21] The positions of the hydrogen atoms were refined without restraints and constraints, leading to C/N/O–H distances between 0.89 and 1.03 \AA . The isotropic hydrogen displacement parameters were refined without restraints and constraints, leading to values between 0.019 and 0.048 \AA^2 . The $Flack(x)$ parameter^[317] as calculated by SHELXL-97 was 0.5(5). The refinement as a racemic twin (TWIN/BASF commands) gave a batch scale factor of 0.3(4). The large estimated standard deviations indicate that the absolute structure cannot be determined

reliably from the very small intensity differences between *Friedel* pairs. A more reliable method of determining the absolute structure (as published by *Parson et al.*^[37]) is implemented in SHELXL-2013 and was used in addition as soon as the program became available. The resulting value of 0.51(6) is much more precise and indicates racemic twinning (the refinement program, however, displays the warning message “absolute structure cannot be determined reliably” rather than “possible racemic twinning”). Some doubts about the nature of the crystal that was used for data collection remain, given that racemic twinning is indicated by some of the used measures but at the same time a refinement as a racemic twin gives ambiguous results. The results of the multipole refinement should be treated having in mind this potential shortcoming of the dataset.

The hydrogen atoms were shifted to neutron diffraction reference distances along their bonding vectors before the XD2006 starting model was set up with XDINI (1.076 Å for aromatic protons; 1.032 Å for the amide proton; 0.964 Å for the hydroxy proton).^[52]

5.2. XD2006 multipole refinement

Table 10. Applied XD2006 refinement strategy. The scale factor (SCA) is refined in every step and is only mentioned in the first one. Abbreviations: D, dipoles; Q, quadrupoles; O, octapoles; H, hexadecapoles; M, monopoles; XYZ, positional coordinates; U_{ij} , displacement parameters; κ , spherical expansion parameters; κ' , aspherical expansion parameters. See also section 1.6. CHEMCON: the monopole and multipole populations of chemically equivalent atoms are constrained to each other.

1.	SCA		11.	κ'	(CHEMCON)
2.	M	(CHEMCON)	12.	M, D, Q, O, H	(CHEMCON)
3.	M, D	(CHEMCON)	13.	κ , M, D, Q, O, H	(CHEMCON)
4.	M, D, Q	(CHEMCON)	14.	U_{ij} , XYZ, κ , M, D, Q, O, H	(CHEMCON)
5.	M, D, Q, O	(CHEMCON)	15.	M	
6.	M, D, Q, O, H	(CHEMCON)	16.	M, D, Q, O, H	
7.	U_{ij} , XYZ(Non-H)	(CHEMCON)	17.	κ'	
8.	M, D, Q, O, H	(CHEMCON)	18.	M, D, Q, O, H	
9.	κ	(CHEMCON)	19.	U_{ij} , XYZ, κ , M, D, Q, O, H	
10.	M, D, Q, O, H	(CHEMCON)			

The refinement was carried out in 19 steps. The parameters that were refined in each step are listed in Table 10. Hydrogen multipole parameters were refined to an order of $l_{\max} = 2$. Reported optimum values for the hydrogen expansion parameters of $\kappa = 1.15$ and $\kappa' = 1.40$ for the hydroxy and amid hydrogen atom and $\kappa = 1.10$ and $\kappa' = 1.18$ for the remaining hydrogen atoms and were used and kept constant.^[42] The hydrogen isotropic displacement parameters were refined at a late stage of the refinement (steps 14 and 19). A modified weighting scheme was used beginning with step 12 after the first eleven steps were refined

using experimental weights. The parameters for the modified weighting scheme were chosen using the program DRKPlot.^[156]

The plot of the resolution dependence Figure 83 (a) reveals a systematic overestimation of the intensities at low resolution. A plot of the fractal dimension of the residual density showed the flatness and featurelessness of the residual density, see Figure 83 (a).^[53] The fractal dimension of zero residual density is sufficiently high with $d^f(0) = 2.68$. A plot of the experimental errors versus the normal probability confirmed the appropriateness of the used modified weights. See Table 11 for further information.

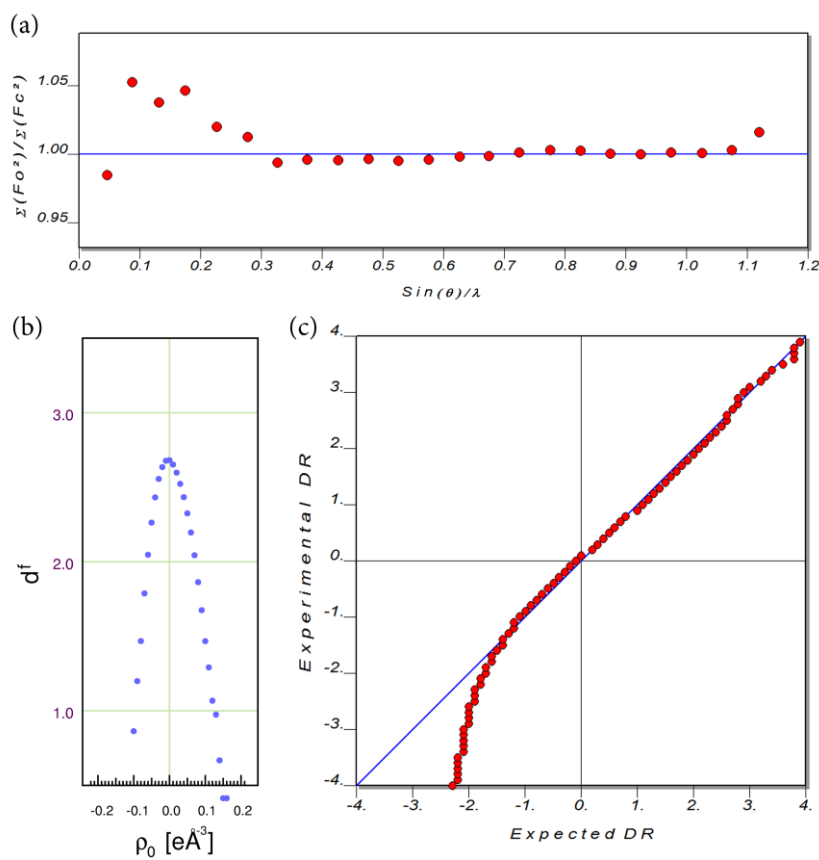
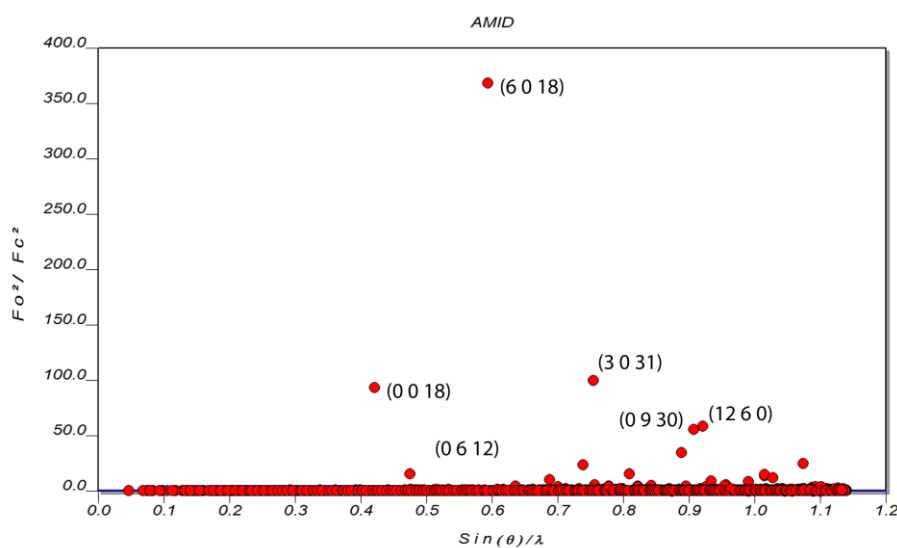


Figure 83. (a) The scale factor as a function of the resolution. There is a systematic positive deviation of the observed intensity in the low resolution area; (b) the fractal dimension of the residual density; (c) the experimental errors versus the normal probability distribution of errors (with modified weighting scheme).

Table 11. Unit cell data and results from XD2006 refinement of **3**. The absolute structure parameter is given as determined by SHELXL-97.

Structure code	SPAnPSmit	Z	4
Empirical formula	C ₅₂ H ₄₄ P ₂ S ₂	Crystal dimensions [mm ³]	0.07 x 0.23 x 0.31
Formula weight [g mol ⁻¹]	1225.91	$\rho_{\text{calcd.}}$ [g cm ⁻³]	1.337
Sample temperature [K]	100(2)	μ [mm ⁻¹]	0.089
Wavelength [Å]	0.71073	<i>F</i> (000)	512
Crystal system	Orthorhombic	θ range [°]	2.771 – 53.86
Space group	<i>P</i> 2 ₁ 2 ₁ 2 ₁	Reflections collected	181519
Unit cell dimensions [Å]		Unique reflections (w/o absences)	14855(14677)
	<i>a</i> = 7.1637(5)	<i>R</i> _{int} / <i>R</i> _{σ}	0.0221/0.0081
	<i>b</i> = 7.8285(6)	Completeness to θ_{max}	99.7 %
	<i>c</i> = 21.373(2)	data/parameter	26.5
	α = 90 °	GoF (weighted GoF)	2.5977 (1.2863)
	β = 90 °	<i>R</i> 1	0.0144
	γ = 90 °	w <i>R</i> 2	0.0441
Volume [Å ³]	1198.6(2)	max. diff. peak/hole [e Å ⁻³]	0.150/−0.108
Extinction coefficient	-	Absolute structure parameter	0.5(5)

Figure 84. It is striking that almost all observed severe outliers in the comparison of F_{obs}^2 and F_{calc}^2 have Miller indices that are multiples of three.

The analysis of $F_{\text{obs}}^2 / F_{\text{calc}}^2$ for single reflections showed a strong deviation for those reflections (*hkl*) with *h*, *k*, *l* being multiples of three, allowing the conclusion that the used radiation was significantly contaminated with low-energy radiation (see Figure 84).^[64] This issue is addressed more thoroughly in section 1.11 and chapter 7.

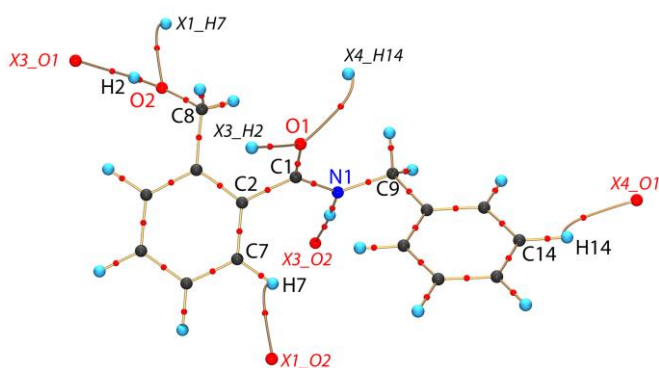
Table 12. Properties at the C=O and C_{carbox}-N BCPs of **3** and reference values from other studies.

		$\rho(\mathbf{r}_{\text{BCP}})$ [$e \text{ \AA}^{-3}$]	$\nabla^2\rho(\mathbf{r}_{\text{BCP}})$ [$e \text{ \AA}^{-5}$]
Average values from the two amide groups in tri(L-valine), values from ref. ^[319]	C=O	2.94(10)	-36(6)
	C _{carbox} -N	2.39(8)	-23(3)
Mean value from the two amide groups in each of the three tripeptides in ref. ^[320]	C=O	2.92 ± 0.06	-33.3 ± 5.5
	C _{carbox} -N	2.45 ± 0.05	-23.2 ± 2.9
Average values from ref. ^[321] (calculated as average values from the ELMAM database)	C=O	2.80(10)	-26.1(3.8)
	C _{carbox} -N	2.40(10)	-23.4(3.2)
Corresponding properties in 3	C1=O1	3.02(3)	-36.69(13)
	C1-N1	2.45(2)	-24.80(10)

5.3. Analysis of the atomic graph

The compound **3** is no uncommon organic structure and the properties at the bond critical points do not need to be discussed in detail. The corresponding values are shown in in the appendix, Table A 4. The QTAIM analysis of the charge density map derived from the multipole refinement yielded a molecular graph with all expected bond paths.

The C=O distance in **3** was found to be 1.2452(2) Å, which is slightly longer than the mean value of C=O double bond distances of 1.21 Å. The C1-N1 distance is 1.3406(2) Å, which is between the mean C(sp²)-N(sp²) distance of 1.40 Å and the mean C=N double bond distance of 1.29 Å.^[318] Thus, the structural parameters confirm the delocalised character of these bonds. The C1-C2 distance is 1.4981(2) Å, which is slightly longer than the mean distance reported of 1.47 Å for C(sp²)-C(sp²). This is in accordance with the O1-C1-C2-C7 dihedral angle of 53.9 °, which prohibits the effective conjugation of the delocalised system in the amide group with the aromatic phenyl ring. This conjugation would only be possible if the atoms of the two groups were coplanar.

Figure 85. Molecular graph of **3** including hydrogen bond paths.

The properties of the charge density map at the BCPs of the C=O bond are typical for strong covalent bonds (see Table 12). The ellipticities at the BCPs are 0.14 (C1-O1) and 0.19 (C=O), indicating significant π character in both bonds. A

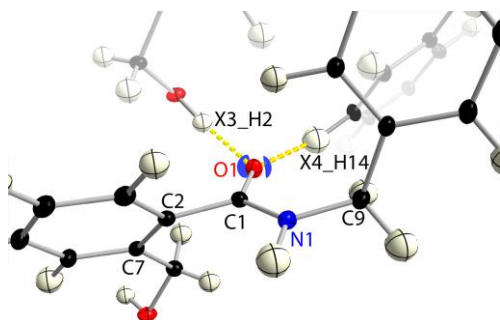


Figure 86. The carboxyl oxygen atom O1 is the acceptor of two hydrogen bonds. One of those bonds is of the O–H...O type, the second is a C–H...O bond. The isosurface of the Laplacian at a level of $-100 \text{ e } \text{Å}^{-5}$ is shown. Two distinct nonbonding VSCCs are located around the carbonyl oxygen atom approximately in the N–C–O plane.

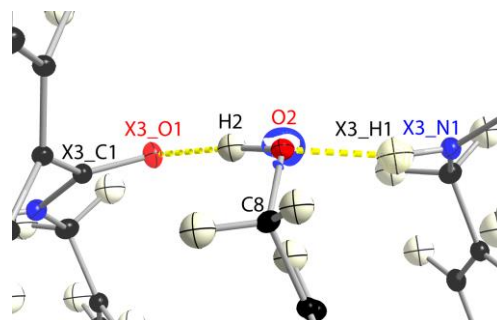


Figure 87. The hydroxy group simultaneously is the acceptor and the donor of a hydrogen bond and thus acts as a bridging fragment. One of the contacts is an N–H...O hydrogen bond, the other is a C=O...H hydrogen bond. A Laplacian isosurface is plotted around the hydroxy oxygen atom O2 at a level of $-110 \text{ e } \text{Å}^{-5}$. The VSCCs are not well isolated from each other.

comparison of these properties with previously determined values from other charge density studies^[319–320] reveals that the values of $\rho(\mathbf{r})$ and $\nabla^2\rho(\mathbf{r})$ for the carboxyl C=O bond are in the same range as the previously reported values.

There are three different types of hydrogen bonds in the solid state structure of **3**. As mentioned earlier, there is no hydrogen bond between the amide proton H1 and the carboxamide oxygen atom O1. Instead, the latter is the acceptor in a C–H...O and an O–H...O hydrogen bond (see Figure 86). The third is an N–H...O hydrogen bond involving the hydroxy group at O2, which serves in a bridging function between amide groups, simultaneously being a hydrogen bond donor and acceptor O2 (see Figure 87).

These intermolecular interactions create infinite threads of hydrogen bonds that have lateral connections via the C–H...O bonds (see Figure 89). The distances and angles involved in the hydrogen bonding are given in Table 13. The topological properties at the Acceptor...Hydrogen BCPs compare well with the values from an extensive charge density study with an emphasis on the characterisation of hydrogen bonds by Ranganathan *et al.*^[308] The hydrogen bonds between the hydroxy group and amido groups are relatively strong in both directions. The topological and the structural parameters correlate well with each other. The strongest bond in terms of the electron

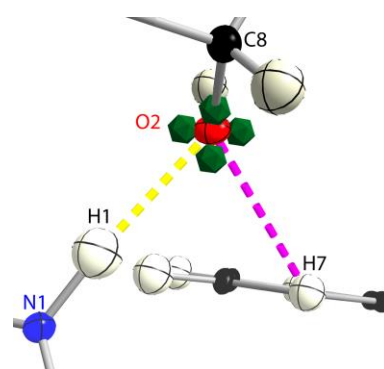


Figure 88. The hydroxy group is the acceptor of two hydrogen bonds. The maxima in the VSCCs are marked as green dodecahedrons. The bonding vectors are displayed in yellow and pink.

Table 13. Distances and angles of the hydrogen bonds in **3**. The topological parameters at the corresponding Acceptor...Hydrogen BCPs are given. They help categorise the strength of the three hydrogen bonds. The hydrogen bonds in **3** are given according to their strength in descending order.

Acceptor...H-Donor	$d(A\cdots H)$ [Å]	$d(A\cdots D)$ [Å]	$\angle(A\cdots H-D)$ [°]	$\rho(\mathbf{r}_{\text{BCP}})$ [$e \text{ \AA}^{-3}$]	$\nabla^2\rho(\mathbf{r}_{\text{BCP}})$ [$e \text{ \AA}^{-5}$]
O1...H2-O2	1.749	2.746	174	0.271	+2.08
O2...H1-N1	1.914	2.966	169	0.199	+0.50
O1...H14-C14	2.259	3.346	148	0.018	+1.11
O2...H7-C7	2.523	3.190	120	0.018	+1.09

density at the BCP also has the shortest distance between the hydrogen and the acceptor atom, and the acceptor...hydrogen-donor angle of this bond is close to 180°, as it is typically reported for strong hydrogen bonds.^[322] Bond paths for all four hydrogen bonds were found in the molecular graph, which is displayed in Figure 85.

A search for critical points in $\nabla^2\rho(\mathbf{r})$ revealed three maxima in VSCCs around the carboxy oxygen atom O1 and *five* maxima in VSCCs around the hydroxy oxygen atom O2. The VSCCs are distributed approximately coplanar with the O1-C1-N1 plane in the case of O1 and the position of the nonbonding VSCCs correlates with the direction of the two hydrogen bonds (see Figure 86).

One of the maxima in the nonbonding VSCCs at the hydroxy oxygen atom O2 is located in the C8-O2-H2 plane and the remaining two are located above and below that plane. The nonbonding VSCCs are not as clearly separated as in the case of O1, which becomes visible from the circular Laplacian isosurface shown in Figure 87. It does not make sense to take the five maxima in the VSCCs around O2 as evidence for the presence of five *Lewis* electron pairs in its valence shell. The nonbonding VSCCs are not oriented directly along the hydrogen bond interatomic vectors. The bonding vectors of the N1-H1...O2 as well as of the C7-H7...O2 hydrogen bond bisect the angles between the VSCCs as shown in Figure 88.

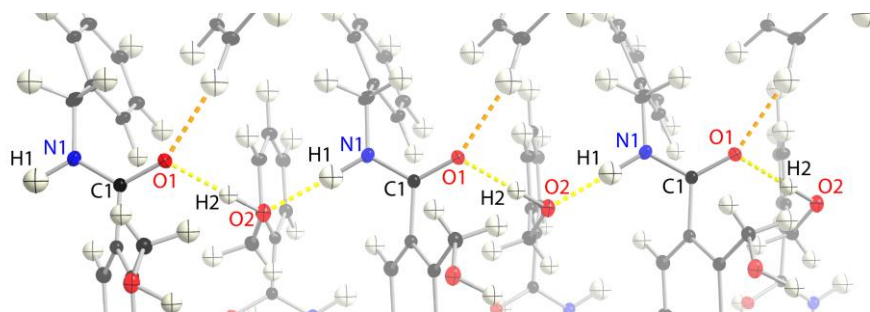


Figure 89. The hydroxy group acts as a bridge between amide groups. The resulting one-dimensional thread is laterally connected to neighbouring molecules by the C-H...O bonds.

5.4. Bond orders from topological parameters

Bader *et al.* were the first to propose a measure for the bond order n solely based on the properties at the bond critical point.^[81] They fitted an exponential function $n = \exp\{A(\rho(\mathbf{r}_{\text{BCP}})-B)\}$ with two parameters A and B to results from theoretical calculations. The parameters are different for each basis set and for each type of bond.

The idea to determine the bond order entirely based on topological parameters of the charge density was picked up by others subsequently.^[323-324] Linear functions with more than two parameters were fitted to results from theoretical calculations by Howard *et al.*^[324] and Tsirelson *et al.*^[323] The latter have shown that the best correlation is given by a fit of $n = a_0 + a_1(\lambda_1 + \lambda_2) + a_2\lambda_3 + a_3\rho(\mathbf{r}_{\text{BCP}})$. The bonds in **3** were examined with this formula. The parameters were taken from Tsirelson *et al.*^[323] According to the results, the C1–O1 bond has a bond order of $n = 1.67$, the C1–N1 bond has a bond order of $n = 1.21$, which both confirms the partial double bond character of the latter and partial single bond character of the former. The C1–C2 bond from the carboxy oxygen atom to the phenyl ring has a bond order of $n = 0.96$, indicating no conjugation between the amide group and the aromatic ring.

5.5. Atomic charges and electrostatic potential

The atomic charges were calculated by integration of $\rho(\mathbf{r})$ along the boundaries of the atomic basins (see section 2.1 on page 19). The atoms in the amide group carry very high unlike charges, O1: $-1.09 e$; C1: $+0.94 e$; N1: $-1.04 e$. This atomic charge distribution is in accordance with the commonly anticipated chemical behaviour of carbonyl groups in general:^[325] the carboxyl carbon atom is subject to nucleophilic attacks and the oxygen atom is subject to electrophilic attacks, which is displayed by the charge accumulation at

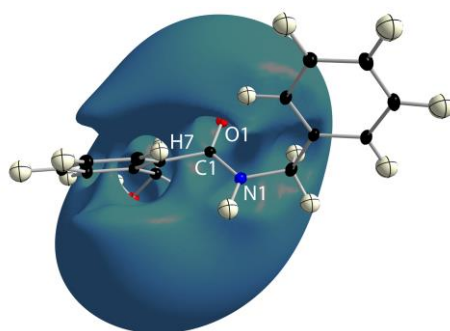


Figure 90. Isosurface of the electrostatic potential at a level of $-0.10 e \text{ \AA}^{-1}$. The surface marks the envelope that repels negatively charged reactants from the carboxyl carbon atom C1.

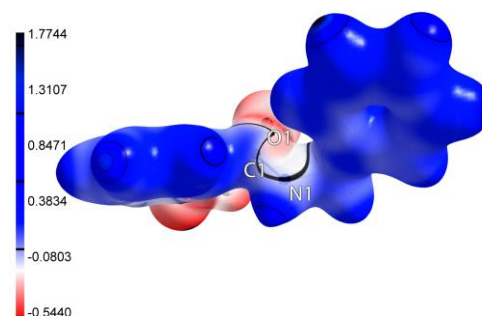


Figure 91. The electrostatic potential mapped on an isosurface of the charge density at $0.20 e \text{ \AA}^{-3}$. The bold black line corresponds to zero electrostatic potential. The legend is in units of $e \text{ \AA}^{-1}$.

the oxygen atom and the charge depletion at the carbon atom.

The trajectory of the nucleophilic reactant in a hydridic reduction can be anticipated to be largely governed by the electrostatic potential (ESP) around the substrate because of the charge of the attacking particle. A three-dimensional grid of the ESP was calculated and isosurfaces were drawn with MoleCoolQt (Figure 90 and Figure 91).^[155] An isosurface of low negative ESP (Figure 90) can be rationalised as the boundary that is unlikely to be crossed by a negatively charged particle. The carboxyl carbon atom C1 is shielded from nucleophilic attacks by this envelope. The shape of the envelope indicates that the carboxy oxygen atom as well as the amide nitrogen atom and the phenyl group contribute to the negative ESP. The only hole that would be accessible by negatively charged reactants is sterically shielded by the phenyl hydrogen atom H7. This prohibits the reduction of the amide although the ESP is positive at points that are close to C1.

The envelope of negative ESP in Figure 90 is presumably caused by the high charge accumulation at the carboxyl and hydroxyl oxygen atoms. A rotation around the C1–C2 bond, which is possible in solution, might in principle cause a significant change of the ESP, thus enabling an opening of the envelope of negative potential and the nucleophilic attack. However, it is likely that the geometry of the molecule would prevent such a rotation because of the steric repulsion between the amide proton H1 and the phenyl *ortho* hydrogen atom H7 or the hydroxymethyl group.

5.6. Conclusion

A rationale for the chemically inert behaviour of the carboxamide **3** has been found based on the electrostatic potential, which effectively prevents a nucleophilic attack by the shielding effect of an envelope of negative ESP around the amide group. The presented rationale might be valid for all derivatives of benzamide because the shielding effect of the ESP coincides with a steric shielding of the reactive site by the *ortho* hydrogen atom of the phenyl ring. Aliphatic carboxamides would thus be more susceptible to the nucleophilic attack of a hydride for two reasons: (a) the volume of negative ESP is not increased by the nearby phenyl group; (b) the steric shielding of the *ortho* substituents of the phenyl ring is not present.

This study further showed that there is no evidence for conjugation between the amide group and the phenyl ring from the QTAIM analysis of the charge density, but the delocalisation of electron density in the amide group is clearly evident.

6. Charge density data collection at a synchrotron source

During the work on this thesis, two periods of time were spent at the beamline 15-ID-B at the Advanced Photon Source (APS) which is part of the Argonne National Laboratory: the first in April 2012, and the second in Juli 2012. The beamline is operated by the *Chemistry and Materials Science Group of the Center for Advanced Radiation Sources (Chem-MatCARS)* at the University of Chicago, Illinois, USA. Dr. *Yu-Sheng Chen* is the beamline scientist.

Our close collaboration with the workgroup of Prof. Dr. *Bo B. Iversen* (Århus, DK) and the Center for Materials Crystallography (CMC) gave us the valuable opportunity to work with very experienced scientific staff. It was the first experience with synchrotron data collection for the present members of our workgroup at that time. We shared beam time with some of the members of *Iversen's* group.

One of the goals was to establish an X-Temp2 device^[133-134] on-site. A specially designed easy-to-disassemble table with space for a bifocal microscope, external light source and for the low-temperature device was commissioned in Göttingen and shipped to the APS together with the low-temperature equipment beforehand. There had been no equipment at beamline 15-ID-B for low-temperature crystal handling before we installed the X-Temp2 device. One of the advantages of the device from Göttingen is its transportability: it can be moved into the experiment hutch easily so that crystal selection, mounting and placement into the cold gas stream on the goniometer were possible without even leaving the stool (see Figure 92).

A number of datasets were collected on different crystals during our beamtime, among them very volatile compounds such as a donor stabilised adduct of 2-thienyllithium,^[326] a phenothiazine-based interpenetrated coordination cage (see section 9.9.2)^[327] or an unpublished indium(I) compound from the workgroup of *J. Overgård*. The data collection on those compounds alone would not have been facile, if

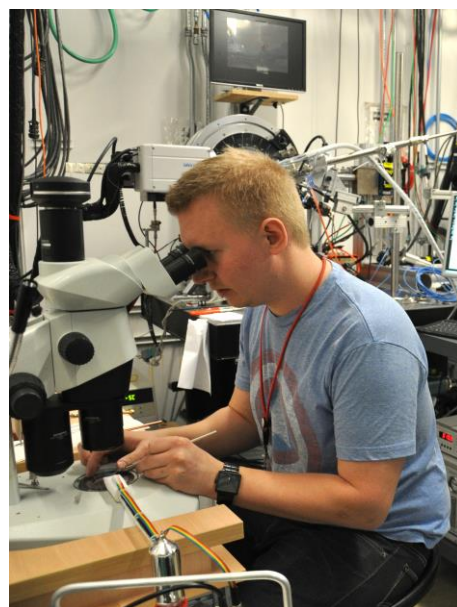


Figure 92. *Mads R. V. Jørgensen* is mounting a crystal using the X-Temp2. The goniometer and the detector can be seen in the background directly behind him.

possible at all, without the low-temperature equipment from Göttingen.

Twelve datasets were collected on crystals brought by our workgroup in April, 2012, and ten datasets were collected in July, 2012. Among them are several datasets of doubtful quality and most of the data have not led to publications. We are currently investigating the reasons for the lack of quality, and some results are presented in the following paragraphs.

6.1. Set-up

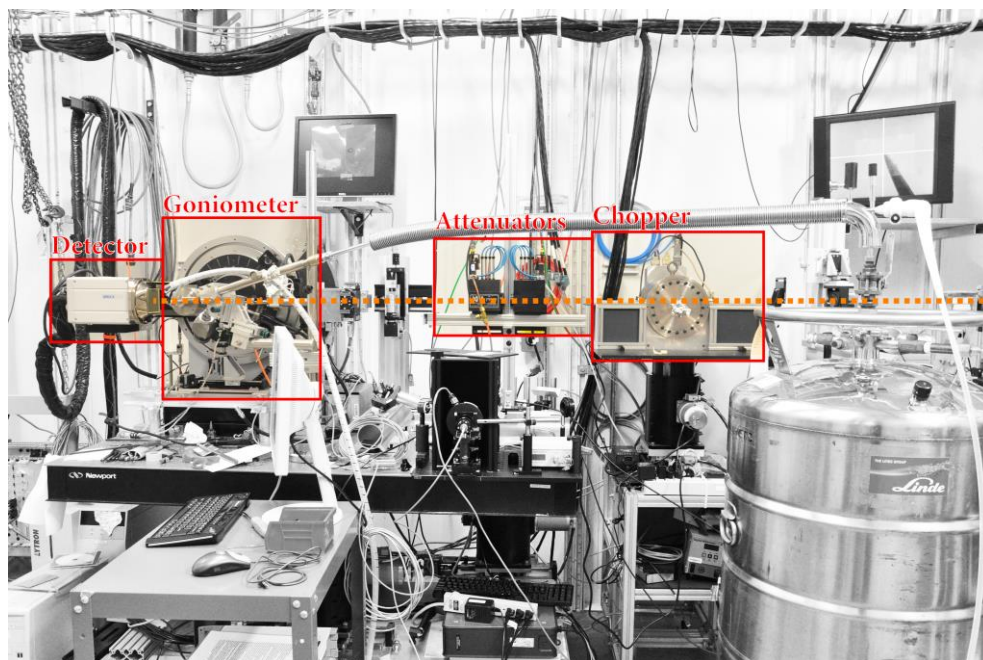


Figure 93. The set-up at beamline 15-ID-B. The vessel in the foreground contains helium for the sample cooling device. The chopper is used for photocrystallographic experiments. It was moved out of the beam path for our experiments. The beam path is marked as an orange dashed line in this figure.

The diffractometer at beamline 15-ID-B is familiar to those who work with equipment from Bruker AXS, and it was designed for the purpose of high-resolution and high-quality charge density data collection. It consists of a stock D8 goniometer, an APEX2 detector and a SMART speed shutter. Open flow helium or nitrogen sample cooling is available and enables sample temperatures between 12 and 400 K. The primary beam is generated by a 3.3 mm undulator in the storage ring. The monochromator for the used wavelength of $\lambda = 0.3936 \text{ \AA}$ is the (311) face of a liquid nitrogen-cooled silicon single crystal. The X-ray photon flux of the generated beam is several orders of magnitude higher than that of a state-of-the-art rotating anode generator, which is why a range of attenuating foils can automatically be inserted into the beam path without entering the experiment hutch if it is desirable to decrease the intensity.

The goniometer, the detector and the speed shutter are controlled *via* the Bruker Instrument Service program (BIS) and the experiment is set up with the APEX2 suite. The attenuators, the primary beam setup (wavelength, position, diameter and other parameters) as well as the radiation safety circles are controlled and observed *via* proprietary software. The experiments are normally set up so that frames for low order reflections are collected with heavy attenuation and exposure times typically ranging between 0.3 and 1.0 seconds per frame; automatic retakes are allowed if overexposure is detected. The detector is positioned at $0^\circ < 2\theta < 15^\circ$ and data are collected using φ scans at multiple ω settings. High order frames are normally collected at $2\theta \approx 30^\circ$ without attenuation and without automatic retakes; exposure times for these frames range between 0.3 and 3.0 seconds. The described practice of high-order data collection results in serious overexposure of the low-order reflections, sometimes even with CCD bleeding that corrupts the intensities of reflections in the vicinity of those areas. Maximum resolutions better than 0.35 Å are practically achievable, a well scattering sample and sufficient beam time for the collection of complete datasets provided.

6.2. The data collections in April and July, 2012

Two datasets are picked that can serve as examples for the discussion of the problems with the collected data. No data were collected on identical samples both in the first and in the second beam time periods, respectively; two datasets of samples from chemically very similar compounds will be compared. The sample from April, 2012, is 9,10-anthracenyl bis(diphenylphosphane sulfide) · toluene **4**; the sample from July, 2012, is the 9-anthracenyldiphenylphosphane sulfide **5**.

The former compound, **5**, had been subject of a study on the refinement of anharmonic motion;^[328-329] a dataset with the highest achievable resolution was the goal with regard to this study, which at the time had not been finished. The compound crystallises in the triclinic space group $P\bar{1}$, which makes data collection very time-consuming even with the high-flux synchrotron radiation.

The latter compound, **4**, crystallises from toluene in the monoclinic space group $P2_1/c$ with two molecules of toluene per molecule of **4** in the lattice; it can also be crystallised from ethyl acetate, yielding solvent-

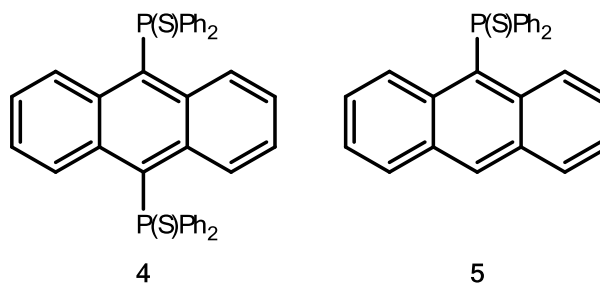


Figure 94. Data were collected on single crystals of these two compounds. The crystals of **5** contain toluene as lattice solvent.

Table 14. The experiments in April and July 2012. The second column for each experiment displays the detector setting and the used maximum resolution for the integration in each run of frames; the third column gives information about exposure time per frame, if constant attenuation was used for the run and if extra attenuated retakes were allowed in the run. The runs emphasised in *italic/bold* are the low order and the additional mid order runs, respectively.

April 2012; Data collection on [4 · 2 toluene]				July 2012; Data collection on 5.			
Run	2 θ /max. int. d	exp./att./retakes	R_{int}	Run	2 θ /max. int. d	exp./att./retakes	R_{int}
1	-30° / 0.40 Å	1.0 s / no / no	0.0712	1	-30° / 0.40 Å	1.0 s / no / no	0.0507
2	-30° / 0.40 Å	2.0 s / no / no	0.0607	2	-10° / 1.20 Å	1.0 s / yes / yes	0.0539
3	-30° / 0.40 Å	2.0 s / no / no	0.0580	3	-10° / 1.20 Å	1.0 s / yes / yes	0.0506
4	-30° / 0.40 Å	2.0 s / no / no	0.0630	4	-10° / 1.20 Å	1.0 s / yes / yes	0.0522
5	-10° / 1.0 Å	0.3 s / yes / yes	0.0840	5	-10° / 1.20 Å	1.5 s / yes / yes	0.0475
6	-10° / 1.0 Å	0.3 s / yes / yes	0.0668	6	-10° / 1.20 Å	1.5 s / yes / yes	0.0495
7	-35° / 0.40 Å	2.5 s / no / no	0.0613	7	-10° / 1.20 Å	1.5 s / yes / yes	0.0427
8	-35° / 0.40 Å	2.5 s / no / no	0.0617	8	-20° / 0.44 Å	0.5 s / no / no	0.0551
9	-30° / 0.40 Å	2.5 s / no / no	0.0729	9	-32° / 0.40 Å	1.0 s / no / no	0.0500
10	-30° / 0.40 Å	2.5 s / no / no	0.0726	10	-32° / 0.40 Å	1.0 s / no / no	0.0492
				11	-32° / 0.40 Å	1.0 s / no / no	0.0498
				12	-32° / 0.40 Å	1.0 s / no / no	0.0593
				13	-20° / 0.44 Å	0.3 s / no / no	0.0649
				14	-32° / 0.40 Å	1.0 s / no / no	0.0507
				15	-10° / 1.20 Å	1.0 s / yes / yes	0.0556
				16	-32° / 0.40 Å	1.0 s / no / no	0.0500
				17	-32° / 0.40 Å	1.0 s / no / no	0.0515
				18	-32° / 0.40 Å	1.0 s / no / no	0.0511
				19	-32° / 0.40 Å	1.0 s / no / no	0.0510

free monoclinic crystals of the polar space group $P2_1$. It can be used as a very sensitive toluene chemosensor;^[330] powder samples show strong solid state fluorescence after contact with toluene vapour, which is quenched in the solvent-free species. This made a comparative charge density study of the toluene-containing and the solvent-free species worthwhile; however, the maximum achievable resolution at the home facilities was too low, and the higher flux was the reason to take samples of both to the synchrotron source. Datasets of both compounds were collected, and the samples were supplied by *N. Finkelmeier* from the *Stalke* workgroup. Only the data from [4 · 2 toluene] and **5** will be exemplarily discussed here.

6.3. Data integration

The first experience with two datasets of **4** and [4 · 2 toluene] were made after April 2012. Data were initially integrated according to the state-of-the-art guidelines in our workgroup (compare paragraph 1.11), SADABS 2012/1 was used for scaling, absorption correction and merging of equivalent reflections. The results seemed quite disastrous concerning charge density refinements, especially given the high effort that had been invested

in the experiments: the data quality was rather low, as indicated by high R_{int} ; the residual densities showed distinct features with concentrations around the heavy atoms and the resolution dependence of the scale factor was unacceptably high for the low angle reflections. These observations were made throughout the experiments for charge density refinement.

The source of these inadequacies was soon sought in the low order runs, and a relatively high number of attenuated retakes was found although an emphasis had been put onto the right choice of the exposure time and attenuation for low and high order frames already in the first period of beam time in April, 2012. As it turned out, a rather high number of overexposures occurred in spite of the efforts made. Based on the gained experience, overexposures were tried to be avoided even more strictly in the second beam time in July, 2012. A comparison of the results of these efforts has not been made up to now.

The small wavelength of $\lambda = 0.3936 \text{ \AA}$ that was used for data collection leads to potentially severe problems if the integrated intensities are not corrected for the angle of incidence of the reflections; see paragraph 1.11. While the phosphor absorption coefficient of stock APEX2 detectors is determined to be 0.9200 for Mo- K_{α} and 1.0 for Cu- K_{α} radiation, the corresponding coefficient is 0.1793 for the APEX2 detector at APS beamline 15-ID-B at the used wavelength. It turned out that the data that is routinely processed at the beamline usually is corrected with the Mo- K_{α} coefficient, which seems to be the default in some Bruker software installations.

Both datasets were integrated in a similar manner:

- Runs were integrated with SAINT 7.68A.
- Those runs with different detector 2θ setting and different attenuator settings were integrated separately with separately refined orientation matrices.
- Active masks were created manually for every 2θ setting; the areas that were obstructed by shadows from the sample cooling device nozzle were excluded from data integration. A large area around the beam stop was severely affected by intense stray scattering in the high order runs and also excluded from integration.
- High order runs were integrated up to a resolution of $d = 0.40 \text{ \AA}$, low order runs were integrated to a resolution of 0.80 \AA .
- Reflections in the low-order runs could well have been integrated up to resolutions better than $d = 0.80 \text{ \AA}$ with R_{int} well below 0.20, but the discrepancy in R_{int} between equivalent reflections in low and high order runs is then very high. The

discrepancy can be made visible best if the data from low and high order runs are examined separately from each other (see Figure 96).

It was to our surprise to see that the low-order data are of inferior quality if the R_{int} and $R_{\text{r.i.m.}}$ values are compared to the high order data. This behaviour is unusual because the highly intense and highly redundant low order reflections are normally not affected by background noise and should show quite satisfying internal agreement. The internal agreement values increase so badly with rising resolution that it would be appropriate to omit low order data beginning at a resolution as low as 1.0 \AA . This, however, is not possible because the completeness of the data from high order data collection is sometimes lower than 50 % in the low resolution shells up to 0.9 \AA , which would create a gap of low redundancy (if not low completeness) in this resolution region.

In addition, a suitable amount of reflections from both high as well as low order runs is needed for the scaling procedure in SADABS in order to work properly. Thus, it has to be aimed at a compromise between data quality and redundancy. The data quality of the high order runs is remarkably good even in spite of the severe overexposure: the SAINT integration program is apparently very efficient in ignoring those reflections and mending the effects of very high background scattering due to the high intensity of the primary beam in high-order runs.

The mentioned “bump” in the progression of R_{int} with the resolution may occur if (a) resolution shells from low order runs with low internal agreement are included or (b) if the redundancy in the overlap regions is very high. The latter effect is discarded if the $R_{\text{r.i.m.}}$ is plotted against the resolution, and it is obvious (Figure 96) that it is indeed the low data quality in the low order runs that causes a “bump” in the low to medium resolution range

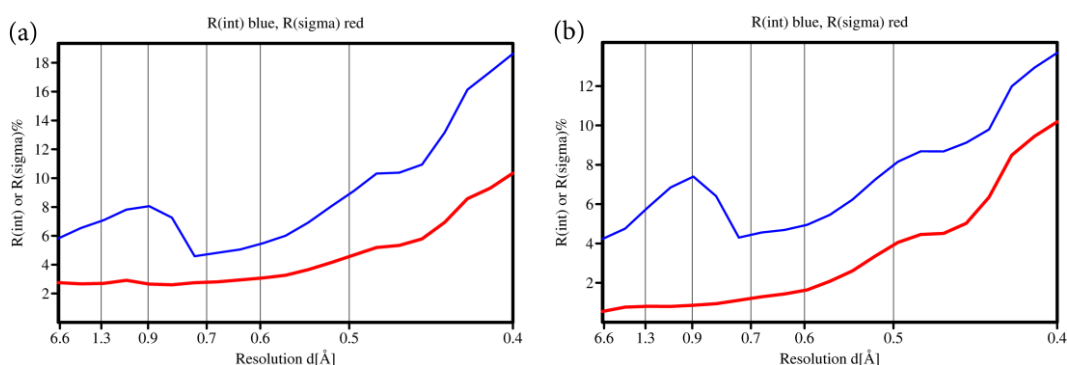


Figure 95. R_{int} against resolution from the diagnostic SADABS plots. (a) data from [4·2 toluene]; (b) data from 5. It is typical to have a temporary increase in R_{int} in the region of high multiplicity where data are merged that were collected in high order as well as in low order runs. The increase in R_{int} is independent of the multiplicity of reflections in this case.

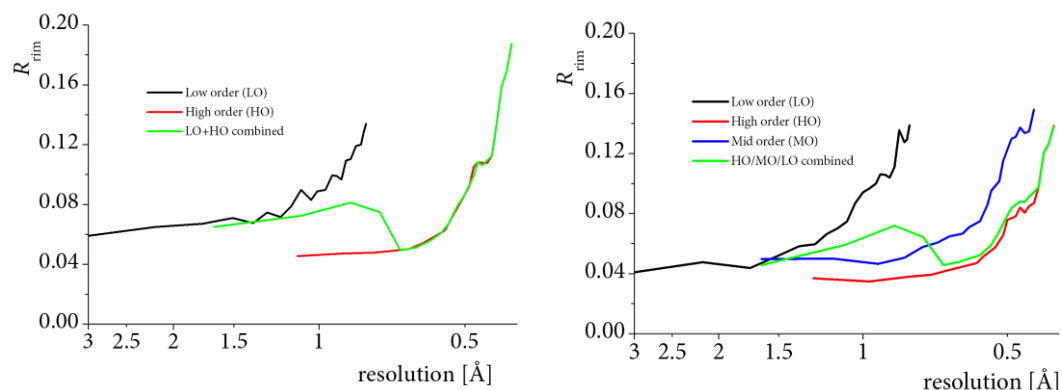


Figure 96. Left: separate representation of $R_{r.i.m.}$ from the low/high order runs against resolution of data from $[5 \cdot 2 \text{ toluene}]$; right: corresponding data from **6**. Additional “mid-order” (MO) runs were collected for **6**. Both datasets were treated exactly alike except that the MO runs were integrated to a maximum resolution of 0.44 \AA instead of 0.40 \AA .

in this case. It was thus tried which effect it would have to omit a part of the low-order reflections by applying a more conservative cut-off in the maximum resolution for raw data integration in SAINT.

In July, 2012, two additional “mid order” runs with shorter exposure time and slightly lower detector 2θ setting were collected to close the gap between low and high order data collection (blue graph in Figure 96, right). This enables a much more restrictive cut-off value for the integration of low-order data without losing too much overlap between the different runs; 1.2 \AA was chosen as maximum resolution, which effectively discards the majority of recorded reflections in the low order runs. The result is displayed in Figure 96.

It is obviously not possible to cure the deficiency in the low resolution reflections by applying this very restrictive resolution cut-off, but the graph of $R_{r.i.m.}$ against resolution is closer to a monotonic increase. The overlap between high and low order batches is unfortunately small if no mid-order runs are collected.

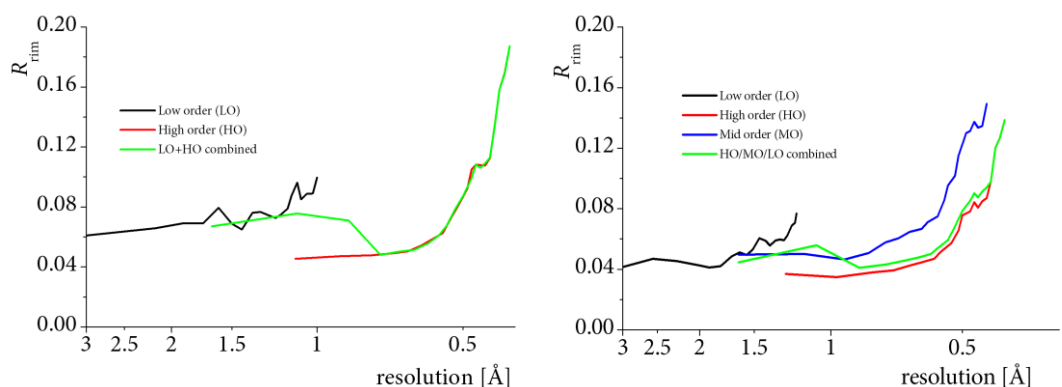


Figure 97. $R_{r.i.m.}$ against resolution for the dataset from $[4 \cdot 2 \text{ toluene}]$ (left) and from **5** (right) after decreasing the maximum resolution of the low order reflections.

6.4. Merging of the data

For the datasets acquired at the synchrotron, the data treatment recommendations from the Danish group around *Bo B. Iversen* were followed.^[27] The recommended procedure includes SADABS for frame-to-frame scaling and absorption correction. The *g*-value is set to zero and the *k*-value has to be eliminated subsequently (see paragraph 1.4 for details). SORTAV is then used for merging equivalent reflections; the option “discard reflections with number of observations < 3” was used.

The latter option generally leads to a slight decrease in overall redundancy because the option affects unique reflections and does not take into account symmetry equivalents; it does not decrease the completeness, which does take into account symmetry equivalents, because the average multiplicity was high enough to ensure that the minimum number of observations was at least three for most reflections. The decrease is so small that it does not affect the redundancy in the output of XPREP.

6.5. Refinement and results

The starting models for XD2006 refinement were taken from a standard SHELXL refinement against those datasets that were processed with a restrictive low-order integration cut-off (0.8 Å for [4 · 2 toluene] and 1.2 Å for 5). The input and master files were initially set up with XDINI, and the automated InvariomTool^[331] and the MoleCoolQt GUI^[155] were used for starting values for the monopole and multipole populations.

The InvariomTool has been designed for cases where structure refinements with aspherical scattering factors are desired and no high resolution data is available, e. g. in macromolecular crystallography.^[319,332-333] It uses a database with a large number of sets of precalculated *Hansen/Coppens* multipole populations and fits an adequate set from the database model parameters to the atomic positions that were determined in an independent atom model refinement. The decision about which set is applied to an atom is based on the chemical environment of the respective atoms, which includes second next neighbouring atoms; it may include atoms that are even further away in delocalised systems such as phenyl rings.^[333]

Other existing databases such as ELMAM^[47-48] or ELMAM2^[334] consist of parameter sets from experiments; the parameters in the invariom database are derived from quantum-chemical calculations. This has several advantages; as *Dittrich et al.* mentioned, the current database would have to be twice as large to be close to complete for purely organic molecules only (third-row elements such as Si, P, S, Cl not included)^[333] New model compounds can be calculated in a short period of time with the theory-derived approach,

which is impossible with an experimental database. This is possibly the biggest advantage, but the lack of experimental error and bias from hydrogen bonds and intermolecular non-covalent interactions in the invarioms is an additional strength of the approach.

The procedure has the comfortable side effect that the time consuming manual set-up of local coordinate systems and of the local symmetry is largely done by the program as well.

All refinements were carried out with the standard settings of XD2006; the spherical scattering factors are taken from the Sue/Coppens/Macchi (SCM) databank,^[146-147] parameter refinement was carried out against F^2 , experimental weights (i. e. no adjusted weighting scheme) were used. The correction factors for anomalous dispersion at the used wavelength are not included in XD2006; they were taken from the XDISP plugin in the WinGX^[335] suite of programs.

After an initial refinement of the scale factor, the atomic positions and U_{ij} were refined. All multipole parameters, atomic positions and U_{ij} were refined simultaneously afterwards. In the subsequent stages, κ and κ' were refined separately, and all parameters including κ and κ' were refined in the last stage. Compared to the refinements in chapters 3 and 0, it is possible to refine more parameters simultaneously in early refinement stages because the starting values for the population parameters from the InvariomTool are already very close to the final values and convergence is thus easier to achieve.

The κ' values are very sensitive parameters, and they should principally not deviate from unity too much.^[42] A range from 0.75 to 1.25 is typical;^[42] based on our experience, numbers outside this range should be considered as problem indicators. The κ' values of the sulfur atoms were refined to 2.00 the case of [4 · 2 toluene] while all others remained at more sensible numbers. The use of adjusted radial functions with altered n_l (see paragraph 1.6) using several sets according to our experience and the recommendations from *Zhurov et al.*^[54] concerning ideal n_l values did not prevent the behaviour of κ' . The refinement of the model of **5** gave acceptable values for κ and κ' , but both refinements did not reach the convergence criterion of a maximum shift of 10^{-5} times the standard uncertainty. See Table 15 and Table 16 for the best results of the XD2006 multipole refinement.

Table 15. Unit cell data and results from XD2006 refinement of [4 · 2 toluene].

Structure code	SPAnPSmit	Z	2
Empirical formula	C ₅₂ H ₄₄ P ₂ S ₂	Crystal dimensions [mm ³]	0.07 x 0.04 x 0.03
Formula weight [g mol ⁻¹]	1225.91	$\rho_{\text{calc.}}$ [g cm ⁻³]	1.286
Sample temperature [K]	15(2)	μ [mm ⁻¹]	0.244
Wavelength [Å]	0.3936	<i>F</i> (000)	836
Crystal system	Monoclinic	θ range [°]	1.72 – 29.45 (0.40 Å)
Space group	<i>P</i> 2 ₁ / <i>n</i>	Reflections collected	249609
Unit cell dimensions [Å]		Unique reflections	33242
	a = 10.693(2)	<i>R</i> _{int} / <i>R</i> _{σ}	0.0676/0.0381
	b = 14.792(2)	Completeness to θ_{max}	99.2 %
	c = 13.365(2)	data/parameter	32.7
	α = 90 °	GoF	1.2649
	β = 103.76(2)	<i>R</i> 1	0.0220
	γ = 90 °	w <i>R</i> 2	0.0457
Volume [Å ³]	2053.2(6)	max. diff. peak/hole [e Å ⁻³]	0.612/−0.570
Extinction coefficient	-	Absolute structure parameter	-

Table 16. Unit cell data and results from XD2006 refinement of 5.

Structure code	SPAnH	Z	2
Empirical formula	C ₅₂ H ₃₈ P ₂ S ₂	Crystal dimensions [mm ³]	0.10 x 0.05 x 0.05
Formula weight [g mol ⁻¹]	1225.91	$\rho_{\text{calc.}}$ [g cm ⁻³]	1.342
Sample temperature [K]	15(2)	μ [mm ⁻¹]	0.257
Wavelength [Å]	0.3936	<i>F</i> (000)	824
Crystal system	Triclinic	θ range [°]	1.11 – 31.21 (0.38 Å)
Space group	<i>P</i> $\bar{1}$	Reflections collected	638121
Unit cell dimensions [Å]		Unique reflections	62516
	a = 10.198(2)	<i>R</i> _{int} / <i>R</i> _{σ}	0.0527/0.0262
	b = 12.259(2)	Completeness to θ_{max}	97.7 %
	c = 17.299(3)	data/parameter	35.4
	α = 101.60(2) °	GoF	0.9092
	β = 91.31(2) °	<i>R</i> 1	0.0174
	γ = 112.02(3) °	w <i>R</i> 2	0.0350
Volume [Å ³]	1952.3(7)	max. diff. peak/hole [e Å ⁻³]	0.493/−0.261
Extinction coefficient	-	Absolute structure parameter	-

Much more eye-catching than the differences in the refined parameters is the difference in the plots of $\sum F_{\text{obs}}^2 / \sum F_{\text{calc}}^2$ between the datasets from April and July (see Figure 98 to Figure 101): the deviations of the low order data have exactly opposite trends. While the observed intensities are underestimated in the former, they are overestimated in the latter. The mid and high order data seem unaffected by such trends.

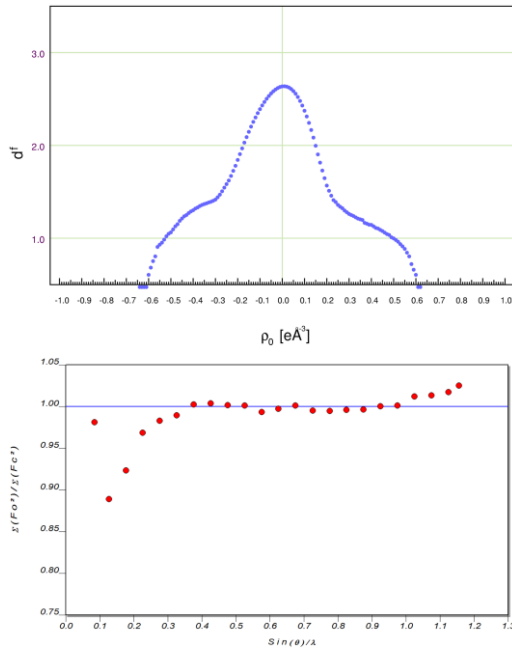


Figure 98. Refinement results from refinement against data from [4·2 toluene]; merged with SORTAV. Top: fractal dimension of the residual density; bottom: resolution dependence of the scale factor.

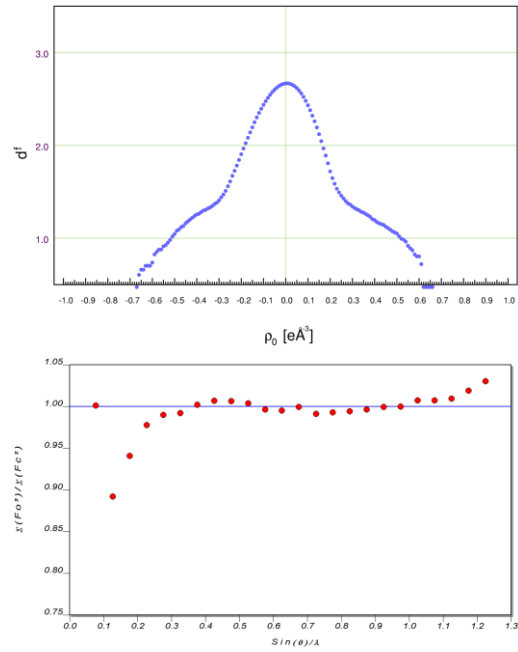


Figure 99. Refinement results from refinement against data from [4·2 toluene]; merged with SADABS. Top: fractal dimension of the residual density; bottom: resolution dependence of the scale factor.

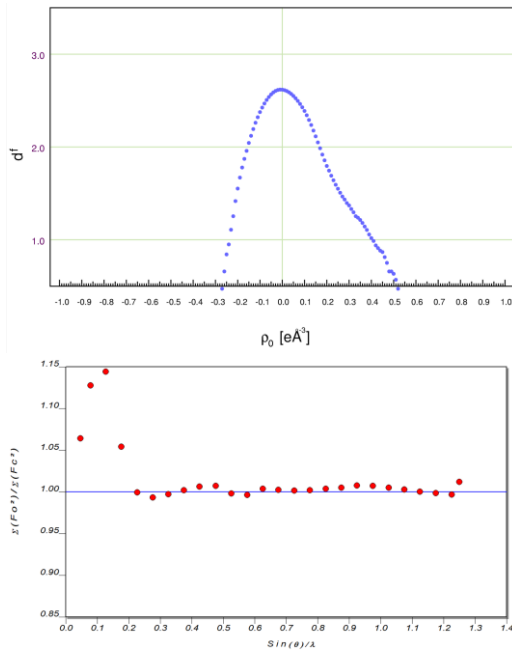


Figure 100. Refinement results against data from 5. Data were merged in SORTAV. Top: fractal dimension of the residual density; bottom: resolution dependence of the scale factor.

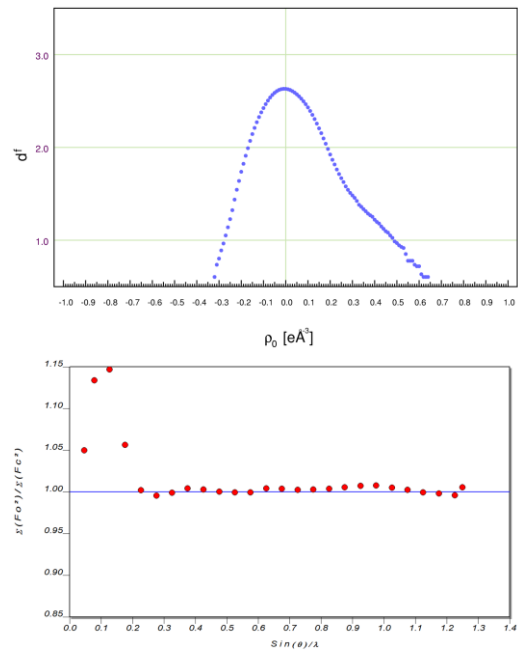


Figure 101. Refinement results against data from 5. Data were merged in SADABS. Top: fractal dimension of the residual density; bottom: resolution dependence of the scale factor.

The dubious internal agreement factor, the structured high residual density (see Figure 98 to Figure 101) after the refinement of the model and the instability of the refinement in connection with improbably high refined κ' values raise doubts in the validity of the data, which is the reason why no QTAIM analysis was carried out on the obtained models.

6.6. About possible sources of error

The two datasets collected at the Advanced Photon Source beamline 15-ID-B are representative for all charge density datasets that have been collected by our workgroup at this synchrotron beamline, which is why a detailed analysis of the possible sources of error is of major interest. We are putting substantial efforts into these investigations in collaboration with the workgroup of Prof. Dr. *Bo B. Iversen* (Århus, DK). Some tentative conclusions about the possible sources of error can already be made at this point.

It is obvious that there are severe problems with the data in the low order reflections.

At the time when the results from the first beam time in April 2012 were first evaluated, the resolution dependence of the scale factor clearly showed that the integrated intensities of the low order reflections were underestimated while the intensities of the high order reflections could very precisely be reproduced by the refined model. The systematic deviation in the integrated intensities of the strong and for charge density studies eminently important low order reflections was at first sight attributed to the large number of attenuated retakes collected in the low order runs. The fact that deviations only occur in those θ ranges that are most strongly affected by attenuated retakes hinted towards a correlation with the retakes. As mentioned in paragraph 1.11, the attenuation factor has to be determined very accurately. It may additionally be that the attenuation factor is dependent on the wavelength, and it is not clear whether the used attenuation factor was accurate for the used wavelength.

Thus, great care was taken to avoid excessive overexposure and attenuation in the data collections of the second beam time. However, it turned out that the overall rather successful avoidance of overexposure in the second beam time in July 2012 has not cured the problems with low order reflections. The plot of the scale factor *versus* resolution now shows a deviation to values *larger* than one for the low order reflections.

Although a deteriorating influence of attenuated frames still cannot be completely excluded from the list of possible errors, our attention was led to another possibility: the used exposure times that go down to 0.3 seconds are short enough for a small fluctuation in the actual exposure time to cause significant deviations in the integrated intensities even if those fluctuations are only on the millisecond scale. Such fluctuations are caused by inac-

curate shutter times. Therefore, the requested and the actual exposure time are reported in the raw data frames.

The Bruker command line tool “SUMMARY” with the keyword “ELAPSDA” was used, which delivers the actual exposure time of every frame. When the frames of the corresponding datasets were inspected, no deviation between the requested and the actual exposure times was observed at all. This was also observed in a random sample of 15 datasets from the Bruker diffractometers in our group. Bruker Support confirmed this behaviour and stated that a measured exposure time is only reported in cases where the actual exposure time is less than the requested time.^[336]

Contrary to that statement, in a dataset that was acquired with the APEX2 Mo I μ S diffractometer and a correlated exposure time of 45 seconds (resulting in two frames of 22.5 seconds exposure time), a positive deviation from 22.5 seconds in actual exposure time was reported by the shutter. An analysis gave a mean actual exposure time of 22.526(7) seconds, which gives an average difference between requested and actual exposure time of 0.026 seconds. The magnitude of this error is essential to know, especially for short exposures. The shutter used in the data collection at beamline 15 ID-B is not identical with the one in the APEX2 Mo I μ S diffractometer. However, if the average error was transferrable between different shutters, the shortest possible exposure time of 0.3 seconds would be increased by almost 9 % if the average timing error of the shutter can be estimated to be constant for every exposure time. It is obvious that such a deviation leads to severe problems with data scaling if it is not reported and corrected for.

Bruker Support brought up another issue when the question was answered regarding how the synchronisation of the shutter and the goniometer motors works:^[336] The exposure is timed so that the shutter is half open and the goniometer is at working speed at the start position of the requested frame. This means that the goniometer motor revs up to the required speed starting at a certain position before the acquisition of the frame and the shutter then opens in time. At the end of the exposure, the shutter closes so that it is half closed when the goniometer is at its end position. Bruker staff have measured the shutter open and close times which are needed to facilitate such an exact

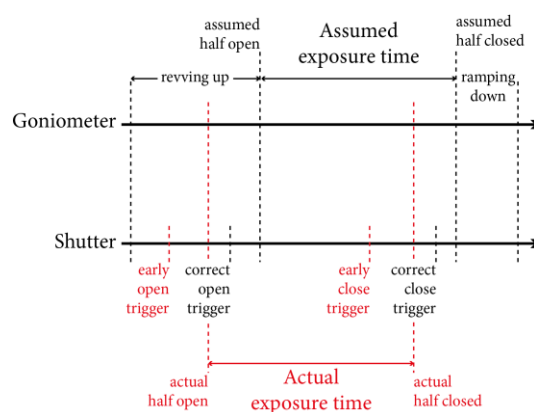


Figure 102. Schematic explanation of the error that emerges from incorrect shutter delay timings.

timing.^[336] The timing parameters were disclosed to us by the Bruker Support staff (Table 17). Some machines were purportedly installed with wrong timing parameters, among them all three machines in our workgroup, as it turned out.

The Bruker *APEX2 Ultra* with Turbo X-ray Source (TXS) in our workgroup is equipped with a “Bruker Rotary Shutter (NEW),” and the machine is configured with values of $OPENDELAY = 0.02$ and $CLOSEDELAY = 0.02$. These parameters are extractable from the file “DE-

Table 17. Half-opening and half-closing times for different shutters in Bruker diffractometers.

“Nonius”	$OPENDELAY = 0.0050$ s
	$CLOSEDELAY = 0.0066$ s
“Bruker Rotary Shutter (OLD)”	$OPENDELAY = 0.0160$ s
	$CLOSEDELAY = 0.0057$ s
“Bruker Rotary Shutter (NEW)”	$OPENDELAY = 0.0120$ s
	$CLOSEDELAY = 0.0043$ s

VICE.INI” in the file system of the D8 control computer in the diffractometer. These values are larger than the actual delay times of the shutter (see Table 17), which causes the controller to trigger the shutter too early (Figure 102). This error affects both the opening and closing timing, but it does not equal out since the opening and the closing delay are not equal. The exposure time is thus decreased by the difference between opening and closing delay. In the case of this particular shutter, the closing delay is shorter than the opening delay and the difference is 7.7 ms, thus shortening the actual exposure time compared to the requested exposure time. This corresponds to an error in the order of magnitude of 1/100 for typical low-order correlated exposures of one or two seconds.

In addition, the early shutter opening causes the exposure to begin when the diffractometer motor may not have reached the operating speed required for the exposure. The implications of this effect, however, are very hard to determine.

6.7. Conclusion and outlook

The on-site conditions at beamline 15 ID-B are very well suited to the experimental needs of the *Stalke* workgroup: a fully equipped chemistry lab is available which has been successfully used by *Markus Granitzka* to synthesise very volatile lithium organic compounds.^[326] Furthermore, the low temperature sample manipulation system X-TEMP2 was shipped to the site and has been successfully used. The conditions would ultimately have to be considered perfect if the last step to low order data quality improvement can be made.

Our investigations and the extensive correspondence with the *Iversen* workgroup have shown already at this point that the flaws in the low order data are not deducible to a single cause. So far the most serious problem seems to be caused by the extremely high photon flux from the undulator of the beamline. The high intensity makes the very high

achievable resolution of the diffraction experiments possible in the first place and very short wavelengths like the one used in our experiments (0.3936 Å) prevent heavy X-ray absorption in the sample and facilitate the collection of the whole desired resolution range in one detector position (compare the Ewald construction of diffraction: Figure 1 on page 2). The dynamic range of the used APEX2 CCD detector is unfortunately too low to cope with the enormous intensity differences of the reflections occurring in one frame, effectively preventing the simultaneous collection of reflections of all desired resolutions. This effect is well known from our in-house data collections as well and specially designed data collection strategies prevent this problem by using different detector positions and exposure times for each resolution shell.

This workaround works well with Mo-K α X-ray sources and was applied in the second beamtime by adding mid order runs to the standard low and high order data collections, leading to an improvement in data quality because more data from the poor-quality low order runs could be omitted. However, the adaption of this approach is less facile for the short wavelength of 0.3936 Å because the resolution shells cannot be separated by changing the detector 2θ position. The ultimate problem of poor quality low order data is not solved by these changes in data collection strategy.

Provided that sufficient beamtime is available for a machine study, a detailed investigation should concentrate on the impact of different exposure times on data quality, preferably with the primary beam intensity adjusted for each setting in a way that approximately the same integrated intensity is diffracted for each exposure time in order to keep crucial parameters like the background and the maximum resolution constant. A comparison of the results should give the answer to the question if it is the short exposure time that causes the poor data quality, but even then the exact reason would remain unclear. An inaccuracy in the mutual synchronisation of shutter and goniometer step motor, shutter jitter or inaccurate phi motor control are possible reasons to investigate.

The influence of alterations in hardware binning (see section 1.11) ought to be investigated as well. The 8 x 8 binning mode in which the experiments have been carried out has been designed to increase the per-pixel intensity, which is very profitable for in-house diffractometers and comparatively weak X-ray sources which create the need to count as many diffracted photons as possible. A finer binning, say 4 x 4 or even 2 x 2, would lead to significantly higher amounts of data to be processed and the overhead time for the detector readout would be slightly increased. The dynamic range of the detector would effectively be increased because the logical pixels are smaller, collecting less photons and thus the readout registers are not as easily saturated. The least-squares reflection fitting for weak

reflections would also benefit from a finer pixel grid for a more precise interpolation of the profiles, especially given the very sharp reflections from the used high-quality crystals in connection with the very monochromatic and non-divergent beam from the X-ray optics.

7. Low-energy contamination in focused X-rays

As mentioned in section 1.11, it has been published by *Storm et al.* 2004 in a technical paper^[63] and recently brought to the attention of a larger public by *Macchi et al.*^[64] that the radiation from the nowadays widely used focusing silicon mirror X-ray optics^[337] is contaminated by significant amounts of low energetic radiation with a spectral maximum at approximately three times the nominal X-ray wavelength. *Macchi et al.* stated in their paper that the peak maximum of the radiation is in the remarkable order of 0.5 % of strong low-order reflection intensities.

7.1. Design of a filter insert

We were interested in reproducing the findings of *Macchi et al.* because all of the diffractometers in our workgroup have focusing mirror optics in their beam paths. The reported amount of energy contamination seemed alarming to us, and large samples that consist only of light elements make up the majority of the charge density samples in our workgroup, are presumably most affected by the effect of the spectral impurities because of their very intense low-order reflections.^[64]

A filter insert was designed for the beam path of the Bruker Turbo X-Ray Source (TXS) in our workgroup. The technical drawing can be found in the appendix (section 10.10). The filter insert allows the insertion of filter foils without having to power down the X-ray generator. The insert has an inlet that enables continuous purging of the component with pressurised air in order to avoid the formation of ozone that might damage the metal surfaces. An accidental exposure to X-rays is impossible because the filter insert is behind the main shutter of the source, which is prohibited from opening as long as the doors of the cabinet are not shut. It is possible to insert filter foils of materials *ad libitum* as long as the material allows to be pressed into discs between 6.0 and 7.0 mm diameter.

The length of the filter insert is chosen so that the distance of the X-ray Source to the sample is slightly (*ca.* 3 cm) longer than the focusing distance of the X-ray optics. This *off-focus* alignment of the diffractometer has been best practice in our workgroup because the beam diameter is increased, which facilitates full sample illumination rather than in the *in-focus* alignment. The *off-focus* configuration has recently been changed to an *in-focus* configuration in favour of higher X-ray photon flux density at the sample position, which is advantageous for very small samples. The filter insert has thus been temporarily decommissioned, but it would be very easy to manufacture a shortened filter insert for an *in-focus* alignment of the diffractometer. If a new filter insert were to be crafted, the pres-

surised air inlet could probably be omitted because the intensity of the radiation behind the optics is not sufficient to create ozone that might damage the filter foil.

7.2. A survey on existing datasets

All recent charge density studies from our workgroup from in-house measurements are based on data that were collected with the TXS using X-ray mirror optics, which means that every dataset should be affected by the contamination in the X-ray spectrum to some extent. A sample of existing charge density studies from our group was examined to get an impression of how seriously different datasets are affected. The dataset of **3** is used as an example because it fulfils the tentative preconditions for severe contamination of the measured intensities by low-energy contamination: it consists of light elements, was collected on a large crystal and little systematic absences are present. The latter condition ensures that a high number of reflections are considered in the statistics.

The APEX2 software^[136] has a plugin that creates precession images from the acquired frames. This was used to create cuts through planes in the reciprocal lattice as shown in Figure 103 (a) to (c). Additional information is obtained from these plots compared to those that can be obtained from *hkl* reflection files in programs like XPREP^[139] because not only the integrated intensity of the reflections (*hkl*) can be displayed but also intensity between reflections.

Macchi et al.^[64] examined the systematic absence violations that are due to the low-energy contamination. In order to be able to gain a more detailed view on the impact of the low energy contamination on the data, the program XDWTAN from the XD2006 suite was used. This program is based on the program WTANAL^[338] and was written to analyse the weighting scheme. It gives very detailed lists of discrepant reflections, amongst them analyses of the dependency of the discrepancy from the magnitude of F_{obs} , from $\sin(\theta)/\lambda$ or as a function of the *Miller* indices. The latter is very helpful to visualise the impact of the low-energy contamination. The diagram in Figure 103 (d) was created from the analysis of XDWTAN. Diagrams from more datasets are displayed in the appendix (section 10.11).

The analysis clearly shows the impact of the low-energy contamination. Most of the intensities of reflections with $(h,k,l) = (3x,3y,3z)$ (with x,y,z being integer numbers) show significant deviations from the corresponding calculated intensities. The wavelength of the contamination is thus approximately three times the Mo- K_{α} wavelength, as reported by *Macchi et al.*^[64] The magnitude of the impact that becomes visible from the diagrams in Figure 105 is striking. XDWTAN lists reflection statistics for all reflections where *one* of

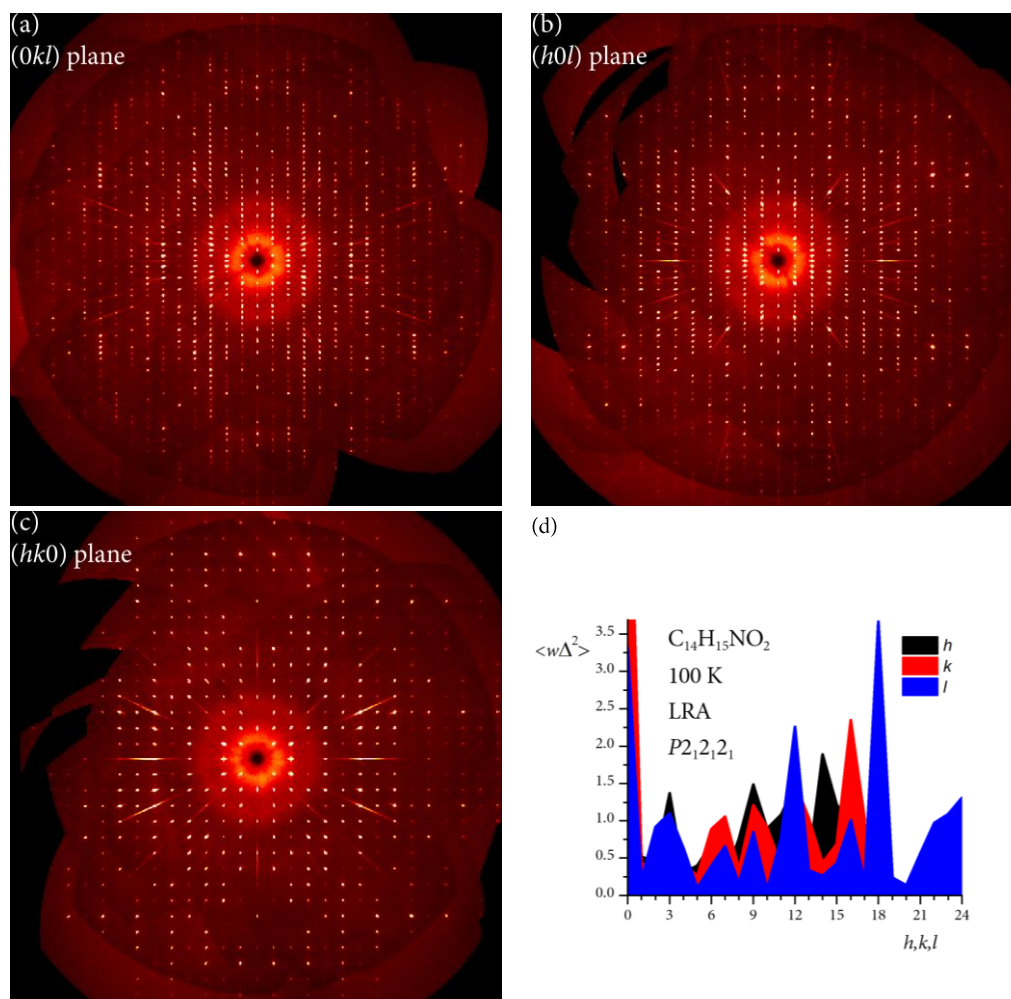


Figure 103. (a), (b), (c) Software reconstructed precession plots of planes through the origin of the reciprocal lattice of the sample of **3**. (d) Diagram of the dependence of $w(F_{obs}^2 - F_{calc}^2)^2$ on the Miller indices. Note that the weighting factor w serves as normalisation factor because it contains the e.s.d. of the intensity as divisor. A close to perfect dataset would thus yield a distribution in a narrow margin around $\langle w\Delta^2 \rangle$ of one.

the Miller indices is equal to a given number. The deviation of those intensities of reflections where *all* indices (hkl) are multiples of three should be even larger.

Contrary to what was expected, not only light atom structures are affected by the low-energy contamination. There is not a single dataset in the sample where the effect is negligible, and the samples include compounds of transition metals or of heavy main group elements as well as organic light atom structures. The only exceptions in the sample that do not show systematically increased deviations due to the low-energy contamination are the dataset that was collected on **1** with an Al/Zr filter (see next section) and one dataset that was collected at a synchrotron on [**4** · 2 toluene] (see chapter 6).

7.3. Comparison of data collected with and without filter

Table 18. Figures of merit and residuals from the refinements against data collected with/without filter foils.

	without filter	with filter
Max. resolution [\AA]	0.44	0.44
R_{int}	0.0324	0.0265
$R_{\text{r.i.m.}}$	0.0332	0.0273
Av. Redundancy	10.46	11.88
Completeness	99.9 %	99.8 %
Highest/Lowest residual density [e \AA^{-3}]	0.126/ -0.164	0.095/ -0.098
Final R_1/wR_2	0.0183/0.0422	0.0159/0.0321
Data/Parameter	26.56	26.16
Weighted goodness-of-fit	1.629	1.173
Weighting Scheme (a/b)	0.014/0.004	0.01/0.007
Fractal dimension $d^f(0)$	2.64	2.64

Compound **1**, consisting of light elements only, was a good object of study for the effect of the low-energy contamination. Two datasets were collected on the sample of **1**. One dataset without any filter foil and one dataset with a filter disc made of two layers of 50 μm aluminium and one layer of 25 μm zirconium foil. *Macchi et al.*^[64] suggested using an aluminium foil of approximately 100 μm thickness, but we chose to add zirconium because of its larger absorption coefficient for higher energies up to close to the energy of Mo- K_{α} . The dataset

with filter foil is the one used for the refinement in chapter 3.

Plots through the origin of the reciprocal lattice from the APEX2 suite^[136] are displayed in Figure 104 (page 127). These plots give an impression of the amount of contamination by mere visual inspection.

There are clearly streaks present in the plots from the data collection without filter, although they seem not as pronounced as those in the data from **3** or those in the paper of *Macchi et al.*^[64] The difference between the datasets that were collected with and without filter is nonetheless visible.

Refinements against the obtained data were carried out in order to be able to judge about the impact of the low energy contamination apart from the optically obvious streaks in the diffraction pattern. Both datasets were processed in the same way; the integration of the reflections was carried out with SAINT 7.68a,^[339] absorption correction, scaling and data merging for XD2006 was done with SADABS 2008/2.^[23] Data statistics were calculated using XPREP 2013/1.^[139]

It has to be noted that the two datasets were not collected on the same sample, only on the same compound. The dataset was collected without filter several weeks before the attention was drawn to the effect of the low-energy contamination. The data collection with filter foil was carried out subsequently. Different crystals had to be used for the two data

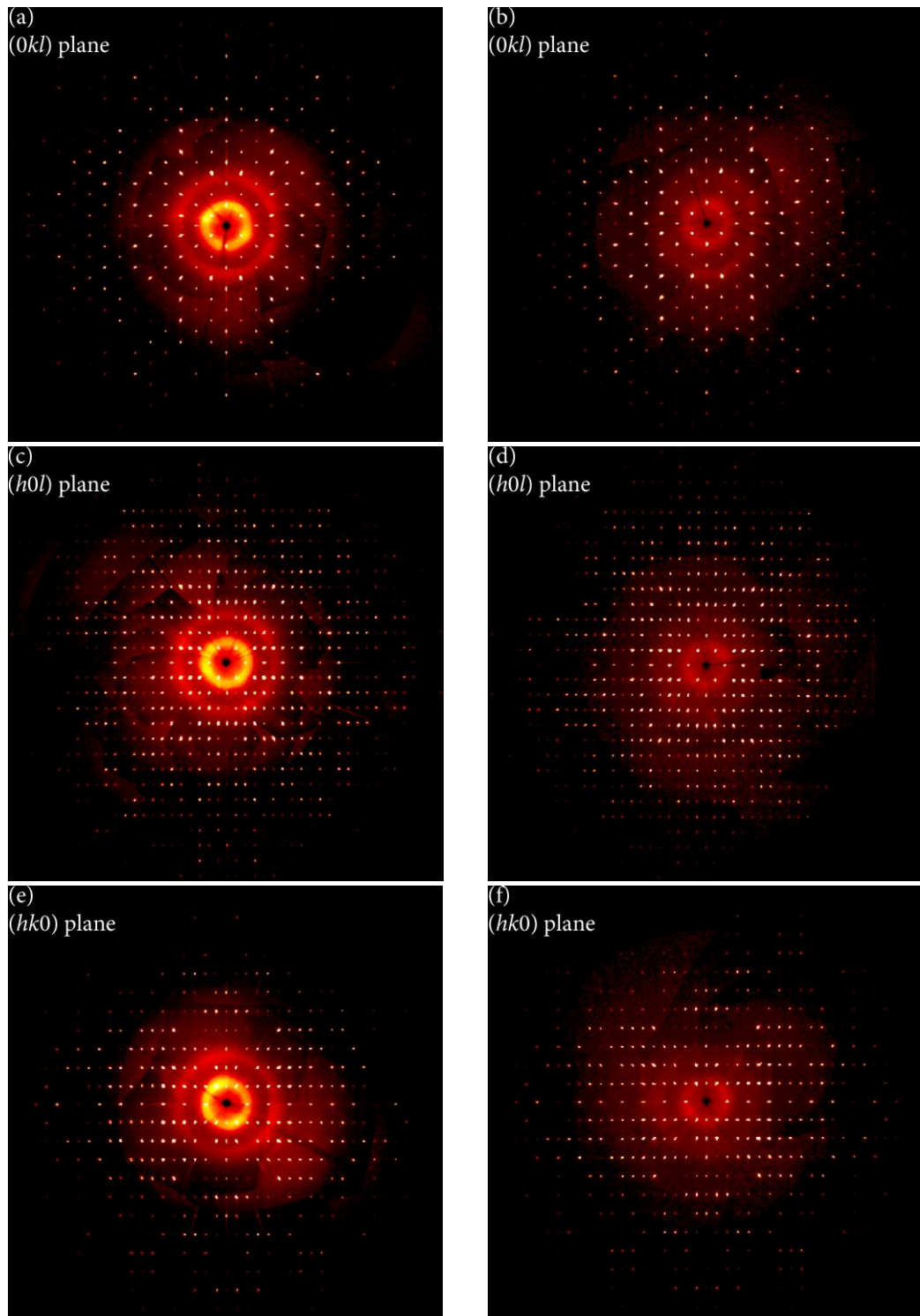


Figure 104. Software reconstructed precession plots of planes through the origin of the reciprocal lattice. Figures (a), (c), (e) are processed from data collected without filter foil, figures (b), (d), (f) are processed from data collected with filter.

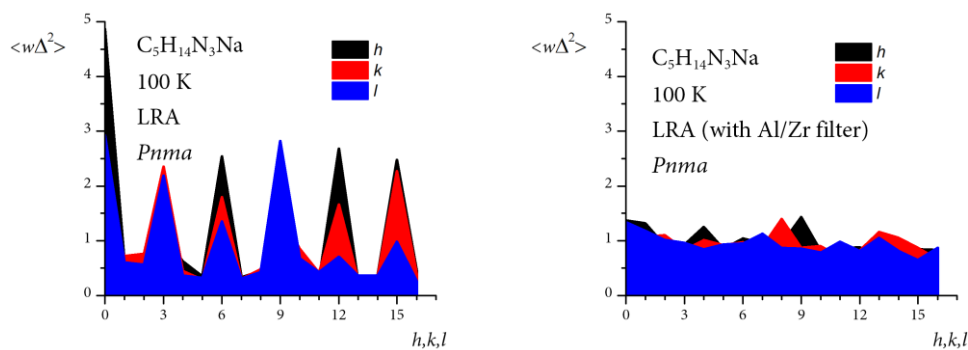


Figure 105. Graphical representation of the mean weighted difference between observed and calculated structure factor as a function of the Miller indices (hkl). Left: analysis of the data collected without filter foil. The deviations of those F_{hkl}^2 with h,k,l being multiples of three are significantly larger than those with other indices. Right: analysis of the data collected with filter foil. The deviations are distributed in a narrower margin and do not show significant outliers.

collections because of the impossibility to store crystals of **1**. The comparability of the datasets is therefore somehow limited.

The subsequent IAM and multipole refinements were carried out in an identical manner for both datasets and ten resolution-dependent scale factors were refined (see chapter 3 for details). Only the weighting schemes were adjusted differently so that the distribution of $w(F_{\text{obs}}^2 - F_{\text{calc}}^2)^2 = w\Delta^2$ was as close to a normal distribution as possible for each of the datasets (compare section 1.9). Some results are displayed in Figure 105. The figures of

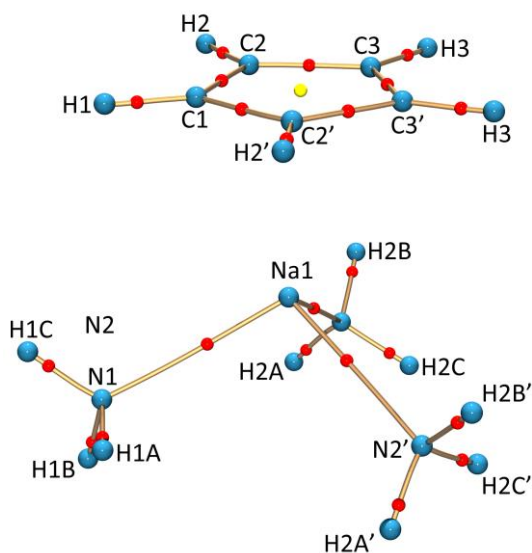


Figure 106. Molecular graph of **1** from the XD2006 refinement against data collected without filter foil. The bond path between Na1 and C1 is missing. It exists in the molecular graph from the refinement against the data from filtered radiation (see chapter 3).

merit and the residual values indicate that the dataset with filter foil facilitates a better fit of the model to the acquired data (Table 18).

The obtained models do not only differ quantitatively from each other. While there is a bond path between Na1 and C1 in the model derived from filtered radiation, this bond path is missing in the model from non-filtered radiation (Figure 106). No bond paths to the remaining carbon atoms are present in both models. An analysis of the absolute deviations between the properties at the BCPs (see Table A 7 in the appendix; page 193) reveals no further qualitative

differences. Laplacian and deformation density contour maps do not indicate significant differences either (see Figure A 3 and Figure A 4 in page 194).

Some preliminary tests were made on the data. The differences between the observed intensities of identical reflections ($3h\ 3k\ 3l$) in the *.fco files from the two XD2006 refinements were set into relation with the intensity of the reflection (hkl):

$$\delta = \frac{F_{\text{contaminated}}^2(3h\ 3k\ 3l) - F_{\text{filtered}}^2(3h\ 3k\ 3l)}{F_{\text{filtered}}^2(hkl)} \quad (\text{Eq. 38})$$

The value δ should be the fraction of the intensity of a contaminated reflection ($3h\ 3k\ 3l$) that is caused by the low-energy reflection (hkl). It should be constant if intensities of identical reflections are proportional to each other at the two different wavelengths.

It turned out that the values of δ scatter in a broad range. There are several very severe outliers at values of $\delta > 5$ if all reflections are considered. If the mean value for δ is calculated, it is strongly biased towards these outliers. The very large values emerge if the reflection (hkl) has a very small intensity and the difference between the intensities of the ($3h\ 3k\ 3l$) reflections is relatively large. The median value of the distribution probably gives a more realistic picture. Statistical figures (based on 214 reflections): mean: $\delta = 0.191$; e.s.d. of the mean: 1.61; median: 0.0065. The median value is close to the value *Macchi et al.* had estimated.^[64]

The cases with very large δ , however, cannot be due to the low-energy contamination. Therefore, another set of statistics was calculated considering only those reflections for which $F_{\text{filtered}}^2(hkl) > F^2(3h\ 3k\ 3l)$ is satisfied. A more sensible result without severe outliers is then obtained (see diagrams in Figure 107).

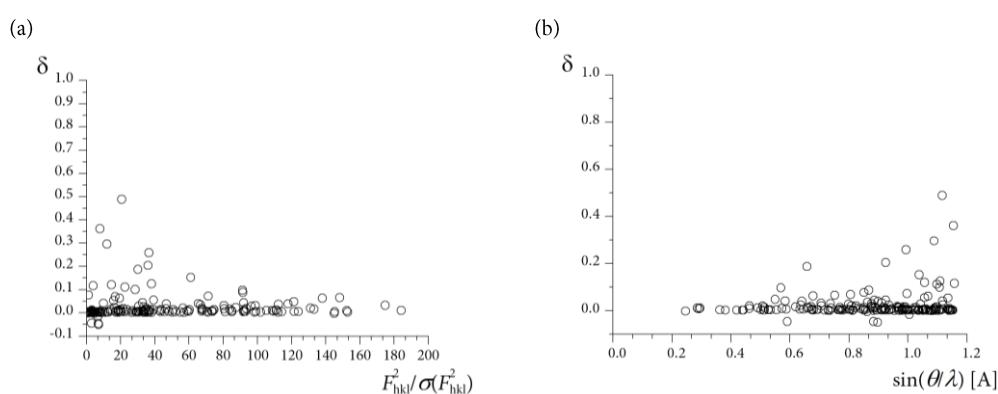


Figure 107. Plots of δ (see (Eq. 38)) as a function of (a) the significance of the contaminated reflections; (b) the resolution of the reflection. Number of reflections: 196; mean: $\delta = 0.024$; e.s.d.: 0.059; median: 0.0058).

7.4. Conclusions and outlook

This chapter of my thesis provides evidence for two points that have been investigated for the first time:

(a) a large variety of different datasets is affected, and the effect is not less pronounced for compounds of heavy elements. This is clearly demonstrated by the plots of $w\Delta^2$ as a function of the *Miller* indices. This allows the tentative conclusion that every dataset collected with mirror optics is affected.

(b) The impact of the low-energy contamination on the intensities is significant enough to induce a bias. This is demonstrated by the qualitative differences between the models obtained from refinements against the two datasets. It is obvious that only a small minority of reflections have systematically overestimated intensities because only those with *Miller* indices that are multiples of three are affected. A bias in the intensities of this small number of reflections was nonetheless decisive for the presence or absence of a bond path in the very shallow region of $\rho(\mathbf{r})$ in this case.

The importance of accurately measured data for charge density studies cannot be emphasised enough.^[340] The comparison of the different refinement results of **1** from datasets with and without filtering foil are a powerful demonstration of the importance of reliably determined intensities.

The presence of the contamination, its impact on measured data and the possibility to remove the contamination by the cheap and simple method of placing a filter foil in the beam path has been known before,^[64] but the extent to which the contamination affects the data and the resulting models is still not well examined and will have to be systematically investigated in the future. An evaluation of the optimal filter material and its thickness for most efficient blocking of the contamination and least attenuation of the primary intensity would be very useful as well.

From the preliminary results in this thesis, a factor of 0.5 – 1.0 % of the (hkl) intensity was determined as contamination of the intensity of the reflections $(3h\ 3k\ 3l)$, which is in the same order of magnitude as reported by *Macchi et al.*^[64] The magnitude of the contamination dependence may also depend on the size and shape of the crystal as well as on the diffraction angle^[30-33] because the absorption of the diffracted intensity is dependent on the path length through the crystal as well as on the wavelength. A very valuable research project for the future would be a series of test measurements with and without filter foil on identical crystals. This would allow conclusions regarding the magnitude of the contamination-induced error for a given reflection $(3h3k3l)$ by direct comparison of identical

reflections from datasets collected with and without filter. The error in the intensity of the reflection $(3h3k3l)$ presumably is a function of the intensity of the reflection (hkl) and it still has to be investigated based on more evidence whether a fixed ratio connects the two for all (hkl) . A reliable measure for this correlation has to be found as well. This is with the prospect on a software based correction, preferably in one of the steps of pre-refinement data processing.

8. Summary and outlook

The current thesis focuses on three detailed experimental QTAIM charge density studies on small molecules based on high resolution X-ray diffraction experiments. Each of the three studies required the application of different analytical methods. The employed measures, the achieved results and possible implications for related work in the future will be briefly reiterated in the following chapter.

The first of the studies (chapter 3) deals with the experimentally challenging piano stool complex tris(ammine)cyclopentadienyl sodium **1**. The anticipated highly ionic character of the metal–cyclopentadienyl interaction^[120] was confirmed by means of the integrated atomic charges and the atomic Source Function contributions in a QTAIM analysis. An out-of-plane bending of the cyclopentadienyl hydrogen atoms, apparently violating traditional theoretical predictions,^[124] was experimentally observed. More sophisticated theoretical calculations taking the lattice environment into account were carried out by our cooperation partner *Diego Andrada* from the *Mata* workgroup. The calculations exactly reproduced the experimentally observed bending angle. The out-of-plane-bending was explained by the charge reorganization and accumulation on top of the Cp ring, caused by strong intermolecular N–H \cdots π interactions with adjacent ammonia molecules. These intermolecular interactions were visualised by a state-of-the-art *Hirshfeld* surface analysis^[178] and traced by the recently published NCI method^[110,112,185] and the Source Function.^[89,94] The results confirm the excellent quality of the acquired data and the appropriateness of the refined model despite a 50:50 disorder in one out of three ammonia groups. Those experimental data might even serve for benchmarking in the development of new, more resilient theoretical methods.

It was demonstrated that the sodium/cyclopentadienyl as well as the N–H \cdots π interactions have a strongly polarising effect on the partially delocalised valence density of the cyclopentadienyl anion. This is visible in plots of the deformation density as well as of the Laplacian distribution. It can be postulated that the strength of the polarising effect of the cation and the ammonia protons compete on similar levels.

The second charge density study elucidates the bis(2-benzothiazolyl)phosphane **2**, a secondary phosphane in an unusual tautomeric form.^[220-222] Embarking on the primary goal to characterize the ambiguous character of the P–C bonds (chapter 4), the investigations turned out to have account for the even more general issue of conjugation and hetero-

aromaticity. The Source Function as a tool for the quantification of delocalisation was evaluated, and the first results on the fuzzy set of heteroaromaticity were presented.

Several complementary measures for aromaticity confirmed the aromaticity of the five- and six-membered rings. They were applied in cooperation with specialists from the Institute of Physical Chemistry (*R. A. Mata* and *J. Dieterich*) and from the University of Oslo (*H. Fliegl*).

It was shown that the interpretation of valence shell charge concentrations as VSEPR-concept lone pairs^[76,287] and the deduction of hybridisation states of third-row elements from these features of the charge density map are accepted in the experimental charge density community. The physical appropriateness of this interpretation was questioned and disproved in this thesis, which is in accordance with other opinions.^[251,294,296,305,307]

Weak intermolecular C–H...S and C–H...P interactions in the crystal packing of **2** were identified as attractive interactions by means of the NCI descriptor. The existence of the corresponding intermolecular bond paths underlines this conclusion.

The experimental charge density study on *N*-benzyl-2-(hydroxymethyl)benzamide **3** had the aim to provide a rationale for the inert behaviour of this compound towards hydridic reduction agents (chapter 5).

A QTAIM analysis of the benzamide **3** was carried out, confirming the long known electron delocalisation in the bonds of the C(=O)–N amide group by their topological bond orders. No double bond character could be found in the C_{amide}–phenyl bond and thus a stabilising conjugation of the amide group to the phenyl ring can be ruled out. A variety of relatively strong intermolecular interactions was characterised, among them two C–H...O interactions.

The analysis of the electrostatic potential around **3** revealed that an envelope of negative potential together with a steric shielding of the positive potential regions by the *ortho* hydrogen atom of the phenyl ring prevents the reaction of the carboxy carbon atom with hydridic reduction agents.

The last two chapters of this thesis (chapters 6 and 7) deal with some sources of errors in modern single crystal X-ray diffraction experiments:

The problems and the observed irregularities in the data sets from a synchrotron source were shown in chapter 6. Different strategies for data acquisition and data procession

were evaluated. A discussion of possible errors was provided and future investigations were suggested.

A hitherto largely neglected flaw in the design of modern focusing optics was subject of chapter 7: the low-energy contamination of the used radiation by total reflection of bremsstrahlung from the target of the X-ray source.^[64]

The chapter provided evidence based on data statistics suggesting that the effect of the contamination should not be neglected in the future. A simple filter insert for the beam path of a diffractometer was designed that enables the filtering of the contamination.

Two multipole refinements against datasets of **1** with and without contamination were compared. While a bond path between the sodium atom and the cyclopentadienyl moiety was observed when the model from the non-contaminated data was analysed, this path was absent in the result from the refinement against contaminated data, which highlighted the importance of accurately measured data.

The current thesis provides several links and cues to possible future projects. Charge density studies are generally considered to be mature,^[341] but it became clear that some of the used methods in the analysis of the results require further development. A lot more studies on the delocalisation in heteroaromatic systems using the Source Function and the delocalisation index^[260] as the measures for delocalisation are needed.

More investigations are needed to enable the efficient exploitation of the enormous potential of the beamline 15 ID-B at the *Advanced Photon Source*. The source of the observed error remains unresolved yet, but the range of potential errors has been narrowed down so that the combined efforts of the German (*Stalke*) and the Danish group (*Iversen*) will eventually lead to success.

The influence of the low energy contamination in multilayer focused X-ray beams will have to be further investigated. The future will show whether the effect should best be tackled by hardware (filter foils) or by software that remains to be developed.

9. Crystal structure determination in collaborations

9.1. Crystal selection and manipulation

The crystal selection was carried out at a moveable table that is equipped with a vacuum line including a high vacuum sliding vane rotary pump, an argon gas supply, a polarisation microscope equipped with an X-TEMP2 crystal cooling device.^[133-134] Air and moisture sensitive crystals were taken directly from Schlenk flasks. Crystal selection and manipulation was carried out under the microscope in a drop of perfluorinated polyether oil. The X-TEMP2 device was used to cool the glass object slide during crystal manipulation. Suitable crystals were selected using the polarisation filter of the microscope. The crystals were mounted in a very small amount of the perfluorinated polyether on the tip of a glass fiber or in a MiTeGen Kryoloop. The sample was very quickly placed in the cold gas stream of the sample cooling device of the diffractometer.

9.2. Data acquisition

The data collections were carried out on Bruker APEX2 Ultra or Quazar diffractometers equipped with Bruker TXS Mo, Incoatec I μ S Mo or Incoatec I μ S Ag sources. The datasets recorded with Cu-K α wavelength were collected on a Bruker SMART6000 diffractometer. The datasets with a wavelength of 0.3936 Å were collected at beamline 15 ID-B at the *Advanced Photon Source*, Argonne, Illinois. The data collection strategy was calculated with the APEX^[136] plugin COSMO where available. The frame width was set between 0.3 ° and 1.0 °.

9.3. Data processing

The unit cell was indexed with the tools in the Bruker APEX2 software suite.^[136] The intensities on the raw frames were integrated with SAINT 7.68a.^[57] The standard settings included: activated least-squares profile fitting of weak reflections with $I/\sigma(I) < 8$ (model profile update from reflections with $I/\sigma(I) > 10$); activated integration box size refinement starting from slightly increased suggested values; no blending of profiles from different detector regions. The orientation matrix was refined in several integration runs and the maximum resolution was adjusted so that only useable data with a maximum R_{int} of around 0.20 were integrated.

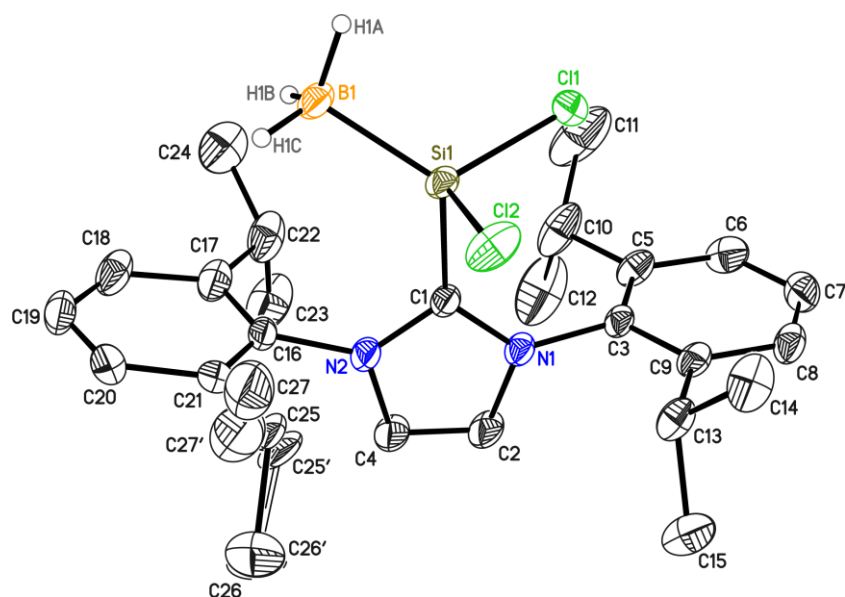
The software SADABS 2008/2^[23] was used for absorption correction and scaling. TWINABS^[342] was used in the cases of non-merohedral twins. XPREP in various versions up to 2013/1^[139] was used for the examination of data statistics and preliminary space

group determination. The program SHELXS^[20] was used before the beta versions of SHELXT^[140] were distributed in our workgroup. This program expands the data to space group *P1*, creates a structure solution from the phases of a Patterson superposition minimum function and then calculates the right space group based on the phases. It automatically carries out a peak search and assigns atom types in a subsequent step. Most of the structure refinements were carried out with SHELXL-97;^[21] only some of the structures were refined with the newer version SHELXL-2013.^[34]

Hydrogen atoms were refined using idealised positions using riding models and isotropic displacement parameters that were constrained to 1.2 or 1.5 times the U_{eq} of their pivot atoms. Disordered groups were refined using appropriate positional parameter and displacement parameter similarity restraints and constraints if necessary.^[343]

9.4. Structures determined for Dr. Gašper Tavčar (Prof. Dr. H. W. Roesky)

9.4.1. JH_TBSiCl45



Asymmetric unit of JH_TBSiCl45. A minor disorder in one of the isopropyl groups, as shown, had to be modeled. The hydrogen atoms at B(1) were found in a residual density Fourier map and isotropically modeled without any restraints on B–H distances or displacement parameters.

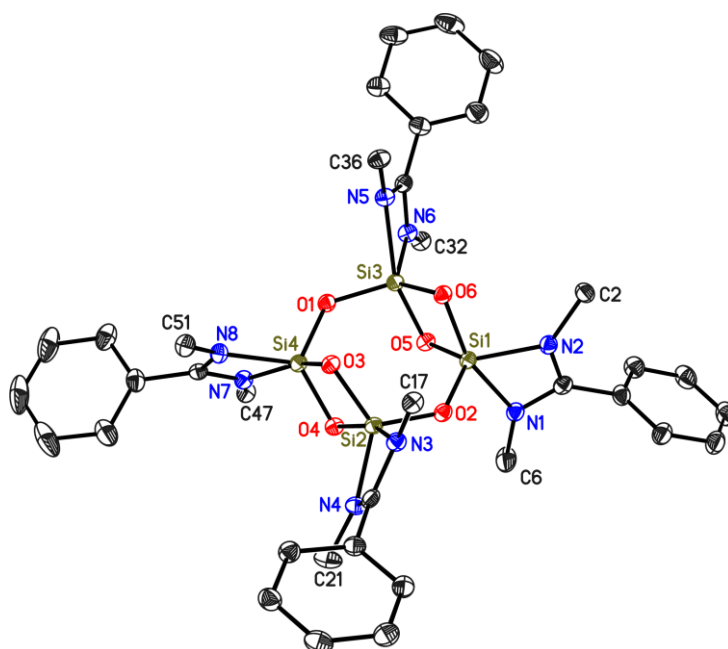
Structure published in:

Ramachandran Azhakar, Gašper Tavčar, Herbert W. Roesky, Jakob Hey, Dietmar Stalke „Facile Synthesis of a Rare Chlorosilylene-BH₃ Adduct" *Eur. J. Inorg. Chem.* **2011**, 475-477.

The structure is also deposited with CSD number: 791729.

Structure code	JH_TBSiCl45	Z	4
Empirical formula	C ₂₇ H ₃₉ BCl ₂ N ₂ Si	Crystal dimensions [mm ³]	0.21 x 0.18 x 0.12
Formula weight [g mol ⁻¹]	501.40	$\rho_{\text{calcd.}}$ [g cm ⁻³]	1.154
Sample temperature [K]	100(2)	μ [mm ⁻¹]	0.284
Wavelength [Å]	0.71073	$F(000)$	1072
Crystal system	Monoclinic	θ range [°]	1.69 to 25.39
Space group	$P2_1/n$	Reflections collected	60796
Unit cell dimensions [Å]		Unique reflections	5303
	a = 9.8531(5)	$R_{\text{int}}/R_{\sigma}$	0.0440/0.0185
	b = 16.2034(8)	Completeness to θ_{max}	100.0 %
	c = 18.1031(9)	restraints/parameters	38/315
	$\alpha = 90^\circ$	Goof	1.043
	$\beta = 92.8810(10)^\circ$	R1 (I > 2 σ (I))	0.0406
	$\gamma = 90^\circ$	wR2 (all data)	0.1035
Volume [Å ³]	2886.6(2)	max. diff. peak/hole [e Å ⁻³]	0.395/–0.468
Extinction coefficient	-	Absolute structure parameter	-

9.4.2. JH_TBCL25



Asymmetric unit of JH_TBCL25. A rotational disorder in the *tert*-butyl group around C6 had to be modeled. The *tert*-butyl methyl groups at C2, C6, C17, C21, C32, C36, C47, and C51 are omitted for clarity. The toluene solvent molecule is omitted.

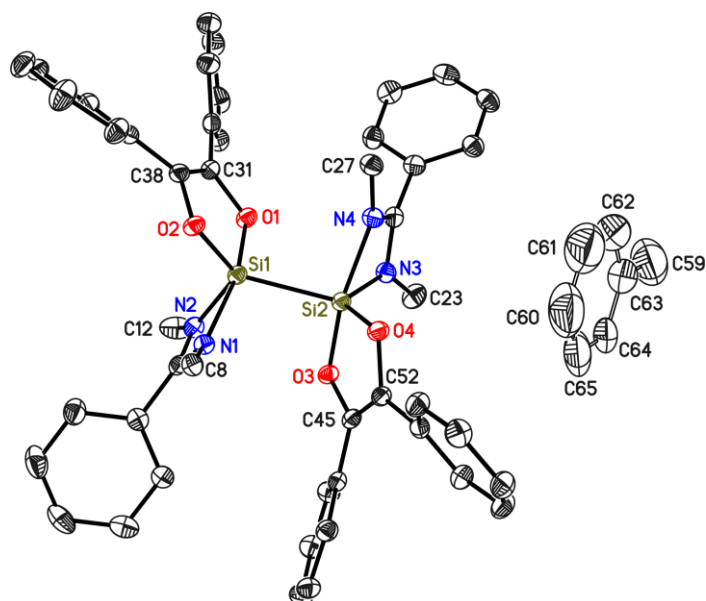
Structure published in:

Sakya S. Sen, Gašper Tavčar, Herbert W. Roesky, Daniel Kratzert, Jakob Hey, and Dietmar Stalke „Synthesis of a Stable Four-membered Si₂O₂ Ring and a Dimer with Two Four-membered Si₂O₂ Rings bridged by Two Oxygen Atoms, the Silicon atoms in both the Ring Systems are Five-coordinate" *Organometallics* **2010**, 29, 2343-2347.

The structure is also deposited with CSD number: 767745.

Structure code	JH_TBCL25	Z	4
Empirical formula	C ₆₇ H ₁₀₀ N ₈ O ₆ Si ₄	Crystal dimensions [mm ³]	0.21 x 0.18 x 0.12
Formula weight [g mol ⁻¹]	1225.91	$\rho_{\text{calcd.}}$ [g cm ⁻³]	1.187
Sample temperature [K]	100(2)	μ [mm ⁻¹]	0.141
Wavelength [Å]	0.71073	$F(000)$	2648
Crystal system	Monoclinic	θ range [°]	1.15 – 26.37
Space group	$P2_1/n$	Reflections collected	162534
Unit cell dimensions [Å]		Unique reflections	14016
	a = 10.7264(16)	$R_{\text{int}}/R_{\sigma}$	0.1051
	b = 28.415(4)	Completeness to θ_{max}	99.9 %
	c = 23.012(3)	restraints/parameters	219/861
	$\alpha = 90^\circ$	GooF	1.019
	$\beta = 101.979(2)^\circ$	R1 ($I > 2\sigma(I)$)	0.0422
	$\gamma = 90^\circ$	wR2 (all data)	0.1053
Volume [Å ³]	6861.2(2)	max. diff. peak/hole [e Å ⁻³]	0.261/–0.337
Extinction coefficient	-	Absolute structure parameter	-

9.4.3. JHGT_TBC19



Asymmetric unit of JHGT_TBC19. A rotational disorder in the *tert*-butyl group around C23 had to be modeled. The *tert*-butyl methyl groups at C8, C12, C23, and C27 are omitted for clarity. The toluene solvent molecule is located on the crystallographic inversion centre and does not obey the symmetry. Its six-membered ring was modelled using the AFIX 69 command. Hydrogen atoms are omitted for clarity.

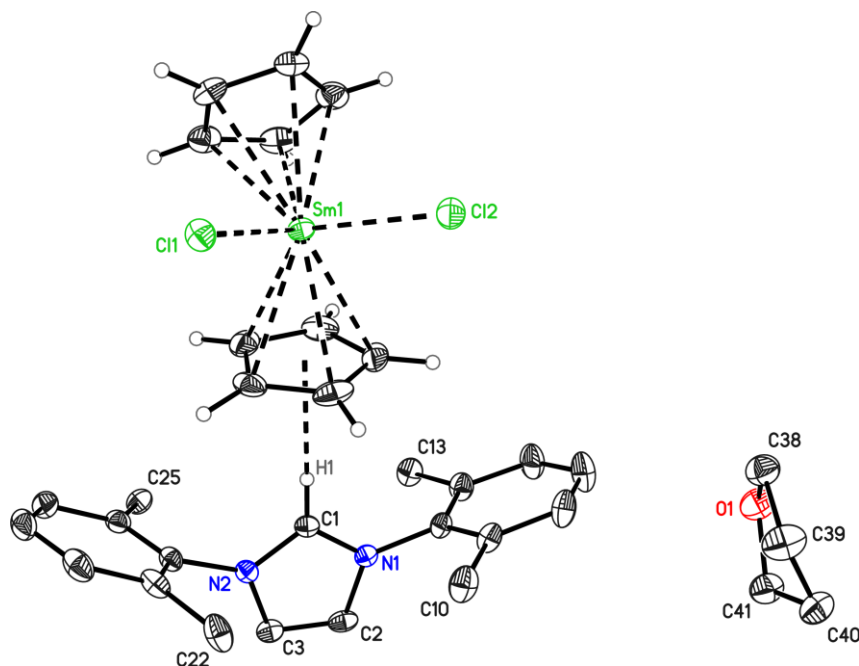
Structure published in:

Gašper Tavčar, Sakya S. Sen, Herbert W. Roesky, Jakob Hey, Daniel Kratzert, Dietmar Stalke „Reaction of a Bis-silylene (LSi-SiL, L = PhC(N^tBu)₂) and a Heteroleptic Chloro Silylene (LSiCl) with Benzil: Formation of Bis(siladioxolene) and Monosiladioxolene Analogue with Five-Coordinate Silicon Atoms in Both Ring Systems" *Organometallics* **2010**, 29, 3930-3935.

The structure is also deposited with CSD number: **780236**.

Structure code	JH_TBC19	Z	4
Empirical formula	C ₆₇ H ₁₀₀ N ₈ O ₆ Si ₄	Crystal dimensions [mm ³]	0.21 x 0.18 x 0.12
Formula weight [g mol ⁻¹]	1225.91	$\rho_{\text{calcd.}}$ [g cm ⁻³]	1.187
Sample temperature [K]	100(2)	μ [mm ⁻¹]	0.141
Wavelength [Å]	0.71073	F(000)	2648
Crystal system	Monoclinic	θ range [°]	1.15 – 26.37
Space group	<i>P</i> 2 ₁ / <i>n</i>	Reflections collected	162534
Unit cell dimensions [Å]		Unique reflections	14016
	a = 10.7264(16)	R _{int} /R σ	0.1051
	b = 28.415(4)	Completeness to θ_{max}	99.9 %
	c = 23.012(3)	restraints/parameters	219/861
	α = 90 °	GooF	1.019
	β = 101.979(2) °	R1 (I > 2 σ (I))	0.0422
	γ = 90 °	wR2 (all data)	0.1053
Volume [Å ³]	6861.2(2)	max. diff. peak/hole [e Å ⁻³]	0.261/–0.337
Extinction coefficient	-	Absolute structure parameter	-

9.4.4. JH_CSiCl6_2_SmCp



Asymmetric unit of JH_CSiCl6_2_SmCp. The *iso*-propyl methyl groups at C10, C13, C22, and C25 are omitted for clarity. Hydrogen atoms except H1 and those at Cp rings are omitted for clarity. The distance between H1 and the Cp best plane is 2.2989(25) Å.

H1 and the Cp hydrogen atoms were refined using a riding model (AFIX 43). A relatively large number of low-order reflections were excluded from refinement because they were obstructed by the beam stop.

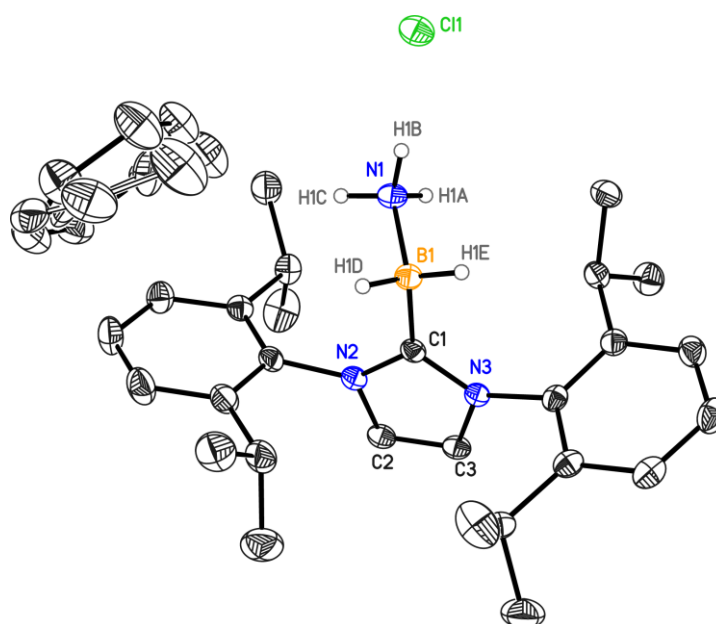
Structure published in:

Gašper Tavčar, Sakya S. Sen, Herbert W. Roesky, Jakob Hey, Daniel Kratzert, Dietmar Stalke „Reaction of a Bis-silylene (LSi-SiL, L = PhC(N^tBu)₂) and a Heteroleptic Chloro Silylene (LSiCl) with Benzil: Formation of Bis(siladioxolene) and Monosiladioxolene Analogue with Five-Coordinate Silicon Atoms in Both Ring Systems" *Organometallics* **2010**, 29, 3930-3935.

The structure is also deposited with CSD number: **780236**.

Structure code	JH_TBCL9	Z	2
Empirical formula	C ₄₁ H ₅₅ Cl ₂ N ₂ O ₂ Sm	Crystal dimensions [mm ³]	0.15 x 0.13 x 0.11
Formula weight [g mol ⁻¹]	813.12	$\rho_{\text{calcd.}}$ [g cm ⁻³]	1.358
Sample temperature [K]	100(2)	μ [mm ⁻¹]	1.642
Wavelength [Å]	0.71073	<i>F</i> (000)	838
Crystal system	Triclinic	θ range [°]	3.496 – 28.379
Space group	<i>P</i> $\bar{1}$	Reflections collected	56368
Unit cell dimensions [Å]		Unique reflections	9893
	a = 11.955(2)	R _{int} /R σ	0.0283
	b = 12.560(2)	Completeness to θ_{max}	99.7 %
	c = 13.777(3)	restraints/parameters	0/436
	α = 80.48(2) °	Goof	1.074
	β = 79.01(2) °	R1 (<i>I</i> > 2 σ (<i>I</i>))	0.0196
	γ = 81.69(2) °	wR2 (all data)	0.0496
Volume [Å ³]	1989.1(7)	max. diff. peak/hole [e Å ⁻³]	0.681/–0.428
Extinction coefficient	-	Absolute structure parameter	-

9.4.5. JH_tavcar_CSiCl6_BH2NH3



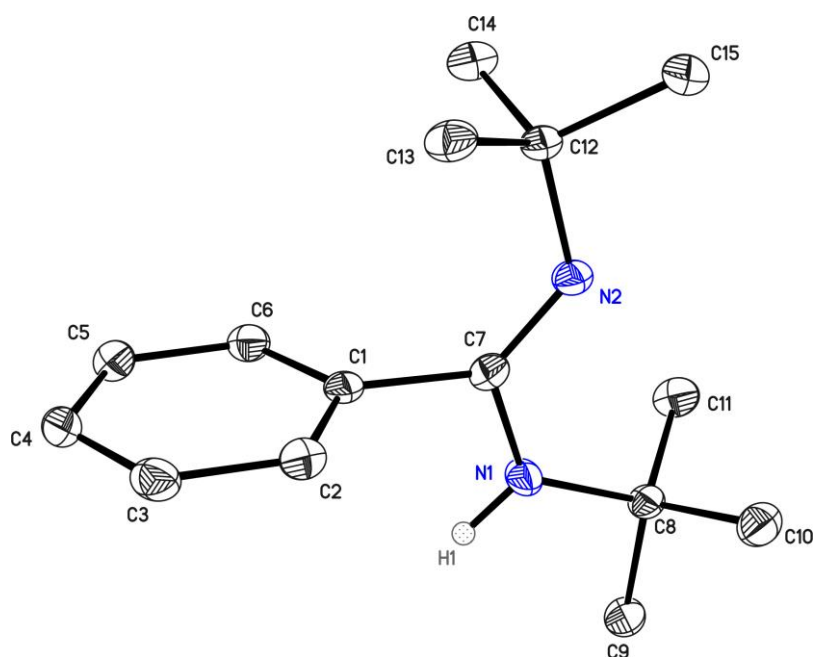
Asymmetric unit of JH_tavcar_CSiCl6_BH2NH3. Hydrogen atoms except those at B1 and N1 are omitted for clarity.

The hydrogen atoms at B1 and N1 were picked from the Fourier difference map, but eventually refined with a riding model (AFIX 23 and 137, respectively). In this dataset, a high number of weak reflections strongly suffered from 3λ contamination so that they were excluded from refinement. One molecule of toluene is disordered over two sites with s.o.f. 0.82/0.18; displacement parameter restraints (RIGU) and 1,2 and 1,3 distance restraints (SAME) were applied for stable refinement of the solvent.

This structure has not been published in an article.

Structural information is deposited and available with CSD number: 939934.

Structure code	JH_TBCL9	Z	4
Empirical formula	C ₃₄ H ₄₉ BCl ₉	Crystal dimensions [mm ³]	0.18 x 0.15 x 0.08
Formula weight [g mol ⁻¹]	546.02	$\rho_{\text{calc.}}$ [g cm ⁻³]	1.100
Sample temperature [K]	100(2)	μ [mm ⁻¹]	0.141
Wavelength [Å]	0.71073	$F(000)$	1184
Crystal system	Monoclinic	θ range [°]	1.573 – 26.716
Space group	$P2_1/c$	Reflections collected	36521
Unit cell dimensions [Å]		Unique reflections	6982
	a = 13.0248(18)	$R_{\text{int}}/R_{\sigma}$	0.0466
	b = 12.3127(18)	Completeness to θ_{max}	99.8 %
	c = 20.683(3)	restraints/parameters	229/419
	$\alpha = 90^\circ$	GooF	1.057
	$\beta = 96.190(3)^\circ$	R1 ($I > 2\sigma(I)$)	0.0408
	$\gamma = 90^\circ$	wR2 (all data)	0.1059
Volume [Å ³]	3297.7(8)	max. diff. peak/hole [e Å ⁻³]	0.295/–0.205
Extinction coefficient	-	Absolute structure parameter	-

9.4.6. *JH_amidinate_protonated*

Asymmetric unit of *JH_amidinate_protonated*. Hydrogen atoms except the one at N1 are omitted for clarity.

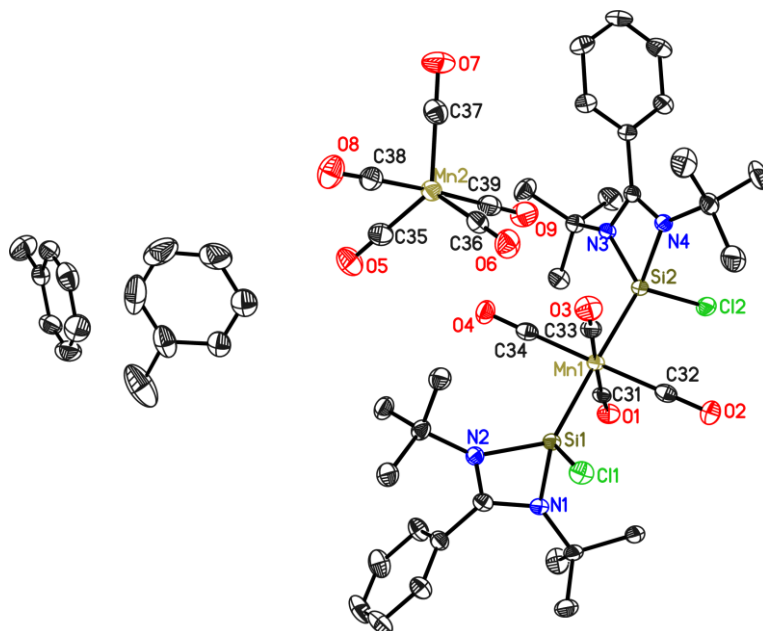
The sample was a split crystal with two domains of the fractions 79/21. Both of the domains were integrated. Data of both domains and composite reflections were used for refinement. H1 was picked from a Fourier difference map.

This structure has not been published in an article or in the CSD.

Structure code	JH_amidinate_protonated	Z	4
Empirical formula	C ₁₅ H ₂₄ N ₂	Crystal dimensions [mm ³]	0.20 x 0.08 x 0.06
Formula weight [g mol ⁻¹]	232.36	$\rho_{\text{calcd.}}$ [g cm ⁻³]	1.085
Sample temperature [K]	100(2)	μ [mm ⁻¹]	0.064
Wavelength [Å]	0.71073	<i>F</i> (000)	512
Crystal system	Monoclinic	θ range [°]	1.907 – 26.827
Space group	<i>P</i> 2 ₁ / <i>c</i>	Reflections collected	20028
Unit cell dimensions [Å]		Unique reflections	4793
	<i>a</i> = 5.8155(3)	<i>R</i> _{int} / <i>R</i> _{σ}	0.0498
	<i>b</i> = 12.9517(7)	Completeness to θ_{max}	100.0 %
	<i>c</i> = 18.9401(11)	restraints/parameters	0/161
	α = 90°	GooF	1.064
	β = 94.662(3)°	<i>R</i> 1 (<i>I</i> > 2 σ (<i>I</i>))	0.0481
	γ = 90°	w <i>R</i> 2 (all data)	0.1341
Volume [Å ³]	1421.86(13)	max. diff. peak/hole [e Å ⁻³]	0.369/−0.216
Extinction coefficient	-	Absolute structure parameter	-

9.5. Structures determined for Dr. Ramachandran Azhakar (Prof. Dr. H. W. Roesky)

9.5.1. JH_az_LSiCl_MnCO



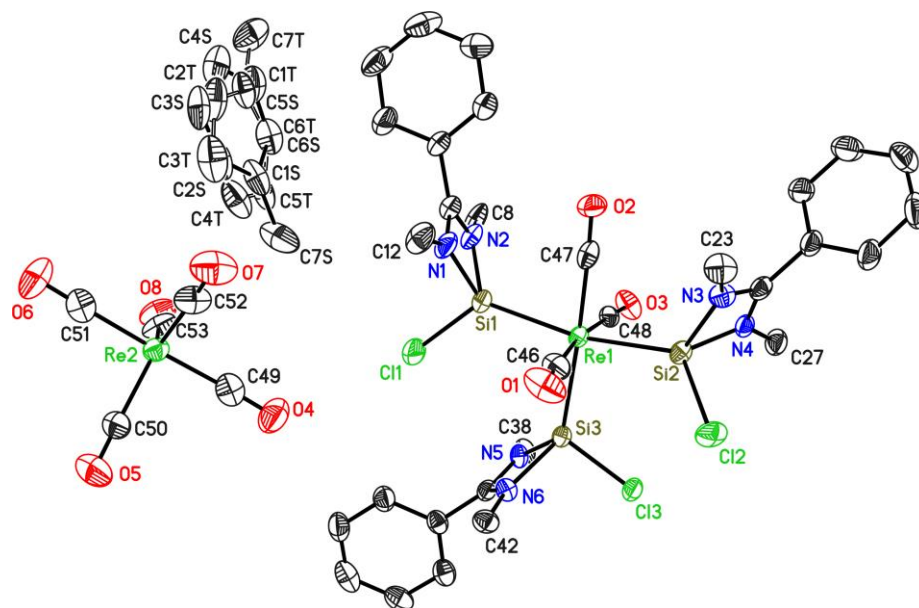
Representation of the asymmetric unit. Hydrogen atoms are omitted for clarity.

Structure published in:

Ramachandran Azhakar, Sankaranarayana Pillai Sarish, Herbert W. Roesky, Jakob Hey, Dietmar Stalke „Syntheses of Group 7 Metal Carbonyl Complexes with a Stable N-Heterocyclic Chlorosilylene" *Inorg. Chem.* **2011**, *50*, 5039-5043.

The structure is also deposited with CSD number: **812641**.

Structure code	JH_az_LSiCl_MnCO	Z	4
Empirical formula	C ₅₃ H ₆₂ Cl ₂ Mn ₂ N ₄ O ₉ Si ₂	Crystal dimensions [mm ³]	0.12 x 0.05 x 0.05
Formula weight [g mol ⁻¹]	1136.03	$\rho_{\text{calcd.}}$ [g cm ⁻³]	1.255
Sample temperature [K]	100 (2)	μ [mm ⁻¹]	0.233
Wavelength [Å]	0.71073	<i>F</i> (000)	2368
Crystal system	Monoclinic	θ range [°]	1.19 – 25.43
Space group	<i>P</i> 2 ₁ / <i>n</i>	Reflections collected	122803
Unit cell dimensions [Å]		Unique reflections	10441
	a = 8.8470(14)	R _{int}	0.0728
	b = 34.141(5)	Completeness to θ_{max}	99.6 %
	c = 19.096(3)	restraints/parameters	40/663
	α = 90°	Goof	1.022
	β = 100.555(4)°	R1 (<i>I</i> > 2 σ (<i>I</i>))	0.0367
	γ = 90°	wR2 (all data)	0.0838
Volume [Å ³]	5670.2(2)	max. diff. peak/hole [e Å ⁻³]	0.352/–0.347
Extinction coefficient	-	Absolute structure parameter	-

9.5.2. *JH_az_Re2CO10*

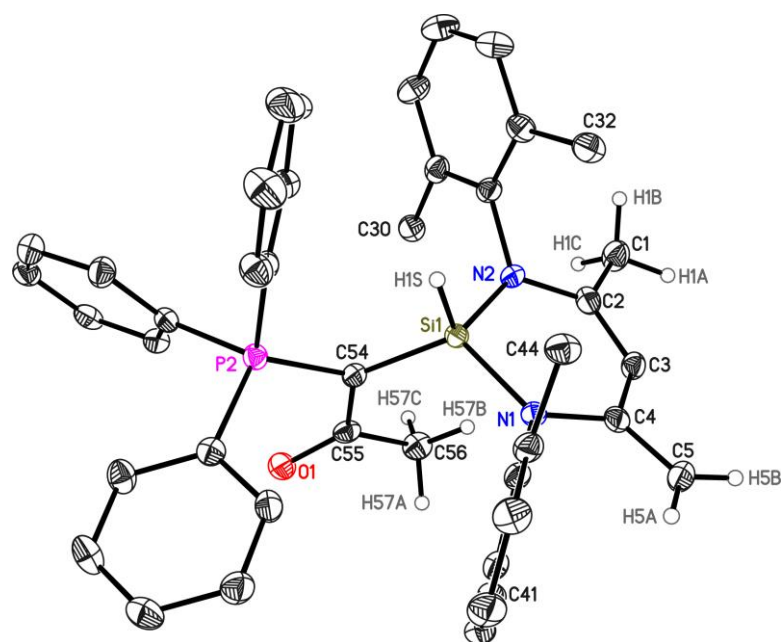
Representation of the asymmetric unit. Hydrogen atoms as well as *tert*-butyl methyl groups at C8, C12, C23, C27, C38, and C42 are omitted for clarity. The C–O distances in carbonyl groups were restrained to be equal within a certain standard deviation. A disorder in the *tert*-butyl group around C12 was modelled.

Structure published in:

Ramachandran Azhakar, Sankaranarayana Pillai Sarish, Herbert W. Roesky, Jakob Hey, Dietmar Stalke „Syntheses of Group 7 Metal Carbonyl Complexes with a Stable N-Heterocyclic Chlorosilylene" *Inorg. Chem.* **2011**, *50*, 5039-5043.

The structure is also deposited with CSD number: **812642**.

Structure code	JH_az_Re2CO10	Z	4
Empirical formula	C ₆₀ H ₇₇ Cl ₃ N ₆ O ₈ Re ₂ Si ₃	Crystal dimensions [mm ³]	0.21 x 0.09 x 0.06
Formula weight [g mol ⁻¹]	1573.32	$\rho_{\text{calcd.}}$ [g cm ⁻³]	1.538
Sample temperature [K]	100 (2)	μ [mm ⁻¹]	3.785
Wavelength [Å]	0.71073	<i>F</i> (000)	3144
Crystal system	Monoclinic	θ range [°]	1.08 – 26.74
Space group	<i>P</i> 2 ₁ / <i>n</i>	Reflections collected	272786
Unit cell dimensions [Å]		Unique reflections	14417
	<i>a</i> = 12.4470(4)	<i>R</i> _{int}	0.0509
	<i>b</i> = 37.8010(13)	Completeness to θ_{max}	99.9 %
	<i>c</i> = 14.4401(5)	restraints/parameters	119/818
	α = 90 °	Goof	1.299
	β = 90.4560(10) °	<i>R</i> 1 (<i>I</i> > 2 σ (<i>I</i>))	0.0484
	γ = 90 °	<i>wR</i> 2 (all data)	0.01093
Volume [Å ³]	6794.0(4)	max. diff. peak/hole [e Å ⁻³]	3.867/–1.939
Extinction coefficient	-	Absolute structure parameter	-

9.5.3. *JH_az_LSiCl_phosphorus_ylide_SQUEEZE*

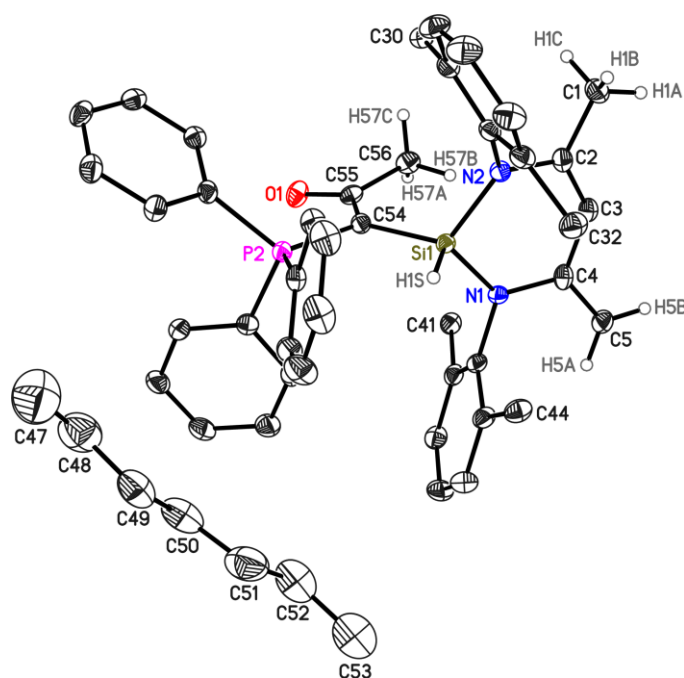
Representation of the asymmetric unit. Only hydrogen atoms that were explicitly picked from the *Fourier* difference map are shown. The *iso*-propyl methyl groups at C30, C32, C41, and C44 are omitted for clarity. The solvent pentane that was present in channel-like voids in the structure was not modelled; the influence of the remaining residual density was extinguished from the recorded intensity data with the program SQUEEZE of the PLATON package of programs.

Structure published in:

Ramachandran Azhakar, Sankaranarayana Pillai Sarish, Herbert W. Roesky, Jakob Hey, Dietmar Stalke „Regiospecific C-H Bond Activation: Reactivity Study of N-Heterocyclic Silylene towards Ambidentate Phosphorus Ylide" *Organometallics* **2011**, *30*, 2897-2900.

The structure is also deposited with CSD number: **812639**.

Structure code	JH_az_Re2CO10	Z	8
Empirical formula	C ₅₀ H ₅₉ Cl ₃ N ₆ O ₈ Re ₂ Si ₃	Crystal dimensions [mm ³]	0.25 x 0.12 x 0.10
Formula weight [g mol ⁻¹]	763.05	ρ_{calc} [g cm ⁻³]	0.993
Sample temperature [K]	110 (2)	μ [mm ⁻¹]	0.064
Wavelength [Å]	0.71073	<i>F</i> (000)	3280
Crystal system	Monoclinic	θ range [°]	0.91 – 20.12
Space group	<i>C2/c</i>	Reflections collected	96732
Unit cell dimensions [Å]		Unique reflections	9829
	a = 24.976(6)	<i>R</i> _{int}	0.0982
	b = 11.607(3)	Completeness to θ_{max}	99.7 %
	c = 35.602(9)	restraints/parameters	0/509
	α = 90 °	Goof	1.038
	β = 98.430(3) °	<i>R</i> 1 (<i>I</i> > 2 σ (<i>I</i>))	0.0497
	γ = 90 °	w <i>R</i> 2 (all data)	0.1222
Volume [Å ³]	10209(4)	max. diff. peak/hole [e Å ⁻³]	0.217/–0.373
Extinction coefficient	-	Absolute structure parameter	-

9.5.4. *JH_az_LSiCl_phosphorus_ylide*

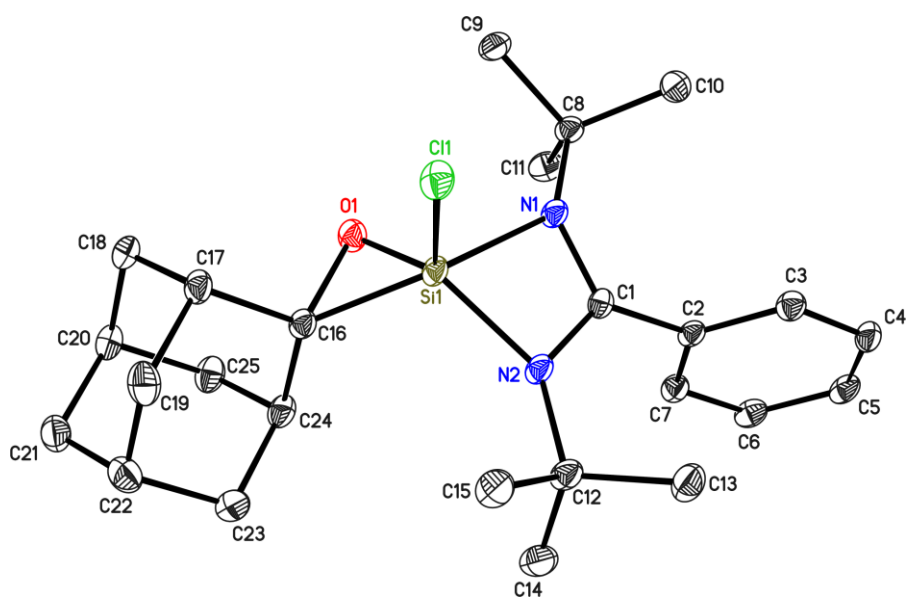
Representation of the asymmetric unit. The same data as for the refinement of the structure in section 9.5.3 were used. Only hydrogen atoms that were explicitly picked from the *Fourier* difference map are shown. The *iso*-propyl methyl groups at C30, C32, C41, and C44 are omitted for clarity. One heptane solvent molecule could be modelled, but diffuse residual density had to remain unmodelled in channels along the crystallographic *b* axis as the attempted refinement of further solvent molecules resulted in unstable refinements.

Structure published in:

Ramachandran Azhakar, Sankaranarayana Pillai Sarish, Herbert W. Roesky, Jakob Hey, Dietmar Stalke „Regiospecific C-H Bond Activation: Reactivity Study of N-Heterocyclic Silylene towards Ambidentate Phosphorus Ylide" *Organometallics* **2011**, *30*, 2897-2900.

The structure is also deposited with CSD number: **812640**.

Structure code	JH_az_Re2CO10	Z	8
Empirical formula	C ₅₇ H ₇₅ N ₂ OPSi	Crystal dimensions [mm ³]	0.21 x 0.09 x 0.06
Formula weight [g mol ⁻¹]	863.25	$\rho_{\text{calcd.}}$ [g cm ⁻³]	1.123
Sample temperature [K]	110 (2)	μ [mm ⁻¹]	0.069
Wavelength [Å]	0.71073	<i>F</i> (000)	3744
Crystal system	Monoclinic	θ range [°]	0.91 – 20.12
Space group	C2/c	Reflections collected	93878
Unit cell dimensions [Å]		Unique reflections	9829
	a = 24.976(6)	R _{int}	0.0994
	b = 11.607(3)	Completeness to θ_{max}	99.7 %
	c = 35.602(9)	restraints/parameters	0/573
	α = 90 °	Goof	1.299
	β = 98.430(3) °	R1 (I > 2 σ (I))	0.0550
	γ = 90 °	wR2 (all data)	0.1588
Volume [Å ³]	10209(4)	max. diff. peak/hole [e Å ⁻³]	0.887/–0.393
Extinction coefficient	-	Absolute structure parameter	-

9.5.5. *JH_az_LSiCl_2Adamantyl*

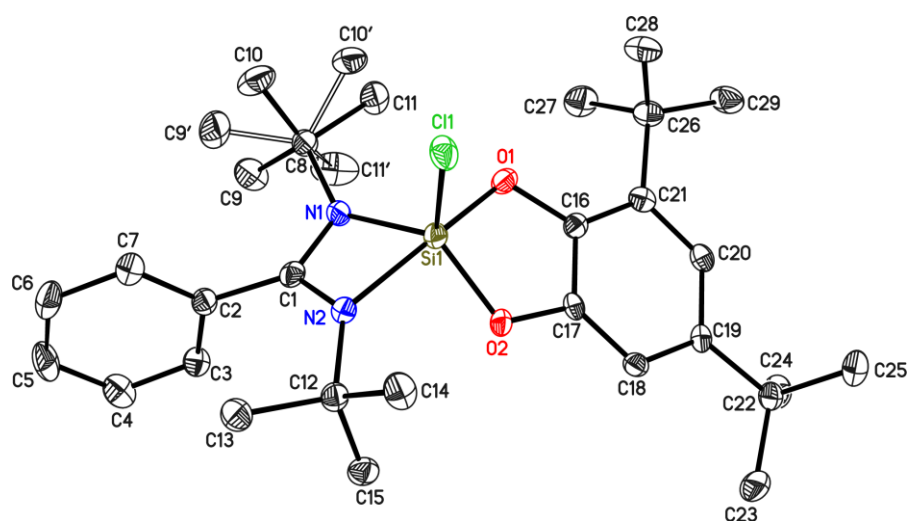
Representation of the asymmetric unit. Hydrogen atoms are omitted for clarity.

Structure published in:

Ramachandran Azhakar, Rajendra S. Ghadwal, Herbert W. Roesky, Jakob Hey, Dietmar Stalke „Reactions of Stable N-Heterocyclic Silylenes with Ketones” *Organometallics* **2011**, 30, 3853-3858.

The structure is also deposited with CSD number: **824154**.

Structure code	JH_az_LSiCl_2Adamantyl	Z	4
Empirical formula	C ₂₅ H ₃₇ ClN ₂ OSi	Crystal dimensions [mm ³]	0.16 x 0.12 x 0.05
Formula weight [g mol ⁻¹]	445.11	$\rho_{\text{calcd.}}$ [g cm ⁻³]	1.255
Sample temperature [K]	90 (2)	μ [mm ⁻¹]	0.233
Wavelength [Å]	0.71073	<i>F</i> (000)	960
Crystal system	Monoclinic	θ range [°]	1.36 – 27.20
Space group	<i>P</i> 2 ₁ / <i>c</i>	Reflections collected	39086
Unit cell dimensions [Å]		Unique reflections	5224
	a = 15.4914 (14)	<i>R</i> _{int}	0.0440
	b = 11.6071 (10)	Completeness to θ_{max}	99.9 %
	c = 13.5417 (12)	restraints/parameters	0/277
	α = 90°	Goof	1.122
	β = 104.728 (2)°	<i>R</i> 1 (<i>I</i> > 2 σ (<i>I</i>))	0.0366
	γ = 90°	w <i>R</i> 2 (all data)	0.0964
Volume [Å ³]	2354.9 (4)	max. diff. peak/hole [e Å ⁻³]	0.373/–0.322
Extinction coefficient	-	Absolute structure parameter	-

9.5.6. *JH_az_LSiCl_tBu2*

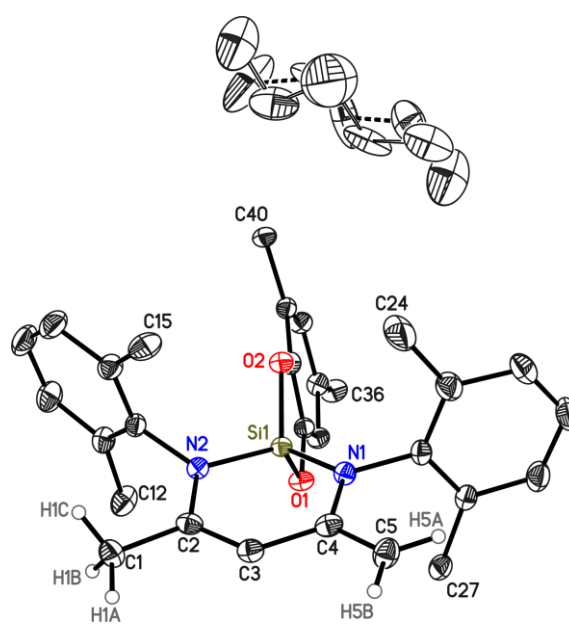
Representation of the asymmetric unit. Hydrogen atoms are omitted for clarity.

Structure published in:

Ramachandran Azhakar, Rajendra S. Ghadwal, Herbert W. Roesky, Jakob Hey, Dietmar Stalke „Reactions of Stable N-Heterocyclic Silylenes with Ketones” *Organometallics* **2011**, *30*, 3853-3858.

The structure is also deposited with CSD number: **824155**.

Structure code	JH_az_LSiCl_tBu2	Z	4
Empirical formula	C ₂₉ H ₄₃ ClN ₂ O ₂ Si	Crystal dimensions [mm ³]	0.07 x 0.07 x 0.07
Formula weight [g mol ⁻¹]	515.19	ρ_{calcd} [g cm ⁻³]	1.189
Sample temperature [K]	100 (2)	μ [mm ⁻¹]	0.202
Wavelength [Å]	0.71073	F(000)	1112
Crystal system	Orthorhombic	θ range [°]	1.79 – 26.03
Space group	<i>P</i> 2 ₁ 2 ₁ 2 ₁	Reflections collected	29073
Unit cell dimensions [Å]		Unique reflections	5657
	a = 10.8117(10)	R _{int}	0.0549
	b = 14.4507 (14)	Completeness to θ_{max}	99.7 %
	c = 18.4194 (18)	restraints/parameters	0/359
	$\alpha = 90^\circ$	GooF	1.038
	$\beta = 90^\circ$	R1 (<i>I</i> > 2 σ (<i>I</i>))	0.0351
	$\gamma = 90^\circ$	wR2 (all data)	0.0764
Volume [Å ³]	2877.8 (3)	max. diff. peak/hole [e Å ⁻³]	0.193/–0.203
Extinction coefficient	-	Absolute structure parameter	0.03(5)

9.5.7. *JH_az_nacnac_tBu2*

Representation of the asymmetric unit.

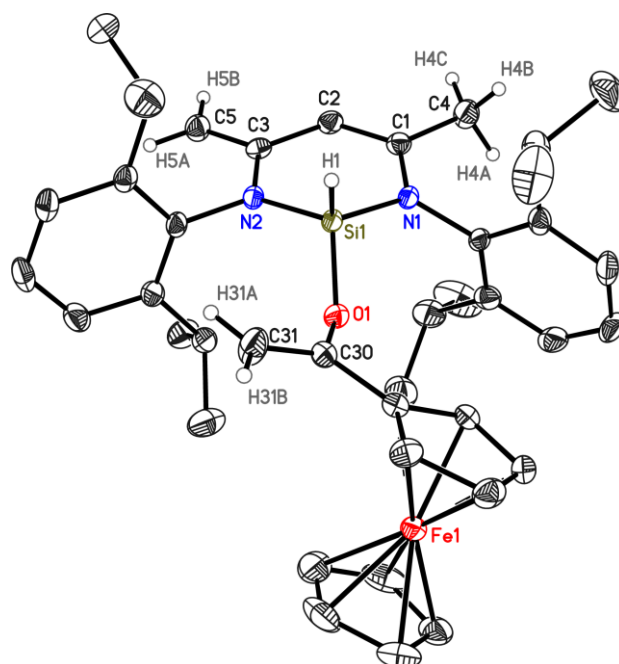
The *iso*-propyl and *tert*-butyl methyl groups at C12, C15, C24, C27, C36 and C40 have been omitted for clarity.

Structure published in:

Ramachandran Azhakar, Rajendra S. Ghadwal, Herbert W. Roesky, Jakob Hey, Dietmar Stalke „Reactions of Stable N-Heterocyclic Silylenes with Ketones" *Organometallics* **2011**, 30, 3853-3858.

Structural information in CIF format is also deposited and available with CSD number: **824156**.

Structure code	JH_az_nacnac_tBu2	Z	2
Empirical formula	C _{15.5} H ₆₆ N ₂ O ₂ Si	Crystal dimensions [mm ³]	0.12 x 0.08 x 0.06
Formula weight [g mol ⁻¹]	701.09	$\rho_{\text{calcd.}}$ [g cm ⁻³]	1.098
Sample temperature [K]	100 (2)	μ [mm ⁻¹]	0.092
Wavelength [Å]	0.71073	<i>F</i> (000)	766
Crystal system	Triclinic	θ range [°]	1.60 – 26.75
Space group	<i>P</i> $\bar{1}$	Reflections collected	59261
Unit cell dimensions [Å]		Unique reflections	8992
	a = 12.9856 (9)	R _{int}	0.0269
	b = 12.9963 (9)	Completeness to θ_{max}	99.7 %
	c = 13.3486 (9)	restraints/parameters	143/485
	α = 73.1430(10)°	GooF	1.028
	β = 79.4280(10)°	R1 (<i>I</i> > 2 σ (<i>I</i>))	0.0439
	γ = 88.4660(10)°	wR2 (all data)	0.1151
Volume [Å ³]	2118.5 (3)	max. diff. peak/hole [e Å ⁻³]	0.455/–0.557
Extinction coefficient	-	Absolute structure parameter	-

9.5.8. *JH_az_nacnac_ferrocene*

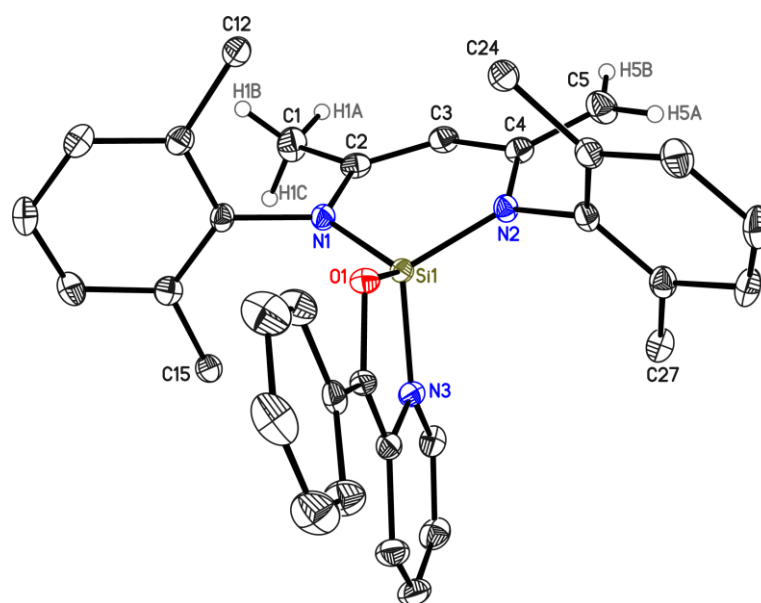
Graphical representation of the symmetric unit. Hydrogen atoms except H1 omitted for clarity. H1 was found in a Fourier difference analysis. No distance restraints were used for the refinement of H1. The isotropic displacement parameter U_{iso} of H1 is fixed to 1.2 times the equivalent isotropic displacement parameter U_{eq} of Si1. Hydrogen atoms at C4 and C5 were found and assigned from a Fourier difference analysis, but refined with riding model using the AFIX 137 and the AFIX 93 command, respectively.

Structure published in:

Ramachandran Azhakar, Rajendra S. Ghadwal, Herbert W. Roesky, Jakob Hey, Dietmar Stalke „Reactions of Stable N-Heterocyclic Silylenes with Ketones" *Organometallics* **2011**, *30*, 3853-3858.

Structural information in CIF format is also deposited and available with CSD number: **824157**.

Structure code	JH_az_nacnac_tBu2	Z	8
Empirical formula	C ₄₁ H ₅₂ FeN ₂ O _{Si}	Crystal dimensions [mm ³]	0.12 x 0.10 x 0.08
Formula weight [g mol ⁻¹]	672.79	$\rho_{\text{calcd.}}$ [g cm ⁻³]	1.216
Sample temperature [K]	100 (2)	μ [mm ⁻¹]	0.476
Wavelength [Å]	0.71073	$F(000)$	2880
Crystal system	Monoclinic	θ range [°]	1.98 – 25.35
Space group	C2/c	Reflections collected	58971
Unit cell dimensions [Å]		Unique reflections	6648
	a = 21.2031 (5)	R_{int}	0.0340
	b = 10.0796 (2)	Completeness to θ_{max}	98.8 %
	c = 35.5186 (8)	restraints/parameters	0/428
	$\alpha = 90^\circ$	GooF	1.037
	$\beta = 104.5550$	$R1$ ($I > 2\sigma(I)$)	0.0335
	$\gamma = 90^\circ$	wR2 (all data)	0.0809
Volume [Å ³]	7347.4 (3)	max. diff. peak/hole [e Å ⁻³]	0.420/–0.370
Extinction coefficient	-	Absolute structure parameter	-

9.5.9. *JH_az_nacnac_PhCOPy*

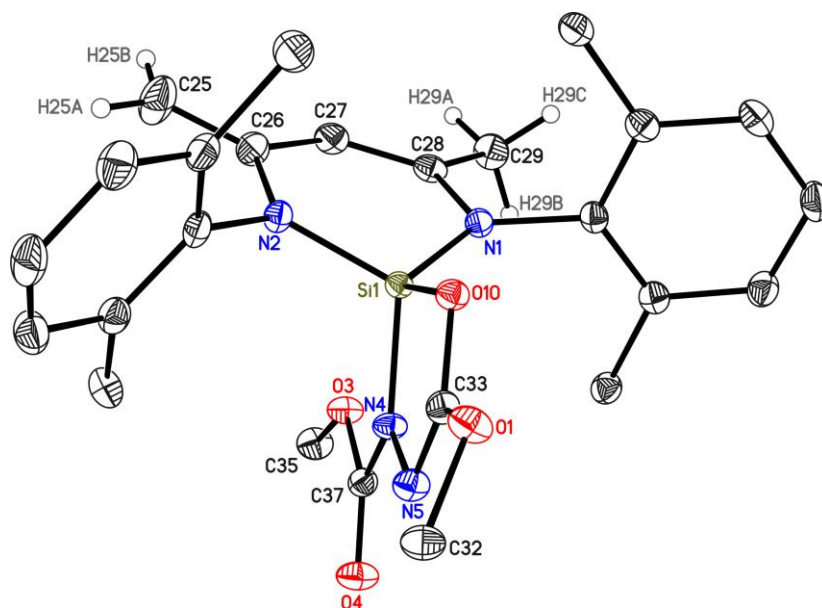
Graphical representation of the symmetric unit. The *iso*-propyl methyl groups at C12, C15, C24, and C27 have been omitted for clarity.

Structure published in:

Ramachandran Azhakar, Sankaranarayana Pillai Sarish, Gašper Tavčar, Herbert W. Roesky, Jakob Hey, Dietmar Stalke, Debasis Koley „Formation of Silicon Centered Spirocyclic Compounds: Reaction of N-Heterocyclic Stable Silylene with Benzoylpyridine, Diisopropyl Azodicarboxylate and 1,2-Diphenylhydrazine" *Inorg. Chem.* **2011**, *50*, 3028-3036.

Structural information in CIF format is also deposited and available with CSD number: **805652**.

Structure code	JH_az_nacnac_PhCOPy	Z	2
Empirical formula	C ₄₁ H ₄₉ N ₃ Osi	Crystal dimensions [mm ³]	0.12 x 0.08 x 0.06
Formula weight [g mol ⁻¹]	627.92	$\rho_{\text{calcd.}}$ [g cm ⁻³]	1.189
Sample temperature [K]	100 (2)	μ [mm ⁻¹]	0.103
Wavelength [Å]	0.71073	<i>F</i> (000)	676
Crystal system	Triclinic	θ range [°]	1.43 – 27.18
Space group	<i>P</i> $\bar{1}$	Reflections collected	43551
Unit cell dimensions [Å]		Unique reflections	7717
	a = 11.2420 (7)	<i>R</i> _{int}	0.0312
	b = 11.5555 (7)	Completeness to θ_{max}	98.9 %
	c = 14.8291 (9)	restraints/parameters	0/424
	α = 78.5770 (10) °	GooF	1.021
	β = 74.8600 (10) °	<i>R</i> 1 (<i>I</i> > 2 σ (<i>I</i>))	0.0399
	γ = 71.9120 (10) °	w <i>R</i> 2 (all data)	0.0977
Volume [Å ³]	1753.22 (19)	max. diff. peak/hole [e Å ⁻³]	0.300/–0.347
Extinction coefficient	-	Absolute structure parameter	-

9.5.10. *JH_az_NCOOiPr*

Graphical representation of the symmetric unit. Isopropyl methyl groups at *dipp* moieties have been omitted for clarity. Hydrogen atoms at C25 and C29 were found and assigned from a Fourier difference analysis, but refined with riding model using the AFIX 93 and the AFIX 137 command, respectively.

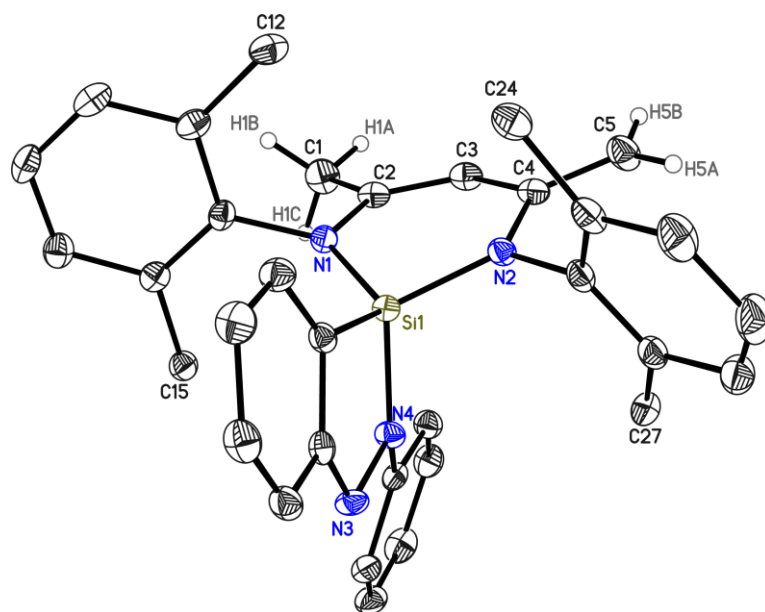
Structure published in:

Ramachandran Azhakar, Sankaranarayana Pillai Sarish, Gašper Tavčar, Herbert W. Roesky, Jakob Hey, Dietmar Stalke, Debasis Koley „Formation of Silicon Centered Spirocyclic Compounds: Reaction of N-Heterocyclic Stable Silylene with Benzoylpyridine, Diisopropyl Azodicarboxylate and 1,2-Diphenylhydrazine" *Inorg. Chem.* **2011**, *50*, 3028-3036.

Structural information in CIF format is also deposited and available with CSD number: **805653**.

Structure code	JH_az_NCOOiPr	Z	4
Empirical formula	C ₃₇ H ₅₄ N ₄ O ₄ Si	Crystal dimensions [mm ³]	0.15 x 0.12 x 0.09
Formula weight [g mol ⁻¹]	646.93	$\rho_{\text{calcd.}}$ [g cm ⁻³]	1.182
Sample temperature [K]	99 (2)	μ [mm ⁻¹]	0.108
Wavelength [Å]	0.71073	<i>F</i> (000)	1400
Crystal system	Orthorhombic	θ range [°]	1.68 – 27.13
Space group	<i>Pca</i> 2 ₁	Reflections collected	66985
Unit cell dimensions [Å]		Unique reflections	8037
	a = 16.6931 (14)	R _{int}	0.0382
	b = 12.1192 (10)	Completeness to θ_{max}	99.9 %
	c = 17.9703 (15)	restraints/parameters	1/428
	α = 90 °	GooF	1.057
	β = 90 °	R1 (<i>I</i> > 2 σ (<i>I</i>))	0.0293
	γ = 90 °	wR2 (all data)	0.0737
Volume [Å ³]	3635.5 (5)	max. diff. peak/hole [e Å ⁻³]	0.219/–0236
Extinction coefficient	-	Absolute structure parameter	0.03(7)

9.5.11. JH_az_PhNNHPh



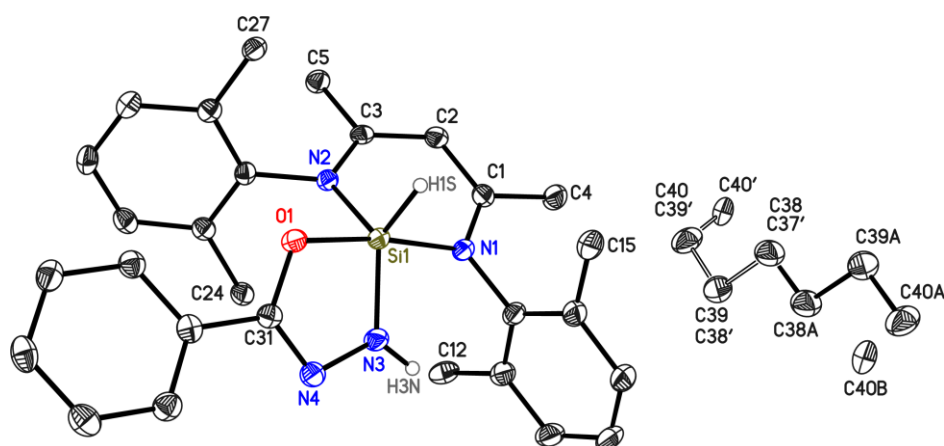
Graphical representation of the asymmetric unit. Isopropyl methyl groups at C12, C15, C24, and C27 have been omitted for clarity. Hydrogen atoms at C1 and C5 were found and assigned from a Fourier difference analysis, but refined with riding model using the AFIX 137 and the AFIX 93 command, respectively.

Structure published in:

Ramachandran Azhakar, Sankaranarayana Pillai Sarish, Gašper Tavčar, Herbert W. Roesky, Jakob Hey, Dietmar Stalke, Debasis Koley „Formation of Silicon Centered Spirocyclic Compounds: Reaction of N-Heterocyclic Stable Silylene with Benzoylpyridine, Diisopropyl Azodicarboxylate and 1,2-Diphenylhydrazine" *Inorg. Chem.* **2011**, *50*, 3028-3036.

Structural information in CIF format is also deposited and available with CSD number: **805654**.

Structure code	JH_az_PhNNHPh	Z	2
Empirical formula	C ₄₁ H ₅₀ N ₄ Si	Crystal dimensions [mm ³]	0.20 x 0.12 x 0.06
Formula weight [g mol ⁻¹]	626.94	$\rho_{\text{calcd.}}$ [g cm ⁻³]	1.172
Sample temperature [K]	80 (2)	μ [mm ⁻¹]	0.100
Wavelength [Å]	0.71073	<i>F</i> (000)	676
Crystal system	Triclinic	θ range [°]	1.58 – 25.35
Space group	<i>P</i> $\bar{1}$	Reflections collected	29684
Unit cell dimensions [Å]		Unique reflections	6480
	a = 10.9890 (17)	<i>R</i> _{int}	0.0487
	b = 12.566 (2)	Completeness to θ_{max}	99.6 %
	c = 12.909 (2)	restraints/parameters	23/427
	α = 92.357(3) °	Goof	1.030
	β = 93.727(3) °	<i>R</i> 1 (<i>I</i> > 2 σ (<i>I</i>))	0.0405
	γ = 90.731(4) °	w <i>R</i> 2 (all data)	0.0979
Volume [Å ³]	1777.1 (5)	max. diff. peak/hole [e Å ⁻³]	0.255/–0.323
Extinction coefficient	-	Absolute structure parameter	-

9.5.12. *JH_az_tollyhydra*

Graphical representation of the formula unit. Isopropyl methyl groups at C12, C15, C24, and C27 have been omitted for clarity. The hydrogen atoms at Si1 and N3 were found and assigned from a Fourier difference analysis. The position and U_{iso} of H15 were refined freely. Positional parameters and U_{iso} of H3N were refined using a riding model (AFIX 43). Several overlapping molecules of *n*-hexane of which each has a different site occupation factor were modelled. The displacement parameters and positions of the solvent molecule atoms were partly constrained to each other.

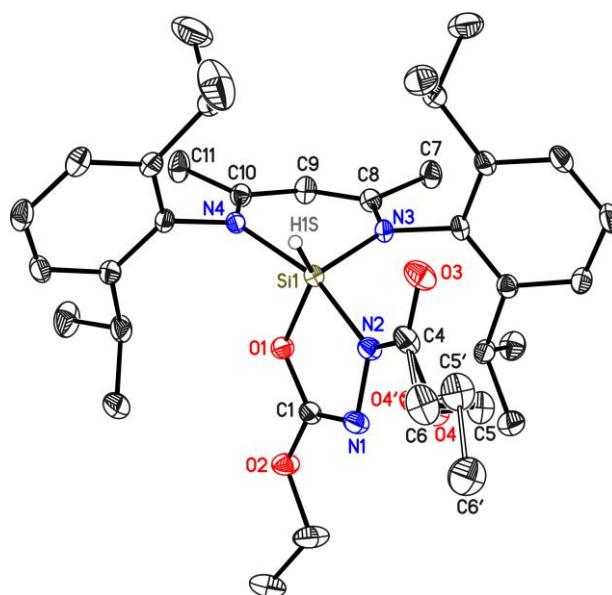
Structure published in:

Ramachandran Azhakar, Rajendra S. Ghadwal, Herbert W. Roesky, Jakob Hey, Dietmar Stalke „Double N-H Bond Activation of Substituted Hydrazines with Stable N-Heterocyclic Silylene” *Dalton Trans.* **2012**, *41*, 1529-1533.

Structural information in CIF format is also deposited and available with CSD number: **817515**.

Structure code	JH_az_PhNNHPH	Z	4
Empirical formula	C _{39.12} H _{62.48} N ₄ OSi	Crystal dimensions [mm ³]	0.22 x 0.16 x 0.12
Formula weight [g mol ⁻¹]	625.64	$\rho_{\text{calcd.}}$ [g cm ⁻³]	1.154
Sample temperature [K]	100 (2)	μ [mm ⁻¹]	0.101
Wavelength [Å]	0.71073	$F(000)$	1360
Crystal system	Monoclinic	θ range [°]	1.56 – 26.11
Space group	$P2_1/n$	Reflections collected	57531
Unit cell dimensions [Å]		Unique reflections	7146
	a = 11.4828(8)	R_{int}	0.0368
	b = 12.0258(9)	Completeness to θ_{max}	99.8 %
	c = 26.1609(19)	restraints/parameters	2/434
	$\alpha = 90^\circ$	GooF	1.042
	$\beta = 94.746(2)^\circ$	$R1$ ($I > 2\sigma(I)$)	0.0367
	$\gamma = 90^\circ$	wR2 (all data)	0.0955
Volume [Å ³]	3600.2(5)	max. diff. peak/hole [e Å ⁻³]	0.306/−0.363
Extinction coefficient	-	Absolute structure parameter	-

9.5.13. JH_az_NHCOOEt2



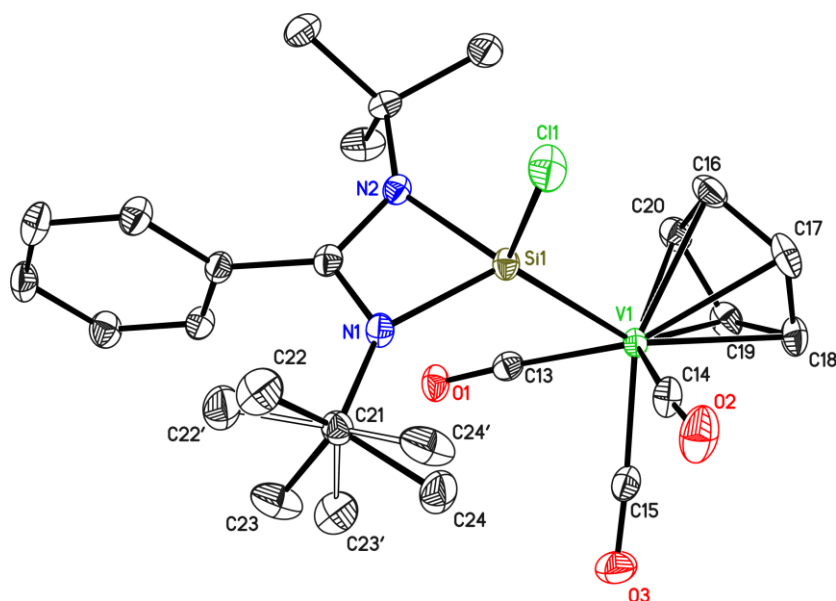
Graphical representation of the asymmetric unit. Hydrogen atoms except H1S have been omitted for clarity. The hydrogen atoms at Si1 was found and assigned from a Fourier difference analysis. Its U_{iso} was constrained to 1.5 times the U_{eq} of Si1. A minor disorder in one of the ethyl groups was modelled.

Structure published in:

Ramachandran Azhakar, Rajendra S. Ghadwal, Herbert W. Roesky, Jakob Hey, Dietmar Stalke „Double N-H Bond Activation of Substituted Hydrazines with Stable N-Heterocyclic Silylene” *Dalton Trans.* **2012**, 41, 1529-1533.

Structural information in CIF format is also deposited and available with CSD number: **817514**.

Structure code	JH_az_PhNNHPh	Z	4
Empirical formula	C ₃₅ H ₅₂ N ₄ O ₄ Si	Crystal dimensions [mm ³]	0.18 x 0.14 x 0.11
Formula weight [g mol ⁻¹]	620.90	$\rho_{\text{calcd.}}$ [g cm ⁻³]	1.187
Sample temperature [K]	100 (2)	μ [mm ⁻¹]	0.065
Wavelength [Å]	0.56086	$F(000)$	1344
Crystal system	Monoclinic	θ range [°]	1.22 – 21.06
Space group	$P2_1/c$	Reflections collected	97129
Unit cell dimensions [Å]		Unique reflections	7620
	a = 13.2681(14)	R_{int}	0.0576
	b = 12.0341(12)	Completeness to θ_{max}	99.7 %
	c = 21.837(2)	restraints/parameters	4/440
	$\alpha = 90^\circ$	GooF	1.099
	$\beta = 94.780(5)^\circ$	$R1$ ($I > 2\sigma(I)$)	0.0456
	$\gamma = 90^\circ$	wR2 (all data)	0.1181
Volume [Å ³]	3474.6(6)	max. diff. peak/hole [e Å ⁻³]	0.337/–0.334
Extinction coefficient	-	Absolute structure parameter	-

9.5.14. *JH_az_LSiCl_cpVCO4*

Graphical representation of the asymmetric unit. Hydrogen atoms have been omitted for clarity. A rotational disorder of the methyl groups around C21 was modelled as shown. Similarity restraints were applied to the displacement parameters of the atoms belonging to carbonyl groups. 1,2 and 1,3 distances in the disordered *tert*-butyl group were restrained on each other.

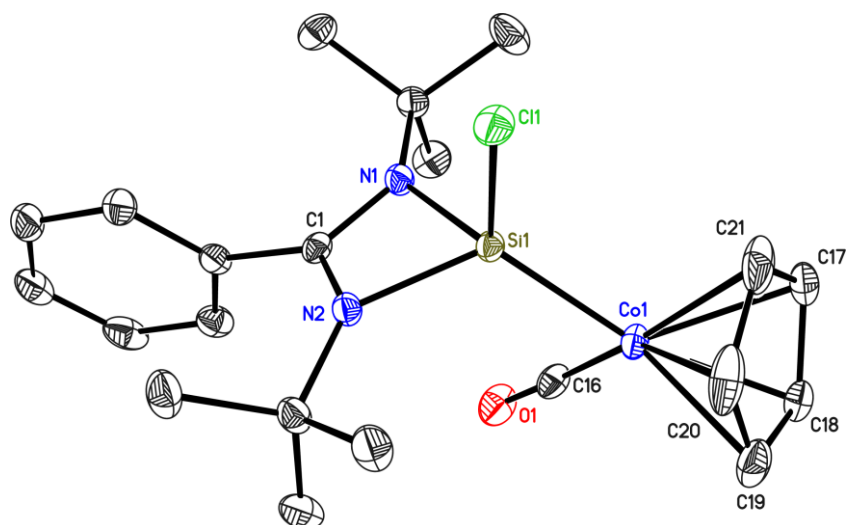
Structure published in:

Ramachandran Azhakar, Rajendra S. Ghadwal, Herbert W. Roesky, Jakob Hey, Dietmar Stalke „Facile Access to Transition-Carbonyl Complexes with an Amidinate-Stabilized Chlorosilylene Ligand”, *Chem. Asian J.* **2012**, *7*, 528-533.

Structural information in CIF format is also deposited and available with CSD number: **827257**.

Structure code	JH_az_LSiCl_CpVCO4	Z	8
Empirical formula	C ₂₃ H ₂₈ ClN ₂ O ₃ SiV	Crystal dimensions [mm ³]	0.18 x 0.14 x 0.11
Formula weight [g mol ⁻¹]	494.95	ρ_{calc} [g cm ⁻³]	1.401
Sample temperature [K]	100 (2)	μ [mm ⁻¹]	0.615
Wavelength [Å]	0.71073	<i>F</i> (000)	2064
Crystal system	Monoclinic	θ range [°]	1.45 – 27.148
Space group	<i>C2/c</i>	Reflections collected	37731
Unit cell dimensions [Å]		Unique reflections	5571
	a = 28.819(4)	R _{int}	0.0333
	b = 8.2139(11)	Completeness to θ_{max}	100.0 %
	c = 20.344(3)	restraints/parameters	43/317
	$\alpha = 90^\circ$	GooF	1.043
	$\beta = 102.955(4)^\circ$	R1 (<i>I</i> > 2 σ (<i>I</i>))	0.0265
	$\gamma = 90^\circ$	wR2 (all data)	0.0697
Volume [Å ³]	4693.3(11)	max. diff. peak/hole [e Å ⁻³]	0.352/–0.279
Extinction coefficient	-	Absolute structure parameter	-

9.5.15. JH_az_LSiCl_cpCoCO



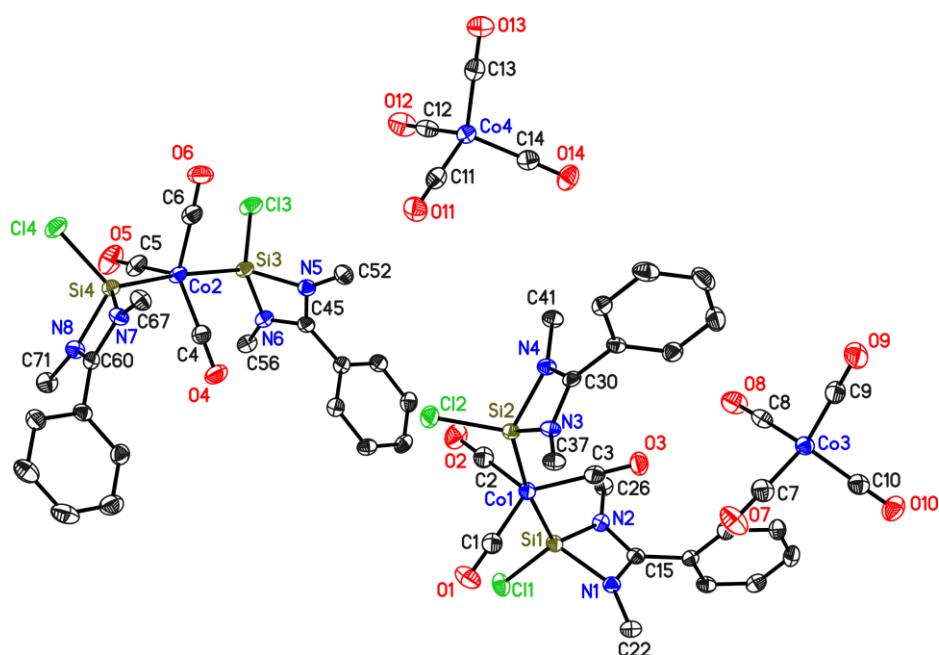
Graphical representation of the asymmetric unit. Hydrogen atoms have been omitted for clarity.

Structure published in:

Ramachandran Azhakar, Rajendra S. Ghadwal, Herbert W. Roesky, Jakob Hey, Dietmar Stalke „Facile Access to Transition-Carbonyl Complexes with an Amidinate-Stabilised Chlorosilylene Ligand”, *Chem. Asian J.* **2012**, 7, 528-533.

Structural information in CIF format is also deposited and available with CSD number: **827256**.

Structure code	JH_az_LSiCl_CpCoCO	Z	4
Empirical formula	C ₂₁ H ₂₈ ClCoN ₂ OSi	Crystal dimensions [mm ³]	0.18 x 0.10 x 0.08
Formula weight [g mol ⁻¹]	446.92	$\rho_{\text{calcd.}}$ [g cm ⁻³]	1.378
Sample temperature [K]	100 (2)	μ [mm ⁻¹]	0.989
Wavelength [Å]	0.71073	$F(000)$	936
Crystal system	Monoclinic	θ range [°]	2.01 – 27.10
Space group	$P2_1/c$	Reflections collected	57764
Unit cell dimensions [Å]		Unique reflections	4738
	a = 9.1281(5)	R_{int}	0.0262
	b = 11.6306(6)	Completeness to θ_{max}	100.0 %
	c = 20.2978(11)	restraints/parameters	113/2507
	$\alpha = 90^\circ$	Goof	1.080
	$\beta = 90.357(2)^\circ$	$R1$ ($I > 2\sigma(I)$)	0.0236
	$\gamma = 90^\circ$	wR2 (all data)	0.0566
Volume [Å ³]	2154.9(2)	max. diff. peak/hole [e Å ⁻³]	0.350/−0.256
Extinction coefficient	-	Absolute structure parameter	-

9.5.16. *JH_az_LSiCl_CoCO8*

Graphical representation of the asymmetric unit. All hydrogen atoms and the *tert*-butyl methyl groups at C22, C26, C37, C41, C52, C56, C67, and C71 have been omitted for clarity.

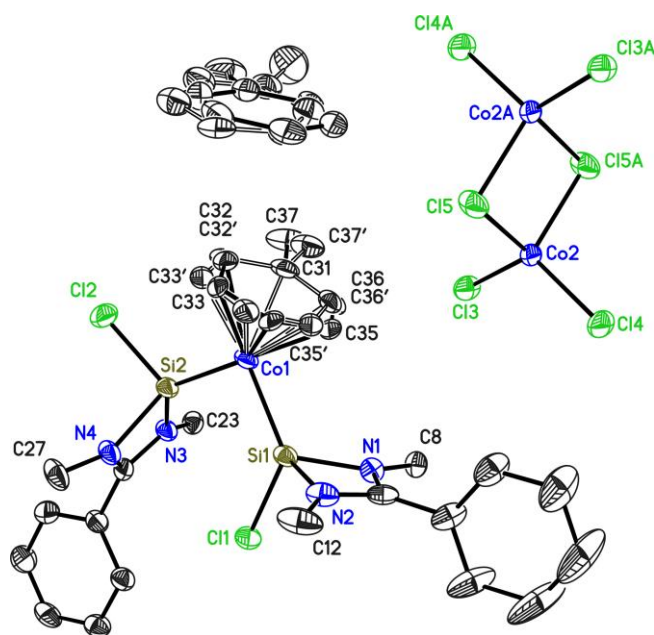
Structure published in:

Ramachandran Azhakar, Sankaranarayana Pillai Sarish, Gašper Tavčar, Herbert W. Roesky, Jakob Hey, Dietmar Stalke, Debasis Koley „Formation of Silicon Centered Spirocyclic Compounds: Reaction of N-Heterocyclic Stable Silylene with Benzoylpyridine, Diisopropyl Azodicarboxylate and 1,2-Diphenylhydrazine" *Inorg. Chem.* **2011**, *50*, 3028-3036.

Structural information in CIF format is also deposited and available with CSD number: **827255**.

Structure code	JH_az_LSiCl_CoCO8	Z	4
Empirical formula	C ₃₇ H ₁₆ Cl ₂ Co ₂ N ₄ O ₇ Si ₂	Crystal dimensions [mm ³]	0.15 x 0.10 x 0.04
Formula weight [g mol ⁻¹]	903.72	$\rho_{\text{calcd.}}$ [g cm ⁻³]	1.375
Sample temperature [K]	100 (2)	μ [mm ⁻¹]	0.985
Wavelength [Å]	0.71073	<i>F</i> (000)	1872
Crystal system	Triclinic	θ range [°]	0.93 – 26.75
Space group	<i>P</i> $\bar{1}$	Reflections collected	98794
Unit cell dimensions [Å]		Unique reflections	18539
	a = 10.4939(8)	<i>R</i> _{int}	0.0460
	b = 19.1774(14)	Completeness to θ_{max}	99.8 %
	c = 22.0925(16)	restraints/parameters	50/997
	α = 97.061(2) °	GooF	1.015
	β = 90.137(2) °	<i>R</i> 1 (<i>I</i> > 2 σ (<i>I</i>))	0.0323
	γ = 98.196(2) °	w <i>R</i> 2 (all data)	0.0736
Volume [Å ³]	4366.3(6)	max. diff. peak/hole [e Å ⁻³]	0.511/–0.303
Extinction coefficient	-	Absolute structure parameter	-

9.5.17. JH_az_Cobalt



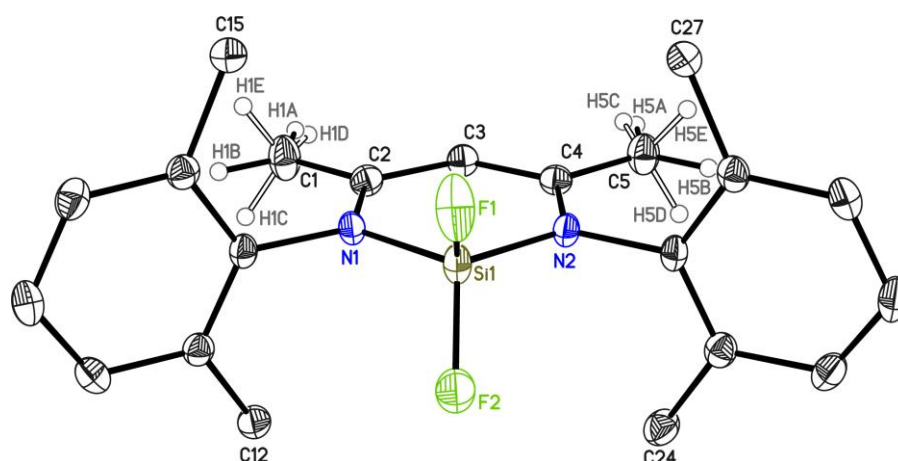
Graphical representation of the formula unit. Hydrogen atoms are omitted. Half of the $\text{Co}_2\text{Cl}_6^{2-}$ anion is created by symmetry; the whole cationic bisamidinate moiety is contained in the asymmetric unit.

The sample was a split crystal. Three domains were integrated (fractions: 90.0%, 8.2%, 1.8%); an HKLF4 file containing data only of the strong domain was used for structure solution. An HKLF5 file containing exclusively reflection data of the strong domain was used for refinement. The toluene molecule coordinated to Co1 is included as a disordered model on two sites with site occupation factors manually set to 0.5. The toluene solvent molecule is disordered over two sites with a refined s.o.f of 0.50.

This structure has not been published in an article yet. A manuscript is in preparation (Ramachandran Azhakar, Rajendra S. Ghadwal, Herbert W. Roesky, Jakob Hey, Lennard Krause, Dietmar Stalke "Diverse Reactivity of stable N-Heterocyclic Monochlorosilylene $\text{PhC}(\text{NtBu})_2\text{SiCl}$ with CoX_2 ($\text{X} = \text{Cl}, \text{Br}$)").

Structural information in CIF format is deposited and available with CSD number: **868295**.

Structure code	JH_az_Cobalt	Z	4
Empirical formula	$\text{C}_{44}\text{H}_{62}\text{Cl}_5\text{Co}_2\text{N}_4\text{Si}_2$	Crystal dimensions [mm^3]	0.06 x 0.05 x 0.04
Formula weight [g mol^{-1}]	998.27	$\rho_{\text{calcd.}}$ [g cm^{-3}]	1.339
Sample temperature [K]	100 (2)	μ [mm^{-1}]	1.022
Wavelength [\AA]	0.71073	$F(000)$	2048
Crystal system	Monoclinic	θ range [$^\circ$]	1.27 – 24.76
Space group	$P2_1/n$	Reflections collected	297646
Unit cell dimensions [\AA]		Unique reflections	9721
	a = 10.4803(19)	R_{int}	0.0862
	b = 32.015(6)	Completeness to θ_{max}	99.5 %
	c = 14.974(3)	restraints/parameters	489/651
	$\alpha = 90^\circ$	GooF	1.024
	$\beta = 99.675(7)^\circ$	$R1$ ($I > 2\sigma(I)$)	0.0428
	$\gamma = 90^\circ$	wR2 (all data)	0.0912
Volume [\AA^3]	4952.6(16)	max. diff. peak/hole [e \AA^{-3}]	0.394/–0.349
Extinction coefficient	-	Absolute structure parameter	-

9.5.18. *JH_az_SiF2*

Graphical representation of the asymmetric unit. Hydrogen atoms except those at C1 and C5 are omitted; *iso*-propyl methyl groups at C12, C15, C24, and C27 are omitted, too.

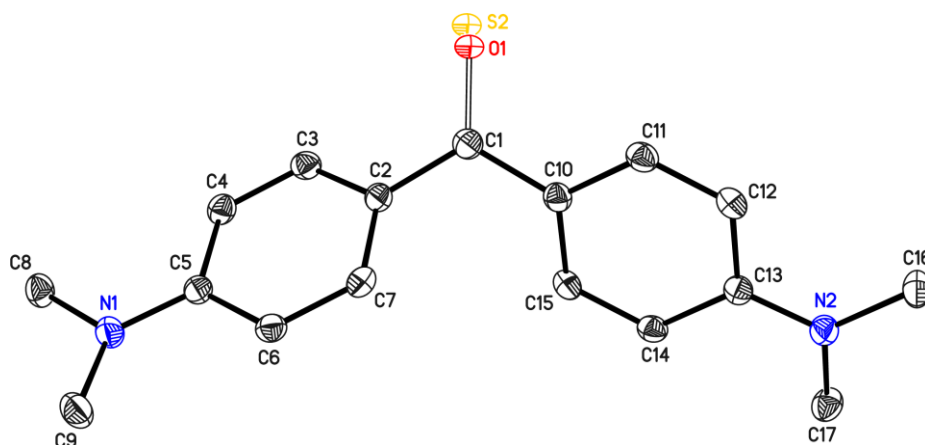
There is a 50/50 disorder of the C1/C2/C3/C4/C5 backbone of the heterocycle as indicated by the hydrogen atoms at C1 and C5. The disorder of the carbon atoms was not modelled.

This structure has not been published in an article yet.

Structural information in CIF format is deposited and available with CSD number: **939931**.

Structure code	JH_az_LSiCl_CoCO8	Z	4
Empirical formula	C ₂₉ H ₄₀ F ₂ N ₂ Si	Crystal dimensions [mm ³]	0.20 x 0.10 x 0.06
Formula weight [g mol ⁻¹]	482.72	ρ_{calcd} [g cm ⁻³]	1.174
Sample temperature [K]	100 (2)	μ [mm ⁻¹]	0.119
Wavelength [Å]	0.71073	<i>F</i> (000)	1040
Crystal system	Monoclinic	θ range [°]	1.95 – 26.76
Space group	<i>P</i> 2 ₁ / <i>n</i>	Reflections collected	78180
Unit cell dimensions [Å]		Unique reflections	5796
	<i>a</i> = 12.466(2)	<i>R</i> _{int}	0.0276
	<i>b</i> = 16.266(2)	Completeness to θ_{max}	99.8 %
	<i>c</i> = 13.950(2)	restraints/parameters	0/319
	α = 90 °	GooF	1.038
	β = 105.06(2) °	<i>R</i> 1 (<i>I</i> > 2 σ (<i>I</i>))	0.0353
	γ = 90 °	w <i>R</i> 2 (all data)	0.0915
Volume [Å ³]	2731.5(7)	max. diff. peak/hole [e Å ⁻³]	0.299/–0.359
Extinction coefficient	-	Absolute structure parameter	-

9.5.19. JH_az_nacnacSi_Net2CS



Graphical representation of the asymmetric unit. Hydrogen atoms are omitted in this figure.

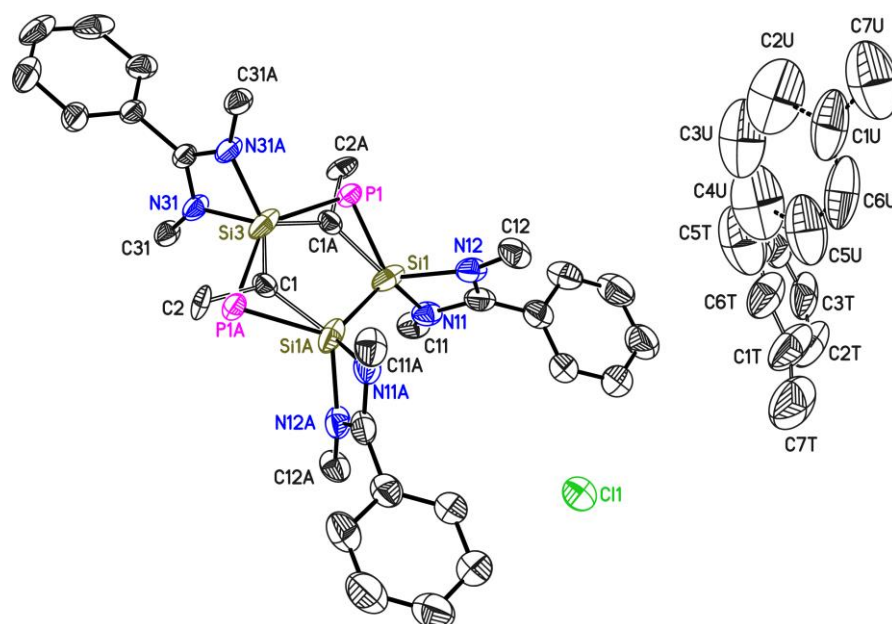
There is a 89/11 sulfur/oxygen disorder at atom C1. The displacement parameters of O1 and S2 were constrained on each other.

This structure has not been published in an article yet. The compound is one of the starting materials for a reaction that Dr. R. Azhakar carried out; it is commercially available, but a crystal structure has not been published elsewhere.

Structure code	JH_az_LSiCl_CoCO8	Z	4
Empirical formula	C ₁₇ H ₂₀ N ₂ O _{0.11} S _{0.89}	Crystal dimensions [mm ³]	0.18 x 0.13 x 0.07
Formula weight [g mol ⁻¹]	282.62	$\rho_{\text{calcd.}}$ [g cm ⁻³]	1.285
Sample temperature [K]	100 (2)	μ [mm ⁻¹]	0.198
Wavelength [Å]	0.71073	$F(000)$	604
Crystal system	Monoclinic	θ range [°]	1.861 – 27.103
Space group	$P2_1/n$	Reflections collected	22755
Unit cell dimensions [Å]		Unique reflections	3232
	a = 5.9505(4)	R_{int}	0.0294
	b = 14.0172(11)	Completeness to θ_{max}	100.0 %
	c = 17.5506(14)	restraints/parameters	0/189
	$\alpha = 90^\circ$	Goof	1.034
	$\beta = 93.557(3)^\circ$	R1 ($I > 2\sigma(I)$)	0.0313
	$\gamma = 90^\circ$	wR2 (all data)	0.0801
Volume [Å ³]	1461.06(19)	max. diff. peak/hole [e Å ⁻³]	0.276/–0.207
Extinction coefficient	-	Absolute structure parameter	-

9.6. Structures determined for Dr. Sakya S. Sen (Prof. Dr. H. W. Roesky)

9.6.1. Sakya_Si_cation



Graphical representation of the formula unit, which consists of two asymmetric units. Hydrogen atoms and *tert*-butyl methyl groups at C11, C12, C31, C11A, C12A, and C31A are omitted for clarity.

An initial data collection led to the observation of a doubled *c* axis. While the structure fulfilled the translational symmetry leading to the smaller *c* axis, the disordered solvent did not. In a second attempt to collect a dataset on another crystal, the sample cooling failed, leading to an annealing of the mounted crystal. The crystal became opaque, but after recovering the crystal and cooling it down, it diffracted again and a dataset with halved *c* axis was recorded. A comparison of the primary dataset (only with the small cell) and the second dataset yielded no significant difference except in solvent content and solvent orientation in the voids.

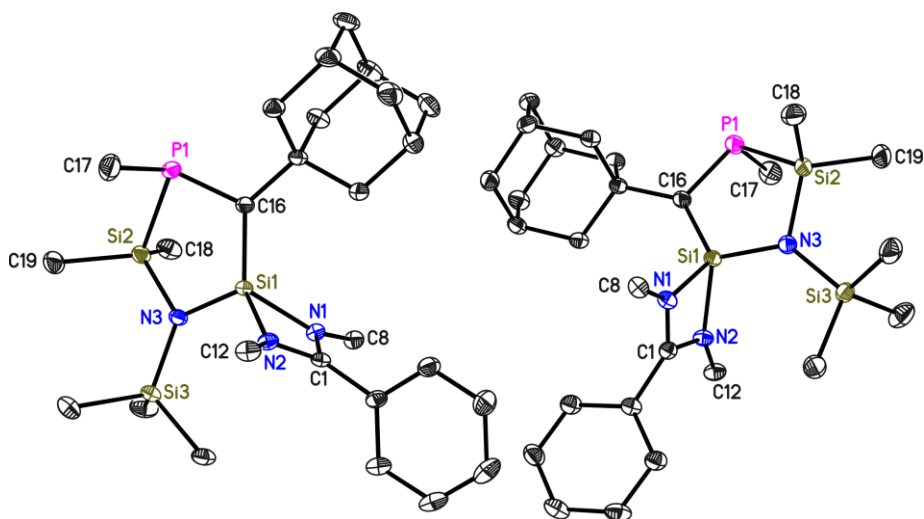
The structure is disordered by the crystallographic twofold axis. The solvent shows disorder. 1,2 and 1,3 distance similarity restraints and displacement parameter similarity restraints were employed in the refinement of large parts of the model. Refinement in space group $P3_1$ was possible but resulted in no improved structure compared to $P3_212$.

Structure published in:

Sakya S. Sen, Jakob Hey, Maria Eckhardt, Regine Herbst-Irmer, Ricardo A. Mata, Herbert W. Roesky, Manfred Scheer, Dietmar Stalke „A Stable Cation of a CS_3P Five-Membered Ring with a Weakly Coordinated Chloride Anion" *Angew. Chem.* **2011**, *123*, 12718-12721; *Angew. Chem. Int. Ed.* **2011**, *50*, 12510-12513 and back cover.

Structural information in CIF format is also deposited and available with CSD number: **826887**.

Structure code	JH_sakya_Si_cation	Z	3
Empirical formula	C ₆₁ H ₈₈ ClN ₆ PSi ₃	Crystal dimensions [mm ³]	0.12 x 0.10 x 0.08
Formula weight [g mol ⁻¹]	1056.06	$\rho_{\text{calcd.}}$ [g cm ⁻³]	1.121
Sample temperature [K]	100(2)	μ [mm ⁻¹]	0.113
Wavelength [Å]	0.71073	<i>F</i> (000)	1710
Crystal system	Trigonal	θ range [°]	1.79 – 26.02
Space group	<i>P</i> 3 ₂ 12	Reflections collected	53639
Unit cell dimensions [Å]		Unique reflections	6185
	a = 13.166(2)	<i>R</i> _{int}	0.0286
	b = 13.166(2)	Completeness to θ_{max}	100.0 %
	c = 31.268(4)	restraints/parameters	563/418
	$\alpha = 90^\circ$	GooF	1.201
	$\beta = 90^\circ$	<i>R</i> 1 (<i>I</i> > 2 σ (<i>I</i>))	0.0535
	$\gamma = 120^\circ$	w <i>R</i> 2 (all data)	0.1421
Volume [Å ³]	4693.9(12)	max. diff. peak/hole [e Å ⁻³]	0.484/−0.210
Extinction coefficient	-	Absolute structure parameter	-0.09(9)

9.6.3. *JH_Sakya_AdCP_Ag*

Graphical representation of the symmetric unit. It consists of two molecules; each was refined in a separate residue using the RESI command of SHELXL-97 (hence the identical numbering). The *tert*-butyl methyl groups at C8 and C12 have been omitted for clarity. A very slight disorder with site occupation factor less than 2% in both of the heterocyclic CNSi₂P rings eventually had to be neglected.

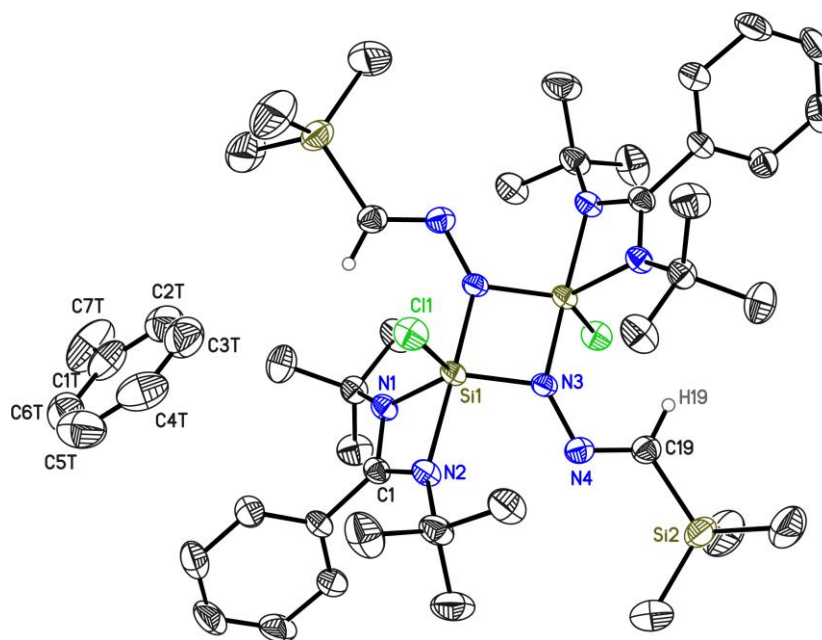
Structure published in:

Sakya S. Sen, Jakob Hey, Regine Herbst-Irmer, Herbert W. Roesky, Dietmar Stalke „Striking Stability of Bis(trimethylsilyl) Amino Silylene and the Facile Si-Me Activation without a Transition Metal Catalyst" *J. Am. Chem. Soc.* **2011**, 133, 12311-12316.

Structural information in CIF format is also deposited and available with CSD number: **828728**.

Structure code	JH_sakya_AdCP_Ag	Z	4
Empirical formula	C ₃₂ H ₅₆ N ₃ PSi ₃	Crystal dimensions [mm ³]	0.18 x 0.10 x 0.08
Formula weight [g mol ⁻¹]	598.04	$\rho_{\text{calcd.}}$ [g cm ⁻³]	1.146
Sample temperature [K]	101(2)	μ [mm ⁻¹]	0.113
Wavelength [Å]	0.56086	$F(000)$	1304
Crystal system	Triclinic	θ range [°]	1.32 – 22.75
Space group	$P\bar{1}$	Reflections collected	119976
Unit cell dimensions [Å]		Unique reflections	19013
	a = 12.866(2)	R_{int}	0.0310
	b = 16.639(2)	Completeness to θ_{max}	99.8 %
	c = 17.090(2)	restraints/parameters	0/727
	$\alpha = 90.72(2)^\circ$	Goof	1.026
	$\beta = 108.43(2)^\circ$	R1 ($I > 2\sigma(I)$)	0.0366
	$\gamma = 91.82(2)^\circ$	wR2 (all data)	0.09998
Volume [Å ³]	3468.2(11)	max. diff. peak/hole [e Å ⁻³]	0.978/–0.392
Extinction coefficient	-	Absolute structure parameter	-

9.6.4. JH_Sakya_azoalk



Graphical representation of the formula unit, which consists of two asymmetric units. Hydrogen atoms are omitted for clarity.

Structure published in:

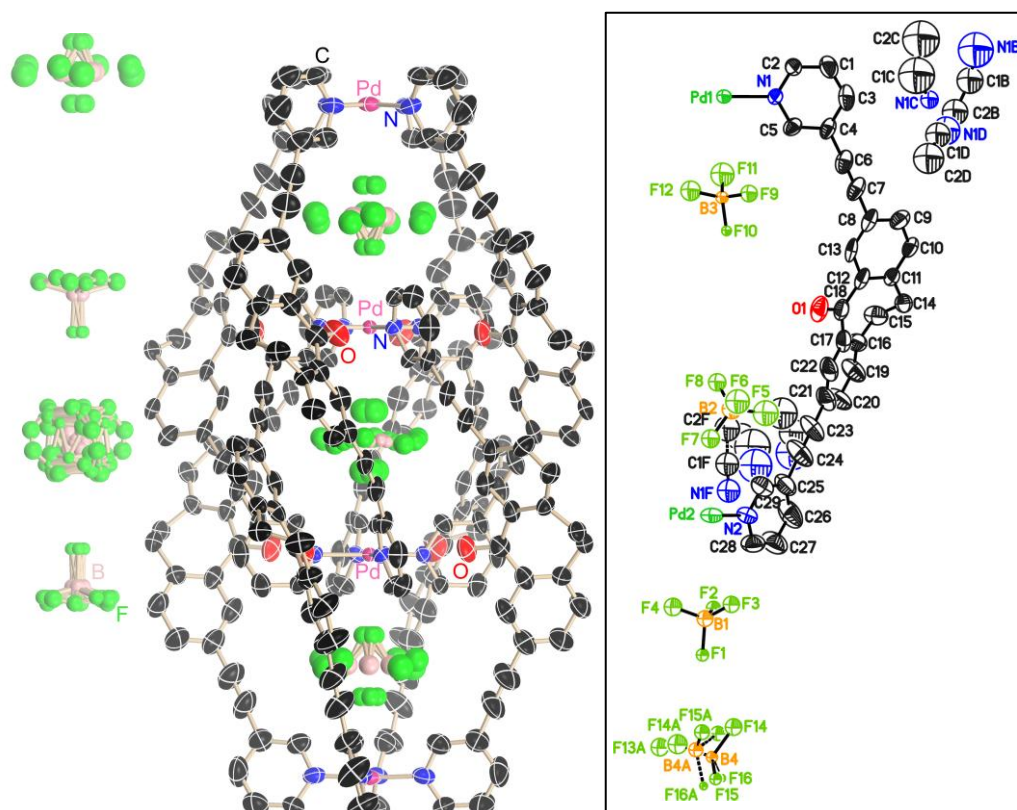
Sakya S. Sen, Jakob Hey, Daniel Kratzert, Herbert W. Roesky, Dietmar Stalke „A Remarkable End-On Activation of Diazoalkane and Cleavage of Both C–Cl Bonds of Dichloromethane with a Silylene to a Single Product with Five-Coordinate Silicon Atoms” *Organometallics* **2012**, *31*, 435–439.

Structural information in CIF format is also deposited and available with CSD number: **843607**.

Structure code	JH_sakya_azoalk	Z	2
Empirical formula	C ₅₂ H ₈₂ Cl ₂ N ₈ Si ₄	Crystal dimensions [mm ³]	0.12 x 0.10 x 0.08
Formula weight [g mol ⁻¹]	1002.52	$\rho_{\text{calcd.}}$ [g cm ⁻³]	1.141
Sample temperature [K]	200(2)	μ [mm ⁻¹]	0.233
Wavelength [Å]	0.71073	<i>F</i> (000)	1080
Crystal system	Trigonal	θ range [°]	1.71 – 25.70
Space group	<i>P</i> 2 ₁ / <i>n</i>	Reflections collected	38753
Unit cell dimensions [Å]		Unique reflections	5502
	<i>a</i> = 12.613(2)	<i>R</i> _{int}	0.0321
	<i>b</i> = 11.307(2)	Completeness to θ_{max}	99.0 %
	<i>c</i> = 21.148(2)	restraints/parameters	0/308
	α = 90 °	Goof	1.059
	β = 104.57(2) °	<i>R</i> 1 (<i>I</i> > 2 σ (<i>I</i>))	0.0404
	γ = 90 °	w <i>R</i> 2 (all data)	0.1101
Volume [Å ³]	2919.0(7)	max. diff. peak/hole [e Å ⁻³]	0.348/–0.280
Extinction coefficient	-	Absolute structure parameter	-

9.7. Structure determined for Sabrina Freye (Prof. Dr. G. Clever)

9.7.1. JH_Clever_15



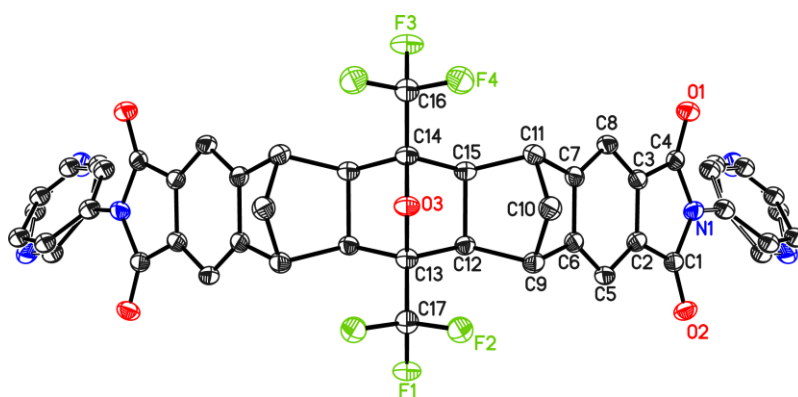
Representation of the formula unit (left, acetonitrile molecules omitted) and the asymmetric unit.

The structure contains significant amounts of disordered lattice solvent molecules (acetonitrile), which could be modeled to a certain extent. Similarity restraints with lowered standard deviation were applied to distances and displacement parameters in disordered parts of the model.

Structure published in: Sabrina Freye, Jakob Hey, Anna Torras-Galán, Dietmar Stalke, Regine Herbst-Irmer, Michael John, Guido H. Clever „Allosteric Binding of Halide Anions by a New Dimeric Interpenetrated Coordination Cage” *Angew. Chem.* **2012**, *124*, 2233-2237; *Angew. Chem. Int. Ed.* **2012**, *51*, 2191-2194.

Structural information in CIF format is also deposited and available with CSD number: **844925**.

Structure code	JH_Clever_Muxin2	Z	2
Empirical formula	C ₂₆₄ H ₁₉₂ B ₆ F ₂₄ N ₃₂ O ₈ Pd ₄	Crystal dimensions [mm ³]	0.01 x 0.01 x 0.02
Formula weight [g mol ⁻¹]	4886.96	$\rho_{\text{calcd.}}$ [g cm ⁻³]	1.379
Sample temperature [K]	100(2)	μ [mm ⁻¹]	3.141
Wavelength [Å]	1.54178	<i>F</i> (000)	4988
Crystal system	Tetragonal	θ range [°]	2.05 to 60.18
Space group	<i>P4/nnc</i>	Reflections collected	56140
Unit cell dimensions [Å]		Unique reflections	4381
	a = 16.542(2)	R_{int}	0.0660
	b = 16.542(2)	Completeness to θ_{max}	99.0 %
	c = 43.002(3)	restraints/parameters	525/468
	$\alpha = 90^\circ$	Goof	1.220
	$\beta = 90^\circ$	<i>R</i> 1 (<i>I</i> > 2 σ (<i>I</i>))	0.1198
	$\gamma = 90^\circ$	w <i>R</i> 2 (all data)	0.2227
Volume [Å ³]	11767(2)	max. diff. peak/hole [e Å ⁻³]	0.580/-0.573
Extinction coefficient	-	Absolute structure parameter	-

9.7.2. *JH_Clever_01*

The crystallographic mirror plane creates the formula unit from the asymmetric unit.

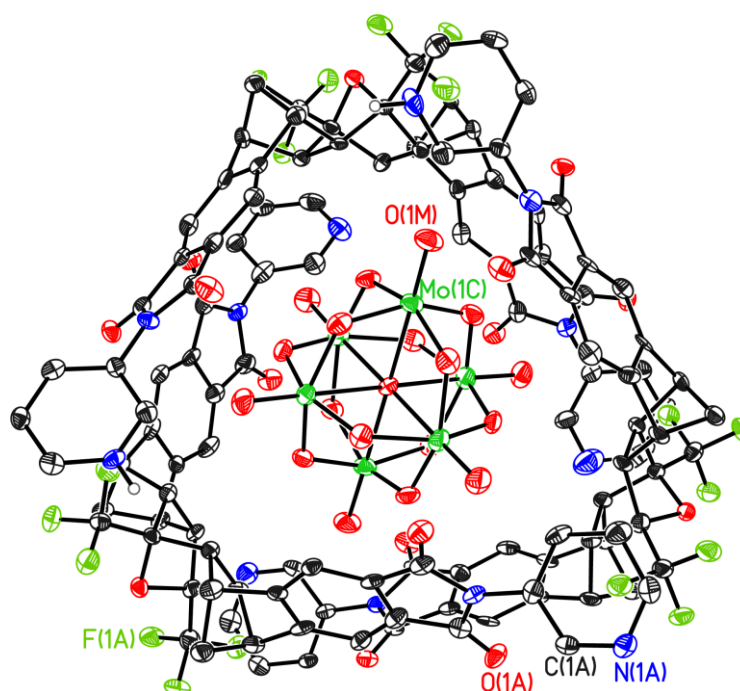
Hydrogen atoms and labels of atoms in the disordered part are omitted.

The atomic displacement parameters of suitable atom pairs in the disordered pyridyl groups were constrained to each other with the EADP command.

Structural information in CIF format is also deposited and available with CSD number: **939932**.

Structure code	JH_Clever01	Z	2
Empirical formula	C ₁₀ H ₂₄ F ₆ N ₄ O ₅	Crystal dimensions [mm ³]	0.15 x 0.12 x 0.10
Formula weight [g mol ⁻¹]	754.63	$\rho_{\text{calcd.}}$ [g cm ⁻³]	1.564
Sample temperature [K]	80(2)	μ [mm ⁻¹]	0.128
Wavelength [Å]	0.71073	<i>F</i> (000)	772
Crystal system	Monoclinic	θ range [°]	1.845 – 25.382
Space group	<i>P</i> 2 ₁ / <i>m</i>	Reflections collected	18706
Unit cell dimensions [Å]		Unique reflections	3014
	a = 6.6295(11)	R _{int}	0.0540
	b = 21.891(4)	Completeness to θ_{max}	100.0 %
	c = 11.1133(19)	restraints/parameters	12 /257
	α = 90 °	GooF	1.031
	β = 96.570(4) °	R1 (<i>I</i> > 2 σ (<i>I</i>))	0.0386
	γ = 90 °	wR2 (all data)	0.0995
Volume [Å ³]	1602.2(5)	max. diff. peak/hole [e Å ⁻³]	0.238/–0.307
Extinction coefficient	-	Absolute structure parameter	-

9.8. Structure determined for Muxin Han (Prof. Dr. Clever)



Graphical representation of the asymmetric unit. Several molecules of disordered lattice solvent acetonitrile (H_3CCN) were modeled but are omitted in this figure for clarity. Three of the terminal pyridyl groups are modelled with protonated nitrogen atoms for the sake of electroneutrality.

The sample was a split crystal consisting of two domains. Data were recorded using a Bruker TXS rotating Mo anode. Reflections of both domains were integrated. Structure refinement was performed against data from the stronger of the two domains as well as composite reflections.

Structure published in:

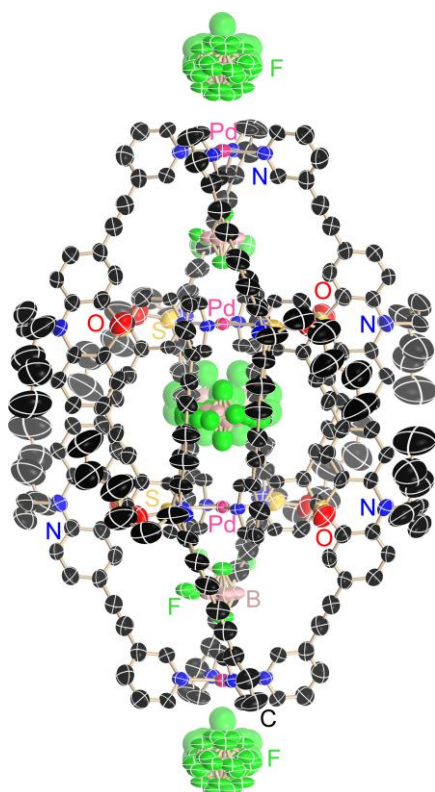
Muxin Han, Jakob Hey, Wataru Kawamura, Dietmar Stalke, Mitsuhiro Shionoya, Guido Clever, „An Inclusion Complex of Hexamolybdate inside a Supramolecular Cage and its Structural Conversion“ *Inorg. Chem.* **2012**, *51*, 9574-9576.

Structural information in CIF format is also deposited and available with CSD number: **857446**.

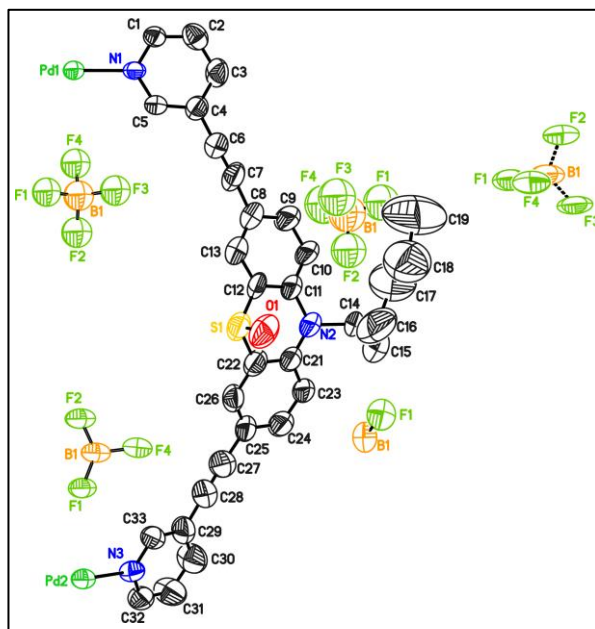
Structure code	JH_Clever_Muxin2	Z	2
Empirical formula	$\text{C}_{138.70}\text{H}_{102.05}\text{F}_{18}\text{Mo}_6\text{N}_{21.35}\text{O}_{34}$	Crystal dimensions [mm^3]	0.02 x 0.015 x 0.01
Formula weight [g mol^{-1}]	3529.41	ρ_{calc} [g cm^{-3}]	1.556
Sample temperature [K]	80 (2)	μ [mm^{-1}]	0.586
Wavelength [\AA]	0.71073	$F(000)$	3546
Crystal system	Triclinic	θ range [$^\circ$]	1.42 – 23.14
Space group	$P\bar{1}$	Reflections collected	119820
Unit cell dimensions [\AA]		Unique reflections	21239
	a = 14.986(4)	R_{int}	0.0774
	b = 23.994(8)	Completeness to θ_{max}	99.5 %
	c = 24.610(9)	restraints/parameters	666/2144
	$\alpha = 62.61(2)^\circ$	GooF	1.063
	$\beta = 82.90(2)^\circ$	R1 ($I > 2\sigma(I)$)	0.0575
	$\gamma = 73.80(2)^\circ$	wR2 (all data)	0.1499
Volume [\AA^3]	7545(4)	max. diff. peak/hole [e \AA^{-3}]	0.709/–0.522
Extinction coefficient	-	Absolute structure parameter	-

9.9. Structures determined for Marina Frank (Prof. Dr. G. Clever)

9.9.1. MF8



The formula unit. Hydrogen atoms are omitted.



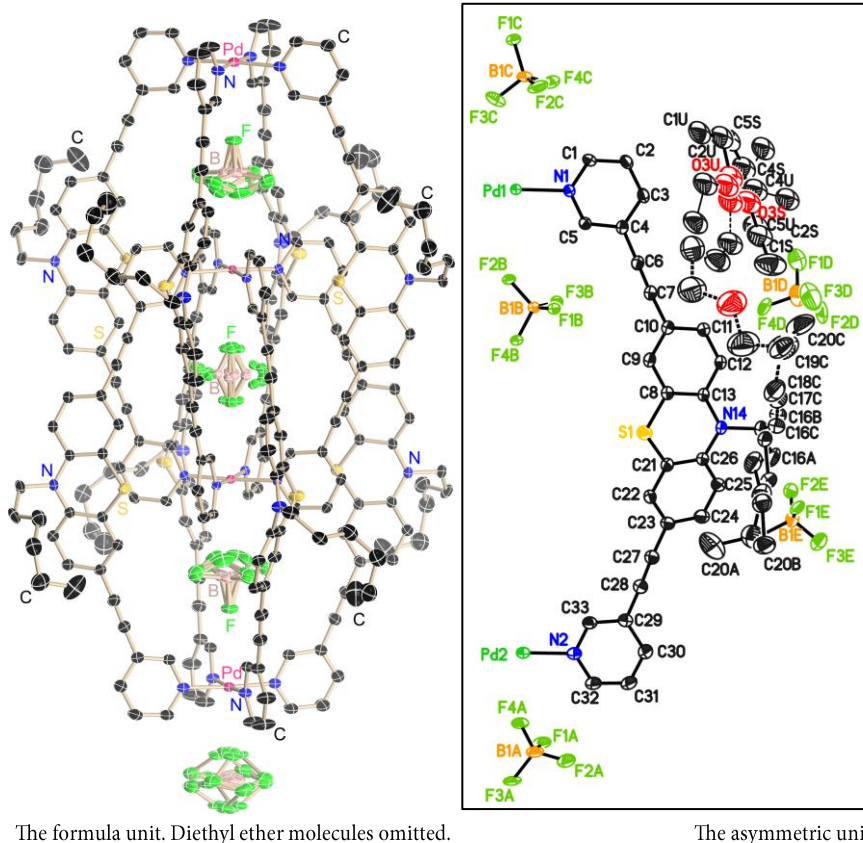
The asymmetric unit.

The structure likely contains significant amounts of disordered lattice solvent molecules, which however could not be modeled due to the rather low resolution of the data. The SQUEEZE routine from the PLATON package of programs was used to reduce the influence of the diffuse electron density from non-modeled solvent in the voids of the structure. Similarity restraints with lowered standard deviation were applied on distances and displacement parameters. The Pd atoms at the special positions $(0,0,z)$ and $(0,0,-z)$ create a pseudo mirror symmetry which is not obeyed by the rest of the molecule. The value of Flack(x) should not erroneously taken as evidence for missed symmetry.

Structure is part of the submitted manuscript: Marina Frank, Jakob Hey, Ilker Balcioglu, Dietmar Stalke, Holm Frauendorf, and Guido H. Clever; submitted to *Angew. Chem.* 2013. Structural information in CIF format is deposited and available with CSD number: **904004**.

Structure code	MF8	Z	2
Empirical formula	C ₂₅₆ H ₂₁₆ B ₈ F ₃₂ N ₂₄ O ₈ Pd ₄ S ₈	Crystal dimensions [mm ³]	0.20 x 0.10 x 0.05
Formula weight [g mol ⁻¹]	5133.09	$\rho_{\text{calcd.}}$ [g cm ⁻³]	1.081
Sample temperature [K]	100(2)	μ [mm ⁻¹]	0.345
Wavelength [Å]	0.71073	F(000)	5248
Crystal system	Tetragonal	θ range [°]	1.12 to 21.51
Space group	I422	Reflections collected	27054
Unit cell dimensions [Å]		Unique reflections	4548
	a = 21.956(2)	R _{int}	0.0532
	b = 21.956(2)	Completeness to θ_{max}	99.5 %
	c = 32.713(4)	restraints/parameters	513/467
	$\alpha = 90^\circ$	GooF	0.946
	$\beta = 90^\circ$	R1 (I > 2 σ (I))	0.0529
	$\gamma = 90^\circ$	wR2 (all data)	0.1560
Volume [Å ³]	15771(3)	max. diff. peak/hole [e Å ⁻³]	1.058/-0.555
Extinction coefficient	-	Absolute structure parameter	0.48(7)

9.9.2. MF9



The structure contains significant amounts of disordered lattice solvent molecules (diethyl ether), which could be modeled to a certain extent due to the rather high resolution of the data. The dataset was collected at the beamline 15ID-B at the *Advanced Photon Source*, Argonne, IL, USA.

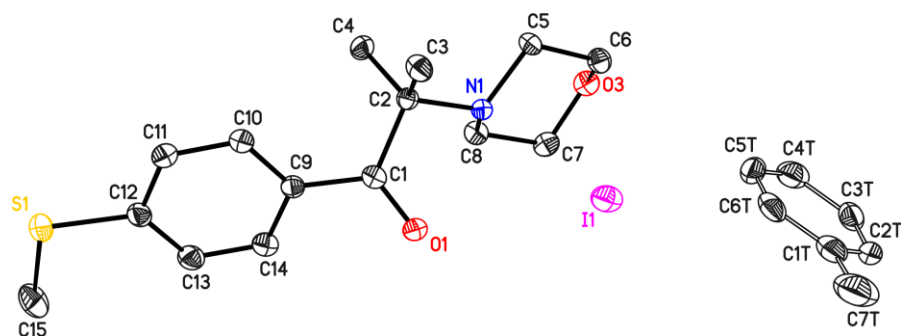
The structure is part of the submitted manuscript:

Marina Frank, Jakob Hey, Ilker Balcioglu, Dietmar Stalke, Holm Frauendorf, and Guido H. Clever; submitted to *Angew. Chem.* **2013**.

Structural information in CIF format is also deposited and available with CSD number: **904005**.

Structure code	MF9	Z	2
Empirical formula	$C_{304}H_{336}B_8F_{32}N_{24}O_{12}Pd_4S_8$	Crystal dimensions [mm ³]	0.20 x 0.10 x 0.05
Formula weight [g mol ⁻¹]	5894.53	$\rho_{\text{calcd.}}$ [g cm ⁻³]	1.281
Sample temperature [K]	15(2)	μ [mm ⁻¹]	0.324
Wavelength [Å]	0.3936	$F(000)$	6128
Crystal system	Tetragonal	θ range [°]	0.63 to 16.31
Space group	<i>P4/nnc</i>	Reflections collected	219452
Unit cell dimensions [Å]		Unique reflections	11661
	a = 21.122(2)	R_{int}	0.1010
	b = 21.122(2)	Completeness to θ_{max}	99.9 %
	c = 34.263(3)	restraints/parameters	2694 /980
	$\alpha = 90^\circ$	GooF	1.012
	$\beta = 90^\circ$	$R1$ ($I > 2\sigma(I)$)	0.0529
	$\gamma = 90^\circ$	wR2 (all data)	0.1671
Volume [Å ³]	11767(2)	max. diff. peak/hole [e Å ⁻³]	1.041/-1.219
Extinction coefficient	-	Absolute structure parameter	-

9.10. Structure determined for Arne Wolpers (Prof. Dr. P. Vana)



Graphical representation of the asymmetric unit.

Hydrogen atoms are omitted. The toluene molecule is located on an inversion centre. Its site occupation factor is 0.5.

This structure has not been published in an article yet.

Structure code	JH_Clever01	Z	8
Empirical formula	C _{18.50} H ₂₆ I NO ₂ S	Crystal dimensions [mm ³]	0.25 x 0.10 x 0.06
Formula weight [g mol ⁻¹]	453.36	$\rho_{\text{calcd.}}$ [g cm ⁻³]	1.531
Sample temperature [K]	101(2)	μ [mm ⁻¹]	1.745
Wavelength [Å]	0.71073	$F(000)$	1832
Crystal system	Monoclinic	θ range [°]	1.724 – 26.800
Space group	C2/c	Reflections collected	36108
Unit cell dimensions [Å]		Unique reflections	4211
	a = 25.869(10)	R _{int}	0.0476
	b = 10.205(3)	Completeness to θ_{max}	100.0 %
	c = 16.311(5)	restraints/parameters	76 /250
	$\alpha = 90^\circ$	GooF	1.014
	$\beta = 114.044(14)^\circ$	R1 (I > 2 σ (I))	0.0380
	$\gamma = 90^\circ$	wR2 (all data)	0.0990
Volume [Å ³]	3933(2)	max. diff. peak/hole [e Å ⁻³]	0.766/−0.528
Extinction coefficient	-	Absolute structure parameter	-

10. Appendix

10.1. Data statistics

Table A 1. Statistics of the collected data on 2 from XPREP 2013/1 output after scaling and absorption correction with SADABS 2008/2.

d [Å]	Data	Theory	Compl.	Red.	<I>	<I/s>	R _{int}	R _{sigma}	R _{rim}	R _{pim}
Inf - 1.97	253	254	99.6	18.73	38.0	101.37	0.0159	0.0084	0.0164	0.0038
1.97 - 1.27	590	591	99.8	21.64	17.3	98.41	0.0207	0.0065	0.0212	0.0045
1.27 - 0.98	862	865	99.7	18.71	10.6	72.56	0.0280	0.0086	0.0288	0.0066
0.98 - 0.85	855	857	99.8	18.30	6.7	64.68	0.0339	0.0102	0.0348	0.0080
0.85 - 0.77	827	827	100.0	24.34	5.0	82.94	0.0329	0.0077	0.0336	0.0067
0.77 - 0.71	895	895	100.0	23.16	4.3	77.50	0.0375	0.0086	0.0383	0.0079
0.71 - 0.67	786	786	100.0	14.91	3.3	62.41	0.0367	0.0106	0.0379	0.0091
0.67 - 0.63	992	995	99.7	9.76	2.5	50.72	0.0279	0.0128	0.0295	0.0093
0.63 - 0.60	904	906	99.8	9.35	2.1	45.45	0.0314	0.0145	0.0332	0.0108
0.60 - 0.58	724	724	100.0	9.25	2.0	45.15	0.0339	0.0151	0.0360	0.0118
0.58 - 0.56	808	808	100.0	8.95	1.5	35.79	0.0400	0.0181	0.0425	0.0141
0.56 - 0.54	979	979	100.0	8.62	1.4	34.86	0.0433	0.0198	0.0461	0.0156
0.54 - 0.52	1065	1067	99.8	8.35	1.1	29.82	0.0500	0.0230	0.0534	0.0184
0.52 - 0.51	627	627	100.0	8.06	0.9	25.53	0.0554	0.0272	0.0592	0.0207
0.51 - 0.49	669	669	100.0	7.98	0.8	23.48	0.0614	0.0297	0.0657	0.0230
0.49 - 0.48	1495	1495	100.0	7.50	0.7	21.23	0.0651	0.0333	0.0700	0.0254
0.48 - 0.47	846	846	100.0	7.34	0.6	18.72	0.0747	0.0384	0.0805	0.0295
0.47 - 0.46	919	919	100.0	6.97	0.5	17.09	0.0792	0.0419	0.0856	0.0321
0.46 - 0.45	1003	1004	99.9	6.57	0.5	16.92	0.0811	0.0434	0.0882	0.0342
0.45 - 0.44	692	733	94.4	4.41	0.4	11.93	0.0938	0.0650	0.1052	0.0463
0.54 - 0.44	7316	7360	99.4 %	7.20	0.70	20.77	0.0640	0.0340	0.0689	0.0251
Inf - 0.44	16791	16847	99.7 %	11.60	3.50	43.34	0.0287	0.0116	0.0296	0.0072

10.2. Topological parameters from QTAIM analysis of 1

Table A 2. Topological parameters from QTAIM analysis of $[(\text{H}_3\text{N})_3\text{Na}(\text{C}_5\text{H}_5)]$ (**1**). Regular numbers correspond to values obtained from the experimental charge density; italic numbers correspond to the density obtained from the DF-LMP2/cc-pCVTZ&cc-pVTZ geometry optimised structure.

Bond A–B	$\rho(\mathbf{r}_{\text{BCP}})$ [e Å ⁻³]	$L(\mathbf{r}_{\text{BCP}})$ [e Å ⁻⁵]	$d(\text{A–B})$ [Å]	$l(\text{A–B})$ [Å]	$l(\text{BCP–A})$ [Å]	$l(\text{BCP–B})$ [Å]	$\epsilon(\mathbf{r}_{\text{BCP}})$
Na1–N1	0.101(1) <i>0.119</i>	+2.509(2) <i>+2.761</i>	2.4599 <i>2.4599</i>	2.46247 <i>2.46007</i>	1.08289 <i>1.06299</i>	1.37958 <i>1.39709</i>	0.01 <i>0.01</i>
Na1–N2	0.101(1) <i>0.118</i>	+2.523(2) <i>+2.727</i>	2.4649 <i>2.4649</i>	2.46511 <i>2.46507</i>	1.08255 <i>1.06445</i>	1.38256 <i>1.40061</i>	0.13 <i>0.00</i>
Na1–C1	0.072(1) <i>0.077</i>	+1.519(2) <i>+1.722</i>	2.7005 <i>2.7005</i>	2.73206 <i>2.71093</i>	1.15998 <i>1.13450</i>	1.57208 <i>1.57644</i>	3.80 <i>4.02</i>
Na1–N2'	0.101(1) <i>0.117</i>	+2.523(2) <i>+2.726</i>	2.4649 <i>2.4649</i>	2.46511 <i>2.46520</i>	1.08256 <i>1.06454</i>	1.38255 <i>1.40066</i>	0.13 <i>0.00</i>
N1–H1A	2.03(2) <i>2.358</i>	–23.8(2) <i>–44.986</i>	1.019 <i>0.9913</i>	1.02051 <i>0.99136</i>	0.75247 <i>0.75012</i>	0.26804 <i>0.24124</i>	0.08 <i>0.03</i>
N1–H1B	2.11(2) <i>2.328</i>	–25.8(2) <i>–46.700</i>	1.017 <i>0.9952</i>	1.01975 <i>0.99528</i>	0.73773 <i>0.76396</i>	0.28202 <i>0.23132</i>	0.07 <i>0.03</i>
N1–H1C	1.65(3) <i>2.358</i>	–5.9(2) <i>–45.642</i>	1.018 <i>0.9913</i>	1.02239 <i>0.99137</i>	0.75438 <i>0.75024</i>	0.26800 <i>0.24112</i>	0.03 <i>0.03</i>
N2–H2A	2.10(3) <i>2.346</i>	–24.4(2) <i>–45.696</i>	1.018 <i>0.9927</i>	1.01893 <i>0.99270</i>	0.73212 <i>0.75570</i>	0.28681 <i>0.23700</i>	0.02 <i>0.03</i>
N2–H2B	2.16(3) <i>2.344</i>	–25.9(2) <i>–46.188</i>	1.018 <i>0.9929</i>	1.01846 <i>0.99292</i>	0.72541 <i>0.75809</i>	0.29304 <i>0.23483</i>	0.03 <i>0.03</i>
N2–H2C	1.99(3) <i>2.356</i>	–22.7(2) <i>–45.642</i>	1.019 <i>0.9911</i>	1.02141 <i>0.99112</i>	0.75414 <i>0.75281</i>	0.26727 <i>0.23830</i>	0.03 <i>0.03</i>
C1–C2	2.073(7) <i>2.108</i>	–16.79(2) <i>–24.845</i>	1.4144(2) <i>1.4144</i>	1.41542 <i>1.41522</i>	0.69772 <i>0.70688</i>	0.71770 <i>0.70834</i>	0.24 <i>0.28</i>
C1–H1	1.81(3) <i>1.978</i>	–17.9(2) <i>–29.172</i>	1.042(2) <i>1.0654</i>	1.04197 <i>1.06541</i>	0.69465 <i>0.68153</i>	0.34732 <i>0.38388</i>	0.01 <i>0.04</i>
C1–C2'	2.073(14) <i>2.109</i>	–16.79(4) <i>–24.855</i>	1.4144(2) <i>1.4144</i>	1.41542 <i>1.41520</i>	0.69773 <i>0.70729</i>	0.71769 <i>0.70791</i>	0.24 <i>0.28</i>
C2–C3	2.097(11) <i>2.109</i>	–18.14(4) <i>–24.939</i>	1.4149(2) <i>1.4149</i>	1.41573 <i>1.41575</i>	0.70588 <i>0.70565</i>	0.70985 <i>0.71010</i>	0.21 <i>0.27</i>
C2–H2	1.89(6) <i>1.958</i>	–18.7(2) <i>–28.701</i>	1.054(2) <i>1.0666</i>	1.05374 <i>1.06656</i>	0.64124 <i>0.67273</i>	0.41249 <i>0.39383</i>	0.05 <i>0.05</i>
C3–H3	1.81(6) <i>1.978</i>	–14.7(2) <i>–29.229</i>	1.024(2) <i>1.0646</i>	1.02459 <i>1.06461</i>	0.68048 <i>0.67758</i>	0.34411 <i>0.38703</i>	0.02 <i>0.04</i>
C3–C3'	2.113(13) <i>2.133</i>	–18.03(5) <i>–25.497</i>	1.4095(2) <i>1.4095</i>	1.41021 <i>1.41030</i>	0.70511 <i>0.70520</i>	0.70510 <i>0.70510</i>	0.21 <i>0.28</i>
N2'–H2A'	2.10(2) <i>2.346</i>	–24.39(7) <i>–45.748</i>	1.018 <i>0.9928</i>	1.01893 <i>0.99284</i>	0.73212 <i>0.75609</i>	0.28681 <i>0.23675</i>	0.02 <i>0.03</i>
N2'–H2B'	2.164(8) <i>2.347</i>	–25.91(4) <i>–45.947</i>	1.018 <i>0.9927</i>	1.01846 <i>0.99273</i>	0.72549 <i>0.75667</i>	0.29297 <i>0.23605</i>	0.03 <i>0.03</i>
N2'–H2C'	1.99(2) <i>2.356</i>	–22.73(5) <i>–45.604</i>	1.019 <i>0.9912</i>	1.02141 <i>0.99125</i>	0.75414 <i>0.75278</i>	0.26727 <i>0.23846</i>	0.03 <i>0.03</i>
C2'–C3'	2.10(2) <i>2.109</i>	–18.14(5) <i>–25.497</i>	1.4149(2) <i>1.4149</i>	1.41573 <i>1.41575</i>	0.70588 <i>0.70933</i>	0.70985 <i>0.70642</i>	0.21 <i>0.27</i>
C2'–H2'	1.89(4) <i>1.961</i>	–18.67(9) <i>–28.747</i>	1.054(2) <i>1.0665</i>	1.05374 <i>1.06650</i>	0.64124 <i>0.67430</i>	0.41249 <i>0.39220</i>	0.05 <i>0.05</i>
C3'–H3'	1.81(2) <i>1.977</i>	–14.69(5) <i>–29.228</i>	1.024(2) <i>1.0646</i>	1.02459 <i>1.06460</i>	0.68049 <i>0.67677</i>	0.34410 <i>0.38783</i>	0.02 <i>0.04</i>
RCP	0.3906 <i>0.333</i>	+6.7 <i>+7.3</i>	-	-	-	-	-

10.3. Topological parameters from QTAIM analysis of **2**

Table A 3. Topological parameters from QTAIM analysis of the experimental charge density of **2**. The suffixes “X2”, “X3”, “X4” and “X6” denote symmetry generated atoms.

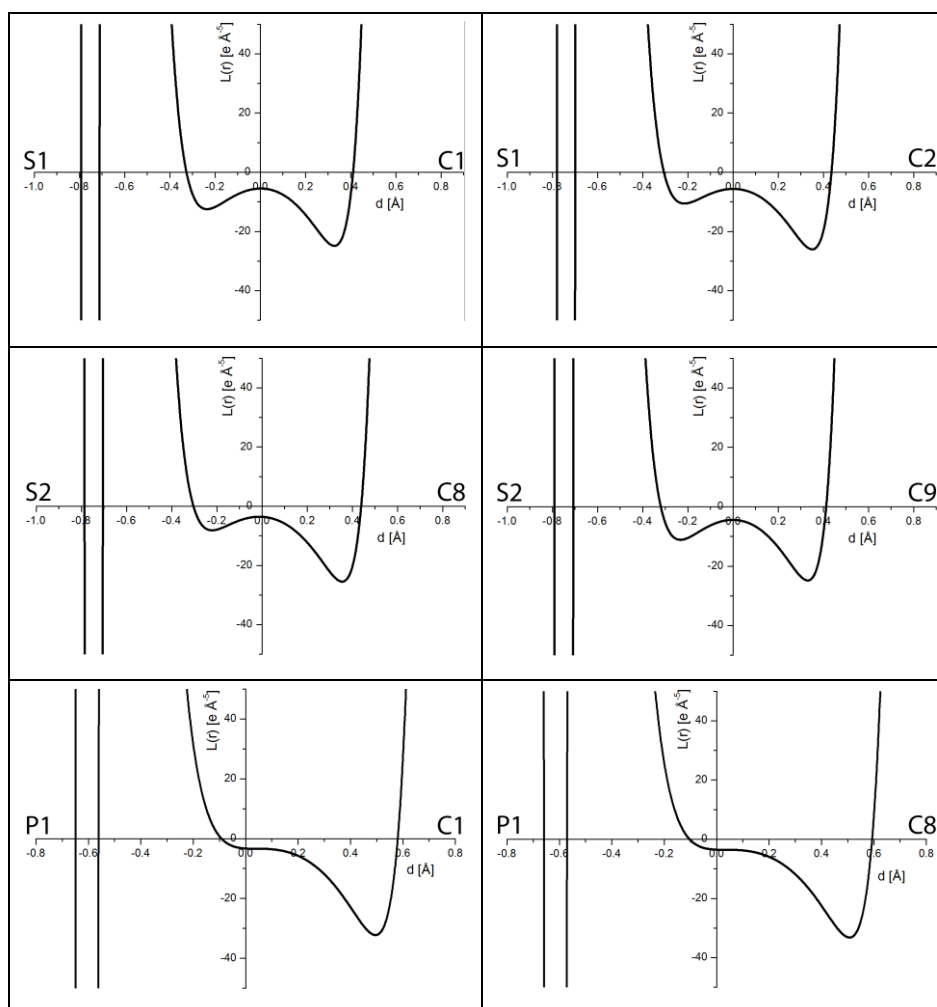
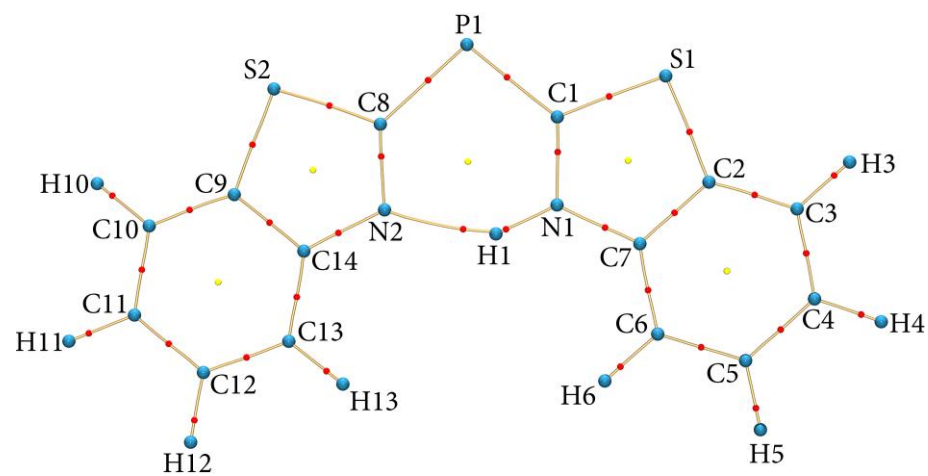
Bond	$\rho(\mathbf{r}_{\text{BCP}})$	$L(\mathbf{r}_{\text{BCP}})$	$l(\mathbf{A}-\mathbf{B})$	$d(\mathbf{A}-\mathbf{B})$	$l(\text{BCP}-\mathbf{A})$	$l(\text{BCP}-\mathbf{B})$	$\varepsilon(\mathbf{r}_{\text{BCP}})$
A-B	[e Å ⁻³]	[e Å ⁻⁵]	[Å]	[Å]	[Å]	[Å]	
S1-C1	1.360	-5.513	1.75524	1.7551	0.9114	0.8437	0.25
S1-C2	1.407	-5.360	1.74074	1.7405	0.9238	0.8167	0.25
S2-C8	1.328	-3.635	1.76414	1.7639	0.9169	0.8470	0.22
S2-C9	1.382	-4.485	1.73895	1.7385	0.9199	0.8186	0.19
P1-C1	1.166	-3.410	1.76915	1.7690	0.7923	0.9767	0.35
P1-C8	1.133	-3.581	1.79121	1.7911	0.8023	0.9888	0.29
N1-C1	2.471	-30.517	1.34047	1.3404	0.8041	0.5363	0.04
N1-C7	2.182	-20.659	1.38266	1.3823	0.8024	0.5799	0.09
N2-C8	2.508	-31.447	1.32302	1.3229	0.8242	0.4987	0.13
N2-C14	2.235	-21.420	1.38246	1.3822	0.7864	0.5958	0.07
C2-C3	2.171	-20.559	1.39425	1.3939	0.7170	0.6770	0.15
C2-C7	2.169	-19.888	1.40239	1.4022	0.6980	0.7043	0.15
C3-C4	2.197	-19.790	1.39176	1.3915	0.6878	0.7037	0.16
C4-C5	2.122	-18.516	1.40196	1.4018	0.6923	0.7095	0.19
C5-C6	2.161	-19.241	1.39113	1.3911	0.7043	0.6868	0.18
C6-C7	2.164	-19.037	1.39666	1.3963	0.6819	0.7144	0.21
C9-C10	2.150	-19.946	1.39753	1.3970	0.7267	0.6704	0.22
C9-C14	2.174	-19.603	1.40602	1.4059	0.7081	0.6978	0.19
C10-C11	2.176	-19.635	1.39201	1.3918	0.6849	0.7069	0.17
C11-C12	2.137	-19.367	1.40397	1.4035	0.7016	0.7019	0.18
C12-C13	2.189	-20.324	1.38755	1.3874	0.6975	0.6899	0.13
C13-C14	2.188	-19.447	1.39769	1.3972	0.6860	0.7111	0.17
N1-H1	1.708	-43.213	1.02372	1.0234	0.8549	0.1685	0.02
N2-H1	0.373	2.008	1.73776	1.7318	1.2309	0.5008	0.16
C3-H3	1.780	-15.899	1.06593	1.0658	0.7555	0.3103	0.06
C4-H4	1.830	-18.681	1.06624	1.0662	0.7433	0.3229	0.06
C5-H5	1.831	-17.775	1.07211	1.0721	0.7377	0.3344	0.07
C6-H6	1.778	-17.230	1.06988	1.0698	0.7498	0.3200	0.05
C10-H10	1.761	-15.299	1.07333	1.0733	0.7612	0.3121	0.04
C11-H11	1.763	-16.927	1.08588	1.0859	0.7561	0.3298	0.07
C12-H12	1.783	-16.309	1.07755	1.0774	0.7396	0.3378	0.06
C13-H13	1.773	-17.447	1.06667	1.0666	0.7443	0.3223	0.06
S(1)-H(11) _{X2}	0.012	0.247	3.25460	3.2187	2.0150	1.2037	
S(1)-H(4) _{X4}	0.042	0.543	2.92573	2.8793	1.7471	1.1323	
S(1)-H(5) _{X4}	0.037	0.486	3.01316	2.9671	1.7918	1.1753	
P(1)-H(10) _{X3}	0.015	0.186	3.56964	3.5141	2.1038	1.4103	
P(1)-H(4) _{X4}	0.020	0.327	3.17437	3.1297	1.9624	1.1672	
S(2)-H(13) _{X6}	0.035	0.519	2.88201	2.8686	1.7965	1.0721	
S(2)-H(6) _{X6}	0.026	0.421	2.97964	2.9642	1.8557	1.1085	

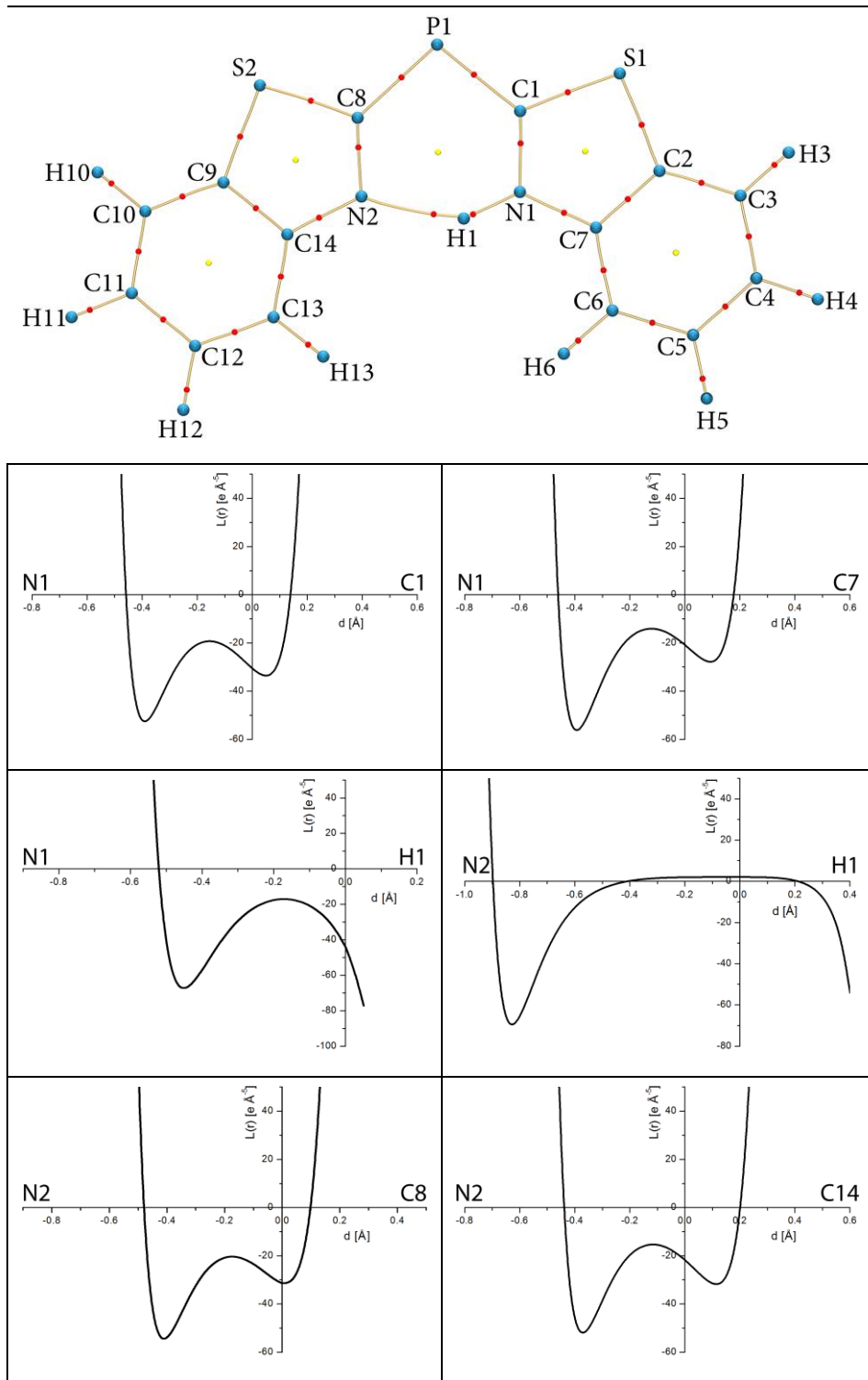
10.4. Topological parameters from QTAIM analysis of 3

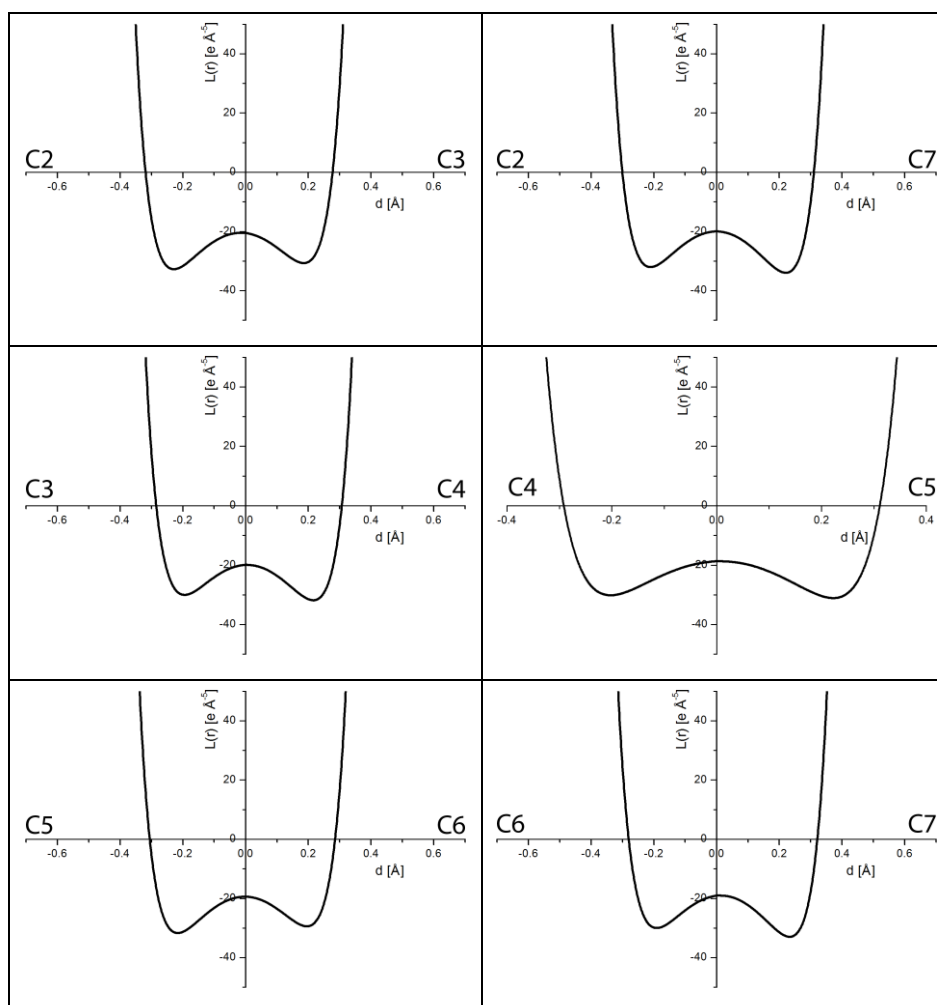
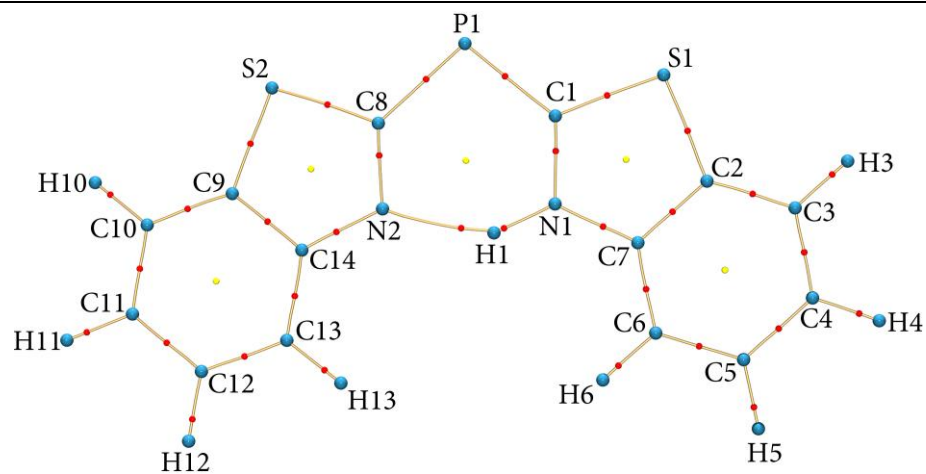
Table A 4. Topological parameters from QTAIM analysis of the experimental charge density of **3**. The prefixes "X3" and "X4" denote symmetry generated atoms.

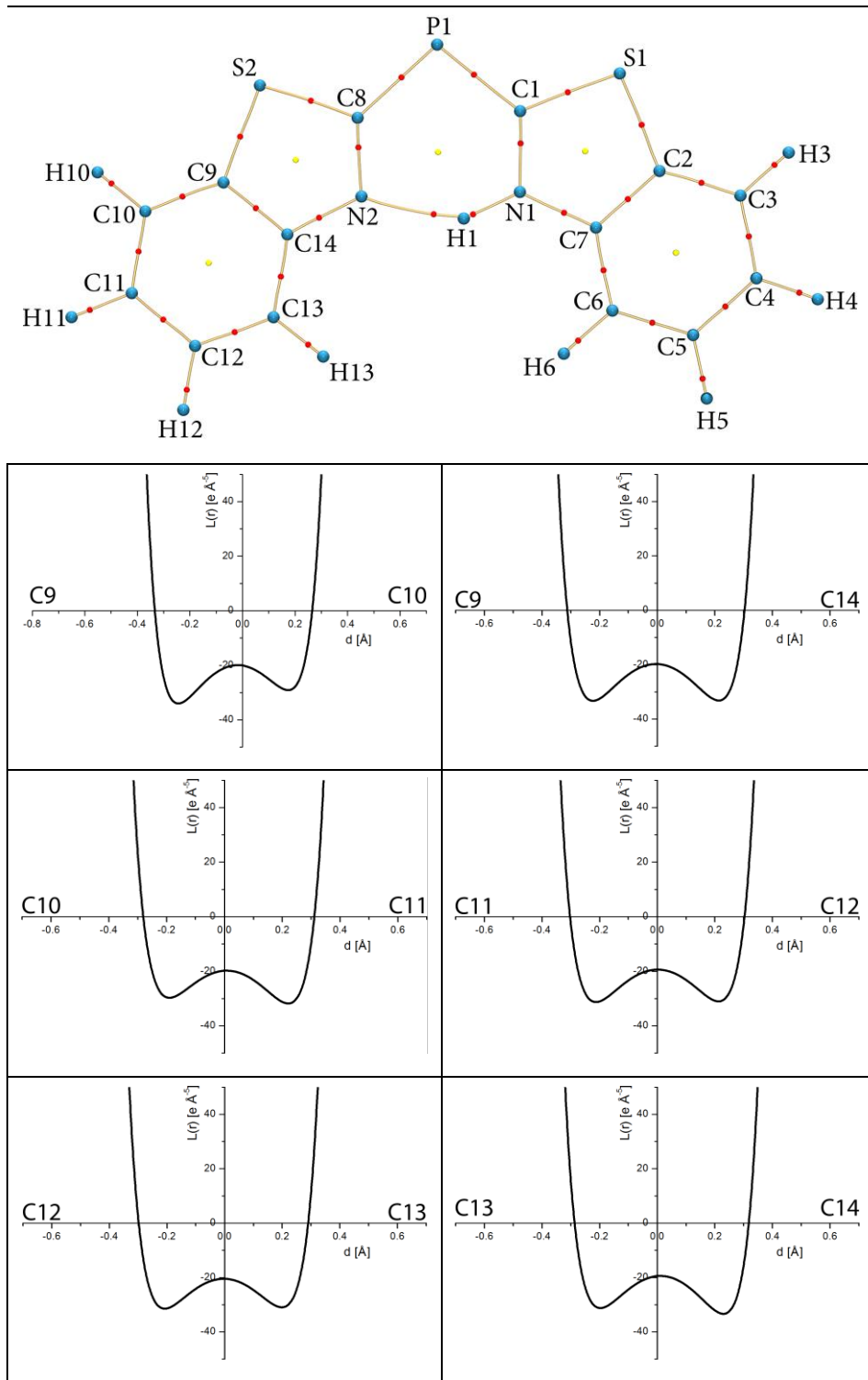
Bond A-B	$\rho(\mathbf{r}_{\text{BCP}})$ [e Å ⁻³]	$L(\mathbf{r}_{\text{BCP}})$ [e Å ⁻⁵]	$l(\mathbf{A}-\mathbf{B})$ [Å]	$d(\mathbf{A}-\mathbf{B})$ [Å]	$l(\text{BCP}-\mathbf{A})$ [Å]	$l(\text{BCP}-\mathbf{B})$ [Å]	$\epsilon(\mathbf{r}_{\text{BCP}})$
O(1)-C(1)	3.022	-36.688	1.2452	1.2452(2)	0.7361	0.5090	0.14
O(2)-C(8)	1.834	-7.721	1.4243	1.4229(3)	0.8355	0.5887	0.16
O(2)-H(2)	2.637	-54.512	0.8863	0.89(4)	0.7154	0.1709	0.05
N(1)-C(1)	2.445	-24.798	1.3406	1.3406(2)	0.7783	0.5622	0.19
N(1)-C(9)	1.805	-9.779	1.4564	1.4562(3)	0.8141	0.6423	0.07
N(1)-H(1)	2.566	-41.967	1.0503	1.05(2)	0.7252	0.3251	0.04
C(1)-C(2)	1.805	-13.235	1.4989	1.4981(2)	0.7816	0.7174	0.09
C(2)-C(3)	2.136	-16.813	1.4058	1.4051(2)	0.6975	0.7083	0.17
C(2)-C(7)	2.058	-16.119	1.3979	1.3979(2)	0.7107	0.6871	0.20
C(3)-C(4)	2.177	-18.617	1.3955	1.3955(2)	0.7015	0.6941	0.21
C(3)-C(8)	1.638	-8.974	1.5173	1.5171(2)	0.8073	0.7100	0.21
C(4)-C(5)	2.247	-19.771	1.3963	1.3962(3)	0.6976	0.6987	0.21
C(4)-H(4)	1.911	-22.200	1.1542	1.15(2)	0.7353	0.4190	0.06
C(5)-C(6)	2.261	-20.346	1.3927	1.3927(3)	0.6973	0.6954	0.15
C(5)-H(5)	1.927	-20.278	1.1578	1.16(2)	0.6973	0.4605	0.07
C(6)-C(7)	2.155	-18.330	1.3973	1.3972(3)	0.7154	0.6819	0.19
C(6)-H(6)	1.832	-18.334	1.1515	1.15(2)	0.7037	0.4478	0.09
C(7)-H(7)	1.853	-20.478	1.0691	1.07(2)	0.7225	0.3466	0.07
C(8)-H(8A)	1.869	-11.640	0.9024	0.90(2)	0.5664	0.3360	0.16
C(8)-H(8B)	1.841	-18.581	1.0786	1.08(2)	0.7381	0.3406	0.15
C(9)-C(10)	1.753	-12.110	1.5174	1.5174(3)	0.7425	0.7749	0.03
C(9)-H(9A)	1.966	-23.089	1.0890	1.09(2)	0.7005	0.3885	0.05
C(9)-H(9B)	1.959	-22.069	1.1028	1.10(3)	0.7009	0.4018	0.05
C(10)-C(11)	2.142	-16.423	1.3972	1.3972(3)	0.7016	0.6956	0.20
C(10)-C(15)	2.143	-16.752	1.4010	1.4007(2)	0.7044	0.6966	0.12
C(11)-C(12)	2.093	-16.559	1.3976	1.3976(3)	0.7050	0.6927	0.19
C(11)-H(11)	1.834	-17.441	1.0538	1.05(3)	0.7166	0.3372	0.06
C(12)-C(13)	2.191	-19.226	1.3947	1.3946(3)	0.6779	0.7168	0.16
C(12)-H(12)	1.862	-18.655	1.1828	1.18(3)	0.6734	0.5094	0.12
C(13)-C(14)	2.221	-19.005	1.3982	1.3981(3)	0.7054	0.6928	0.18
C(13)-H(13)	1.965	-20.769	1.1319	1.13(2)	0.6506	0.4813	0.12
C(14)-C(15)	2.187	-18.298	1.3981	1.3977(3)	0.6989	0.6992	0.06
C(14)-H(14)	1.863	-19.031	1.1687	1.17(2)	0.6843	0.4843	0.03
C(15)-H(15)	1.91	-21.447	1.1203	1.12(3)	0.7073	0.4130	0.06
X3_O(2)-H(1)	0.199	+0.504	1.9317	1.928	1.2499	0.6818	0.04
O(1)-X3_H(2)	0.271	+2.082	1.8623	1.861	1.1649	0.6975	0.02
O(1)-X4_H(14)	0.018	+1.106	2.5103	2.288	1.5267	0.9836	0.43
X1_H(7)-O(2)	0.018	+1.086	2.6466	2.523	1.1853	1.4614	0.06

10.5. Laplacian profiles along bond paths of 2

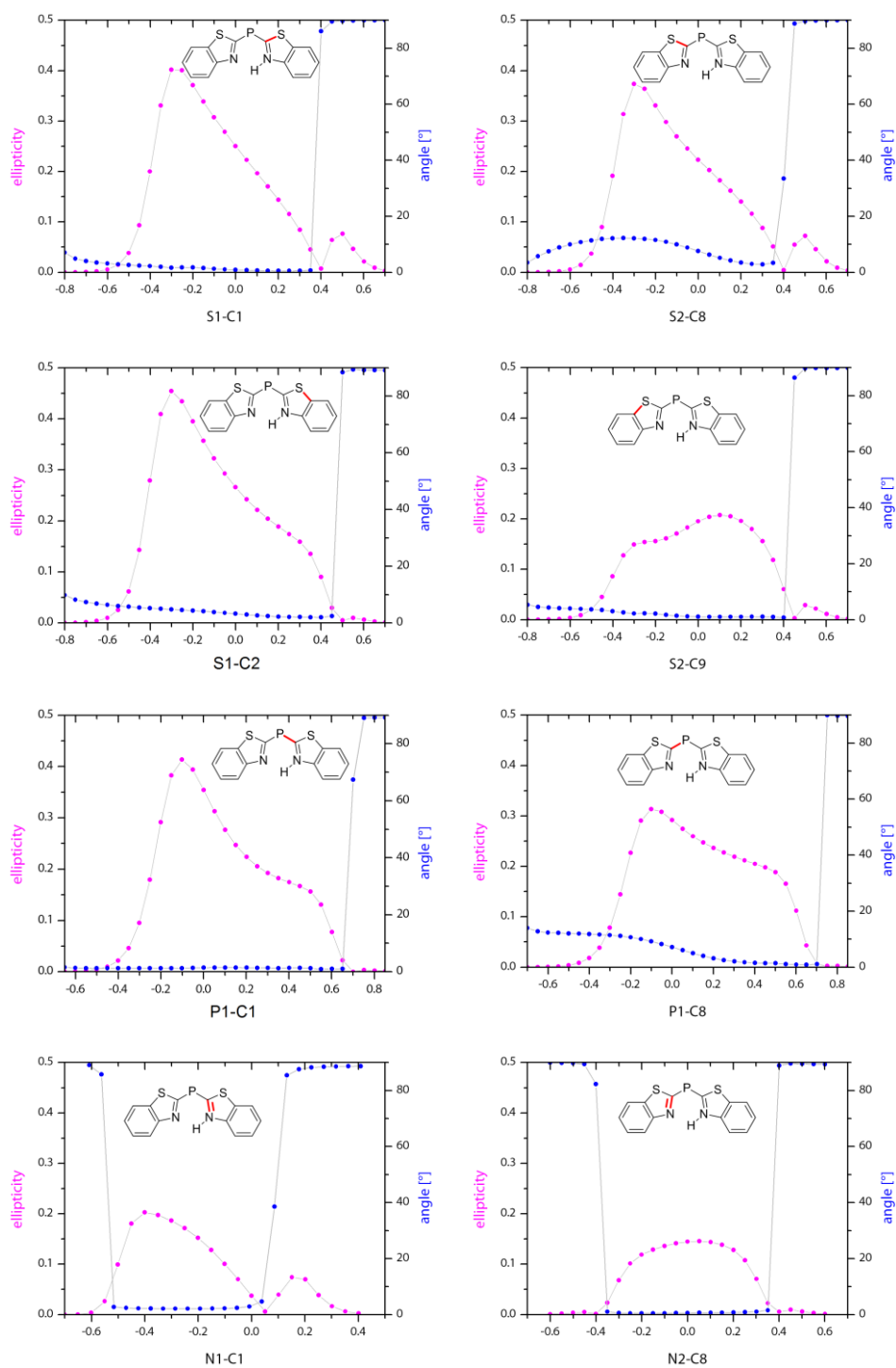




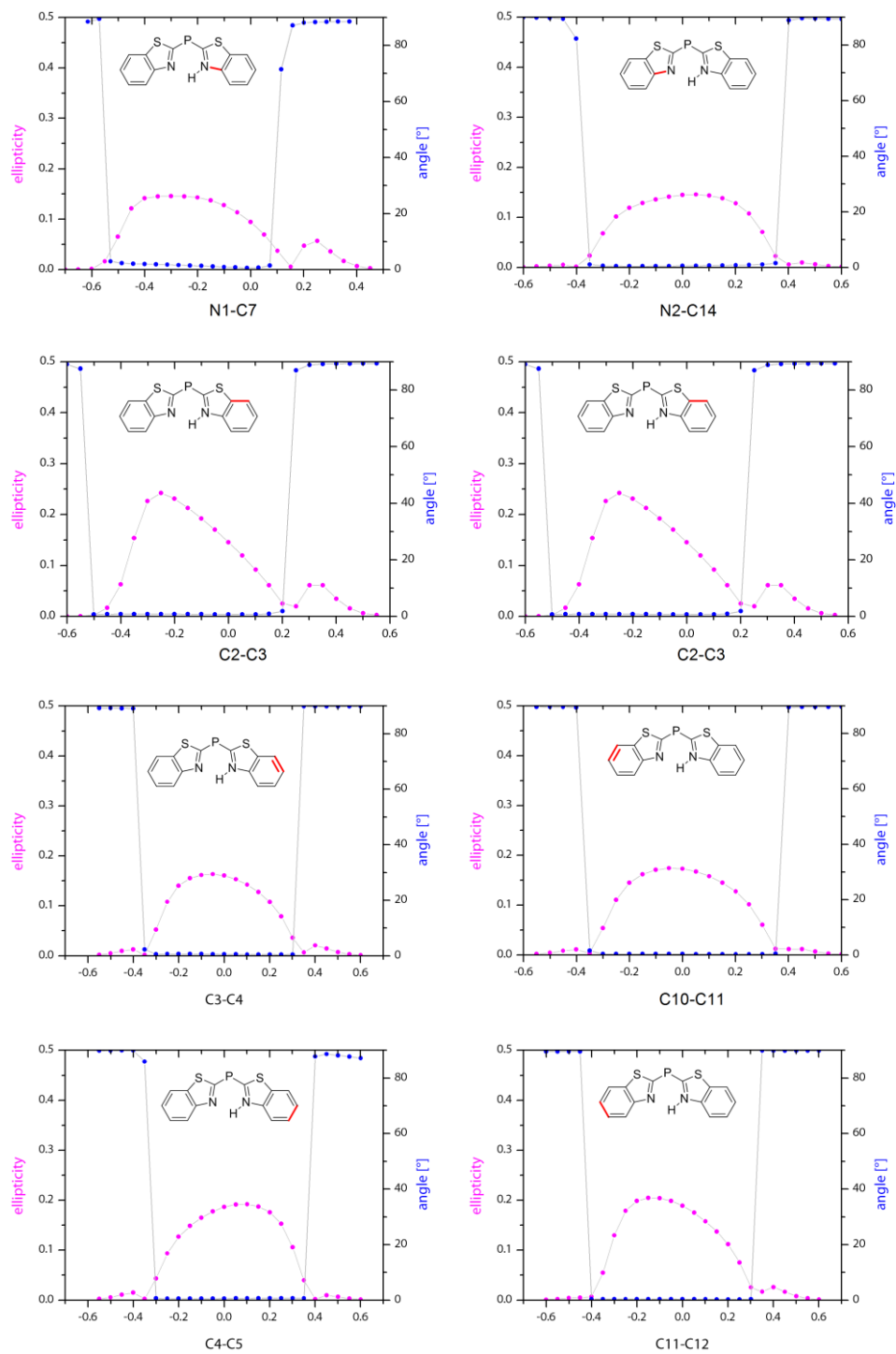


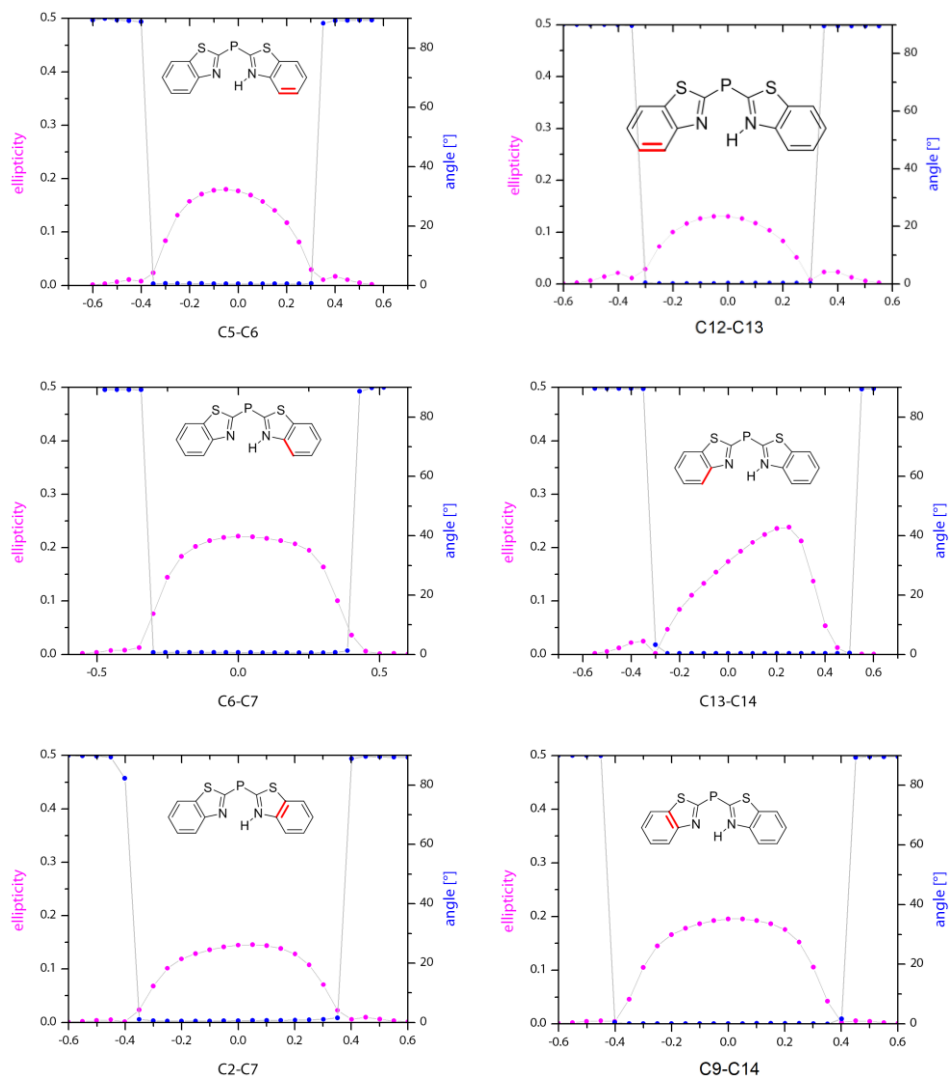


10.6. Bond ellipticity profiles in 2



Bond ellipticity profiles in 2





10.7. The Source Function quality criterion in calculations on 2

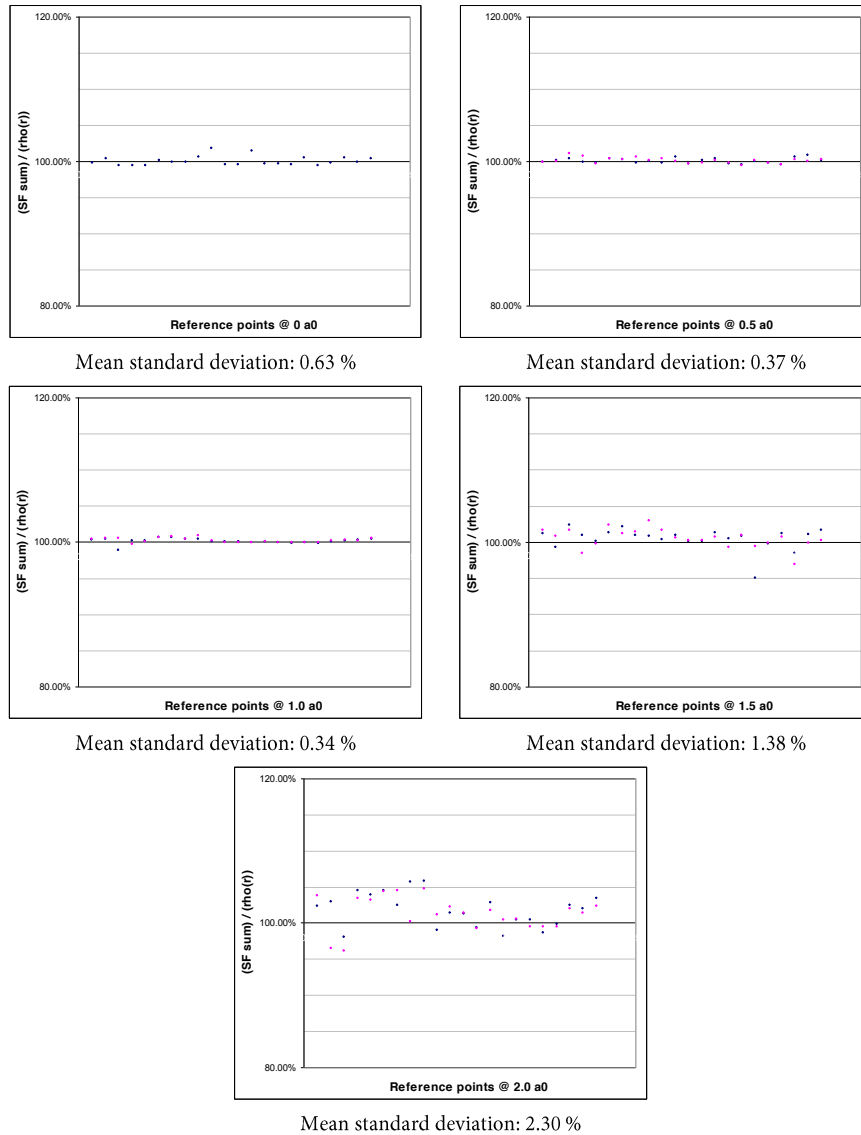
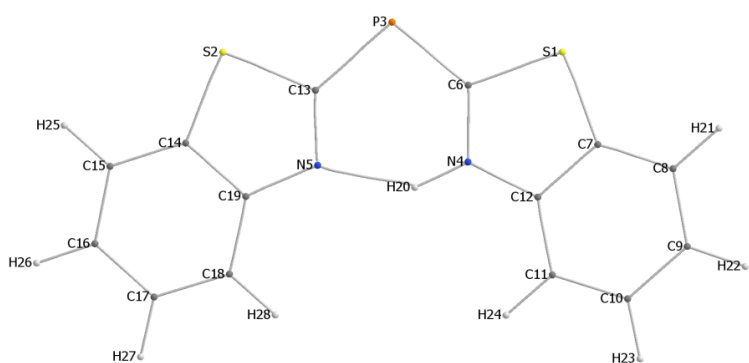


Figure A 1. The sum of SF contributions to each reference point in 2 relative to the total density at each reference point is given here. Each diagram corresponds to a complete set of reference points at a constant distance to the ring plane. Blue and pink colour corresponds to reference points above and below the ring plane, respectively.

10.8. Delocalisation indices in 2

Table A 5. Selected DI values between atom pairs in 2. See paragraph 4.11 for computational details.

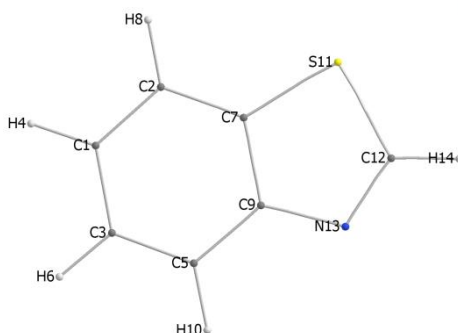
Atom pair A-B	$\delta(A,B)$
S1 - N4	$1.09 \cdot 10^{-1}$
S2 - N5	$1.43 \cdot 10^{-1}$
S1 - C6	$9.52 \cdot 10^{-1}$
N4 - C6	$1.02 \cdot 10^0$
N5 - C6	$2.74 \cdot 10^{-2}$
S1 - C7	$9.88 \cdot 10^{-1}$
N4 - C7	$8.41 \cdot 10^{-2}$
C6 - C7	$4.72 \cdot 10^{-2}$
C7 - C12	$1.04 \cdot 10^{-1}$
C7 - C10	$4.98 \cdot 10^{-2}$
C8 - C11	$5.48 \cdot 10^{-2}$
S1 - C12	$6.35 \cdot 10^{-2}$
N4 - C12	$8.86 \cdot 10^{-1}$
C6 - C12	$3.33 \cdot 10^{-2}$
C9 - C12	$4.63 \cdot 10^{-2}$
S2 - C13	$0.99 \cdot 10^{-1}$
N4 - C13	$2.27 \cdot 10^{-2}$
N5 - C13	$1.18 \cdot 10^0$
S2 - C14	$1.02 \cdot 10^{-1}$
N5 - C14	$7.76 \cdot 10^{-2}$
C13 - C14	$5.98 \cdot 10^{-2}$
C14 - C17	$4.63 \cdot 10^{-2}$
C15 - C18	$5.59 \cdot 10^{-2}$
N5 - C19	$9.46 \cdot 10^{-1}$
S2 - C19	$6.88 \cdot 10^{-2}$
C13 - C19	$4.33 \cdot 10^{-2}$
C14 - C19	$1.02 \cdot 10^{-1}$
C16 - C19	$4.32 \cdot 10^{-2}$
P3 - H20	$2.45 \cdot 10^{-3}$
P3 - C6	$1.01 \cdot 10^0$
P3 - C13	$8.63 \cdot 10^{-1}$
P3 - S1	$8.15 \cdot 10^{-2}$
P3 - S2	$6.49 \cdot 10^{-2}$
P3 - N4	$9.23 \cdot 10^{-2}$
P3 - C7	$1.04 \cdot 10^{-2}$
P3 - C12	$8.37 \cdot 10^{-3}$
P3 - C14	$7.36 \cdot 10^{-3}$
P3 - C19	$8.34 \cdot 10^{-3}$
P3 - N5	$5.69 \cdot 10^{-2}$
N4 - H20	$5.02 \cdot 10^{-2}$
N5 - H20	$1.21 \cdot 10^{-2}$



10.9. Delocalisation indices in benzothiazole

Table A 6. Selected values of delocalisation indices $\delta(A,B)$ between given atom pairs in benzothiazole.

Atom pair A-B	$\delta(A,B)$
C7 - C9	$1.03 \cdot 10^0$
C7 - S11	$1.02 \cdot 10^0$
S11 - C12	$1.02 \cdot 10^0$
C9 - N13	$9.60 \cdot 10^{-1}$
C12 - N13	$1.24 \cdot 10^0$
C2 - C5	$5.73 \cdot 10^{-2}$
C3 - C7	$4.58 \cdot 10^{-2}$
C1 - C9	$4.28 \cdot 10^{-2}$
C9 - S11	$7.23 \cdot 10^{-2}$
C7 - C12	$6.81 \cdot 10^{-2}$
C9 - C12	$4.75 \cdot 10^{-2}$
C7 - N13	$8.04 \cdot 10^{-2}$
S11 - N13	$1.66 \cdot 10^{-1}$



10.10. The filter insert for the beam path of Stalke's Bruker APEX2 Ultra

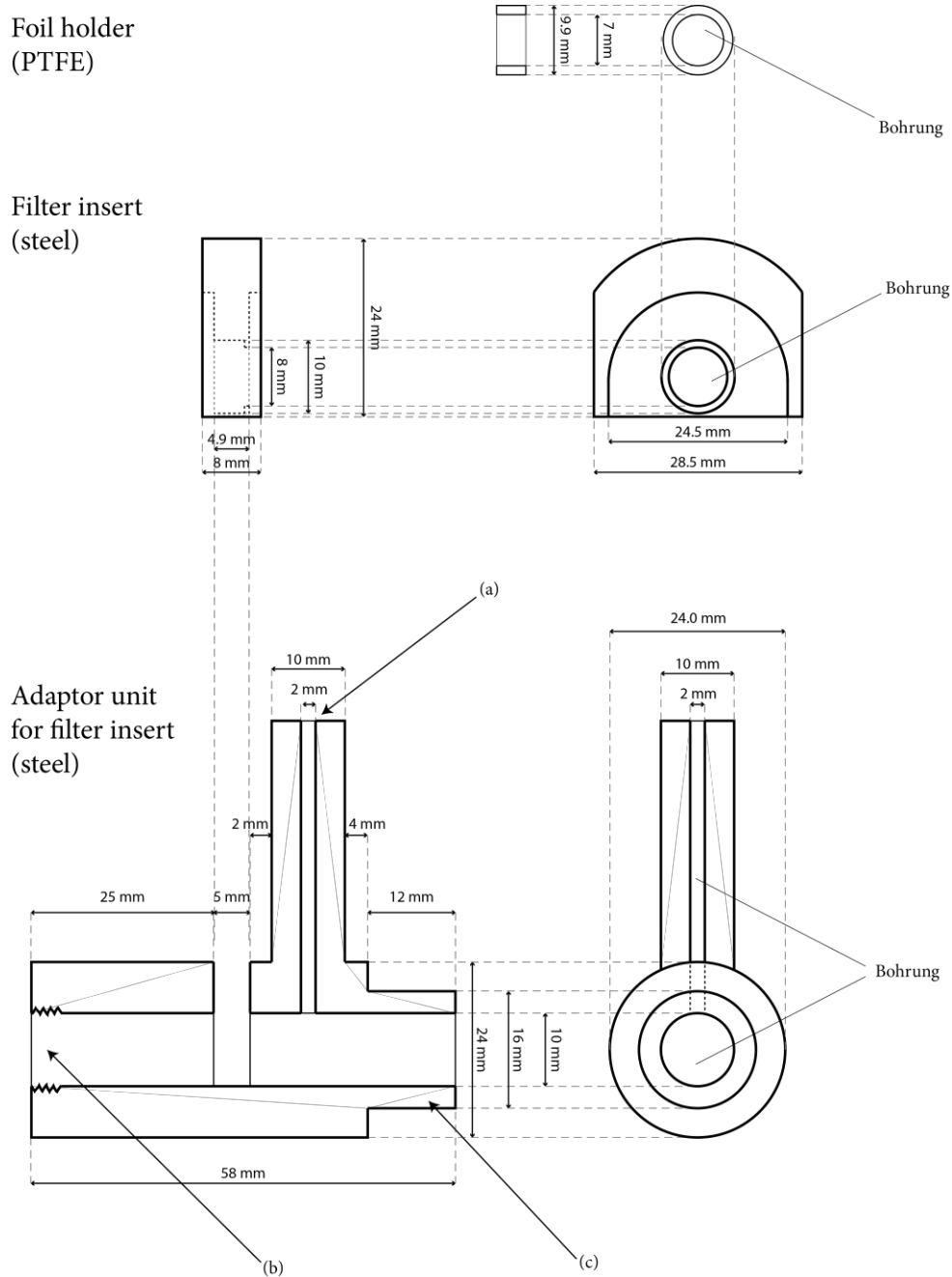
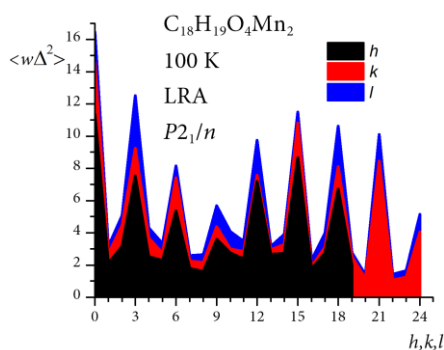


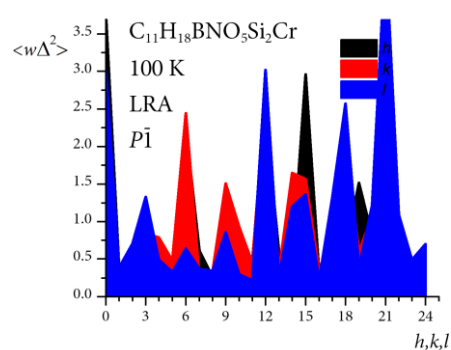
Figure A 2. Technical drawing of the filter insert for the Bruker APEX2 Ultra diffractometer. (a) a 6 mm Swagelok connector is attached here for pressurised air purging; (b) a thread for the connection with the collimator bed is cut into this end; (c) this end is pushed into the mirror optics housing. A piece of filter foil in the appropriate size can be inserted into the opening of the filter insert. The PTFE foil holder is then used to fixate the foil in the insert. Several of the inserts with different foils can be held available and changed in the adaptor unit without having to power down the source.

10.11. The impact on low energy X-ray contamination on data statistics

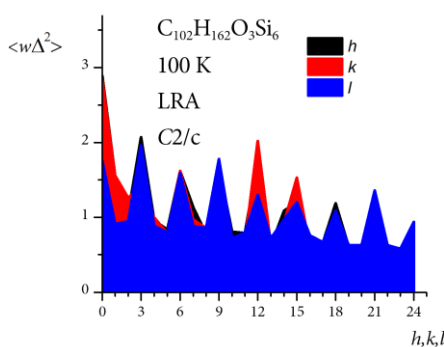
The following graphics were made with statistical data from the program XDWTAN, which is part of the XD2006 package.^[44] The diagrams display the mean of the deviations $\Delta^2 = F_{obs}^2 - F_{calc}^2$ as a function of the Miller indices. Data for all three indices are displayed in each diagram. The sum formula, the sample temperature and the space group are given in each diagram.



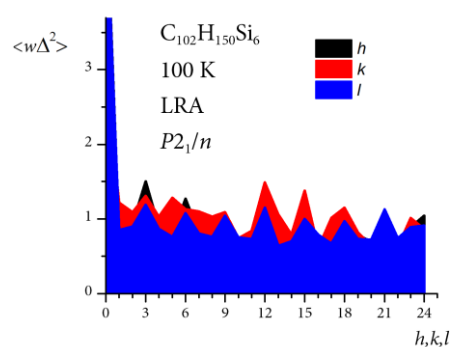
Data from U. Flierler, M. Burzler, D. Leusser, J. Henn, H. Ott, H. Braunschweig, D. Stalke, *Angew. Chem.* **2008**, *120*, 4393-4397; *Angew. Chem. Int. Ed.* **2008**, *47*, 4321-4325.



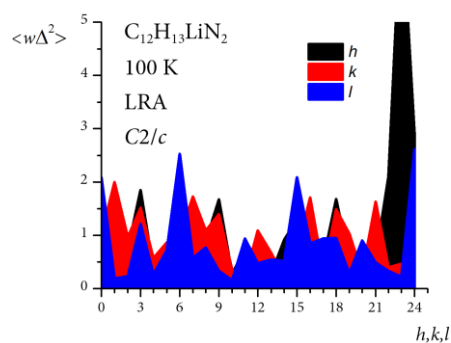
Data not published.



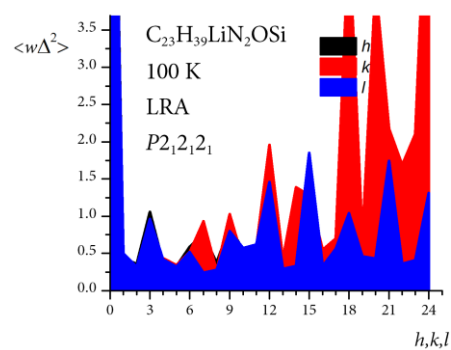
D. Kratzert, D. Leusser, J. J. Holstein, B. Dittrich, K. Abersfelder, D. Scheschkewitz, D. Stalke, *Angew. Chem.* **2013**, *125*, 4574-4578; *Angew. Chem. Int. Ed. Engl.* **2013**, *52*, 4478-4482.



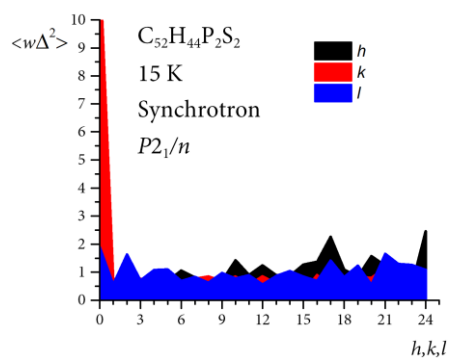
D. Kratzert, D. Leusser, J. J. Holstein, B. Dittrich, K. Abersfelder, D. Scheschkewitz, D. Stalke, *Angew. Chem.* **2013**, *125*, 4574-4578; *Angew. Chem. Int. Ed. Engl.* **2013**, *52*, 4478-4482.



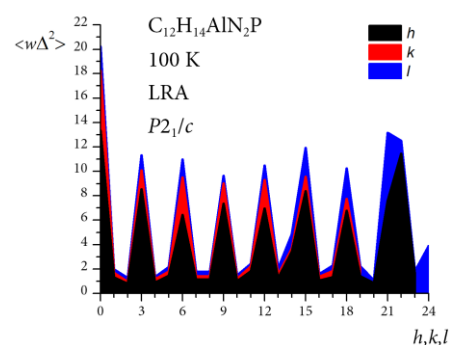
Data from H. Ott, U. Pieper, D. Leusser, U. Flierler, J. Henn, D. Stalke, *Angew. Chem.* **2009**, *121*, 3022-3026; *Angew. Chem. Int. Ed.* **2009**, *48*, 2978-2982.



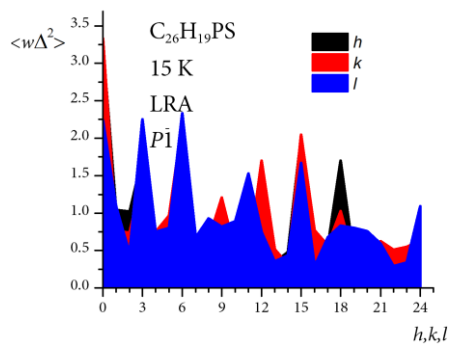
Data from H. Ott, C. Däschlein, D. Leusser, D. Schildbach, T. Seibel, D. Stalke, C. Strohmam, *J. Am. Chem. Soc.* **2008**, *130*, 11901-11911.



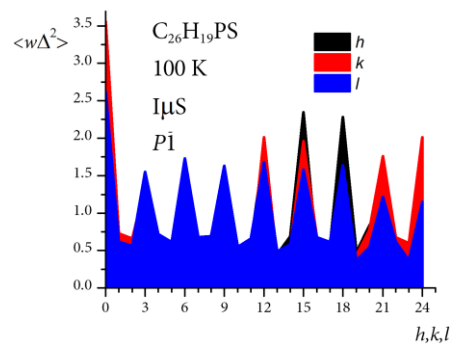
Unpublished data.



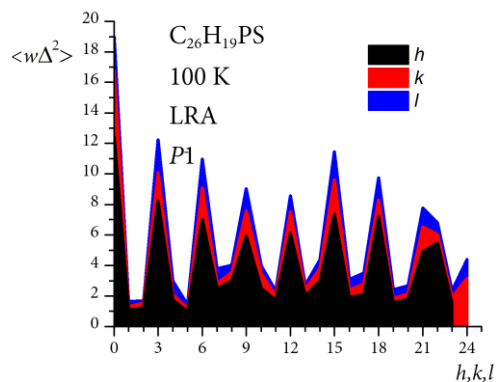
Data from J. Henn, K. Meindl, A. Oechsner, G. Schwab, T. Koritsanzky, D. Stalke, *Angew. Chem. Int. Ed.* **2010**, *49*, 2422-2426.



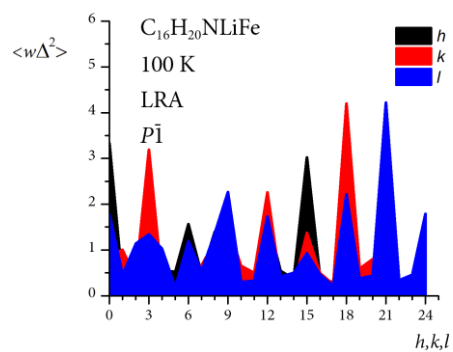
Data from R. Herbst-Irmer, J. Henn, J. J. Holstein, C. B. Hübschle, B. Dittrich, D. Stern, D. Kratzert, D. Stalke, *J. Phys. Chem. A* **2013**, *117*, 633-641.



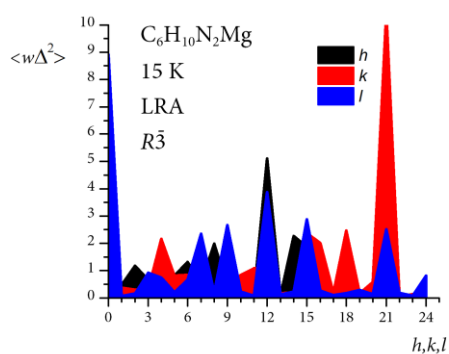
Data from R. Herbst-Irmer, J. Henn, J. J. Holstein, C. B. Hübschle, B. Dittrich, D. Stern, D. Kratzert, D. Stalke, *J. Phys. Chem. A* **2013**, *117*, 633-641.



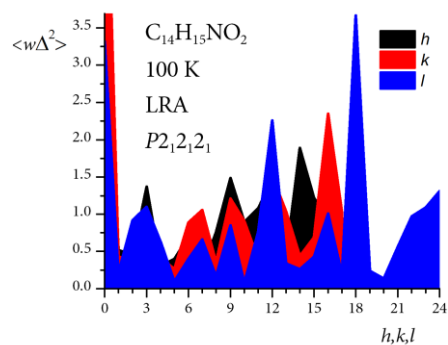
Data from R. Herbst-Irmer, J. Henn, J. J. Holstein, C. B. Hübschle, B. Dittrich, D. Stern, D. Kratzert, D. Stalke, *J. Phys. Chem. A* **2013**, *117*, 633-641.



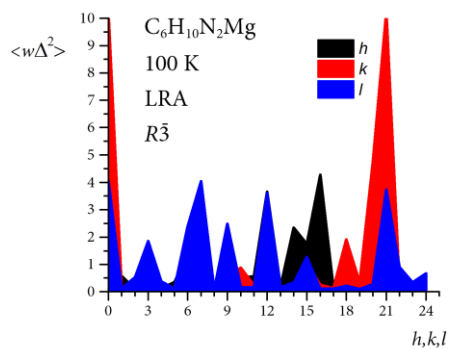
Unpublished data.



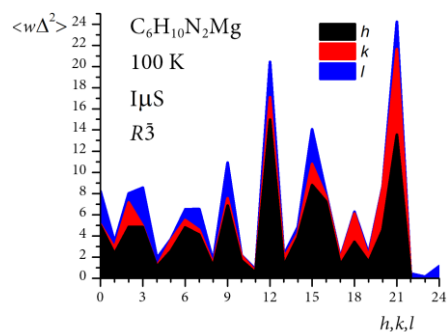
Data from D. Kratzert, D. Leusser, D. Stern, J. Meyer, F. Breher, D. Stalke, *Chem. Commun.* **2011**, *47*, 2931-2933.



Dataset from crystals of 3.



Unpublished data.



Unpublished data.

Table A 7. Comparison between the topological parameters obtained from models derived from data collections with and without filter. The values obtained from the filtered radiation are set in regular characters. They match those in Table A 2. The numbers in italic are derived from the model from non-filtered data collection.

Bond	$\rho(\mathbf{r}_{\text{BCP}})$	$L(\mathbf{r}_{\text{BCP}})$	$d(\mathbf{A}-\mathbf{B})$	$l(\mathbf{A}-\mathbf{B})$	$l(\text{BCP}-\mathbf{A})$	$l(\text{BCP}-\mathbf{B})$	$\epsilon(\mathbf{r}_{\text{BCP}})$
A-B	[e Å ⁻³]	[e Å ⁻⁵]	[Å]	[Å]	[Å]	[Å]	
Na1-N1	0.101 <i>0.096</i>	+2.509 <i>+2.431</i>	2.45990 <i>2.45991</i>	2.46247 <i>2.46290</i>	1.08289 <i>1.08830</i>	1.37958 <i>1.37460</i>	0.01 <i>0.08</i>
Na1-N2	0.101 <i>0.098</i>	+2.523 <i>+2.504</i>	2.46491 <i>2.46491</i>	2.46511 <i>2.4673</i>	1.08255 <i>1.08520</i>	1.38256 <i>1.3821</i>	0.13 <i>0.13</i>
Na1-C1	0.072 -	+1.519 -	2.70046 -	2.73206 -	1.15998 -	1.57208 -	3.80 -
Na1-N2'	0.101 <i>0.098</i>	+2.523 <i>+2.505</i>	2.46491 <i>2.46491</i>	2.46511 <i>2.4673</i>	1.08256 <i>1.08520</i>	1.38255 <i>1.3821</i>	0.13 <i>0.12</i>
N1-H1A	2.028 <i>2.025</i>	-23.785 <i>-22.791</i>	1.01928 <i>0.99132</i>	1.02051 <i>0.99136</i>	0.75247 <i>0.75012</i>	0.26804 <i>0.24124</i>	0.08 <i>0.07</i>
N1-H1B	2.114 <i>2.147</i>	-25.760 <i>-25.488</i>	1.01720 <i>0.99524</i>	1.01975 <i>1.0187</i>	0.73773 <i>0.74100</i>	0.28202 <i>0.2777</i>	0.07 <i>0.07</i>
N1-H1C	1.648 <i>1.716</i>	-5.916 <i>-5.75</i>	1.01843 <i>0.99133</i>	1.02239 <i>1.01980</i>	0.75438 <i>0.73370</i>	0.26800 <i>0.28620</i>	0.03 <i>0.04</i>
N2-H2A	2.103 <i>2.169</i>	-24.394 <i>-26.551</i>	1.01775 <i>0.99266</i>	1.01893 <i>1.01520</i>	0.73212 <i>0.72280</i>	0.28681 <i>0.29240</i>	0.02 <i>0.04</i>
N2-H2B	2.164 <i>2.221</i>	-25.893 <i>-27.89</i>	1.01833 <i>0.99288</i>	1.01846 <i>1.01660</i>	0.72541 <i>0.72500</i>	0.29304 <i>0.29160</i>	0.03 <i>0.01</i>
N2-H2C	1.985 <i>2.069</i>	-22.725 <i>-23.572</i>	1.01884 <i>0.99108</i>	1.02141 <i>1.01920</i>	0.75414 <i>0.73370</i>	0.26727 <i>0.28550</i>	0.03 <i>0.02</i>
C1-C2	2.073 <i>2.079</i>	-16.794 <i>-17.112</i>	1.41440 <i>1.41441</i>	1.41542 <i>1.41690</i>	0.69772 <i>0.70140</i>	0.71770 <i>0.71550</i>	0.24 <i>0.24</i>
C1-H1	1.810 <i>1.871</i>	-17.859 <i>-18.689</i>	1.04163 <i>1.06541</i>	1.04197 <i>1.02890</i>	0.69465 <i>0.66710</i>	0.34732 <i>0.36180</i>	0.01 <i>0.05</i>
C1-C2'	2.073 <i>2.079</i>	-16.794 <i>-17.111</i>	1.41440 <i>1.41441</i>	1.41542 <i>1.41690</i>	0.69773 <i>0.70140</i>	0.71769 <i>0.71550</i>	0.24 <i>0.24</i>
C2-C3	2.097 <i>2.089</i>	-18.139 <i>-16.649</i>	1.41493 <i>1.41494</i>	1.41573 <i>1.41760</i>	0.70588 <i>0.70190</i>	0.70985 <i>0.71570</i>	0.21 <i>0.22</i>
C2-H2	1.887 <i>1.945</i>	-18.666 <i>-20.607</i>	1.05353 <i>1.06656</i>	1.05374 <i>1.06350</i>	0.64124 <i>0.63380</i>	0.41249 <i>0.42970</i>	0.05 <i>0.06</i>
C3-H3	1.813 <i>1.837</i>	-14.693 <i>-16.745</i>	1.02383 <i>1.06461</i>	1.02459 <i>1.06630</i>	0.68048 <i>0.68860</i>	0.34411 <i>0.37770</i>	0.02 <i>0.02</i>
C3-C3'	2.113 <i>2.108</i>	-18.029 <i>-16.532</i>	1.40950 <i>1.40951</i>	1.41021 <i>1.41200</i>	0.70511 <i>0.70600</i>	0.70510 <i>0.70600</i>	0.21 <i>0.21</i>
N2'-H2A'	2.103 <i>2.169</i>	-24.394 <i>-26.551</i>	1.01775 <i>0.99280</i>	1.01893 <i>1.01520</i>	0.73212 <i>0.72280</i>	0.28681 <i>0.29240</i>	0.02 <i>0.04</i>
N2'-H2B'	2.164 <i>2.221</i>	-25.913 <i>-27.89</i>	1.01833 <i>0.99269</i>	1.01846 <i>1.01660</i>	0.72549 <i>0.72500</i>	0.29297 <i>0.29160</i>	0.03 <i>0.01</i>
N2'-H2C'	1.985 <i>2.069</i>	-22.725 <i>-23.572</i>	1.01884 <i>0.99121</i>	1.02141 <i>1.01920</i>	0.75414 <i>0.73370</i>	0.26727 <i>0.28550</i>	0.03 <i>0.02</i>
C2'-C3'	2.097 <i>2.089</i>	-18.140 <i>-16.649</i>	1.41493 <i>1.41494</i>	1.41573 <i>1.41760</i>	0.70588 <i>0.70190</i>	0.70985 <i>0.71570</i>	0.21 <i>0.22</i>
C2'-H2'	1.887 <i>1.945</i>	-18.667 <i>-20.607</i>	1.05353 <i>1.06650</i>	1.05374 <i>1.06350</i>	0.64124 <i>0.63380</i>	0.41249 <i>0.42970</i>	0.05 <i>0.06</i>
C3'-H3'	1.813 <i>1.837</i>	-14.694 <i>-16.745</i>	1.02383 <i>1.06460</i>	1.02459 <i>1.06630</i>	0.68049 <i>0.68860</i>	0.34410 <i>0.37770</i>	0.02 <i>0.02</i>
RCP	0.3906 <i>0.4057</i>	+6.7 <i>+6.6</i>	-	-	-	-	-

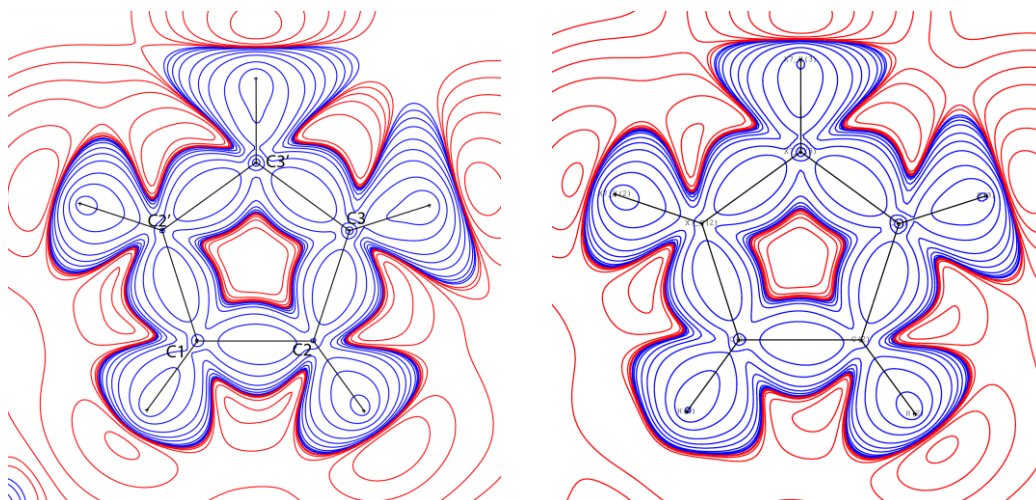


Figure A 3. Deformation density contour plots in the best plane of the cyclopentadiene ring in **1**. Left: model from data obtained with filtered radiation; right: model from data obtained from unfiltered radiation.

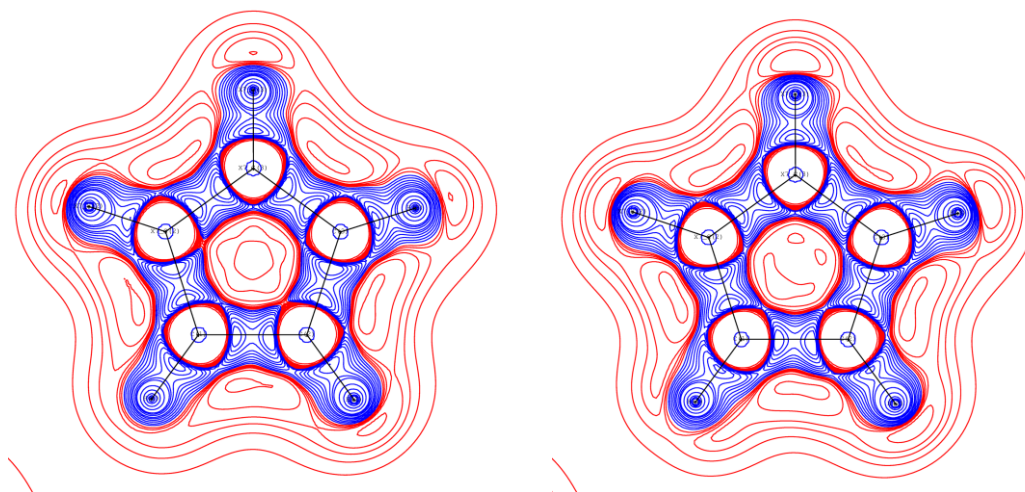


Figure A 4. Laplacian contour plots in the best plane of the cyclopentadiene ring in **1**. Left: model from data obtained with filtered radiation; right: model from data obtained from unfiltered radiation.

Danksagung

Ich möchte zunächst meinem Doktorvater Dietmar Stalke für das in mich gesetzte Vertrauen während der gesamten Zeit der Arbeit an dieser Dissertation danken. Die gewährten Gelegenheiten, mich selbst auf Vortrags- und Forschungsreisen in fernen Ländern auszutesten, weiß ich sehr zu schätzen.

Dem Koordinator meines Promotionsstudienganges CaSuS, Franc Meyer, möchte ich herzlich für die Übernahme des Korreferats danken. Ich danke auch den weiteren Mitgliedern der Prüfungskommission und dem Drittgutachter für ihre Arbeit.

Dem Land Niedersachsen und dem Center for Materials Crystallography gebührt Dank für die finanzielle Unterstützung meines Promotionsstudiums und der damit verbundenen Reisen und Projekte. Andere Mitglieder CMC, allen voran Mette Schmökel, Mads Jørgensen und Gabriele Saleh, haben in vielen Diskussionen für neue Ideen und Erkenntnisse gesorgt. Vielen Dank!

Meinen Kooperationspartnern Ricardo Mata, Diego Andrada und Johannes Dieterich danke ich für die umfangreichen theoretischen Rechnungen und die engagierte Mitarbeit an unseren Manuskripten. Ebenso danke ich meinen kristallographischen Kooperationspartnern für ihre interessanten kristallographischen Probleme und die Möglichkeit, mit ihnen Publikationserfahrung zu sammeln.

Ich danke Heike Tappe, der guten Seele im Vorzimmer des Chefs, für den einen oder anderen Plausch und die Organisation der einen oder anderen Flugreise in ferne Länder. Frau Stückl, die in ziemlich selbstzerstörerischem Tempo immer alles möglich macht und Frau Linne, die aus unübersichtlichen Abrechnungshaufen saubere Überweisungen erstellen kann, will ich ebenfalls herzlich danken.

Dem ganzen Arbeitskreis Stalke danke ich für die außerordentlich kollegiale und freundliche Stimmung. Elli und Sven-Ole, ihr seid zwei gute Seelen, die ich in mein Herz geschlossen habe. Daniel, hab vielen Dank für die Ausflüge und Maschinen- und Fahrrad-reparatur-Sessions, bei denen ich viel von Dir gelernt habe. Fink, der Du alles, was Du machst, gut machst – danke für die praktische Erläuterung des Begriffs des Rock'n'Roll. Vielen Dank für die eine oder andere Lehrstunde am Kicker, am Tresen und am Strand! Felix, vielen Dank für jederzeit schnelle Hilfe am Rechner. Dachs, die Wochen im Kabuff wären ohne Dich nur halb so erheiternd gewesen. Alles Gute in München. Ann-Christin und Fatme danke ich für die vielen netten Gespräche bei einer Stulle mit Sultans Freude. Bergziege Maaßi will ich danken für die schönen Radtouren rund um Göttingen.

Der Crew in den Werkstätten Hajo Heymel, Rainer Erhardt, (Pumpen-) Bernd Wichmann, Benjamin Bock, Mariusz Burzynski und Stephan Dullnig danke ich für ihre immer schnelle, hilfsbereite und gute Arbeit.

Meinen Lieblings-Hausmeistern Uwe Beckmann und Acker Hille danke ich für viele nette Gespräche sowie häufiges Helfen, Anpacken und das Ausliefern von wichtigen dienstlichen Postsendungen.

Meinen Korrekturlesern Hilke und Lennard bin ich sehr dankbar für ihre schnelle und zuverlässige Hilfe und die eine oder andere Pöbelei aber auch Lob an der richtigen Stelle.

Ohne Holger Ott wäre es wahrscheinlich nie dazu gekommen, dass ich den Weg in die Elektronendichte gefunden habe. Dirk Leußner, der vielgereiste *spiritus rector*, hat mir vieles von dem beigebracht, was man in dieser Welt der Elektronendichte braucht. Hierfür den verbindlichsten Dank, und auch für allerlei Ratschläge, die weiter tragen als bis zur Promotion.

Regine Herbst-Irmer ist in jeder Hinsicht eine Koryphäe und hat sowohl den richtigen Riecher als auch das notwendige Knowhow, wenn es um kristallographische Probleme geht. Gut, dass Du zu uns gestoßen bist – vielen Dank für die Diskussionen und für viele neue Ideen und gute Stimmung in der Ladungsdichte-Gruppe.

Meinen Freunden seit dem ersten Semester Adam, Arne, Bastian und Stefan (zweites Semester) will ich sagen, dass ich von ganzem Herzen dankbar dafür bin, dass ich sie kennengelernt habe. Und für den unvergesslichsten, unfassbarsten und überwältigendsten Junggesellenabschied der Welt, der wahrscheinlich niemals zu übertreffen sein wird.

Reent, in den Wochen und Monaten im Kabuff bist Du mir ein noch engerer Freund geworden als Du es ohnehin schon warst. Danke für Dein Vertrauen und für Deine Freundschaft.

Meine Mutter Philine und mein Vater Gerhard, meine Schwestern Greta und Lisa, meine Großeltern Ami, Grete und Hans sowie meine Schwiegereltern Ruth und Eberhard haben in den nunmehr zehn Jahren fern der Heimat meinen Weg verfolgt, unterstützt und erstere haben ihn über weite Strecken auch finanziert. Vielen, vielen Dank dafür!

– mein größter Dank aber gilt Eva für das Durchschreiten von diversen Durststrecken und fernbeziehungsähnlichen Zuständen, für die Unterstützung, für all die schöne Zeit, den weltbesten Alltag und einfach dafür, dass es sie gibt.

11. References

- [1] D. Schwarzenbach, *Acta Crystallogr., Sect. A* **2012**, 68, 57-67.
- [2] W. Friedrich, P. Knipping, M. von Laue, *Sitzungsbericht der kaiserlich Akademischen Wissenschaften München* **1912**, 303-322.
- [3] W. L. Bragg, *Proceedings of the Cambridge Philosophical Society* **1913**, 17, 43-57.
- [4] W. H. Bragg, W. L. Bragg, *P. Roy. Soc. Lond. A Mat.* **1913**, 88, 428-438.
- [5] W. H. Bragg, W. L. Bragg, *P. Roy. Soc. Lond. A Mat.* **1913**, 89, 246-248.
- [6] P. Debye, P. Scherrer, *Nach. d. Kgl. Ges. d. Wiss. Göttingen* **1915**.
- [7] P. Debye, P. Scherrer, *Physikalische Zeitschrift* **1916**, 17, 277-283.
- [8] P. Debye, *Annalen der Physik* **1915**, 351, 809-823.
- [9] A. W. Hull, *Phys. Rev. Lett.* **1917**, 10, 661-696.
- [10] M. Born, *Z. Phys. A* **1926**, 38, 803-827.
- [11] W. Borchardt-Ott, *Kristallographie*. Springer, Berlin, **2002**.
- [12] W. Massa, *Crystal Structure Determination*. Springer, Berlin, **2004**.
- [13] P. Coppens, *X-Ray Charge Densities and Chemical Bonding*. Oxford University Press, Oxford, **1997**.
- [14] J. Krogh-Moe, *Acta Crystallogr.* **1956**, 9, 951-953.
- [15] A. Fischer, D. Tiana, W. Scherer, K. Batke, G. Eickerling, H. Svendsen, N. Bindzus, B. B. Iversen, *J. Phys. Chem. A* **2011**, 115, 13061-13071.
- [16] J. Overgaard, C. Jones, D. Dange, J. A. Platts, *Inorg. Chem.* **2011**, 50, 8418-8426.
- [17] W. Scherer, C. Hauf, M. Presnitz, E.-W. Scheidt, G. Eickerling, V. Eyert, R.-D. Hoffmann, U. C. Rodewald, A. Hammerschmidt, C. Vogt, R. Pöttgen, *Angew. Chem.* **2010**, 122, 1623-1627; *Angew. Chem. Int. Ed.* **2010**, 49, 1578-1582.
- [18] W. Scherer, V. Herz, A. Brück, C. Hauf, Florian Reiner, S. Altmannshofer, D. Leusser, D. Stalke, *Angew. Chem.* **2011**, 123, 2897-2902; *Angew. Chem. Int. Ed.* **2011**, 50, 2845-2849.
- [19] R. F. W. Bader, H. Essén, *J. Chem. Phys.* **1984**, 80, 1943-1960.
- [20] G. M. Sheldrick, *Acta Crystallogr., Sect. A* **1990**, 46, 467-473.
- [21] G. M. Sheldrick, *Acta Crystallogr., Sect. A* **2008**, 64, 112-122.
- [22] SADABS User Manual (Area Detector Absorption and Other Corrections) Version 2.03, Bruker AXS GmbH, Karlsruhe, Germany.
- [23] G. M. Sheldrick, SADABS 2008/2, Madison, WI, USA, **2008**.
- [24] C. H. Görbitz, *Acta Crystallogr., Sect. B* **1999**, 55, 1090-1098.
- [25] R. H. Blessing, *J. Appl. Crystallogr.* **1997**, 30, 421-426.
- [26] G. M. Sheldrick, "Data scaling with SADABS", scientific seminar talk, November 8th, 2012, Göttingen, Germany.

-
- [27] M. R. V. Jørgensen, H. Svendsen, M. S. Schmøkel, J. Overgaard, B. B. Iversen, *Acta Crystallogr., Sect. A* **2012**, *68*, 301–303.
- [28] K. Diederichs, *Acta Crystallogr., Sect. D* **2010**, *66*, 733–740.
- [29] B. Rupp, *Acta Crystallogr., Sect. F* **2012**, *68*, 366–376.
- [30] R. Huber, G. Kopfmann, *Acta Crystallogr., Sect. A* **1969**, *25*, 143–152.
- [31] R. H. Blessing, *Acta Crystallogr., Sect. A* **1995**, *51*, 33–38.
- [32] C. Katayama, N. Sakabe, K. Sakabe, *Acta Crystallogr., Sect. A* **1972**, *28*.
- [33] G. Kopfmann, R. Huber, *Acta Crystallogr., Sect. A* **1968**, *24*, 348–351.
- [34] G. M. Sheldrick, SHELXL-2013, Göttingen, **2013**.
- [35] R. W. W. Hooft, L. H. Straver, A. L. Spek, *J. Appl. Crystallogr.* **2008**, *41*, 96–103.
- [36] J. M. Bijvoet, A. F. Peerdeman, A. J. van Bommel, *Nature* **1951**, *168*, 271–272.
- [37] S. Parsons, H. D. Flack, T. Wagner, *Acta Crystallogr., Sect. B* **2013**, *69*, 249–259.
- [38] D. Stalke, H. Ott, *Nachr. Chem.* **2008**, *56*, 131–135.
- [39] N. K. Hansen, P. Coppens, *Acta Crystallogr., Sect. A* **1978**, *34*, 909–921.
- [40] E. Clementi, D. L. Raimondi, *J. Chem. Phys.* **1963**, *38*, 2686–2689.
- [41] E. Clementi, C. Roetti, *Atom. Data Nuc. Data Tab.* **1974**, *14*, 177–478.
- [42] A. Volkov, Y. A. Abramov, P. Coppens, *Acta Crystallogr., Sect. A* **2001**, *57*, 272–282.
- [43] P. M. Dominiak, P. Coppens, *Acta Crystallogr., Sect. A* **2006**, *62*, 224–227.
- [44] A. Volkov, P. Macchi, L. J. Farrugia, C. Gatti, P. R. Mallinson, T. Richter, T. Koritsanszky, XD2006, A Computer Program Package for Multipole Refinement, Topological Analysis of Charge Densities and Evaluation of Intermolecular Energies from Experimental or Theoretical Structure Factors, **2006**.
- [45] C. Jelsch, B. Guillot, A. Lagoutte, C. Lecomte, *J. Appl. Crystallogr.* **2001**, *38*, 38–54.
- [46] V. Petricek, M. Dusek, L. Palatinus, *Jana2006. The crystallographic computing system*. Praha, Czech Republik, **2006**.
- [47] B. Zarychta, V. Pichon-Pesme, B. Guillot, C. Lecomte, C. Jelsch, *Acta Crystallogr., Sect. A* **2006**, *38*, 38–54.
- [48] C. Jelsch, V. Pichon-Pesme, C. Lecomte, A. Aubry, *Acta Crystallogr., Sect. D* **1998**, *54*, 1306–1318.
- [49] C. A. Coulson, M. W. Thomas, *Acta Crystallogr., Sect. B* **1971**, *27*, 1354–1359.
- [50] R. F. Stewart, E. R. Davidson, W. T. Simpson, *J. Chem. Phys.* **1965**, *42*, 3175–3187.
- [51] W. Kolos, C. C. J. Roothaan, *Rev. Mod. Phys.* **1960**, *32*, 219–232.
- [52] F. H. Allen, *Acta Crystallogr., Sect. B* **1986**, *42*, 515–522.
- [53] K. Meindl, J. Henn, *Acta Crystallogr., Sect. A* **2008**, *64*, 404–418.
- [54] V. V. Zhurov, E. A. Zhurova, A. A. Pinkerton, *J. Appl. Crystallogr.* **2008**, *41*, 340–349.
-

-
- [55] S. C. Abrahams, E. T. Keve, *Acta Crystallogr., Sect. A* **1971**, 27, 157-165.
- [56] D. Schwarzenbach, S. C. Abrahams, H. D. Flack, W. Gonschorek, T. Hahn, K. Huml, R. E. Marsh, E. Prince, B. E. Robertson, J. S. Rollett, A. J. C. Wilson, *Acta Crystallogr., Sect. A* **1989**, 45, 63-75.
- [57] Bruker SAINT v7.68A, Madison, WI, USA, **2009**.
- [58] SAINT+ Integration Engine Reference, Madison, WI, **2010**.
- [59] W. Kabsch, *J. Appl. Crystallogr.* **1988**, 21, 916-924.
- [60] R. Bolotovskiy, M. A. White, A. Darovskiy, P. Coppens, *J. Appl. Crystallogr.* **1995**, 28, 86-95.
- [61] J. Zaleski, G. Wu, P. Coppens, *J. Appl. Crystallogr.* **1998**, 31, 302-304.
- [62] G. Wu, B. L. Rodrigues, P. Coppens, *J. Appl. Crystallogr.* **2002**, 35, 356-359.
- [63] A. B. Storm, C. Michaelsen, A. Oehr, C. Hoffmann, *Proc. SPIE* **2004**, 5537, 177-181.
- [64] P. Macchi, H.-B. Bürgi, A. S. Chimpri, J. Hauser, Z. Gál, *J. Appl. Crystallogr.* **2011**, 44, 763-771.
- [65] R. F. W. Bader, *Acc. Chem. Res.* **1975**, 8, 34-40.
- [66] R. F. W. Bader, T.-H. Tang, Y. Tal, F. W. Biegler-König, *J. Am. Chem. Soc.* **1982**, 104, 946-952.
- [67] R. F. W. Bader, T. H. Tang, Y. Tal, F. W. Biegler-König, *J. Am. Chem. Soc.* **1982**, 104, 940-945.
- [68] R. F. W. Bader in *The Quantum Theory of Atoms in Molecules*. 1st Ed., Oxford University Press, New York, **1990**.
- [69] R. F. W. Bader, *J. Phys. Chem. A* **1998**, 102, 7314-7323.
- [70] R. F. W. Bader, P. M. Beddall, *J. Chem. Phys.* **1972**, 56, 3320-3329.
- [71] K. Collard, G. G. Hall, *Int. J. Quantum Chem.* **1977**, 12, 623-637.
- [72] D. Cremer, E. Kraka, *Angew. Chem.* **1984**, 96, 612-614; *Angew. Chem. Int. Ed. Engl.* **1984**, 23, 627.
- [73] R. F. W. Bader, R. J. Gillespie, P. J. MacDougall, *Mol. Struct. Energ.* **1989**, 11, 1-51.
- [74] R. F. W. Bader, P. J. MacDougall, *J. Am. Chem. Soc.* **1985**, 107, 6788-6795.
- [75] T.-H. Tang, R. F. W. Bader, P. J. MacDougall, *Inorg. Chem.* **1985**, 24, 2047-2053.
- [76] R. F. W. Bader, R. J. Gillespie, P. J. MacDougall, *J. Am. Chem. Soc.* **1988**, 110, 7329-7336.
- [77] W. Scherer, M. Spiegler, B. Pedersen, M. Tafipolsky, W. Hieringer, B. Reinhard, A. J. Downs, G. S. McGrady, *Chem. Commun.* **2000**, 635-636.
- [78] D. Leusser, B. Walfort, D. Stalke, *Angew. Chem.* **2002**, 114, 2183-2186.
- [79] N. Kocher, C. Selinka, D. Leusser, D. Kost, I. Kalikhman, D. Stalke, *Z. Anorg. Allg. Chem.* **2004**, 630, 1777-1793.
-

-
- [80] D. Leusser, J. Henn, N. Kocher, B. Engels, D. Stalke, *J. Am. Chem. Soc.* **2004**, *126*, 1781-1793.
- [81] R. F. W. Bader, T. S. Slee, D. Cremer, E. Kraka, *J. Am. Chem. Soc.* **1983**, *105*, 5061-5068.
- [82] D. Cremer, E. Kraka, T. S. Slee, R. F. W. Bader, C. D. H. Lau, T. T. Nguyen-Dang, P. J. MacDougall, *J. Am. Chem. Soc.* **1983**, *105*, 5069-5075.
- [83] J. R. Cheeseman, M. T. Carroll, R. F. W. Bader, *Chem. Phys. Lett.* **1988**, *143*, 450-458.
- [84] M. Presselt, C. Schnedermann, M. Schmitt, J. Popp, *J. Phys. Chem. A* **2009**, *113*, 3210-3222.
- [85] M. Presselt, B. Dietzek, M. Schmitt, S. Rau, A. Winter, M. Jäger, U. S. Schubert, J. Popp, *J. Phys. Chem. A* **2010**, *114*, 13163-13174.
- [86] M. Presselt, C. Schnedermann, M. Müller, M. Schmitt, J. Popp, *J. Phys. Chem. A* **2010**, *114*, 10287-10296.
- [87] L. J. Farrugia, A. D. Khalaji, *J. Phys. Chem. A* **2011**, *115*, 12512-12522.
- [88] M. Tafipolsky, W. Scherer, K. Öfele, G. Artus, B. Pedersen, W. A. Herrmann, G. S. McGrady, *J. Am. Chem. Soc.* **2002**, *124*, 5865-5880.
- [89] R. F. W. Bader, C. Gatti, *Chem. Phys. Lett.* **1998**, *287*, 233-238.
- [90] C. Gatti, F. Cargnoni, L. Bertini, *J. Comp. Chem.* **2003**, *24*, 422-436.
- [91] C. Gatti, L. Bertini, *Acta Crystallogr., Sect. A* **2004**, *60*, 438-449.
- [92] L. J. Farrugia, C. Evans, D. Lentz, M. Roemer, *J. Am. Chem. Soc.* **2009**, *131*, 1251-1268.
- [93] L. J. Farrugia, C. Evans, M. Tegel, *J. Phys. Chem. A* **2006**, *110*, 7952-7961.
- [94] C. Gatti in *Structure and Bonding Vol. 147*, (Eds.: U. Flierler, D. Stalke), Springer, Berlin, New York, **2012**, pp. 193-286.
- [95] E. Monza, C. Gatti, L. Lo Presti, E. Ortoleva, *J. Phys. Chem. A* **2011**, *115*, 12864-12878.
- [96] M. R. V. Jørgensen, S. Cenedese, H. F. Clausen, J. Overgaard, Y.-S. Chen, C. Gatti, B. B. Iversen, *Inorg. Chem.* **2013**, *52*, 297-305.
- [97] L. Lo Presti, A. Ellern, R. Destro, R. Soave, B. Lunelli, *J. Phys. Chem. A* **2011**, *115*, 12695-12707.
- [98] C. Gatti, D. Lasi, *Faraday Discuss.* **2007**, *135*, 55-78.
- [99] J. Overgaard, C. Jones, A. Stasch, B. B. Iversen, *J. Am. Chem. Soc.* **2009**, *131*, 4208-4209.
- [100] L.-C. Wu, C.-W. Hsu, Y.-C. Chuang, G.-H. Lee, Y.-C. Tsai, Y. Wang, *J. Phys. Chem. A* **2011**, *115*, 12602-12615.
- [101] A. Makal, W. Schilf, B. Kamiński, A. Szady-Chelmieniecka, E. Grechd, K. Woźniak, *Dalton Trans.* **2011**, *40*, 421-430.
-

-
- [102] J. Overgaard, B. Schiøtt, F. K. Larsen, B. B. Iversen, *Chem. Eur. J.* **2001**, *7*, 3756-3767.
- [103] S. Grabowsky, T. Schirmeister, C. Paulmann, T. Pfeuffer, P. Luger, *J. Org. Chem.* **2011**, *76*, 1305-1318.
- [104] L. J. Farrugia, D. S. Middlemiss, R. Sillanpää, P. Seppälä, *J. Phys. Chem. A* **2008**, *112*, 9050-9067.
- [105] D. Stalke *Chem. Eur. J.* **2011**, *17*, 9264-9278.
- [106] J. J. Holstein, C. B. Hübschle, B. Dittrich, *CrystEngComm* **2012**, *14*, 2520-2531.
- [107] H. Ott, C. Däschlein, D. Leusser, D. Schildbach, T. Seibel, D. Stalke, C. Strohmman, *J. Am. Chem. Soc.* **2008**, *130*, 11901-11911.
- [108] A. Volkov, H. F. King, P. Coppens, L. J. Farrugia, *Acta Crystallogr., Sect. A.* **2006**, *62*, 400-408.
- [109] A. M. Pendás, E. Francisco, M. A. Blanco, C. Gatti, *Chem. Eur. J.* **2007**, *13*, 9362-9371.
- [110] E. R. Johnson, S. Keinan, P. Mori-Sánchez, J. Contreras-García, A. J. Cohen, W. Yang, *J. Am. Chem. Soc.* **2010**, *132*, 6498-6506.
- [111] J. Contreras-García, W. Yang, E. R. Johnson, *J. Phys. Chem. A* **2011**, *115*, 12983-12990.
- [112] G. Saleh, C. Gatti, L. L. Presti, J. Contreras-García, *Chem. Eur. J.* **2012**, *18*, 15523 - 15536.
- [113] A. D. Becke, *Physical Review* **1988**, *A38*, 3098-3100.
- [114] A. D. Becke in *Modern Electronic Structure Theory*, (Ed.: D. R. Yarkony), World Scientific, River Edge, **1995**, pp. 1022 -1046.
- [115] J. Contreras-García, E. R. Johnson, S. Keinan, R. Chaudret, J.-P. Piquemal, D. N. Beratan, W. Yang, *J. Chem. Theory Comput.* **2011**, *7*, 625-632. See also <http://www.chem.duke.edu/~yang/software.htm>.
- [116] E. O. Fischer, W. Hafner, H. O. Stahl, *Z. Anorg. Allg. Chem.* **1955**, *10b*, 47-62.
- [117] E. O. Fischer, R. Jira, K. Hafner, *Z. Naturforsch., B: Chem. Sci.* **1953**, *8*, 327.
- [118] K. Ziegler, H. Froitzheim-Kühlhorn, K. Hafner, *Chem. Ber.* **1956**, *89*, 434-443.
- [119] J. Thiele, *Ber. Dtsch. Chem. Ges.* **1901**, *34*, 68-71.
- [120] S. Harder, *Coord. Chem. Rev.* **1998**, *176*, 17-66.
- [121] S. Alexandratos, A. Streitwieser jr., H. F. Schaefer III, *J. Am. Chem. Soc.* **1976**, *98*, 7959-7962.
- [122] R. Janoschek, G. Diercksen, H. Preuss, *Int. J. Quantum Chem.* **1967**, *1*, 205-208.
- [123] V. Rayón, G. Frenking, *Chem. Eur. J.* **2002**, *8*, 4693-4707.
- [124] K. C. Waterman, A. S. Jr., *J. Am. Chem. Soc.* **1984**, *106*, 3138-3140.
- [125] E. D. Jemmis, P. v. R. Schleyer, *J. Am. Chem. Soc.* **1982**, *104*, 4781-4788.
-

-
- [126] I. A. Ronova, D. A. Bochvar, A. L. Chistjakov, Y. T. Struchkov, N. V. Alekseev, *J. Organomet. Chem.* **1969**, *18*, 337-344.
- [127] R. K. Bohn, A. Haaland, *J. Organomet. Chem.* **1966**, *5*, 470-476.
- [128] S. Shibata, L. S. Bartell, R. M. Gavin, *J. Chem. Phys.* **1964**, *41*, 717-722.
- [129] R. Michel, T. Nack, R. Neufeld, J. M. Dieterich, R. A. Mata, D. Stalke, *Angew. Chem.* **2013**, *125*, 762-766; *Angew. Chem. Int. Ed.* **2013**, *52*, 734-738.
- [130] R. Michel, R. Herbst-Irmer, D. Stalke, *Organometallics* **2010**, *29*, 6169-6171.
- [131] R. Michel, R. Herbst-Irmer, A. Schönleber, D. Stalke, unpublished work.
- [132] R. Michel, R. Herbst-Irmer, D. Stalke, *Organometallics* **2011**, *30*, 4379-4386.
- [133] D. Stalke, *Chem. Soc. Rev.* **1998**, *27*, 171-178.
- [134] T. Kottke, D. Stalke, *J. Appl. Crystallogr.* **1993**, *26*, 615-619.
- [135] COSMO, Madison (WI), Bruker-AXS, **2011**.
- [136] Bruker APEX v2011.4-1, Madison, WI, USA, **2011**.
- [137] W. R. Busing, H. A. Levy, *Acta Crystallogr.* **1957**, *10*, 180-182.
- [138] G. M. Sheldrick, SADABS 2012/1, Madison, WI, USA, **2012**.
- [139] G. M. Sheldrick, XPREP 2013/1, Madison, WI, USA, **2013**.
- [140] G. M. Sheldrick, SHELXT, Göttingen, **2013**.
- [141] Bruker AXS Inc., Madison, **1997**.
- [142] F. L. Hirshfeld, *Acta Crystallogr., Sect. A.* **1976**, *32*, 239-244.
- [143] H. Hope, T. Ottersen, *Acta Crystallogr., Sect. B.* **1978**, *34*, 3623-3626.
- [144] M. Helliwell, D. G. d. Anderez, J. R. Helliwell, J. Vernon, *Acta Crystallogr., Sect. B.* **1989**, *45*, 591-596.
- [145] R. I. Cooper, A. L. Thompson, D. J. Watkin, *J. Appl. Crystallogr.* **2010**, *43*, 1100-1107.
- [146] Z. Su, P. Coppens, *Acta Crystallogr., Sect. A.* **1998**, *54*, 646-652.
- [147] P. Macchi, P. Coppens, *Acta Crystallogr., Sect. A.* **2001**, *57*, 656-662.
- [148] shade.ki.ku.dk.
- [149] A. Ø. Madsen, *J. Appl. Crystallogr.* **2006**, *39*, 757-758.
- [150] L. Arnberg, S. Hovmöller, S. Westman, *Acta Crystallogr., Sect. A.* **1979**, *35*, 497-499.
- [151] F. L. Hirshfeld, D. Rabinovich, *Acta Crystallogr., Sect. A.* **1973**, *29*, 510-513.
- [152] *International Tables for X-Ray Crystallography Vol. 4*, (Eds.: C. K. Johnson, H. A. Levy), Kynoch Press, Birmingham, **1974**.
- [153] M. S. Schmøkel, S. Cenedese, J. Overgaard, M. R. V. Jørgensen, Y.-S. Chen, C. Gatti, D. Stalke, B. B. Iversen, *Inorg. Chem.* **2012**, *51*, 8607-8616.
- [154] H. Ott, U. Pieper, D. Leusser, U. Flierler, J. Henn, D. Stalke, *Angew. Chem.* **2009**, *121*, 3022-3026; *Angew. Chem. Int. Ed.* **2009**, *48*, 2978-2982.
-

-
- [155] C. B. Hübschle, B. Dittrich, *J. Appl. Crystallogr.* **2011**, *44*, 238-240.
- [156] A. Stash, DRKplot for XD and SHELX, Moscow, **2007**.
- [157] J. Henn, K. Meindl, *Acta Crystallogr., Sect. A.* **2010**, *66*, 676-684.
- [158] J. Henn, K. Meindl, *Acta Crystallogr., Sect. A.* **2012**, *68*, 304.
- [159] D. Kratzert, PhD thesis, Institute of Inorganic Chemistry, Georg August University (Göttingen), **2013**. <http://hdl.handle.net/11858/00-1735-000-001C-63A3-B>.
- [160] T. A. Keith, AIMAll Version 11.10.16, <http://aim.tkgristmill.com>, **2012**.
- [161] H.-J. Werner, P. J. Knowles, G. Knizia, F. R. Manby, M. Schütz, P. Celani, T. Korona, R. Lindh, A. Mitrushenkov, G. Rauhut, K. R. Shamasundar, T. B. Adler, R. D. Amos, A. Bernhardsson, A. Berning, D. L. Cooper, M. J. O. Deegan, A. J. Dobbyn, F. Eckert, E. Goll, C. Hampel, A. Hesselmann, G. Hetzer, T. Hrenar, G. Jansen, C. Köppl, Y. Liu, A. W. Lloyd, R. A. Mata, A. J. May, S. J. McNicholas, W. Meyer, M. E. Mura, A. Nicklass, D. P. O'Neill, P. Palmieri, D. Peng, K. Pflüger, R. Pitzer, M. Reiher, T. Shiozaki, H. Stoll, A. J. Stone, R. Tarroni, T. Thorsteinsson, M. Wang, MOLPRO, version 2012.1, a package of ab initio programs, <http://www.molpro.net>, **2012**.
- [162] P. Pulay, *Chem. Phys. Lett.* **1983**, *100*, 151-154.
- [163] S. Sæbø, P. Pulay, *Chem. Phys. Lett.* **1985**, *113*, 13-18.
- [164] P. Pulay, S. Sæbø, *Theor. Chim. Acta* **1986**, *69*, 357-368.
- [165] S. Sæbø, P. Pulay, *J. Chem. Phys.* **1987**, *86*, 914-922.
- [166] S. Sæbø, P. Pulay, *J. Chem. Phys.* **1988**, *88*, 1884-1890.
- [167] T. H. Dunning Jr, *J. Chem. Phys.* **1989**, *90*, 1007-1023.
- [168] D. E. Woon, T. H. Dunning Jr, *J. Chem. Phys.* **1993**, *98*, 1358-1371.
- [169] G. Hetzer, P. Pulay, H. J. Werner, *Chem. Phys. Lett.* **1998**, *290*, 143-149.
- [170] G. Rauhut, P. Pulay, H. J. Werner, *J. Comp. Chem.* **1998**, *19*, 1241-1254.
- [171] M. Schütz, G. Hetzer, H. J. Werner, *J. Chem. Phys.* **1999**, *111*, 5691-5705.
- [172] G. Hetzer, M. Schütz, H. Stoll, H. J. Werner, *J. Chem. Phys.* **2000**, *113*, 9443-9455.
- [173] B. P. Prascher, D. E. Woon, K. A. Peterson, T. H. Dunning Jr, A. K. Wilson, *Theoretical Chemistry Accounts* **2011**, *128*, 69-82.
- [174] F. L. Hirshfeld, *Theor. Chim. Acta* **1977**, *44*, 129-138.
- [175] M. A. Spackman, P. G. Byrom, *Chem. Phys. Lett.* **1997**, *267*, 215-220.
- [176] J. J. McKinnon, A. S. Mitchell, M. A. Spackman, *Chem. Eur. J.* **1998**, *4*, 2136-2141.
- [177] M. A. Spackman, J. J. McKinnon, D. Jayatilaka, *CrystEngComm* **2008**, *10*, 377-388.
- [178] M. A. Spackman, D. Jayatilaka, *CrystEngComm* **2009**, *11*, 19-32.
- [179] J. J. McKinnon, M. A. Spackman, A. S. Mitchell, *Acta Crystallogr., Sect. B.* **2004**, *60*, 627-668.
- [180] J. J. McKinnon, D. Jayatilaka, M. A. Spackman, *Chem. Commun.* **2007**, 3814-3816.
-

-
- [181] S. K. Wolff, D. J. Grimwood, J. J. McKinnon, M. J. Turner, D. Jayatilaka, M. A. Spackman, *CrystalExplorer 3.0*, Perth, Australia, **2005-2009**.
- [182] J. Henn, D. Leusser, D. Stalke, *J. Comp. Chem.* **2007**, *28*, 2317-2324.
- [183] H. A. Sparkes, A. B. Chaplin, A. S. Wellerb, J. A. K. Howard, *Acta Crystallogr., Sect. B.* **2010**, *66*, 503-514.
- [184] A. Jana, D. Leusser, I. Objartel, H. W. Roesky, D. Stalke, *Dalton Trans.* **2011**, *40*, 5458-5463.
- [185] G. Saleh, C. Gatti, L. Lo Presti, *Comp. Theor. Chem.* **2012**, *998*, 148-163.
- [186] G. Saleh, L. Lo Presti, C. Gatti, NCI Milano, Milan, Italy, **2012**.
- [187] H. Ott, C. Däschlein, D. Leusser, D. Schildbach, T. Seibel, D. Stalke, C. Strohmam, *J. Am. Chem. Soc.* **2008**, im Druck.
- [188] S. Deuerlein, D. Leusser, U. Flierler, H. Ott, D. Stalke, *Organometallics* **2008**, *27*, 2306-2315.
- [189] T. Kottke, D. Stalke, *Angew. Chem.* **1993**, *105*, 619-621; *Angew. Chem. Int. Ed. Engl.* **1993**, *32*, 580-582.
- [190] K. Meindl, J. Henn, N. Kocher, D. Leusser, K. A. Zachariasse, G. M. Sheldrick, T. Koritsanszky, D. Stalke, *J. Phys. Chem. A* **2009**, *113*, 9684-9691.
- [191] J. M. Bąk, P. M. Dominiak, C. C. Wilson, K. Woźniak, *Acta Crystallogr., Sect. A.* **2009**, *65*, 490-500.
- [192] D. Kratzert, D. Leusser, J. J. Holstein, B. Dittrich, K. Abersfelder, D. Scheschkewitz, D. Stalke, *Angew. Chem.* **2013**, *125*, 4574-4578; *Angew. Chem. Int. Ed. Engl.* **2013**, *52*, 4478-4482.
- [193] W. Scherer, G. Eickerling, M. Tafipolsky, G. S. McGrady, P. Sirsch, N. P. Chatterton, *Chem. Commun.* **2006**, 2986-2988.
- [194] A. Reisinger, N. Trapp, I. Krossing, S. Altmannshofer, V. Herz, M. Presnitz, W. Scherer, *Angew. Chem.* **2007**, *119*, 8445-8449; *Angew. Chem. Int. Ed.* **2007**, *46*, 8295.
- [195] B. Rohmoser, G. Eickerling, M. Presnitz, W. Scherer, V. Eyert, R.-D. Hoffmann, U. C. Rodewald, C. Vogt, R. Pöttgen, *J. Am. Chem. Soc.* **2007**, *129*, 9356-9365.
- [196] N. Kocher, D. Leusser, A. Murso, D. Stalke, *Chem. Eur. J.* **2004**, *10*, 3622-3631.
- [197] J. A. Osborn, F. H. Jardine, J. F. Young, G. Wilkinson, *J. Chem. Soc. A* **1966**, 1711-1732.
- [198] R. J. P. Corriu, J. P. Masse, *J. Chem. Soc., Chem. Commun.* **1972**, *3*, 144.
- [199] K. Tamao, K. Sumitani, M. Kumada, *J. Am. Chem. Soc.* **1972**, *94*, 4374-4376.
- [200] H. A. Dieck, F. R. Heck, *J. Organomet. Chem.* **1975**, *93*, 259-263.
- [201] L. Cassar, *J. Organomet. Chem.* **1975**, *93*, 253-257.
- [202] K. Sonogashira, Y. Tohda, N. Hagihara, *Tetrahedron Lett.* **1975**, *50*, 4467-4470.
- [203] A. O. King, N. Okukado, E.-i. Negishi, *J. Chem. Soc., Chem. Commun.* **1977**, *19*, 683-684.
-

-
- [204] N. Miyaura, K. Yamada, A. Suzuki, *Tetrahedron Lett.* **1979**, 36, 3437-3440.
- [205] Y. Hatanaka, T. Hiyama, *J. Org. Chem.* **1988**, 53, 918-920.
- [206] A. Miyashita, A. Yasuda, H. Takaya, K. Toriumi, T. Ito, T. Souchi, R. Noyori, *J. Am. Chem. Soc.* **1980**, 102.
- [207] J. P. Wolfe, S. Wagaw, S. L. Buchwald, *J. Am. Chem. Soc.* **1996**, 118, 7215-7216.
- [208] B. C. Hamann, J. F. Hartwig, *J. Am. Chem. Soc.* **1008**, 120.
- [209] F. Rataboul, A. Zapf, R. Jackstell, S. Harkal, T. Riermeier, A. Monsees, U. Dingerdissen, M. Beller, *Chem. Eur. J.* **2004**, 10, 2983-2990.
- [210] S. M. Wong, C. M. So, F. Y. Kwong, *Synlett* **2012**, 23, 1132-1153.
- [211] M. Pfeiffer, F. Baier, T. Stey, D. Leusser, D. Stalke, B. Engels, D. Moigno, W. Kiefer, *J. Mol. Modeling* **2000**, 6, 299-311.
- [212] S. Wingerter, M. Pfeiffer, A. Murso, C. Lustig, T. Stey, V. Chandrasekhar, D. Stalke, *J. Am. Chem. Soc.* **2001**, 123, 1381-1388.
- [213] F. Baier, Z. Fei, H. Gornitzka, A. Murso, S. Neufeld, M. Pfeiffer, I. Rüdener, A. Steiner, T. Stey, D. Stalke, *J. Organomet. Chem.* **2002**, 661, 111-127.
- [214] A. Murso, D. Stalke, *Dalton Trans.* **2004**, 2563-2569.
- [215] A. Murso, D. Stalke, *Z. Anorg. Allg. Chem.* **2004**, 630, 1025-1030.
- [216] T. Kottke, D. Stalke, *Chem. Ber.* **1997**, 130, 1365-1374.
- [217] H. Gornitzka, D. Stalke, *Angew. Chem.* **1994**, 106, 695-697; *Angew. Chem. Int. Ed. Engl.* **1994**, 33, 693-695.
- [218] A. Steiner, D. Stalke, *Angew. Chem.* **1995**, 107, 1908-1910; *Angew. Chem. Int. Ed. Engl.* **1995**, 34, 1752-1754.
- [219] M. Pfeiffer, T. Stey, H. Jehle, B. Klüpfel, W. Malisch, D. Stalke, V. Chandrasekhar, *Chem. Commun.* **2001**, 4, 337-338.
- [220] T. Stey, D. Stalke, *Z. Anorg. Allg. Chem.* **2005**, 651, 2931-2936.
- [221] T. Stey, J. Henn, D. Stalke, *Chem. Commun.* **2007**, 413-415.
- [222] T. Stey, M. Pfeiffer, J. Henn, S. K. Pandey, D. Stalke, *Chem. Eur. J.* **2007**, 13, 3636-3642.
- [223] C. Kling, D. Leusser, T. Stey, D. Stalke, *Organometallics* **2011**, 30, 2461-2463.
- [224] F. Leca, C. Lescop, E. Rodriguez-Sanz, K. Costuas, J.-F. Halet, R. Réau, *Angew. Chem.* **2005**, 117, 4436-4439; *Angew. Chem. Int. Ed.* **2005**, 44, 4362-4365.
- [225] B. Nohra, E. Rodriguez-Sanz, C. Lescop, R. Réau, *Chem. Eur. J.* **2008**, 14, 3391-3403.
- [226] S. Welsch, B. Nohra, E. V. Peresyphkina, C. Lescop, M. Scheer, R. Réau, *Chem. Eur. J.* **2009**, 15, 4685-4703.
- [227] J. Henn, K. Meindl, A. Oechsner, G. Schwab, T. Koritsanszky, D. Stalke, *Angew. Chem. Int. Ed.* **2010**, 49, 2422-2426.
-

-
- [228] P. Coppens in *X-Ray Charge Densities and Chemical Bonding*, Oxford University Press, Oxford, **1997**.
- [229] The mean P-C distance values were taken from the Cambridge Structural Database. 467284 distances from bonds classified as "single" bond were considered. Distances from bonds classified as "double" bond were only considered if the phosphorus atom had a maximum number of three bonding partners, which effectively ruled out bias from ylidic bonds.
- [230] P. J. MacDougall, M. B. Hall, R. F. W. Bader, J. R. Cheeseman, *Can. J. Chem.* **1989**, *67*, 1842-1846.
- [231] E. Matito, J. Poater, M. Solà, P. v. R. Schleyer in *Chemical Reactivity Theory*, (Ed.: P. K. Chattaraj), Taylor and Francis/CRC Press, Boca Raton, **2009**, pp. 419-438.
- [232] P. v. R. Schleyer, *Chem. Rev.* **2001**, *101*, 1115-1117.
- [233] P. v. R. Schleyer, *Chem. Rev.* **2005**, *105*, 3433-3435.
- [234] *Phys. Chem. Chem. Phys.* **2011**, *13*, themed issue: Aromaticity, electron delocalisation and related molecular properties.
- [235] A. R. Katritzky, K. Jug, D. C. Oniciu, *Chem. Rev.* **2001**, *101*, 1421-1449.
- [236] T. M. Krygowski, *J. Chem. Inf. Comp. Sci.* **1993**, *33*, 70-78.
- [237] C. W. Bird, *Tetrahedron* **1985**, *41*, 1409-1414.
- [238] C. W. Bird, *Tetrahedron* **1986**, *42*, 89-92.
- [239] C. W. Bird, *Tetrahedron* **1992**, *48*, 335-340.
- [240] R. C. Haddon, V. R. Haddon, L. J. Jackman in *Top. Curr. Chem. Vol. 16*, Springer, Berlin, **1971**, p. 2.
- [241] R. H. Mitchell, *Chem. Rev.* **2001**, *101*, 1301-1315.
- [242] J. A. N. F. Gomes, R. B. Mallion, *Chem. Rev.* **2001**, *101*, 1359-1383.
- [243] P. Lazzeretti, *Prog. Nucl. Magn. Reson. Spectrosc.* **2000**, *36*, 1-88.
- [244] P. Lazzeretti, *Phys. Chem. Chem. Phys.* **2004**, *6*, 217-223.
- [245] Z. Chen, C. S. Wannere, C. Corminboeuf, R. Puchta, P. v. R. Schleyer, *Chem. Rev.* **2005**, *105*, 3842-3888.
- [246] P. v. R. Schleyer, C. Maerker, A. Dransfeld, H. Jiao, N. J. R. v. E. Hommes, *J. Am. Chem. Soc.* **1996**, *118*, 6317-6318.
- [247] H. Fliegl, S. Taubert, O. Lehtonen, D. Sundholm, *Phys. Chem. Chem. Phys.* **2011**, *13*, 20500-20518.
- [248] H. Fliegl, D. Sundholm, S. Taubert, F. Pichierri, *J. Phys. Chem. A* **2010**, *114*, 7153-7161.
- [249] H. Fliegl, D. Sundholm, S. Taubert, J. Jusélius, W. Klopper, *J. Phys. Chem. A* **2009**, *113*, 8668-8676.
- [250] G. Frenking, A. Krapp, *J. Comp. Chem.* **2007**, *28*, 15-24.
-

-
- [251] W. Kutzelnigg, *Angew. Chem.* **1984**, *96*, 262-285; *Angew. Chem. Int. Ed. Engl.* **1984**, *23*, 272-295.
- [252] J. E. Lennard-Jones, *Trans. Faraday Soc.* **1929**, *25*, 668-686.
- [253] E. Hückel, *Z. Phys.* **1931**, *70*, 204-286.
- [254] W. Kutzelnigg, *J. Comp. Chem.* **2007**, *28*, 25-34.
- [255] J. Poater, M. Duran, M. Sola, B. Silvi, *Chem. Rev.* **2005**, *105*, 3911-3947.
- [256] J. Poater, M. Duran, M. Solà, B. Silvi, *Chem. Rev.* **2009**, *105*, 3911-3947.
- [257] W. Scherer, P. Sirsch, M. Grosche, M. Spiegler, S. A. Mason, M. G. Gardiner, *Chem. Commun.* **2001**, 2072-2073.
- [258] W. Scherer, P. Sirsch, D. Shorokhov, M. Tafipolsky, G. S. McGrady, E. Gullo, *Chem. Eur. J.* **2003**, *9*, 6057-6070.
- [259] R. F. W. Bader, A. Streitwieser, A. Neuhaus, K. E. Laidig, P. Speers, *J. Am. Chem. Soc.* **1996**, *118*, 4959-4965.
- [260] J. Poater, X. Fradera, M. Duran, M. Solà, *Chem. Eur. J.* **2003**, *9*, 400-406.
- [261] A. R. Katritzky, P. Barczynski, G. Musumarra, D. Pisano, M. Szafran, *J. Am. Chem. Soc.* **1989**, *111*, 7-15.
- [262] K. Jug, A. M. Köster, *J. Phys. Org. Chem.* **1991**, *4*, 163-169.
- [263] M. Cyrański, T. M. Krygowski, A. R. Katritzky, P. v. R. Schleyer, *J. Org. Chem.* **2002**, *67*, 1333-1338.
- [264] H.-J. Werner, F. R. Manby, P. J. Knowles, *J. Chem. Phys.* **2003**, *118*, 8149-8160.
- [265] T. H. Dunning, *J. Chem. Phys.* **1989**, *90*, 1007-1023.
- [266] L. J. Farrugia, P. Macchi, *J. Phys. Chem. A* **2009**, *113*, 10058-10067.
- [267] A. D. McNaught, A. Wilkinson in *IUPAC Compendium of Chemical Terminology, 2nd ed. (the "Gold Book")*, Blackwell Scientific Publications, Oxford, **1997**.
- [268] C. Gatti, G. Saleh, *private communication*. **2012**.
- [269] L. J. Farrugia, WinXD v1.023, Glasgow, Scotland, UK, **2007**.
- [270] Persistence of Vision Raytracer Pty. Ltd., Persistence of Vision Raytracer (Version 3.7), Williamstown, Victoria, Australia, **2010**.
- [271] D. B. Chesnut, L. J. Bartolotti, *Chem. Phys.* **2000**, *257*, 175-181.
- [272] X. Fradera, M. A. Austen, R. F. W. Bader, *J. Phys. Chem. A* **1999**, *103*, 304-314.
- [273] P. Macchi, *Angew. Chem.* **2009**, *121*, 5905-5907; *Angew. Chem. Int. Ed.* **2009**, *48*, 5793-5795.
- [274] S. Loibl, F. R. Manby, M. Schütz, *Mol. Phys.* **2010**, *108*, 477-485.
- [275] J. Jusélius, D. Sundholm, J. Gauss, *J. Chem. Phys.* **2004**, *121*, 3952-3963.
- [276] S. Taubert, D. Sundholm, J. Jusélius, *J. Chem. Phys.* **2011**, *134*, 054123:054121-054112.
- [277] M. P. Johansson, J. Jusélius, D. Sundholm, *Angew. Chem.* **2005**, *117*, 1877-1880; *Angew. Chem. Int. Ed.* **2005**, *44*, 1843-1846.
-

-
- [278] Y. C. Lin, J. Jusélius, D. Sundholm, J. Gauss, *J. Chem. Phys.* **2005**, *122*, 214308:214301–214309.
- [279] S. Taubert, D. Sundholm, F. Pichierri, *J. Org. Chem.* **2009**, *74*, 6495–6502.
- [280] H. Fliegl, O. Lehtonen, M. Patzschke, D. Sundholm, Y. C. Lin, *Theor. Chem. Acc.* **2011**, *129*, 701–713.
- [281] H. Fliegl, D. Sundholm, F. Pichierri, *Phys. Chem. Chem. Phys.* **2011**, *13*, 20659–20665.
- [282] M. Kaipio, M. Patzschke, H. Fliegl, F. Pichierri, D. Sundholm, *J. Phys. Chem. A* **2012**, *116*, 10257–10268.
- [283] J. A. N. F. Gomes, R. B. Mallion, *Chem. Rev.* **2001**, *101*, 1349–1384.
- [284] R. Zanasi, P. Lazzeretti, M. Malagoli, F. Piccinini, *J. Chem. Phys.* **1995**, *102*, 7150–7157.
- [285] R. F. W. Bader, *Chem. Rev.* **1991**, *91*, 893–928.
- [286] G. N. Lewis, *J. Am. Chem. Soc.* **1916**, *38*, 762–785.
- [287] R. J. Gillespie, *Molecular Geometry*. Reinhold Van Nostrand, London, **1972**.
- [288] R. F. W. Bader, P. L. A. Popelier, T. A. Keith, *Angew. Chem.* **1994**, *106*, 647–658; *Angew. Chem. Int. Ed. Engl.* **1994**, *33*.
- [289] There is a video of one of *Bader's* talks at www.chemistry.mcmaster.ca/bader/ which shows his lecture "There are no bonds, only bonding" from January 2008, four years before his death.
- [290] F. Cortés-Guzmán, R. F. W. Bader, *Coord. Chem. Rev.* **2005**, *249*, 633–662.
- [291] There is a video of one of *Bader's* talks at www.chemistry.mcmaster.ca/bader/ which shows his lecture "There are no bonds, only bonding" from January 2008, four years before his death.
- [292] S. Dahaoui, V. Pichon-Pesme, J. A. K. Howard, C. Lecomte, *J. Phys. Chem. A* **1999**, *103*, 6240–6250.
- [293] E. Espinosa, E. Molins, C. Lecomte, *Phys. Rev.* **1997**, *B56*, 1820–1833.
- [294] M. Laing, *J. Chem. Educ.* **1987**, *64*, 124–128.
- [295] A. D. Clauss, S. F. Nelsen, M. Ayoub, C. R. Landis, F. Weinhold, "Rabbit Ears Hybrids, VSEPR Sterics, and Other Orbital Absurdities" **2011**, not published in a journal; downloaded May 5th, 2013 from: "[sites.harvard.edu/fs/docs/icb.topic818673.files/Lecture 2 - Weinhold et al - Shape of Oxygen Lone Pairs.pdf](http://sites.harvard.edu/fs/docs/icb.topic818673.files/Lecture%20-%20Weinhold%20et%20al%20-%20Shape%20of%20Oxygen%20Lone%20Pairs.pdf)".
- [296] R. Ahlrichs, *Chem. Unserer Zeit*, **1980**, *14*, 18–24.
- [297] H. A. Bent, *J. Chem. Educ.* **1960**, *37*, 616–624.
- [298] A. Streitwieser, *Molecular Orbital Theory for Organic Chemists*, 1st Ed., John Wiley & Sons, Inc., New York, London, **1961**.
- [299] A. E. Reed, F. Weinhold, *J. Chem. Phys.* **1985**, *83*, 1736–1740.
- [300] A. E. Reed, R. B. Weinstock, F. Weinhold, *J. Chem. Phys.* **1985**, *83*, 735–746.
-

-
- [301] F. Weinhold, C. R. Landis, *Chem. Educ. Res. Pract. Eur.* **2001**, *2*, 91-104.
- [302] J. Kapp, C. Schade, A. M. El-Nahasa, P. v. R. Schleyer, *Angew. Chem.* **1996**, *108*, 2373-2376; *Angew. Chem. Int. Ed. Engl.* **1996**, *35*, 2373-2376.
- [303] J. Neufeind, H. E. Fischer, W. Schröer, *J. Phys.: Condens. Matter* **2000**, *12*, 8765-8776.
- [304] A. Haaland, *Molecules and Models: The molecular structures of main group element compounds*. Oxford University Press, Oxford, New York, **2012**.
- [305] P. P. Power, *Nature* **2010**, *463*, 171-177.
- [306] P. P. Power, *Chem. Rev.* **1999**, *99*, 3463-3503.
- [307] R. C. Fischer, P. P. Power, *Chem. Rev.* **2010**, *110*, 3877-3923.
- [308] A. Ranganathan, G. U. Kulkarni, C. N. R. Rao, *J. Mol. Struct.* **2003**, *656*, 249-263.
- [309] P. Munshi, T. N. G. Row, *Acta Crystallogr., Sect. B.* **2006**, *62*, 612-626.
- [310] P. Munshi, T. S. Thakur, T. N. G. Row, G. R. Desiraju, *Acta Crystallogr., Sect. B.* **2006**, *62*, 118-127.
- [311] J. Hey, Diplomarbeit, Georg August University, (Göttingen), **2009**.
- [312] G. Pifferi, L. Fontanella, E. Occelli, R. Monguzzi, *J. Heterocycl. Chem.* **1972**, 1209-1214.
- [313] J. Clayden, N. Greeves, S. Warren, P. Wothers in *Organic Chemistry*, Oxford University Press, Oxford, New York, **2001**.
- [314] S. Kano, Y. Tanaka, E. Sugino, S. Hibino, *Synthesis* **1980**, 695-697.
- [315] D. Liebschner, C. Jelsch, E. Espinosa, C. Lecomte, E. Chabrière, B. Guillot, *J. Phys. Chem. A* **2011**, *115*, 12895-12904.
- [316] M. S. Weiss, *J. Appl. Crystallogr.* **2001**, *34*, 130-135.
- [317] H. D. Flack, *Acta Crystallogr., Sect. A.* **1983**, *39*, 876-881.
- [318] F. H. Allen, O. Kennard, D. G. Watson, L. Brammer, A. G. Orpen, R. Taylor, *J. Chem. Soc., Perkin Trans. 2* **1987**, S1-S19.
- [319] B. Dittrich, T. Koritsanzky, P. Luger, *Angew. Chem.* **2004**, *116*, 2773-2776; *Angew. Chem. Int. Ed.* **2004**, *43*, 2718-2721.
- [320] R. Kalinowski, B. Dittrich, C. B. Hübschle, C. Paulmann, P. Luger, *Acta Crystallogr., Sect. B.* **2007**, *63*, 753-767.
- [321] C. Lecomte, M. Souhassou, S. Pillet, *J. Mol. Struct.* **2003**, *647*, 53-64.
- [322] T. Steiner, *Angew. Chem.* **2002**, *114*, 50-80; *Angew. Chem. Int. Ed.* **2002**, *41*, 48-78.
- [323] V. G. Tsirelson, E. V. Bartashevich, A. I. Stash, V. A. Potemkin, *Acta Crystallogr., Sect. B.* **2007**, *63*, 142-150.
- [324] S. T. Howard, O. Lamarche, *J. Phys. Org. Chem.* **2003**, *16*, 133-141.
- [325] R. Brückner, *Reaktionsmechanismen*. Elsevier, München, **2004**.
- [326] M. Granitzka, A.-C. Pöppler, E. K. Schwarze, D. Stern, T. Schulz, M. John, R. Herbst-Irmer, S. K. Pandey, D. Stalke *J. Am. Chem. Soc.* **2012**, *134*, 1344-1351.
-

-
- [327] M. Frank, J. Hey, I. Balcioglu, D. Stalke, H. Frauendorf, G. H. Clever, **2013**, in preparation.
- [328] R. Herbst-Irmer, J. Henn, J. J. Holstein, C. B. Hübschle, B. Dittrich, D. Stern, D. Kratzert, D. Stalke, *J. Phys. Chem. A* **2013**, *117*, 633-641.
- [329] K. Meindl, R. Herbst-Irmer, J. Henn, *Acta Crystallogr., Sect. A* **2010**, *66*, 362-371.
- [330] Z. Fei, N. Kocher, C. J. Mohrschladt, H. Ihmels, D. Stalke, *Angew. Chem.* **2003**, *115*, 807-811; *Angew. Chem. Int. Ed.* **2003**, *42*, 783-787.
- [331] C. B. Hübschle, P. Luger, B. Dittrich, *J. Appl. Crystallogr.* **2007**, *40*, 623.
- [332] B. Dittrich, C. B. Hübschle, P. Luger, M. A. Spackman, *Acta Crystallogr., Sect. D* **2006**, *62*, 1325-1335.
- [333] B. Dittrich, C. B. Hübschle, K. Pröpper, F. Dietrich, T. Stolper, J. J. Holstein, *Acta Crystallogr.* **2013**, *69*, 91-104.
- [334] S. Domagala, B. Fournier, D. Liebschner, B. Guillot, C. Jelsch, *Acta Cryst., Sect. A* **2012**, *68*, 337-351.
- [335] L. J. Farrugia, *J. Appl. Crystallogr.* **1999**, *32*, 837-838.
- [336] K. L. Smith, *personal communication*. **2013**.
- [337] T. Schulz, K. Meindl, D. Leusser, D. Stern, J. Graf, C. Michaelsen, M. Ruf, G. M. Sheldrick, D. Stalke, *J. Appl. Crystallogr.* **2009**, *42*, 885-891.
- [338] P. R. Mallinson, K. W. Muir, *J. Appl. Crystallogr.* **1985**, *18*, 51-53.
- [339] Bruker APEX v2009.3-0, Madison, WI, USA, **2007**.
- [340] R. Destro, L. Loconte, L. Lo Presti, P. Roversi, R. Soave, *Acta Crystallogr., Sect. A* **2004**, *60*, 365-370.
- [341] P. Coppens, *Angew. Chem.* **2005**, *117*, 6970-6972; *Angew. Chem. Int. Ed.* **2005**, *44*, 6810.
- [342] G. M. Sheldrick, TWINABS-2008/4, Göttingen, **2008**.
- [343] P. Müller, R. Herbst-Irmer, A. L. Spek, T. R. Schneider, M. R. Sawaya in *Crystal Structure Refinement - A Crystallographer's Guide to SHELXL Vol. 8*, (Ed.: P. Müller), Oxford University Press, Oxford (England), **2006**.

12. Curriculum vitae

Name: Jakob Hey
Date of birth: 30.12.1982 in Oldenburg/Olbg.
Nationality: German
Marital status: Married to Eva Hey
Address: Goßlerstraße 24, 37075 Göttingen
E-mail: jakob.hey@gmx.de

Scientific career

- 10.2009 – 06.2013 Ph.D studies in the CaSuS doctoral programme at the Georg August University Göttingen with a scholarship of the state of Lower Saxony (until 10.2012). Work on the doctoral thesis “From X-ray diffraction data annealing to comprehensive charge density analysis” in the *Stalke* workgroup.
- 01.2009 – 09.2009 Work on the synthetic chemical graduation thesis “*Asymmetrische Amide als Basis zur enantioselektiven Metallierung*” in Prof. Dr. D. *Stalke*’s workgroup at the Georg August University Göttingen.
- 04.2007 – 08.2007 Erasmus exchange to the Institute of Organic Chemistry at the University of Stockholm, workgroups Prof. Dr. J.-E. Bäckvall and Prof. Dr. B. Åkermark. Defence of the thesis “*Towards a new Manganese(III) catalyst for oxidation reactions*”.
- 10.2003 – 09.2009 Chemistry studies at the Georg August University Göttingen. Grades in the intermediate exam 2005 (*Vordiplomprüfung*): 1.33; final exam 2009 (*Diplomprüfung*): 1.05.
- 06.2002 Abitur at *Öffentlich-Stiftisches Gymnasium Bethel*, Bielefeld. Grade: 1.8.

Professional career

- 10.2009 – 09.2013 Maintenance and application of Bruker APEX2 diffractometers.
- 11.2007 – 12.2011 Active participation in the youth association of the GDCh. Member of the organisation committee of the *Jungchemikerforum 2010* hosted in Göttingen.
- 04.2006 – 09.2013 Scientific assistant (teaching): *Chemistry for students of medicine; Advanced inorganic synthesis lab course; Lab course in catalytic chemistry; Modern methods in Inorganic Chemistry; Introduction to catalytic chemistry.*

-
- 09.2002 – 07.2003 Substitution service (*Zivildienst*) at a home for mentally handicapped children run by *Margarethe-Wehling-Stiftung*, Bielefeld.
- 1998 – 2002 Voluntary work at *Evangelische Jugend* Bielefeld. Organisation of several youth camps.

Awards

- 12.2012 Elected for the award „Preis für die beste nichtselbstständige Lehre am Institut für Anorganische Chemie“ in a student poll.
- 09.2012 Prize for the best poster, 6th European Charge Density Meeting, Štrbské Pleso, High Tatras, Slovakia.
- 1996 Third prize in the *Bundeswettbewerb Jugend Musiziert* and first prizes in the *Regionalwettbewerb* and *Landeswettbewerb*.

Skills and Interests

- Languages: English (fluent), Latin, Swedish (basics).
- Sports: Snowboarding, Road Cycling.
- Instruments: Drum Set and percussion.

Scientific Publications in Print

1. Jakob Hey, Dirk Leusser, Daniel Kratzert, Heike Fliegl, Johannes M. Dieterich, Ricardo A. Mata, Dietmar Stalke, *accepted for publication in PhysChemChemPhys*.
2. Jakob Hey, Diego Andrada, Reent Michel, Ricardo M. Mata, Dietmar Stalke, *Angew. Chem.* **2013**, *125*, 10555-10559; *Angew. Chem. Int. Ed.* **2013**, *52*, 10365-10369.
3. Muxin Han, Jakob Hey, Wataru Kawamura, Dietmar Stalke, Mitsuhiro Shionoya, Guido Clever, *Inorg. Chem.* **2012**, *51*, 9574-9576.
4. Sabrina Freye, Jakob Hey, Anna Torras-Galán, Dietmar Stalke, Regine Herbst-Irmer, Michael John, Guido H. Clever, *Angew. Chem.* **2012**, *124*, 2233-2237; *Angew. Chem. Int. Ed.* **2012**, *51*, 2191-2194.
5. Ramachandran Azhakar, Rajendra S. Ghadwal, Herbert W. Roesky, Jakob Hey, Dietmar Stalke, *Chem. Asian J.* **2012**, *7*, 528-533.
6. Ramachandran Azhakar, Rajendra S. Ghadwal, Herbert W. Roesky, Jakob Hey, Dietmar Stalke, *Dalton Trans.* **2012**, *41*, 1529-1533.
7. Sakya S. Sen, Jakob Hey, Daniel Kratzert, Herbert W. Roesky, Dietmar Stalke, *Organometallics* **2012**, *31*, 435-439.
8. Sakya S. Sen, Jakob Hey, Maria Eckhardt, Regine Herbst-Irmer, Ricardo A. Mata, Herbert W. Roesky, Manfred Scheer, Dietmar Stalke, *Angew. Chem.* **2011**, *123*, 12718-12721; *Angew. Chem. Int. Ed.* **2011**, *50*, 12510-12513 and back cover.

-
- Ramachandran Azhakar, Rajendra S. Ghadwal, Herbert W. Roesky, Jakob Hey, Dietmar Stalke, *Organometallics* **2011**, *30*, 3853-3858.
 - Sakya S. Sen, Jakob Hey, Regine Herbst-Irmer, Herbert W. Roesky, Dietmar Stalke, *J. Am. Chem. Soc.* **2011**, *133*, 12311-12316.
 - Ramachandran Azhakar, Sankaranarayana Pillai Sarish, Herbert W. Roesky, Jakob Hey, Dietmar Stalke, *Organometallics* **2011**, *30*, 2897-2900.
 - Ramachandran Azhakar, Sankaranarayana Pillai Sarish, Herbert W. Roesky, Jakob Hey, Dietmar Stalke, *Inorg. Chem.* **2011**, *50*, 5039-5043.
 - Ramachandran Azhakar, Sankaranarayana Pillai Sarish, Gašper Tavčar, Herbert W. Roesky, Jakob Hey, Dietmar Stalke, Debasis, *Inorg. Chem.* **2011**, *50*, 3028-3036.
 - Ramachandran Azhakar, Gašper Tavčar, Herbert W. Roesky, Jakob Hey, Dietmar Stalke, *Eur. J. Inorg. Chem.* **2011**, 475-477.
 - Gašper Tavčar, Sakya S. Sen, Herbert W. Roesky, Jakob Hey, Daniel Kratzert, Dietmar Stalke, *Organometallics*, **2010**, *29*, 3930-3935.
 - Sakya S. Sen, Gašper Tavčar, Herbert W. Roesky, Daniel Kratzert, Jakob Hey, and Dietmar Stalke, *Organometallics* **2010**, *29*, 2343-2347.

Presentations

- Gordon Research Conference on Electron Density and Chemical Bonding*, June 7th **2013**, Les Diablerets, Switzerland; Invited Talk.
- Meeting of the Center for Materials Crystallography (CMC)* **2012**, Göttingen; Oral Presentation.
- 6th European Charge Density Meeting*, Strbske Pleso, Slovakia, **2012**; Poster Presentation.
- JSPS/DFG Bilateral Seminar on X-Ray Free Electron Lasers* **2011**, Kyoto, Japan; Oral Presentation.
- CaSuS workshop* **2011**, Goslar; Poster Presentation.
- IUCr triennial meeting* **2011**, Madrid, Spain; Poster Presentation.
- Workshop of the workgroup of Prof. Dr. Scherer*, **2010**, Sion, Switzerland; Oral Presentation.
- Meeting of the Center for Materials Crystallography (CMC)* **2010**, Göttingen; Oral Presentation.
- Niedersächsisches Katalyse-Symposium* **2010**, Göttingen; Poster Presentation.
- CaSuS Workshop* **2010**, Bad Mariaspring; Oral Presentation.
- Gordon Research Conference on Electron Density and Chemical Bonding* **2010**, Mount Holyoke, USA; Poster Presentation.